REPUBLIC OF BENIN

------000------

MINISTRY OF HIGHER EDUCATION AND SCIENTIFIC RESEARCH

------000------

UNIVERSITY OF ABOMEY - CALAVI

------000------

DOCTORAL SCHOOL OF LIFE AND EARTH SCIENCES

------000------

Registered under N°: 440

A DISSERTATION

Submitted

In partial fulfillment of the requirements for the degree of
DOCTOR of Philosophy (PhD) of the University of Abomey-Calavi
In the framework of the
Graduate Research Program on Climate Change and Water Resources (GRP-CCWR)
By

MAWULOLO YOMO

Public defense on: 10/31/2024

======

DYNAMICS OF SEAWATER INTRUSION IN THE COASTAL SEDIMENTARY BASIN OF TOGO UNDER CLIMATE CHANGE AND LAND USE, LAND COVER CHANGE. A CASE STUDY OF THE MULTI-LAYERED AQUIFER OF THE AGOENYIVE PLATEAU.

======

Supervisors:

Euloge Nicaise YALO	Full Professor	University of Abomey Calavi (UAC), Benin
Masamaéya D. T. GNAZOU	Full Professor	University of Lomé (UL), Togo

Reviewers:

Mahamadou KOITA	Full Professor	International Institute for Water and Environmental Engineering (2iE), Burkina Faso
Geophrey Kwame ANORNU	Full Professor	Kwame Nkrumah University of Science and Technology (KNUST), Ghana
Casimir Yélognissè DA-ALLADA	Associate Professor	Université Nationale des Sciences, Technologie, Ingénierie et Mathématiques (UNSTIM), Benin

JURY

Agnidé Emmanuel LAWIN	Full Professor, University of Abomey Calavi (UAC), Benin	President
Mahamadou KOITA	Full Professor, International Institute for Water and Environmental Engineering (2iE), Burkina Faso	Reviewer
Geophrey Kwame ANORNU	Full Professor, Kwame Nkrumah University of Science and Technology (KNUST), Ghana	Reviewer
Casimir Yélognissè DA-ALLADA	Associate Professor, Université Nationale des Sciences, Technologie, Ingénierie et Mathématiques (UNSTIM), Benin	Reviewer
Christophe KAKI	Full Professor, University of Abomey Calavi (UAC), Benin	Examiner
Euloge Nicaise YALO	Full Professor, University of Abomey Calavi (UAC), Benin	Supervisor
Masamaéya D. T. GNAZOU	Full Professor, University of Lomé (UL), Togo	Co-supervisor
Stephen SILLIMAN	Full Professor, Trevecca Nazarene University, USA	Advisor
Christoph SCHÜTH	Full Professor, Technische Universität Darmstadt, Germany	Advisor

WASCAL West African Science Service Centre on Climate Change and Adapted Land Use
Federal Ministry of Education and Research

REPUBLIQUE DU BENIN

------000------

MINISTERE DE L'ENSEIGNEMENT SUPERIEUR ET DE LA RECHERCHE SCIENTIFIQUE

------000------

UNIVERSITE D'ABOMEY - CALAVI

------000------

ECOLE DOCTORALE SCIENCES DE LA VIE ET DE LA TERRE

------000------

Enregistrée sous N°: 440

THESE

Soumise pour obtenir le grade de
DOCTEUR de l'Université d'Abomey-Calavi
Dans la Spécialité:
Changement climatique et Ressources en Eau
Par
YOMO MAWULOLO

Soutenue publiquement le : 31/10/2024

======

DYNAMIQUE DE L'INTRUSION MARINE DANS LE BASSIN SÉDIMENTAIRE CÔTIER DU TOGO DANS LE CONTEXTE DES CHANGEMENTS CLIMATIQUES ET LES CHANGEMENTS DANS L'OCCUPATION ET L'UTILISATION DES SOLS. UNE ÉTUDE DE CAS DE L'AQUIFÈRE MULTICOUCHE DU PLATEAU D'AGOENYIVE.

======

Directeurs de thèse:		
YALO Euloge Nicaise	Professeur Titulaire	Université d' Abomey Calavi (UAC), Benin
GNAZOU D. T. Masamaéya	Professeur Titulaire	Université de Lomé (UL), Togo
Rapporteurs:		
KOITA Mahamadou	Professeur Titulaire	Institut International d'Ingénierie de l'Eau et de l'Environnement ((2iE), Burkina Faso
ANORNU Geophrey Kwame	Professeur Titulaire	Kwame Nkrumah University of Science and Technology (KNUST), Ghana
DA-ALLADA Casimir Yélognissè	Maître de Conférences	Université Nationale des Sciences, Technologie, Ingénierie et Mathématiques (UNSTIM), Benin

JURY

LAWIN Agnidé Emmanuel	Professeur Titulaire, Université d'Abomey Calavi (UAC), Benin	President
KOITA Mahamadou	Professeur Titulaire, Institut International d'Ingénierie de l'Eau et de l'Environnement (2iE), Burkina Faso	Rapporteur
ANORNU Geophrey Kwame	Professeur Titulaire, Kwame Nkrumah University of Science and Technology (KNUST), Ghana	Rapporteur
DA-ALLADA Casimir Yélognissè	Maître de Conférences, Université Nationale des Sciences, Technologie, Ingénierie et Mathématiques (UNSTIM), Benin	Rapporteur
KAKI Christophe	Professeur Titulaire, Université d'Abomey Calavi (UAC), Benin	Examinateur
YALO Euloge Nicaise	Professeur Titulaire, Université d'Abomey Calavi (UAC), Benin	Superviseur
GNAZOU D. T. Masamaéya	Professeur Titulaire, Université de Lomé (UL), Togo	Co-superviseur
SILLIMAN Stephen	Professeur Titulaire, Université de Trevecca Nazarene, USA	Membre d'encadrement
SCHÜTH Christoph	Professeur Titulaire, Technische Universität Darmstadt, Allemagne	Membre d'encadrement

WASCAL West African Science Service Centre on Climate Change and Adapted Land Use
Federal Ministry of Education and Research

Dedication

I dedicate this work to God Almighty for taking me through the entire process and to my beautiful and caring mother, Francoise Balamwe AMAYI, for her sacrifice, for being an inspiration to me, and for her continuous support, care, prayers, and love. I love you deeply and dearly.

Acknowledgment

My first appreciation goes to the German Ministry of Education and Research (BMBF) for fully funding this PhD project and to the West African Science Service Center on Climate Change and Adapted Land Use (WASCAL) in collaboration with the Benin Ministry of Higher Education and Scientific Research (MESRS), under whose auspices this research has been carried out.

I do also appreciate the administration of the Université of Abomey Calavi and especially WASCAL Doctoral Graduate School (Climate Change and Water Resources) for their support.

I am highly indebted and grateful to my supervisors, Prof. Nicaise Yalo, Prof. Masamaéya D. T. Gnazou, and my scientific advisors, Prof. Stephen Silliman and Prof. Christoph Schüth. Your valuable input, patience, and support have helped me through the entire process. God bless you. Furthermore, I would like to give my special thanks to Prof. GNAZOU for believing in me since my master's degree, supporting me, and releasing your materials for my fieldwork. Another special thanks goes to Prof. Silliman. You have always challenged me throughout this PhD journey to bring out the best in me. God bless you. I would also like to appreciate Dr. Isaac Larbi. You have been a great blessing to me. At the same time, I would like to acknowledge the geophysics unit and the Laboratory of Applied Hydrology and Environment (LHAE) of the University of Lomé, and the hydrogeology unit of the Technische Universität Darmstadt, for their tireless and continuous support throughout this study.

My deep gratitude and acknowledgment also go to UNESCO and the L'Oréal Foundation for bestowing upon me the Young Talents Sub-Saharan Africa Awards for Women in Science, which have greatly aided in the funding of this research project. A special thank you also goes to the International Atomic Energy Agency (IAEA) in collaboration with the National Engineering School of Sfax, Tunisia (Laboratory of Radio-analysis and Environment) for supporting my isotope hydrology training and the isotopic analysis of my water samples. I would also like to express my gratitude to the Togolese Meteorological Agency for providing climate data to support this study endeavor.

Lastly, and above all, my sincere thanks go to my beautiful and sweet mother, Balamwe AMAYI, as well as to my siblings, Claudia, Roi Joel, and Sonia, and my aunties and uncles for their unwavering prayers, support, and encouragement, which have been essential to me during this journey. To my lovely nieces Light Polle and Believe Polle, as well as my friends Emmanuel Alfa, Josue Lukabwe, and Rose Amegnoka, thank you for your companionship during this journey.

Abstract

In coastal settings where groundwater represents a critical resource for industries and is a source of drinking water for a growing population, anticipating the response of the groundwater lens (in terms of its quality and quantity) to climate change, changes in land use and land cover, as well as continuous groundwater withdrawal, becomes a requirement. This is the case of the Agoènyivé plateau (AP), which hosts up to 25 percent of the national population and is characterised by high rates of population growth and urbanisation. This step becomes necessary to ensure the sustainability of the resource but also to protect the ecosystem that holds it. Thus, this study investigated the dynamics of seawater intrusion in the context of climate change, land use and land cover change, and continuous groundwater withdrawal in the Sedimentary Coastal Basin of Togo, considering the multi-layered aquifer of the AP as a case study.

The assessment of land use and land cover (LULC) using ENVI and Land Change Modeller revealed the predominance of built-up areas in the AP, the area of which has increased over the years at the expense of croplands/bare surfaces, mixed vegetation/savannah, and wetlands, with an estimated land gain of 38.71% from 1986 to 2020. For the future, the trend in LULC is expected to follow the same dynamics as in the past under the Business as Usual (BAU) scenario. The area of built-up areas is expected to increase, with an estimated 12.5% by 2030 and 31.7% by 2050, compared to the year 2020.

To capture climate evolution in the AP, the ensemble mean of the outputs of the four Regional Climate Models considered (CanESM2-RCA4, NorESM1-RCA4, CCLM4-8-17, and RACMO22T), obtained from the COordinated Regional climate Downscaling EXperiment project (CORDEX), projects a drier climate over the period 2021–2050 compared to the period 1991–2020. This period will be characterised by a non-significant ($p > 0.05$) slight increase in annual rainfall of 0.05 mm under RCP 4.5 against an annual decrease of 0.69 mm under RCP 8.5. Additionally, a significant ($p < 0.05$) annual increase in the mean temperature is projected, amounting to 0.01 °C under RCP 4.5 and 0.02 °C under RCP 8.5.

The hydrochemistry and isotopic signatures of the analysed water samples suggested marine input, dissolution of evaporitic minerals (Halite, Gypsum, and Anhydrite), base exchange, and evaporation as the main pathways contributing to the mineralisation of the existing aquifers in the AP. The upper aquifers (Continental Terminal and the Coastal Marine Sands) are particularly affected by constant seawater intrusion, exhibiting chlorinated sodic-potassic and hyper-

chlorinated sodic facies. These findings were corroborated by electrical resistivity tomography profiles, which suggested a lateral intrusion reaching approximately 2.5 km inland and an up coning of seawater in these aquifers. The seawater-freshwater interface was found at an average depth of 21 m (thickness ranging between 10 and 28 m).

Finally, the SEAWAT model, successfully calibrated and validated for the upper aquifers of the AP, showing R^2, KGE, and NSE values ranging between 0.6 and 0.9, 0.7 and 0.9, and 0.5 and 0.9, respectively, reproduced the dynamics of seawater intrusion under various scenarios. These scenarios included the increased water withdrawal rate (A); changes in the recharge considering current and future LULC and climate parameters (B1, B2, B3); sea level rise (C); and a combination of all scenarios (D). The results revealed that the salinity (TDS) is expected to increase in areas close to the ocean and at some points in areas close to the Cacaveli and Agoè Télessou water pumping fields (Obs 14 and Obs 15). By 2030/2050, salinity values are expected to range between 2.5/71.3 and 8739.6/22799.6 $mg.L^{-1}$ under scenario A; 7.33/142.73 and 8739.38/22776.98 $mg.L^{-1}$ under scenario B1; 236.5/1363.51 and 8741/22842 $mg.L^{-1}$ under scenario B2; 243.42/1363 and 8740.66/22810.65 $mg.L^{-1}$ under scenario B3; 0.05/51.43 and 10291.49/25228.78 $mg.L^{-1}$ under scenario C; and 0/44.38 and 10290.03/25211.85 $mg.L^{-1}$ under scenario D. These findings confirm both the lateral intrusion and up coning of seawater in the upper aquifers, as suggested by other methods. Under scenario D, the intruded area is projected to increase by 2.2% and 3.1%, respectively, by 2030 and 2050 with reference to the year 2021. These results underscore the need to consider additional water sources (deep aquifers or surface water) and/or redefine the exploitation conditions of the Continental Terminal in order to sustain the resource and the ecosystem that holds it.

Key Words: Agoènyivé Plateau, Climate change, Electrical Resistivity Tomography, Land use and land cover change, Modelling, SEAWAT

Synthèse de la Thèse

1. Résumé

Dans les zones côtières où les eaux souterraines représentent une ressource essentielle pour les industries et sont une source d'eau potable pour une population croissante, anticiper la réponse de la lentille d'eau souterraine (du point de vue de sa qualité et de sa quantité) aux changements climatiques, aux changements dans l'utilisation et l'occupation des terres, ainsi qu'aux prélèvements continus des eaux souterraines, devient un requis. C'est le cas du plateau d'Agoènyivé (PA) qui héberge jusqu'à 25 pour cent de la population nationale et est caractérisé par de forts taux de croissance démographique et d'urbanisation. Cette étape est nécessaire pour garantir la durabilité de la ressource et protéger l'écosystème qui l'héberge. Ainsi, cette étude a exploré la dynamique de l'intrusion marine dans le contexte des changements climatiques, des changements dans l'utilisation et de l'occupation des terres et des prélèvements continus dans le bassin sédimentaire côtier du Togo, en considérant l'aquifère multicouche du plateau d'Agoènyivé (PA) comme une étude de cas.

L'évaluation de l'utilisation et de l'occupation des terres (LULC) à l'aide des logiciels ENVI et Land Change Modeler a révélé la prédominance des zones bâties dans le PA, dont la surface a augmenté au fil des années au détriment des terres cultivées/surfaces nues, de la végétation mixte/savane et des zones humides, avec une augmentation estimée à 38,71% entre 1986 et 2020. Pour le futur, la tendance de l'utilisation et de l'occupation des terres devrait suivre la même dynamique que par le passé selon le scénario du statu quo. La surface des zones bâties devrait continuer à augmenter, avec une estimation de 12,5% en 2030 et de 31,7% en 2050, par rapport à l'année 2020.

En ce qui concerne l'évolution du climat dans le PA, la moyenne d'ensemble des quatre modèles climatiques régionaux considérés (CanESM2-RCA4, NorESM1-RCA4, CCLM4-8-17 et RACMO22T), obtenue dans le cadre du projet COordinated Regional climate Downscaling EXperiment (CORDEX-Africa), dépeint un climat plus sec sur la période de 2021–2050 en comparaison avec la période de 1991–2020. Cette période sera caractérisée par une non significative légère augmentation ($p > 0.05$) des précipitations annuelles de 0,05 mm selon le RCP 4.5 contre une diminution annuelle de 0,69 mm selon le RCP 8.5. En outre, une augmentation significative ($p < 0.05$) de la température moyenne est projetée, s'élevant à 0,01 °C selon le RCP 4.5 et 0,02 °C selon le RCP 8.5 annuellement.

L'hydrochimie et la signature isotopique des échantillons d'eau analysés ont évoqué l'apport marin, la dissolution des minéraux évaporitiques (Halite, Gypse et Anhydrite), l'échange de bases et l'évaporation comme voies principales contribuant à la minéralisation des aquifères existants. Les aquifères supérieurs (Continental Terminal et le Quaternaire) sont particulièrement affectés par l'intrusion constante d'eau de mer, exposant des faciès sodique-potassique chlorurés et sodique hyper-chlorurés. Ces découvertes ont été corroborées par les profils de tomographie de résistivité électrique, ayant suggéré une intrusion latérale atteignant approximativement 2,5 km à l'intérieur des terres et une remontée d'eau de mer dans ces aquifères. L'interface eau douce-eau salée a été localisée à une profondeur moyenne de 21 mètres (épaisseur comprise entre 10 et 28 mètres).

Enfin, le modèle SEAWAT, calibré et validé avec succès pour les aquifères supérieurs du PA, montrant des valeurs de R^2, KGE et NSE comprises entre 0,6 et 0,9 ; 0,7 et 0,9 et 0,5 et 0,9 ; respectivement, a reproduit la dynamique de l'intrusion marine selon divers scénarios. Ces scénarios incluent l'augmentation du taux des prélèvements (A), les changements de la recharge tenant compte de l'utilisation et de l'occupation des terres et les paramètres climatiques actuels et futurs (B1, B2 et B3), l'élévation du niveau de la mer (C) et la combinaison de tous les scénarios (D). Les résultats ont révélé que la salinité (TDS) devrait augmenter dans les zones proches de l'océan et à certains points dans les zones proches des champs de captage d'eau de Cacaveli et d'Agoè Télessou (Obs 14 et Obs 15). D'ici 2030/2050, les valeurs de salinité devraient être comprises entre 2,5/71,3 et 8739,6/22799,6 $mg.L^{-1}$ selon le scénario A ; 7,33/142,73 et 8739,38/22776,98 $mg.L^{-1}$ selon le scénario B1 ; 236,5/1363,51 et 8741/22842 $mg.L^{-1}$ selon le scénario B2 ; 243,42/1363 et 8740,66/22810,65 $mg.L^{-1}$ selon le scénario B3 ; 0,05/51,43 et 10 291,49/25 228,78 $mg.L^{-1}$ selon le scénario C ; et entre 0/44,38 et 10 290,03/25 211,85 $mg.L^{-1}$ selon le scénario D. Ces résultats confirment l'intrusion latérale et la remontée d'eau de mer dans les aquifères supérieurs mis en évidence par d'autres méthodes. Selon le scénario D, la zone intruse est projetée d'augmenter de 2,2% et 3,1% respectivement d'ici 2030 et 2050 en référence à l'année 2021. Ces résultats soulignent la nécessité de recourir à des sources d'eau supplémentaires (les aquifères profonds ou les eaux de surface) et/ou de redéfinir les conditions d'exploitation de l'aquifère du Continental Terminal afin d'assurer la pérennité de la ressource et de l'écosystème qui l'héberge.

Mots clés : Changements climatiques, Changement dans l'utilisation et de l'occupation des terres, Modélisation, Plateau d'Agoènyivé, SEAWAT, Tomographie de Résistivité Électrique

2. Introduction

Au Togo, le bassin sédimentaire côtier (principalement constitué du Paléocène, du Continental Terminal, du Maastrichtien et du Quaternaire), reconnu comme la principale source d'eau douce pour la population et les industries (DHE, 1984 ; Gnazou et al., 2015a), a été rapporté comme sujet à l'intrusion marine depuis les années 1980 (DHE, 1984 ; Amegadje, 2007 ; MERF/PANA, 2009 ; Gnazou et al., 2015a ; Gnazou et al., 2015b ; Gnazou et al., 2018). Le Continental Terminal, qui alimente jusqu'à 70 pour cent de l'approvisionnement public en eau par l'intermédiaire de la Société togolaise des eaux et environ 11 870 forages industriels et privés dans le plateau d'Agoènyivé (Gnazou et al., 2015b), a été considéré comme le plus impacté (ANTEA, 2013).

Hébergeant la plupart des industries du pays, le plateau d'Agoènyivé (PA) devrait connaître une croissance démographique importante. Cela aura pour conséquence une demande accrue en eau qui conduirait à son tour à la surexploitation des aquifères existants si des sources additionnelles d'eau ne sont pas prises en compte. De plus, étant un milieu urbain et côtier, le PA devrait être soumis à un changement continu d'utilisation et d'occupation des terres (LULC). En outre, les changements, incluant ceux des paramètres climatiques (précipitations, température et évapotranspiration) et l'élévation du niveau de la mer associée, tels que rapportés par le GIEC, ne peuvent être minimisés. Tous les facteurs mis en évidence ci-dessus, notamment les changements climatiques, les changements dans l'utilisation et l'occupation des terres, ainsi que l'augmentation des prélèvements, devraient affecter vraisemblablement les eaux souterraines du PA, menaçant ainsi la ressource (sa quantité comme sa qualité). Pour contribuer aux efforts visant à pérenniser la ressource et à protéger l'écosystème qui l'héberge dans le contexte de tous ces changements dans le PA, cette étude vise à évaluer la réponse des aquifères supérieurs (charge hydraulique et salinité) dans le contexte de l'augmentation des prélèvements à l'élévation du niveau de la mer, aux changements climatiques (précipitations et température) et aux changements dans l'utilisation et l'occupation des terres (LULC) à l'aide du code/programme SEAWAT.

3. Zone d'Etude

Le plateau d'Agoènyivé (PA) est situé dans la partie occidentale du Bassin Sédimentaire Côtier au Togo (situé entre Lomé et Mission Tové) entre les latitudes 6° 06' et 6° 21' Nord et les longitudes 1° 01' et 1° 17' Est. Il est bordé par les affleurements du socle cristallin panafricain au nord, la partie offshore sous l'océan Atlantique au sud, le Ghana à l'ouest et la vallée de Zio à l'est. Il s'étend sur 420 km² et couvre l'ensemble des préfectures du Golfe (y compris la commune de

Lomé) et partiellement celles de Zio, d'Ave et d'Agoènyivé. Les principales caractéristiques de la zone d'étude sont résumées dans le Tableau 1.

Tableau 1 : Les Caractéristiques du Plateau d'Agoènyivé

Caractéristique	**Agoènyivé Plateau**
Population	1627437 habitants (2010)
Climat	Climat subéquatorial (Pluviométrie moyenne annuelle : 864 mm à Lomé, Température moyenne mensuelle : 25–29 °C à Lomé, Pluviométrie : Bi-modal avec 2 saisons des pluies incluant Mars–Juillet et septembre–novembre)
Zone écologique et Végétation	Zone V avec un paysage de savane boisée ou arbustive : espèces végétales incluant Cocoteraies, tapis de graminées et débris de mangrove, Fourrés (Mitragyna inermis, Elaeophorbia drupifera et Capparis), Cultures, Graminées, Jardins
Types de sol	Sols ferrallitiques, sols hydromorphes et sols de contribution peu évolués
Contexte géologique	Mésozoïque (Maastrichtien : 79 km^2), Xénozoïque (Paléocène et Éocène couvrant une superficie de 78 km^2 et 225 km^2, respectivement), Continental Terminal (382 km^2) et les dépôts quaternaires (41 km^2)
Contexte hydrogéologiques	Trois aquifères principales : Continental Terminal (avec le Quaternaire considéré comme une continuité), le Paléocène et le Maastrichtien

Source : Compilées à partir de Slansky (1962), PNUD (1975), Ern (1979), Millet (1986), Johnson (1987), Fontaine (1991), Le Barbé et al. (1993), Blivi (2005), Da Costa (2005), Gnazou (2008), DGSCN (2011), Gnazou et al. (2015a), Gnazou et al. (2015b) et Akakpo (2017)

4. Matériel et Méthodes

Différents types d'ensembles de données, ainsi que de multiples méthodes et outils, ont été pris en compte pour comprendre la dynamique de l'intrusion marine dans les aquifères du PA.

Les images satellitaires Landsat 5 et 7 d'une résolution spatiale de 30 m pour les années 1986, 2001, 2011 et 2020 ont été considérées en plus des données de référence (points de contrôle sur le terrain, points de contrôle des cartes topographiques, points de contrôle des images Google Earth et des cartes classifiées), ainsi que les perceptions locales de la dynamique de l'utilisation et de l'occupation des terres. Les logiciels ENVI et le Land Change Modeler (LCM) ont été utilisés pour élucider respectivement les tendances historiques et futures du LULC (les scénarios incluant le statu quo, le reboisement, la restauration des zones humides et la politique de la construction).

Dans ce contexte, les données d'observations provenant des satellites (CHIRPS et NASA POWER) et des stations in situ d'une part, et les sorties dépourvues de biais des modèles climatiques régionaux (CanESM2-RCA4, NorESM1-RCA4, CCLM4-8-17 et RACMO22T) du projet COordinated Regional climate Downscaling EXperiment (CORDEX-Africa) d'autre part,

ont été considérées et analysées au moyen des tests de Mann-Kendall et Mann-Kendall modifié combinés au test de Sen afin d'évaluer la tendance climatique historique (1991–2020) et future (2021–2050).

Pour comprendre les principales voies de minéralisation des aquifères existants dans le PA, 269 échantillons d'eau ont été collectés des aquifères existants (Quaternaire, Continental Terminal, Paleocene, Maastrichtien) et des eaux de surfaces (système lagunaire de Lomé et l'océan) pendant les deux saisons principales. L'analyse des paramètres physicochimiques obtenus a été réalisée en utilisant plusieurs méthodes et outils, incluant les statistiques descriptives, les tracés bivariés, les index et les diagrammes. De plus, la signature isotopique des aquifères (49 échantillons d'eau) illustrée au travers des tracés (δ^2H/chlorures/conductivité électrique contre d^{18}O) ainsi que la distribution de la vraie résistivité du sous-sol obtenue au travers des profils de tomographie de résistivité électrique ont été considérées afin d'approfondir la compréhension de l'origine de la salinisation des aquifères considérés et de mettre en évidence l'interface d'eau douce-eau salée, si existante. Enfin, les niveaux statiques de certains forages considérés ont été mesurés afin d'établir les cartes piézométriques des aquifères existants.

Le bilan hydrique prenant en compte la méthode du Soil Conservation Service Curve Number (SCS-CN) et la méthode combinée de Coutagne-Turc a été utilisée pour estimer la recharge dans le contexte du PA considérant divers scénarios (basés sur les changements dans l'utilisation et l'occupation des terres et les changements dans les paramètres climatiques) pour les années 2020, 2030 et 2050. Les valeurs obtenues ont été utilisées comme une des données d'entrée du modèle SEAWAT pour simuler la réponse actuelle et future (en termes de la salinité et de la charge hydraulique) de la lentille d'eau des aquifères supérieurs du PA (Continental Terminal et Quaternaire). Les scénarios considérés, incluent l'augmentation des prélèvements (scénario A), l'élévation du niveau de la mer (scénario C), les changements dans les paramètres climatiques et dans l'utilisation et l'occupation des terres (scénarios B1, B2 et B3) et la combinaison de tous les scénarios (D).

5. Résultats et Discussion

La tendance historique de l'utilisation et de l'occupation des terres révèle une augmentation des surfaces bâties (gain de terres de 38,71%) au détriment des surfaces nues et des terres cultivées (perte de terres de 22,89%), qui à leur tour se sont accrues par la conversion des zones humides (perte de terres de 3,36%) et des zones mixtes végétation/savane (perte de terres de 22,69%). Selon

le scénario du statu quo, la tendance de l'utilisation et de l'occupation futures des terres devrait suivre la même dynamique que celle du passé. Cependant, les scénarios considérés ont démontré leur potentiel d'accroître les zones humides (scénario de politique des zones humides) ou les zones de végétation mixte/savane (scénario de reboisement). Néanmoins, il est prévu que la politique de construction sera à long terme associée à l'augmentation des superficies des zones de végétation mixte/savane, de terres cultivées/surfaces nues et de zones humides en même temps (comparé au scénario du statu quo).

Les tendances climatiques historiques dans le PA ont mis en évidence une augmentation non significative ($p > 0,05$) des précipitations estimées à 0,81 mm annuellement (avec un cumul estimé à 24,3 mm) contre une augmentation significative ($p < 0,05$) de la température estimée à 0,02 °C annuellement (avec un cumul estimé à 0,6 °C) pour la période 1991–2020. Dans le futur, une légère augmentation des précipitations annuelles représentant 0,05 mm par an (avec un cumul estimé à 1,5 mm) selon le RCP 4.5 contre une diminution représentant 0,69 mm par an (avec un cumul estimé à 20,7 mm) selon le RCP 8.5 sont attendues. Quant à la température moyenne, un réchauffement annuel estimé à 0,01 °C (avec un cumul estimé à 0,31 °C) et à 0,02 °C (avec un cumul estimé à 0,6 °C) est attendu selon le RCP 4.5 et le RCP 8.5, respectivement.

L'hydrochimie et la signature isotopique des échantillons d'eau considérés ont révélé que l'intrusion d'eau de mer, la dissolution des minéraux évaporitiques (halite, gypse et anhydrite), l'échange de bases et l'évaporation représentent les voies clés de minéralisation des aquifères considérés dans le PA. Néanmoins, la présence des faciès chloruré sodique et potassique et du faciès hyper chloruré sodique pour les aquifères supérieurs (Continental Terminal et le Quaternaire) témoignent d'une intrusion continue d'eau de mer. Pour le Paléocène, l'apparition brutale (sans transition) observée du faciès chloruré sodique et potassique pour certains échantillons d'eau suggère une intrusion isolée d'eau de mer (voie de salinisation 2 avec un mélange des faciès Ca-Mg-HCO3 et Na-Cl). Cela peut être dû à la proximité des points d'eau de l'océan ou de la lagune, mais aussi à la pression de pompage (majoritairement à usage industriel ou pour l'approvisionnement en eau potable). De plus, les résultats de la tomographie de résistivité électrique (avec la profondeur d'investigation couvrant uniquement les aquifères supérieurs) suggèrent à la fois une intrusion latérale (dans les zones proches de l'océan comme la plage et Ahanoukopé, avec l'interface eau douce-eau salée atteignant 2,5 km à l'intérieur des terres) et une intrusion ascendante (dans la zone de Cacaveli près du champ captant de la TdE à Cacaveli), avec

l'interface eau douce-eau salée (une zone de mélange) retrouvée à une profondeur moyenne de 21 m avec une épaisseur comprise entre 10 m et 28 m. En effet, considérant les cartes piézométriques, ces deux zones sont caractérisées par un niveau piézométrique bas et proche du niveau de la mer. De plus, la présence du champ de captage de la TdE dans la zone de Cacaveli est associée à un cône de dépression, qui agirait comme un puits secondaire avec une contribution plausible de l'océan à la recharge de l'aquifère.

Les valeurs de la recharge future pour le PA sont projetées en référence à la recharge estimée pour l'année 2020 (62,21 mm). Pour le scénario LULC-CC, la recharge devrait augmenter de 30/1 mm et diminuer de 34/4 mm d'ici 2030/2050 pour le RCP 4.5 et RCP 8.5, respectivement. Pour le scénario LULCC, la recharge devrait diminuer de 14/52 mm d'ici 2030/2050. Enfin, pour le scénario CC, il est attendu une augmentation de la recharge de 51/55 mm d'ici 2030/2050 pour le RCP 4.5, pendant que pour le RCP 8.5, une diminution de 21 mm et une augmentation de 65 mm sont attendues d'ici 2030 et 2050, respectivement. De là, les scénarios construits à partir de ces résultats (B1, B2 et B3) en plus des scénarios A (augmentation des prélèvements), C (élévation du niveau de la mer) et D (scénarios combinés) ont été utilisés pour appréhender la dynamique de l'intrusion d'eau de mer dans les aquifères supérieurs.

Les variations de la charge hydraulique et de la salinité aux points d'observation considérés sont illustrées dans les figures 1a-b. En référence à l'année 2021, la charge hydraulique dans les zones proches de l'océan devrait diminuer entre 0,01/0,02 et 0,3/0,7 m ; 0,01/0,02 et 0,32/0,7 m ; 0,01/0,01 et 0,33/0,73 m ; 0,01/0,02 et 0,4/0,73 m ; 0,03/0,05 et 0,22/0,58 m ; et 0,03/0,07 et 0,49/0,58 m d'ici 2030/2050 pour les scénarios A, B1, B2, B3, C et D, respectivement. Cette tendance devrait être associée à une augmentation de la salinité (en référence au TDS simulé en 2021) variant entre 2,5/71,3 et 8739,6/22799,6 $mg.L^{-1}$; 7,33/142,73 et 8739,38/22776,98 $mg.L^{-1}$; 236,5/1363,51 et 8741/22842 $mg.L^{-1}$; 243,42/1363 et 8740,66/22810,65 $mg.L^{-1}$; 0,05/51,43 et 10291,49/25228,78 $mg.L^{-1}$ et 0/44,38 et 10290,03/25211,85 $mg.L^{-1}$ d'ici 2030/2050 pour les scénarios A, B1, B2, B3, C et D, respectivement. Pour les zones proches des champs de captage de Cacaveli et d'Agoè Télessou, une diminution de la charge hydraulique est projetée (en référence aux charges hydrauliques simulées de l'année 2021) avec des valeurs comprises entre 0,05/0,11 et 4,65/7,15 m ; 0,02/0,06 et 5,04/9,79 m ; 0,02 et 2,19 m ; 0,03/0,09 et 4,65/7,15 m ; 0,03/0,09 et 4,65/7,15 m ; et 0,02/0,09 et 5,6/7,56 m d'ici 2030/2050 pour les scénarios A, B1, B2, B3, C et D, respectivement. Ces changements au niveau de la charge hydraulique sont projetés être associés à

une absence de changement de salinité (observée dans la partie nord du PA), à l'exception des points d'observation Obs14 et Obs15 qui montrent respectivement une augmentation de la salinité atteignant des valeurs variant entre 510,5/1708,9 $mg.L^{-1}$ et 709,4/782,15 $mg.L^{-1}$; 510,54/1198,22 $mg.L^{-1}$ et 734,48/752,04 $mg.L^{-1}$; 510.51–510.53/1701.44–1709.06 et 713.76–1050.02/733.04–782.22 $mg.L^{-1}$ d'ici 2030/2050 pour les scénarios A, B1 et B3. Pour les scénarios B2 et B3, seul le point d'observation Obs 14 devrait connaître une augmentation continue de la salinité, atteignant des valeurs de 510,54/1709,33 $mg.L^{-1}$ d'ici 2030/2050. Pour les scénarios C et D, une augmentation de la salinité est espérée pour les points d'observation Obs 14 (707,18/782,15 $mg.L^{-1}$ d'ici 2030/2050) et Obs 15 (705,18–818,7/750,54–863,7 $mg.L^{-1}$ d'ici 2030/2050).

Outre les changements mentionnés ci-dessus, une augmentation plausible de la charge hydraulique est également attendue, notamment pour les scénarios B2, C et D. Dans les zones proches de l'océan, l'augmentation de la charge hydraulique devrait atteindre des valeurs tels que 0,01–0,15/0,04–0,23 m ; 0,07–0,22/0,04–0,2 m ; et 0,02–0,24/0,03–0,22 m d'ici 2030/2050 pour les scénarios B2, C et D, respectivement. Cette tendance devrait être associée à une augmentation de la salinité estimée à 0–242,83/0–925,91 $mg.L^{-1}$; 192,66–1011,62/727,69–3227,73 $mg.L^{-1}$; et 182,54–1011,66/719,69–3228,27 $mg.L^{-1}$ d'ici 2030/2050 pour les scénarios B2, C et D respectivement. Quant aux zones proches des champs de captage de Cacaveli et d'Agoè Télessou, l'augmentation de la charge hydraulique est projetée atteindre respectivement 0,03–0,43/0,06–1,18 m ; 0,21–0,23/0,17–0,19 m ; et 0,21–0,79/0–0,19 m d'ici 2030/2050 pour les scénarios B2, C et D. À l'exception du point d'observation Obs15 qui montre une augmentation attendue de la salinité s'élevant respectivement à des valeurs de 763,88/653,65 $mg.L^{-1}$; 509,3/1702,07 $mg.L^{-1}$; et 509,41/1702,19 $mg.L^{-1}$ d'ici 2030/2050 pour les scénarios B2, C et D, les autres points d'observation dans cette zone ne montrent aucun changement dans la salinité. Finalement, selon le scénario D (considéré comme le plus probable), l'intrusion des aquifères supérieurs du PA par l'eau de mer est caractérisée par un pied de l'interface ou la zone de transition s'étendant jusqu'à 5 km à l'intérieur des terres (avec une salinité comprise entre 1000 et 8635 $mg.L^{-1}$, 1000 et 18800 $mg.L^{-1}$ et 1000 et 33600 $mg.L^{-1}$ pour les années 2021, 2030 et 2050, respectivement). La superficie de la zone intruse représente 140,92 km^2 en 2021 (~16% du PA au sens large) avec une augmentation attendue de 2,2% et de 3,1% d'ici 2030 et 2050, respectivement.

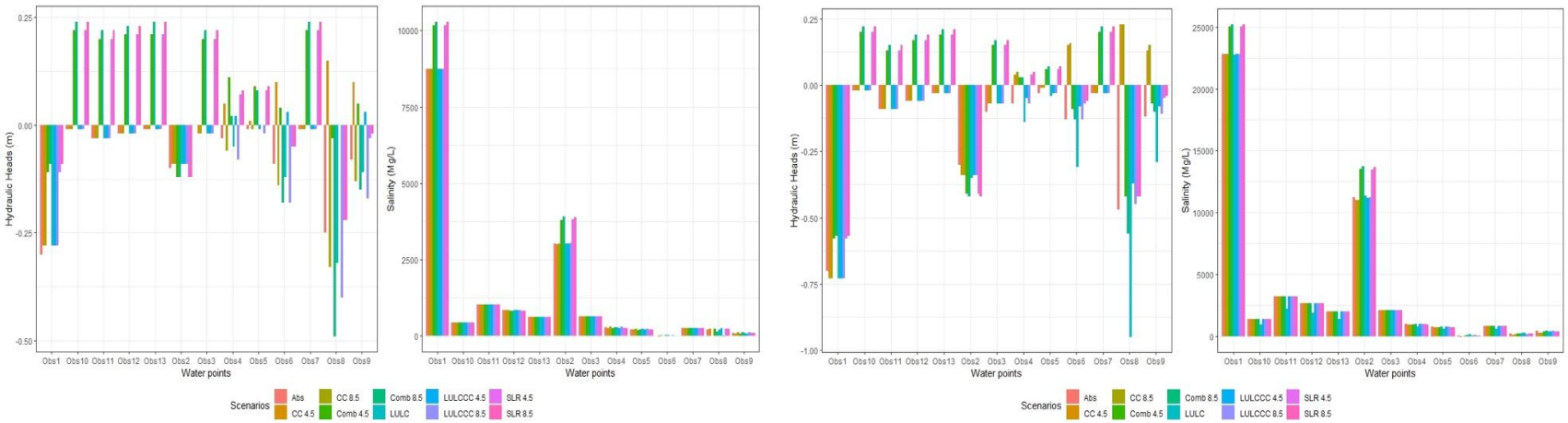

Figure 1a : Dynamique de la charge hydraulique et de la salinité (TDS) pour les échantillons situés dans la partie sud du PA à l'horizon 2030 (Gauche) et 2050 (Droite) : Scénario D

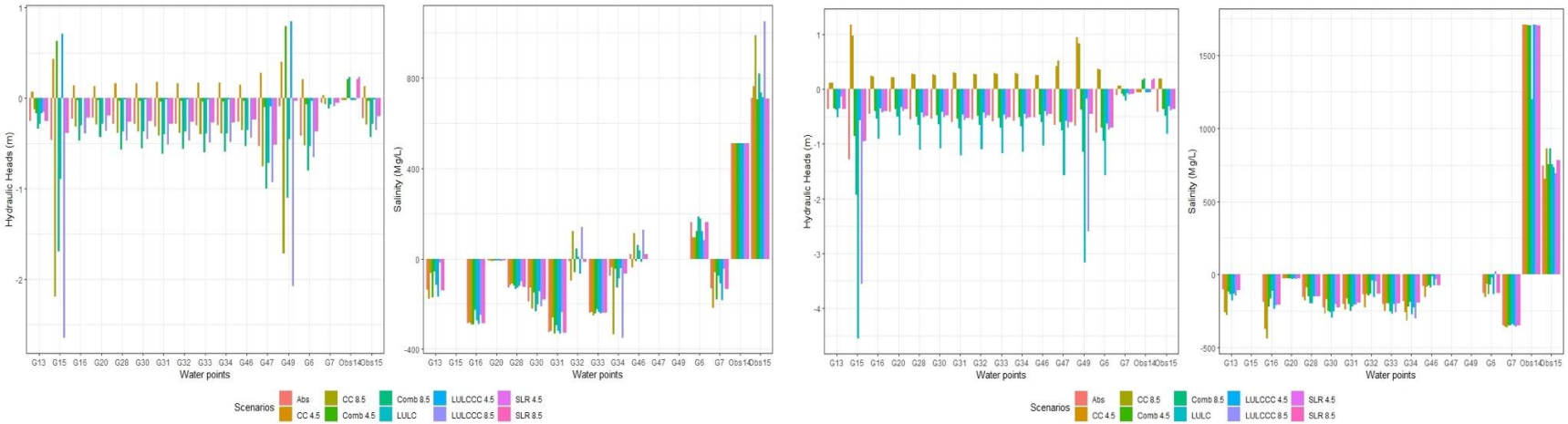

Figure 1b : Dynamique de la charge hydraulique et de la salinité (TDS) pour des échantillons situés autour de Cacaveli à l'horizon 2030 (à gauche) et 2050 (à droite) : Scénario D

6. Conclusion

Cette étude a exploré quatre menaces majeures pesant sur la gestion durable des eaux souterraines dans le BSCT, incluant les changements climatiques, les changements dans l'utilisation et l'occupation des sols, l'augmentation continue des prélèvements d'eau souterraine et l'élévation du niveau de la mer. Elle a combiné la géophysique (distribution de la vraie résistivité), l'hydrochimie (méthodes et outils conventionnels et statistiques), l'isotopie (δ^2H and $\delta^{18}O$) et la modélisation hydrogéologique (programme/code SEAWAT) afin de comprendre la dynamique de l'intrusion marine dans l'aquifère multicouche du plateau d'Agoènyivé (PA).

Face aux changements attendus dans le PA incluant l'assèchement du climat, l'augmentation des battis au détriment des autres classes d'utilisation et d'occupation des terres, l'augmentation continue des prélèvements et l'élévation du niveau de la mer, le modèle SEAWAT prédit une diminution des charges hydrauliques dans la plupart des scénarios, notamment A, B1, B2, B3, C et D. Néanmoins, il est à souligner que bien que plusieurs tendances dans le changement de la salinité soient associées à la variation de la charge hydraulique, il est clair que la salinité devrait augmenter dans les zones proches de l'océan et à certains points d'observation autour des champs de captage de Cacaveli et d'Agoè Télessou, confirmant ainsi une intrusion latérale (avec une zone de transition atteignant jusqu'à 5 km à l'intérieur des terres) et les remontées d'eau salée suggérées par les profils géophysiques (avec l'interface eau douce-eau salée localisée à une profondeur moyenne de 21 m avec une épaisseur comprise entre 10 et 28 m). Selon le scénario D, la zone intruse, représentant 140,92 km^2 en 2021, devrait augmenter de 2,2/3,1% d'ici 2030/2050.

La situation observée dans le PA pourrait conduire à la fermeture de certains points d'eau en raison de l'augmentation de la salinité, ce qui menace l'approvisionnement en eau potable de la ville de Lomé et de ses environs. Les résultats ci-dessus appellent à envisager des sources d'eau supplémentaires ou à redéfinir les conditions d'exploitation des aquifères supérieurs en particulier le Continental Terminal afin de pérenniser la ressource et l'écosystème qui l'héberge.

Table of Contents

Abbreviations and Acronyms

AP	:	Agoènyivé Plateau
AR5	:	Fifth Assessment Report
CC	:	Climate Change
CORDEX	:	CO-ordinated Regional Downscaling Experiment
DEM	:	Digital Elevation Model
DS	:	Dry Season
ETM	:	Enhanced Thematic Mapper
ERT	:	Electrical Resistivity Tomography
FAO	:	Food and Agriculture Organization of the United Nations
GCM	:	Global Climate Model
GIS	:	Geographic System of Information
GWW	:	Groundwater Withdrawal
IPCC	:	Intergovernmental Panel on Climate Change
LULC	:	Land Use and Land Cover
MEFR	:	Ministry of the Environment and Forest Resources
NNW	:	North–North–West
PA	:	Plateau d' Agoènyivé
RCM	:	Regional Climate Model
RCP	:	Representative Concentrative Pathways
REDD+	:	Reducing Emissions from Deforestation and forest Degradation
RS	:	Rainy Season
SCBT	:	Sedimentary Coatal Basin of Togo
S-N	:	South-North
SSE	:	South–South–East
SRTM	:	Shuttle Radar Topography Mission
SWI	:	Seawater Intrusion
WASCAL	:	West African Science Service Center on Climate Change and Adapted Land Use
W-E	:	West-East

List of Figures

List of Tables

CHAPTER ONE: GENERAL INTRODUCTION

This section includes the major constraints groundwater resources are undergoing in the Sedimentary Coastal Basin of Togo (SCBT) in general and the Agoènyivé plateau (AP) in particular, the existing works related to the topic addressed in the context of this study, the research needs, and finally the research questions and objectives.

1.1 Context and Problem Statement

Groundwater represents an important source of freshwater in many areas across the world. Though it is not the only form of water available to man, key factors such as its availability (especially in arid, semi-arid areas and populated areas) as well as its quality (especially in highly industrialised areas) define the resource preference over other sources of water like surface water (Ohwoghere-Asuma and Essi, 2017).

Groundwater resources represent a significant portion of the hydrologic cycle, particularly when considering only freshwater sources. However, in coastal settings, these resources stored in aquifers are endangered by depletion due to increasing water withdrawal associated with socioeconomic growth. Another factor contributing to this threat is the reduced recharge, which results from climate change, land use, and land cover change, or both, among others. Furthermore, Sophiya and Syed (2013) reported that these ecosystems are also threatened by phenomena like seawater intrusion (SWI). As a matter of fact, aquifers in the Sedimentary Coastal Basin (SCB) of the Gulf of Guinea extending from Côte d'Ivoire to Nigeria (including the sedimentary coastal basin of Togo) are reported to be under significant threats, including coastal erosion, climate change and pollution resulting in quality issues and reduced groundwater availability associated with either overexploitation or recharge reduction (Sterckx, 2021; Tetra Tech, 2014).

The coastal zone of Togo is part of the geosystem of the Gulf of Guinea in West Africa, known as the SCBT, representing the development hub for the country. In addition, the basin is recognized as the main source of freshwater for the population and industries (Gnazou et al., 2015a; DHE, 1984). Various aquifers can be identified within the basin, with the mains being the Coastal Marine Sands (MaS aquifer), Continental Terminal (CT aquifer), Palaeocene (Pa aquifer), and Maastrichtian (Ma aquifer). Since the 1980s, some of these aquifers have been reported to be subject to salinization (Bleza et al., 2020a; Gnazou et al., 2018; Gnazou et al., 2015a; Gnazou et al., 2015b; MERF/PANA, 2009; Amegadje, 2007; DHE, 1984). The

recorded electrical conductivities range between 100 and 22,000 µS.cm^{-1}, between 400 and 1600 µS.cm^{-1}, and between 60 and 520 µS.cm^{-1} for the CT aquifer, Pa aquifer, and Ma aquifer, respectively (Gnazou et al., 2018).

The Agoènyivé plateau (AP) belongs to the SCBT and hosts up to 25 percent of the national population (1,627,437 inhabitants as of 2010), with an annual growth rate of 2.88% (DGSCN, 2011). In addition, this part of the basin is characterised by strong urbanization, especially around the capital city, Lomé (Bawa, 2017). Furthermore, the area represents a center of concentrated economic and industrial activities in the country due to its opening onto the Atlantic Ocean (Gnazou et al., 2015a). Based on the above, the AP relies heavily on groundwater, both as a raw material for their production processes (i.e., washing, heating, or cooling manufactured products or equipment) and for domestic supply to the local population. This domestic supply is ensured by the TdE and supplemented by over a thousand informal private boreholes. In terms of water supply, the CT aquifer (an unconfined aquifer) in the AP, which sources up to 70 percent of the public water supply through the Togolese Water Company as well as 11870 industrial and private boreholes (Gnazou et al., 2015a), has been reported to experience an increase in chloride concentration over time. Recorded chloride concentrations evolve from 1400 mg.L^{-1} (as of 2008 at the near CT aquifer, which is 5 times above the value allowed by the World Health Organization) (Djibril and Agrell, 2011) to 1700 mg.L^{-1} as of 2020 in certain areas (Bleza et al., 2020a). In addition, the CT aquifer is reported to undergo a decrease in the hydraulic heads, estimated between 0.10 and 12 m (as of 2002 compared to the date of their realisation), depending on the borehole (N'dim, 2002).

The hydrogeology of the SCBT aquifers has been subject to studies for six decades with a focus on water resources estimation and the definition of groundwater exploitation conditions with the overall purpose of providing water but also satisfying the growing water demand (Bleza et al., 2020a; Bleza et al., 2020b; Akakpo, 2017; Bleza, 2017; Gnazou et al., 2017; Gnazou et al., 2015a; Gnazou et al., 2015b; Akouvi, 2005; DHE, 1983; DHE, 1982; PNUD, 1975; Gallo, 1974; Slansky, 1962). Some authors have focused on the general definition of the sedimentary structure of these aquifers (Gnazou et al., 2017; Gnazou et al., 2015a; Gnazou et al., 2015b; Akouvi et al., 2008; Da Costa, 2005; Johnson, 1987; DHE, 1982; Slansky, 1962). Other authors have streamed their efforts to focus on the aquifers' structure, hydrodynamics, and hydrochemistry (Bleza et al., 2020a; Bleza et al., 2020b; Gnazou et al., 2017; Akakpo, 2017; Bleza, 2017; Gnazou et al., 2017; Gnazou et al., 2015a; Gnazou et al., 2015b; Akouvi et al., 2008; DHE, 1983; DHE, 1982; PNUD, 1975). PNUD (1975) opted for geophysical

prospections of water resources under various projects supported by Togo (Togo 4, 2nd phase, and TOG-70-511) with the aim of improving knowledge on existing aquifers, the water requirements, and the conditions for groundwater exploitation in the basin. These definitions of the structure of the existing aquifers are best captured by the works of Gnazou et al. (2015a) and Bleza et al. (2020b). Gnazou et al. (2015b) evaluated the potential of the Pa aquifer by updating its structure. Gnazou et al. (2015a) carried out a hydrogeological characterization of the CT aquifer for its preservation. On the other hand, groundwater flow has been modelled both for a specific site (DHE, 1984) and the entire basin (Gnazou et al., 2017; Gnazou, 2008), considering either multi-layered modelling (Gnazou et al., 2017; Akouvi et al., 2008; DHE, 1984) or a monolayered modelling approach (Gnazou, 2008). Akouvi et al. (2008) assessed the origin and evolution of the salinity in the basin, considering the paleo-position of the wedge in the aquifer and its implications for current groundwater salinity, using a combined geochemical evaluation and hydrodynamic modelling and emphasized the mineralisation of unconfined aquifers (Continental Terminal and Quaternary sediments) and deep aquifers (Palaeocene and Maastrichtian) relating to human activities and the mixture with the trapped fossil seawater, respectively.

Though it has been recognized that apart from the human pressure associated with socio-economic growth, climate change (changes in temperature and precipitation and sea level rise) and other non-climatic factors (such as land use and land cover) have a plausible impact on the rate of SWI in the aquifers of the basin (MERF/PANA, 2009; MERF/CNI, 2001). In addition, the Togolese Littoral National Action Plan for the Development and Adaptation to Climate Change (PADACCLT) recommended as one of its main pillars the assessment of risks (including aquifer salinization) dynamics under environmental factors such as climate change, as well as socio-economic factors (ANTEA, 2017). Against what has been highlighted above, little has been done considering these factors in evaluating the dynamics of groundwater, especially in terms of its quality. Hence, modelling the dynamics of the SWI considering these key drivers becomes a requirement in the basin to link climate change (CC) and land use and land cover (LULC) change to groundwater quality. This research work will also help understand the link between climatic and non-climatic drivers and future groundwater resources quality. Therefore, this study aims at filling this gap by assessing the dynamics of SWI in the Coastal Sedimentary Basin of Togo under climate change and land use and land cover change using the case study of the multi-layered aquifer of the AP.

1.2 Literature Review

1.2.1 Seawater Intrusion

1.2.1.1 Seawater Intrusion: Definition, Modes, Drivers and Consequences

According to Dogan and Fares (2008), SWI is a phenomenon that consists of seawater flowing from the sea toward inland freshwater aquifers by pushing the seawater-freshwater interface landward and/or upward, mainly due to the density difference between freshwater, characterised by the low density of the freshwater (1000 $kg.m^{-3}$) against the high density of seawater (1025 $kg.m^{-3}$). SWI occurs in various modes, including *(i) lateral density-driven (dispersion) intrusion; (ii) up coning, (iii) tidal plume; and (iv) vertical salinization. Seawater up coning* represents the vertical rise of seawater toward the production or pumping wells located in the freshwater zone, where freshwater is underlain by seawater (Jakovovic et al., 2016). This phenomenon is attributed to the rise of the freshwater-seawater interface, or transition zone, resulting in the reduction of the freshwater zone below the pumping well. *The tidal plume*, on the other hand, occurs as the result of tidal variations of sea level associated with fluctuations in groundwater level, thus causing oscillation of the seawater-freshwater interface and the creation of an upper saline plume of recirculating seawater (Kuan et al., 2012; Robinson et al., 2007). When it comes to the *vertical salinization*, it occurs as the result of a rapid rise in sea level associated with either seawater spilling over into the lakes, rivers, and canals located at a short distance from the coastline. This process is followed by a re-infiltration in subsurface layers or convective instabilities of density-driven flow associated with the downward fingering of salt that may couple with the original intruded seawater wedge (Laattoe et al., 2013; Kooi et al., 2000).

Several parameters have been reported to control the SWI phenomenon, including regional factors (regional flow rate) as well as local factors such as the decrease in aquifer water table level, the increase in sea level, geological properties of the aquifer, and the initial position of the interface, among others.

Doğan and Fares (2008) highlighted the key role played by the aquifer water table level (in reference to the sea level) in the SWI phenomenon. One factor contributing to the lowering of the aquifer water level is the over-pumping (associated with an increase in water demand). This process results in a lower hydraulic head compared to that of the adjacent saline water body, leading to the creation of a new hydraulic gradient (Hussain and Javadi, 2016), thus moving the seawater-freshwater interface or mixing zone landward with potential SWI (Akbarpour and Niksokhan, 2018). Another contributor to the reduction of aquifer water table

level is the reduction of groundwater recharge, mainly resulting from changes in land use and land cover (LULC), changes in climatic parameters such as precipitation and temperature (Field et al., 2014; PEIDELJ, 2011; IPCC, 2007), and soil properties (Dogan and Fares, 2008). As a matter of fact, changes in LULC are associated with changes in the proportions of impervious areas, which in turn influence the hydrological processes (Veldkamp and Lambin, 2001), including the recharge. When it comes to climate change's contribution to the reduced recharge, Crosbie et al. (2013) highlighted that the most direct way through which climate change will impact groundwater is by modifying the renewable portion of the resource storage, either through the increase in evapotranspiration associated with the increased temperature (Sanford and Pope, 2010). As an example, the increase in rain event intensity is associated with high runoff and low aquifer recharge, and or the prolonged droughts (Kouzana et al., 2007). In addition, the common agreement about the exacerbating effects of climate change on SWI through sea level rise cannot be undermined (Ketabchi et al., 2016; Field et al., 2014; Werner et al., 2013; IPCC, 2007). Besides the factors highlighted above, the aquifer geological parameters, including hydraulic conductivity and porosity, among others, also play a key role when it comes to the extent of the intrusion, as they play a key role in the transport of the solute (Werner et al., 2013; Dogan and Fares, 2008).

SWI is reported to be associated with both direct and indirect damages as the result of individual or synergic impacts of its key drivers (Safi et al., 2018). These damages range from the unavailability of the resource to the destruction of the ecosystem holding the resource. Groundwater contamination by seawater is directly associated with the reduction of the productivity and consumptive values of the resource (Selmi, 2013; Park et al., 2012; Bobba, 2002), thus reducing its availability. In addition, the consumption of the resource, regardless of its quality, may directly affect human health (Nahian et al., 2018; Howard, 1987). Finally, the intrusion of the salt in the ecosystem holding this resource can be associated with partial or complete destruction of the ecosystem, thus potentially limiting their ability to render their services, which in the long run threatens the sustainability of the resource. Furthermore, polluted aquifers can contaminate other water sources such as local rivers, marine ecosystems, and other aquifers (through discharge or recharge). Based on the above, it can be deduced that the unavailability or limited groundwater storage volume, resulting from the deterioration of water quality (one of the primary detrimental impacts associated with SWI, as noted by Werner et al., 2013), may trigger water insecurity in coastal communities that are highly dependent on the resource.

SWI has been experienced all over the world for decades. Outside Africa, studies to understand the SWI process include those carried out in the USA (Johnson, 2007; Guvanasen et al., 2000), Europe (Custódio, 2009), Australia (Werner and Gallagher, 2006), and Asia (Chun et al., 2018; Bobba, 2002). In Africa, several cases of seawater intrusion into coastal aquifers have been reported (Steyl and Dennis, 2010), with cases in Northern Africa (El Hamidi et al., 2021; El Mokhtar et al., 2018), Southern Africa (Casillas-Trasvina et al., 2019), Eastern Africa (Walraevens et al., 2015), and Western Africa (Agossou et al., 2022; Hounsinou, 2020; Ohwoghere-Asuma and Essi, 2017; Ayolabi et al., 2013; Akouvi et al., 2008; Edet and Okereke, 2001). The above-listed research works confirm the common agreement on the general similarities in the trends governing various interaction processes (physical, geological, and chemical) between key drivers of SWI. Nevertheless, it has been highlighted that context-based differences exist when it comes to the rate and magnitude of these interactions (Niang et al., 2010; Oude Essink, 2001). This makes local assessment of seawater intrusion a key step in designing sound adaptation and mitigation measures. As a matter of fact, carrying out seawater intrusion assessment in the SCBT, beyond being a key step in designing sound adaptation and mitigation measures, will contribute to filling the gap of linking climate change and other factors, such as changes in land use and land cover, to groundwater quality in West Africa in order to capture their implications for future groundwater (Niang et al., 2014).

1.2.1.2 Seawater Intrusion: Assessment Approach and Methods

Various methods have been considered when it comes to investigating seawater intrusion in coastal settings. In the context of this research work, studies that focused on determining the position of the freshwater/saltwater interface as well as the prediction of the seawater intrusion process were considered. These approaches include geophysical, geochemical, physical, and mathematical methods, as described below:

Geophysical Approach/Methods: The geophysical method is based on the large differences between the resistivity values of saltwater-saturated zones and freshwater-saturated zones (Loke, 2000). Initially used to measure the spatial distribution of physical properties of the earth (including bulk conductivity of the seismic), these methods have been considered for hydrogeological assessments (Bear et al., 1999). These methods include surface geophysical methods like electrical methods (i.e., DC resistivity, frequency domain electromagnetic methods, airborne EM, loop-loop EM, time-domain electromagnetic sounding, and very low frequency EM), seismic methods (i.e., seismic refraction and seismic reflection, ground penetrating radar), and also integrated geophysical surveys and borehole methods (i.e.,

integrated use of borehole logs, electric logs, and radiometric logs). This approach is highly considered in the context of SWI assessment due to its ability to depict a significant contrast between saturated seawater layers (0.2 Ωm) (Loke, 1999) and saturated freshwater layers (> 10 Ωm) electrical resistivity (Loke, 1999). This difference gives way to mapping out the subsurface groundwater salinity distribution (Najib et al., 2017; Werner et al., 2013), thus an ideal technique for mapping the position of the seawater-freshwater interface (Chabaane et al., 2018; Loke, 1999). In addition, the reputation of these methods comes from their ability to deliver high-quality data, including high spatial resolution and continuous data (Batayneh et al., 2010; Dahlin, 2001). Some key research projects have adopted geophysical methods to assess saltwater intrusion in various coastal settings (Chabaane et al., 2018; Sognon et al., 2018; Bouderbala and Remini, 2014; Ayolabi et al., 2013; Abdalla et al., 2010; De Breuck and De Moor, 1969). Abdalla et al. (2010) investigated using a combination of time domain electromagnetic surveys, vertical sounding surveys, and seismic refraction methods to delineate the saline plume, identify the saline and freshwater zones, and estimate the migration rate of the plume. In all, the study brought to light the key role played by recharging dams in the extension of the saline intrusion. Ayolabi et al. (2013), on their side, carried out a hydrogeological investigation using a combination of geophysical and geochemical techniques to map and confirm the source of saltwater intrusion in coastal aquifers. Sognon et al. (2018), considering the resistivity maps along with the Archie law, characterized the seawater-freshwater interface in the Continental Terminal aquifer of the sedimentary coastal basin of Benin and found that the average depth of the interface is 20 m with a thickness ranging between 8 and 20 m.

***Classic Geochemical or and Isotopic Approach*:** Reported to be of great utility in identifying the origin of salinity in coastal aquifers (Bear et al., 1999), these methods have been considered to capture the evolution of the hydro-chemical composition of groundwater across the world (Hounsinou, 2020; Ganyaglo et al., 2017; Akouvi et al., 2008). These geochemistry-based methods include the chloride concentration and ratios (Na/Cl, Ca/Mg, and Ca / (HCO3+SO4)) among others. In fact, using essentially the geochemistry of the considered samples, Hounsinou (2020) reported a potential marine intrusion in the CT aquifer of the Sedimentary Coastal Basin of Benin with high electrical conductivity (EC) and chloride content observed in the southern part (along the coast). As for the isotopes, both stable ($\delta\ ^{18}O$ and $\delta\ ^{2}H$) and radioactive ($\delta\ ^{14}C$) isotopes have been considered alone or in combination with geochemistry to investigate seawater intrusion in coastal settings. As an example, Ganyaglo et al. (2017) considered geochemistry and stable isotopes to investigate groundwater salinity in the Ochi-Narkwa Basin

in Ghana. The authors have concluded that salinization results from the dissolution of halite, the weathering of silicates, and seawater intrusion.

***Experimental Approach*:** Motz (2004) performed a series of experiments to investigate ways to approximate the saltwater-freshwater interface in a groundwater flow model to yield accurate values of hydraulic heads in the freshwater zone. So, the study considered inactive cells to represent both the saltwater part of the aquifer and the no-flow boundary along the interface. Van Meir et al. (2004) focused on saltwater intrusion process characterisation in a hard rock aquifer with an appreciable level of heterogeneity. The study used an integrated set of tools previously developed in situ and yielded an input (3-D porosity and permeability models) for the analysis of specific saltwater intrusion experiments.

***Mathematical models*:** These tools include analytical and numerical solutions and are built on theories dealing with the thickness of the freshwater/seawater interface, which is the contact boundary between freshwater and seawater. This interface is subject to movement either seaward or landward as the result of hydrogeological heterogeneities of the aquifer but also dynamic forces (both natural and manmade). Theories supporting the SWI process are conceptualised into two hydraulic approaches, including the sharp interface (immiscible saline water and freshwater bodies) and the dispersive interface (miscible saline water and freshwater bodies with the creation of a transition zone) (Werner et al., 2013). The sharp interface and dispersive interface are, respectively, the basis of analytical solutions or methods and numerical solutions. On the one hand, most of the analytical solutions were based on the assumptions of the Ghyben-Herzberg theory (Herzberg, 1901), with the assumptions that the flow system is characterised by a very low hydraulic gradient, steady-state conditions with hydrostatic distribution of pressure, and where the two liquids (freshwater and saline water) are separated by a sharp interface and defined by the Hubbert equation (Hubbert, 1940). On the other hand, the dispersive interface or variable density approach assumes that the advection process and the hydrodynamic dispersion of the solute are key in the seawater intrusion process. Considering the latter approach, SWI simulation involves a highly nonlinear process, thus requiring numerical methods to solve the associated equations (especially for temporal and spatial simulation). The main equations include the flow equation (with the partial differential equation of the flow made up of the flux equation for the water of variable density and the water mass balance equation) and the transport or advection-dispersion equation (combining the flux equation of the solute and its mass balance equation). Finally, coupling and solving these equations using appropriate boundary and initial conditions completes the numerical solution of SWI (Dogan and Fares, 2008). Nevertheless, the theory of the transition zone has

been reported by several authors to be more realistic and closer to the actual physical behaviour of the flow and solute transport in the system (Bear and Zhou, 2007). The existing studies include those of Pinder and Cooper (1970), who considered the method of characteristics to simulate the two-dimensional transient advance of SWI in one of the benchmark aquifers known as Henry's problem. Lee and Cheng (1974), on their side, considered the finite element (FE) method to simulate two-dimensional SWI in Henry's confined aquifer and Biscayne unconfined aquifer (which are two benchmark problems). This approach has been proposed using the equivalent freshwater head in the governing equations to account for the density gradient effects (Frind, 1982). Nevertheless, over the years, many models and computer codes have been developed and considered for saltwater intrusion assessment in coastal settings, including SUTRA (Voss and Provost, 2010), SEAWAT (Guo and Langevin, 2002; Zheng and Wang, 1999), FEFLOW (Diersch, 1988), and SWIFT (Ward and Benegar, 1998), among others. The SEAWAT code has been considered across the world to understand seawater intrusion in both coastal and low-lying aquifers in recent years (Agossou et al., 2022; El Hamidi et al., 2021; Comte et al., 2014), including the sedimentary coastal basin in the Gulf of Guinea. In fact, Agossou et al. (2022) have considered the SEAWAT model in assessing the current and future impacts of climate change and anthropogenic activities on seawater intrusion (SWI) in the sedimentary coastal basin of Benin and found that the hydraulic head has declined over time in the study area (2015–2020), which is associated with an increase in the seawater intruded area. Considering the predicted sea level rise (SLR) and estimated groundwater pumping rate, the study projected a decline in the hydraulic heads and an increase in the seawater-intruded area.

***Combined Methods*:** While some research work considered solely either geophysical or geochemical methods or a numerical model, several research studies have integrated two or many methods highlighted. When it comes to the determination of the position and geometry of the seawater and freshwater interface or monitoring seawater intrusion, most research works have considered a combined approach of geochemical and geophysical methods (Chabaane et al., 2018; Supriyadi and Putro, 2017; Bouderbala and Remini, 2014; Edet and Okereke, 2001; Archie, 1942). Edet and Okereke (2001) examined the extent of seawater intrusion into shallow aquifers beneath the coastal plains of southeastern Nigeria using vertical electrical sounding and hydro-chemical data. Supriyadi and Putro (2017) considered an integrated geophysical and hydro-chemical approach to determining subsurface geologic formation and assessing seawater intrusion in the Tanah Mas residential area of North Semarang, Indonesia. On the other hand, other authors rather considered a combination of geochemistry and a modelling approach,

including Akouvi et al. (2008). The authors captured the origin of the salinity and its temporal and spatial evolution in the deep aquifers of the sedimentary coastal basin of Togo.

The above studies demonstrate the need to deeply assess seawater dynamics in the SCBT, considering factors such as climate change, land use, land cover change, and continuous groundwater withdrawal. Additionally, the combination of a geochemical and geophysical approach to the numerical modelling was proven effective and accurate in capturing the location and geometry of the seawater-freshwater interface as well as estimating the future extent of seawater intrusion. Among the questions raised based on the above review are: what happens to land use and land cover in the AP over time; what are the historical trends and future projections in climate parameters; and finally, how do these changes affect the SWI process over time?

1.2.2 Land Use and Land Cover: Concept and Methods

"Land cover" refers to the physical surface characteristics of land (i.e., vegetation, built-up areas, wetlands), while "land use" has to do with the functions of land (economic and social) or the purposes behind humans' exploitation of land cover (i.e., agricultural land, livestock production, recreation) (Van Soesbergen, 2016). Nevertheless, these two concepts are interlinked. As a matter of fact, land use can be associated with changes in the land cover, with the worst case being the land degradation, which can result in the degradation. In fact, occurring worldwide, the estimated current degraded land and potential future degraded land represent 75% and 90% (by 2050) of the Earth's land, according to the third edition of the World Atlas of Desertification (Cherlet et al., 2018).

Some resources and ecosystems, such as water resources and terrestrial ecosystems, among others, highly depend on the health of lands (soil properties) for their sustainability and may face direct threats from land degradation. When it comes to water resources, it has been highlighted since the fourth Intergovernmental Panel on Climate Change (IPCC) Assessment Report (AR4) with high confidence the impact of land use and land cover (LULC) change among other factors on future water scarcity (Niang et al., 2014). The above highlighted threat calls for continuous knowledge on the future LULC to anticipate the impacts through sound adaptation measures. As a matter of fact, an increase in the peak discharge in the Dano watershed has been reported as a result of agricultural land expansion and savannah degradation, posing a significant flood risk to the population (Yira et al., 2016). In addition, water balance components (including surface runoff, evapotranspiration, and water yield) in the Mono River Basin and Vea catchment were found to be influenced by many factors,

including LULC change (Larbi et al., 2021; Houteta et al., 2021). Furthermore, the increase in agricultural lands and built-up areas at the expense of the forest areas is found to be associated with an increase in runoff and a decrease in recharge in Abidjan (Abdelaziz et al., 2020). In fact, the decrease in recharge, as highlighted by Abdelaziz et al. (2020), can be associated with the decrease in the hydraulic head of the aquifers, creating an imbalance in hydraulic potential between the seawater and fresh waters in coastal settings with potential seawater intrusion.

The United States Geological Survey (USGS)/United States Agency for International Development (USAID) regional assessment of LULC dynamics in West Africa, considering three-time steps (1975, 2000, and 2013), has highlighted the large-scale loss of existing natural land cover classes at the expense of heavily human-influenced landscapes dominated by agriculture. The widest land cover class change observed over the region is the increase in cropland, estimated to be 10.7 percent of the area. Countries such as Togo, Benin, Chad, Mauritania, and Burkina Faso have been reported to be characterised by the fastest average annual expansion rates and the most severe decrease in forest cover. Nevertheless, the expansion of human settlements associated with population growth is observed in coastal regions like Togo. In fact, the regional and national assessments of LULC attested that Togo as a whole is under land cover change materialised through agricultural (estimated to be annually seven percent and ranked as the highest over the period 1975–2013) and settlements/urban areas expansion at the expense of natural ecosystems such as savannas, woodlands, and gallery forests (MERF, 2018a; Tappan et al., 2016). In addition, LULC assessment has been carried out at the local level (Kpedenou et al., 2016; Kpedenou et al., 2017; Folega et al., 2017; Koumoi et al., 2013; Houedakor, 1997). Houedakor (1997) worked on the environmental dynamics in the southeastern part of Togo and highlighted that demographic pressure and agricultural techniques are the main contributors to the degradation of vegetation, soils, and surface water and reported the generalised "savanization" of different units from the geomorphological point of view. Koumoi et al. (2013) assessed the spatio-temporal dynamics of land use in the central part of the country over the period of 1986–2010 using unsupervised classification. The findings depicted a decreasing trend of forest at the expense of savannah and croplands (an increase of 41.26%). According to Kpedenou et al. (2017), land use of the Ouatchi land in the southeastern part of the country has also seen change, with a decreasing pattern of forest (loss of up to 92%) at the expense of settlements and croplands. Folega et al. (2017) have focused on mangrove mapping (1986–2014) using Landsat images along with supervised classification and reported a loss of vegetation cover (47.19%).

The forward-thinking character, also known as anticipatory governance, which consists of the ability to have an idea of the future of a system or how the future will look, has been highlighted as one of the key factors in adequately facing potential future issues. Boyd et al. (2015) highlighted the relevance of a longer-term vision for developing strategies for uncertain environmental futures. In fact, one constraint in the context of the preparation for future adaptation considering the Institutional Readiness for Adaptation Framework has been reported to be the limitation of knowing the future or the lack of forward-thinking character, particularly when planning for a long-term horizon (Yomo, 2018). Geoinformation, a forward-thinking method, popped up as a commonly and widely used method in assessing LULC dynamics for its multidisciplinary applications (Larbi et al., 2019; Megahed et al., 2015), including its change detection and projection capacity (modelling), which are key in quantifying impacts associated with these changes. As a matter of fact, LULC change modelling has been highlighted to improve the understanding of land-use systems, help explore the behaviour of land-use systems under changes and recount the impacts of scenarios and strategies (Van Soesbergen, 2016). Contrary to what has been highlighted above, most of the studies carried out in Togo focused on past and current LULC change and have not considered future LULC, but also the AP, considering its importance for the country.

When it comes to the methodology for historical LULC assessment, several tools and algorithms or classifiers have been considered across West Africa, including the Maximum Likelihood Algorithm (Alshari and Gawali, 2021; Folega et al., 2017; Larbi et al., 2019), Support Vector Machines (Akodéwou et al., 2020), and Random Forest (RF) technique (Thiam et al., 2022), among others. Though each classifier has its advantages and disadvantages, Li et al. (2014) reported that classification accuracy depends highly on the size of the training sample rather than the selected algorithm (Li et al., 2014). The Maximum Likelihood Algorithm (MLA) has been reported to be robust in heterogenous settings like urban and semi-urban areas as well as coastal settings characterised by medium-resolution images (Heydarian et al., 2013). In addition, the algorithm is reported to be keen on better capturing residential areas, water, farmland, and bare lands (Li et al., 2014), which are typical of the Agoènyivé plateau. In addition, several studies have brought out the ability of the algorithm to classify images' pixels on a probabilistic basis (Girard and Girard, 1999) by highlighting the standard margin of error between the values of the pixels and those of the different training sites (Wilmet, 1995). Furthermore, the MLA has also proven its accuracy in classifying both spectrally unimodal and multimodal classes over the same region and beyond (Alshari and Gawali, 2021; Larbi et al., 2019; Folega et al., 2017). Finally, the MLA has been reported to reach its highest accuracy

with limited training samples, making it one of the least affected algorithms by training sample size (Li et al., 2014).

For the evaluation of expected LULC change in the future, several models have been considered across the world, including single models such as fuzzy logic (Han, 2014), GEOMOD (Nahib et al., 2018), STochastic CHOICE markov chain (STCHOICE) model (Mithun et al., 2022), the agent-based model (Arsanjani, 2011), and logistic regression (Dhali et al., 2019), but also hybrid models such as the Multi-Layer Perceptron Neural Network (MLPNN)-Markov chain (Thiam et al., 2022; Idrissou et al., 2022; Larbi et al., 2019), CA-Markov (Munthali et al., 2020), and GEOMOD-Markov Chain model (Andaryani et al., 2021), among others with great findings. Comparison studies have highlighted the strengths and weaknesses of these models in capturing urban land use and land cover dynamics. As a matter of fact, a study comparing the Land Change Modeller (Markov analysis-based) and the GOEMOD model in accounting for changes in land cover. The findings highlighted the limitation of the GEOMOD in capturing multiple transitions at a time (Nahib et al., 2018), which is characteristic of urban and coastal settings subject to continuous change. Another study that considered two different models (GEOMOD and CA-MARKOV) for predicting the future. The results reported the ability and robustness of CA-MARKOV in predicting LULC from many classes compared to GEOMOD (Regmi et al., 2017). In addition, though all these models rely on the understanding of the past LULC dynamics trend to predict the future, their accuracy in predicting the future varies. As a matter of fact, a comparison of the accuracy of three LULC models, including the STCHOICE, CA-MARKOV, and Multi-Layer Perceptron Neural Network (MLPNN)-Markov in modelling urban growth dynamics, has concluded based on the per-category-wise percentage of correct predictions and the Kappa agreement that the MLPNN-Markov approach or model is the best (Mithun et al., 2022).

1.2.3 Climate Change and Climate Models

The Intergovernmental Panel on Climate Change (2018) refers to climate change as “a change in the state of the climate that can be identified (i.e., using statistical tests) considering the changes in the mean and/or the variability of its properties and that persists for an extended period, typically decades or longer." This phenomenon is reported to be associated with changes in climate parameters such as precipitation, temperature, evapotranspiration, and sea level, among others. These changes represent a threat to both humans directly and indirectly through the ecosystems they rely on. The Intergovernmental Panel on Climate Change (IPCC) in its Fifth Assessment Report (AR5) highlighted an unequivocal warming of the climate

system with a historical decadal warming rate estimated at 0.12 °C in the Northern Hemisphere (1951–2012). In addition, the mean surface temperature is expected to increase, reaching values ranging between 0.3–0.7 and 0.3–4.8 °C over the periods of 2016–2035 and 2080–2100 (in reference to the period of 1986–2005), under various future emission scenarios. Due to the unequal vulnerability and impacts of climate change as a result of its non-uniform spatial and temporal extent across the world (Field et al. 2014), continuous investigation of changes in climate and weather patterns has been reported to be very important (Vincent et al., 2005). In addition, as adaptation is local (IPCC, 2007), local assessment of the climate becomes key to avoiding maladaptation.

West Africa has been reported to witness huge variability in rainfall along with an increasing trend in the temperature (Sylla et al., 2016). These changes are associated with changes in the hydrological cycle along with extremes such as droughts (as those of the 1970s and 1980s), floods (Diasso and Abiodun, 2015; Nicholson, 2013), and changes in water balance components (Larbi et al., 2022; Gassama-Jallow, 2021; Amoussou et al., 2012; Karambiri et al., 2011). Other impacts include those on activities such as agriculture (Carr et al., 2022; Gadedjisso-Tossou et al., 2021; Sultan et al., 2019) and ecosystems and their services, among others (Sanogo et al., 2020; Anyamba et al., 2014). Based on the above, it becomes clear that further warming could worsen the current climatic stress in the region, resulting in a plausible crisis in the future. As a matter of fact, an increase in the average temperature along with high variability in rainfall associated with increased frequency and intensity of extreme events is expected (Field et al., 2014; Kouamé et al., 2013).

To robustify adaptation and mitigation actions over the region, several studies have been carried out both at local and regional scales (including projects and individual research works) to capture how much change has been experienced so far, how much change is expected, and the resulting impacts (Yeboah et al., 2022; Fofana et al., 2022; Akpegnon, 2021; Patchali et al., 2020; World Bank, 2020; Houteta et al., 2020; Lawin et al., 2019; Larbi et al., 2018; Ahokpossi, 2018; Koudahe et al., 2017; Djaman et al., 2017; Sylla et al., 2016; Akinsanola and Ogunjobi, 2015a; Nicholson, 2013). Most of these research works considered the climatic trend analysis to capture the past and current climate patterns, while the future climate assessment in most of these cases relied on climate models with the bias corrected (as recommended by Teutschbein and Seibert, 2010) regional climate models (RCMs) privileged. These RCMs are downscaled from the Global Climate Models (GCMs), which are coarser in nature compared to their downscaled outputs. In fact, the mismatch of their outputs with the

local-level data requirement for models (Maraun et al., 2010) and their inability to capture the key local climate features and their dynamics, like the West African Monsoon (WAM) in West Africa (Sylla et al., 2013), have reduced their consideration. As for the RCMs, their value is associated with their ability to provide regional-to-local scale information (Giorgi, 2019), as well as their ability to resolve smaller-scale atmospheric features embedded within large-scale forcings, therefore providing more detailed climate information (Mezghani et al., 2017; Giorgi and Mearns, 1999), making them central tools to bridge the gap between climate models and vulnerability, impacts, and adaptation assessment carried out at the local level. Nevertheless, contrary to the West African Sahel, coastal West Africa has been reported to have received limited climatology studies (Ndehedehe et al., 2021). As a matter of fact, in the SCBT, historical trend assessment and future climate projections have not been well articulated, with limited works carried out focusing on the historical period (Akpegnon, 2021; Koudahe et al., 2017) and with very limited consideration of other climate data sources (satellite-based products) to palliate discrepancies in the available and accessible climate observations.

1.2.4 Recharge: Concept and Methods

Boerner and Weaver (2012) refer to recharge as surface water that percolates into the ground and replenishes the saturated zone. Recharge rates are expressed as potential (an estimate based on recharge flux that has not yet reached the water table, thus subject to losses during the flow process through the unsaturated zone) or actual (an estimate based on recharge flux that has reached the water table). As part of the hydrological cycle, recharge has been reported to be key to sustaining current and future groundwater use (Kotchoni et al., 2018). Nevertheless, this component, among others, can be subject to change as a result of changes in the climate, land use, land cover, and soil properties, therefore needing to be continually estimated, especially in challenging environments such as coastal and urban settings.

Methods designed to estimate the recharge process are classified based on hydrogeological zones (Lerner, 1990), hydrologic zones (Scanlon et al., 2002), and techniques (Scanlon et al., 2002; Lerner, 1990). The methods classes based on Scanlon et al. (2002) consider three hydrologic zones, including the surface water, unsaturated zone, and saturated zone. Within each class or hydrologic zone, sub-classes such as physical techniques, tracers, and numerical modelling can be seen. On one hand, physical methods (i.e., channel-water budget, seepage meters, and baseflow discharge), tracer methods (i.e., stable isotopes of oxygen and hydrogen), and numerical modelling methods (i.e., deep percolation model, SWAT model, WAVES model, and water budget equation) are part of recharge estimation methods

based on surface water studies. On the other hand, physical methods (i.e., lysimeters, Darcy's law, and the zero-flux plane), tracer techniques (i.e., bromide, ^{3}H, and visible dyes, ^{36}Cl, and Cl^{-}), and numerical modelling methods (i.e., soil water storage routing, quasi-analytical approaches, and numerical solutions to the Richards equation such as WAVES) have been considered for unsaturated zone recharge estimation. Finally, recharge estimation methods based on the saturated zone studies include physical methods (i.e., water table fluctuation and Darcy's law), groundwater dating (using tracers such as CFC, $^{3}H/^{3}He$, and ^{14}C), and numerical modelling methods (i.e., groundwater flow modelling such as MODFLOW).

1.3 Research Questions

The main question is: will groundwater resources (from the multi-layered aquifer) in AP's be secure under the changing climate, land use, land cover, and population dynamics? From there, secondary questions are raised, including how did land use and land cover evolve spatially and temporally, and what land use and land cover pattern is expected in the Agoènyivé Plateau under various scenarios? What is the climate trend over the AP, and what are the expected future projections for the area? What are the characteristics (in terms of hydrochemistry, isotopy, hydraulic head, and true resistivity distribution) of the multilayered aquifer in the AP? Which aquifers are the most impacted, and finally, what is the multi-layered aquifer considered response over time in terms of the hydraulic head and salinity concentration, and what is the future extent of the SWI associated with changes in the climate, land use, and land cover, as well as the continuous groundwater withdrawal over the study area?

1.4 Thesis Objectives

1.4.1 Main Objective

This research work aims at contributing to water security by assessing the dynamics of seawater intrusion (SWI) in the Sedimentary Coastal Basin of Togo under climate change and land use and land cover change using the case study of the multi-layered aquifer of the Agoènyivé Plateau.

1.4.2 Specific Objectives

More specifically, this work will:

- **SO1**: Assess historical (1986–2020) and future (2030, 2050) LULC in the AP.
- **SO2**: Analyse the climatic trends and future projections in the AP.
- **SO3:** Characterise existing aquifers in the AP (physico-chemistry, isotopy, hydraulic heads, and true resistivity distribution).

- **SO4:** Model the future groundwater lens response (hydraulic head, salinity, and intrusion extent) of the upper aquifers in the context of climate change, land use and land cover change, and increasing groundwater withdrawal in the AP.

1.5 Novelty

Limited hydrogeological and climatic data of sufficient quality have hindered sound research and in-depth investigations of groundwater dynamics and limited efforts in linking LULC change and climate change to groundwater quality in West Africa, as well as in understanding the uptake of non-climatic and climatic drivers as related to future groundwater resources. Nevertheless, there is a need to start the assessment with the available data in order to pave the way for future work that will consider more data for a sounder output. The above-mentioned points have been lacking in the coastal sedimentary basin in general and in the AP in particular, thus requiring more attention. Above all, this work will contribute to the worldwide effort to achieve the Sustainable Development Goals (SDGs), including SDG 3 (good health and well-being), SDG 6 (clean water and sanitation), SDG 11 (sustainable cities and communities), SDG 12 (responsible consumption and production), SDG 13 (climate action), and SDG 15 (life on land).

1.6 Scope of the Thesis

This study focuses on the assessment of seawater intrusion dynamics at the hydrogeological unit scale. It considers recharge induced by climate parameters (rainfall and temperature) and land use and land cover, as well as groundwater withdrawal, sea level rise, and aquifer hydrodynamic characteristics. The seawater-freshwater interface position is determined through a combined geophysics-geochemical approach. Finally, groundwater lens response to the current and future climate and land use and land cover change in terms of hydraulic head and salinity concentration was assessed using the SEAWAT model.

1.7 Expected Results and Benefits

The outcomes of this research include: (i) historical and future LULC maps and quantified changes to inform decision-making for land management and planning at plateau level; (ii) climate trend and future climate projections based on observations and regional climate models; (iii) historical and future recharge profiles of the AP based on LULCC and climate change; (iv) physicochemical and isotopic characteristics and the hydraulic head of the aquifers considered; (v) the position of the seawater-freshwater interface at AP scale; and (vi) current and future hydraulic heads and salinity concentration and the intrusion extent. Beyond the expected outcomes, this study represents a strong database to build in the future a tool for

continuous monitoring of the dynamics of seawater in the study area, as well as information to build a decision support system for integrated and sustainable groundwater development to ensure water security at the basin level.

1.8 Thesis Structure

The thesis is organised into eight chapters. Chapter one, which is the general introduction, provides the context and problem statement, a literature review of existing studies, research questions, thesis objectives, novelty of the study, scope of the study, and expected results or outcomes. Chapter two provides a detailed description of the Agoènyivé plateau, including the location, topography, drainage network, vegetation, climate, hydrology, geology, hydrogeology, demography, environmental, and socio-economic activities. The data collected, tools, and methods used for analysis are provided in Chapter three. Chapter four deals with the results of land use and land cover assessment and prediction, while Chapter five gives the current and future climate trends prevailing on the Agoènyivé plateau. Chapter six characterises the existing aquifers in the AP based on the hydrochemistry and isotopic signature of the water samples considered, as well as the true resistivity distribution of their subsurface and the hydraulic heads of aquifers. Then, chapter seven models the upper aquifer's response (hydraulic head, salt concentration, and intrusion extent) under climate change, land use and land cover change, and continuous groundwater withdrawal. Finally, Chapter eight gives the conclusions, recommendations, and future perspectives.

CHAPTER TWO: STUDY AREA

This chapter describes the study area in detail, including the location, topography, vegetation, climate, hydrology, geology, hydrogeology, demography, and socio-economic activities.

2.1 Location

The Agoènyivé Plateau is located at the western part of the Coastal Sedimentary Basin in Togo (between Lomé and Mission Tové), lying between latitudes 06° 7' and 06° 21' North, and between longitudes 01° 01 'and 01° 18' East (Figure 2.1). It is bordered by the outcrops of the Pan-African crystalline basement in the north, the offshore portion under the Atlantic Ocean in the south, Ghana to the west, and the Zio Valley to the east. Covering a total area of 420 km^2, the area includes the entire Gulf district and partially the Zio, Ave, and Agoènyivé districts, with relatively constant altitudes ranging between 30 and 50 m (Johnson et al., 2000; DHE, 1982).

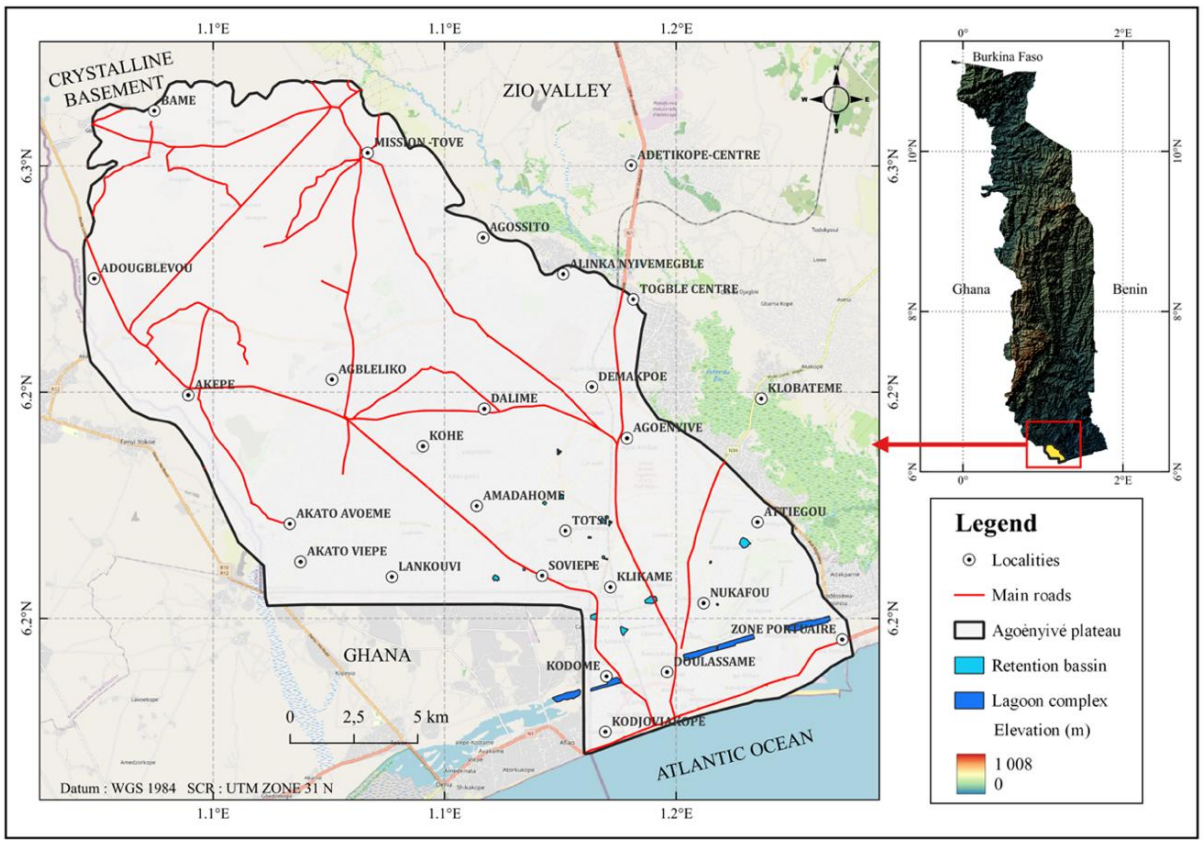

Figure 2.1: Location of Agoènyivé Plateau (Johnson et al., 2000; Modified)

The Sedimentary Coastal Basin enjoys a Guinean equatorial climate type driven by the position of the Inter Tropical Front (ITF) at the regional level (Le Barbé and Lebel, 1997). The resultant rainfall mechanism is characterised by two rainy seasons (with the amount increasing when moving towards the continent) separated by two dry seasons of unequal length. Rainfall

is heterogeneous in the basin, with an average annual rainfall ranging between 800 mm near the southwest coast (864 mm in Lomé) and 1400 mm in the northeast of the basin (1445 mm in Tabligbo) (Gnazou, 2008; Fontaine, 1991). The mean annual air temperature ranges from 24 to 30 °C, with an average potential evapotranspiration of 1030 mm.year^{-1} against a real evapotranspiration of approximately 700 mm.year^{-1} (Akouvi et al., 2008; Akouvi, 2005). Significant variation was observed in the relative humidity over the basin, especially during the day and over the course of the year. In June, the least humidity is observed in the northeast part of the basin (higher than 60% at Tabligbo), while the highest is observed on the coast (up to 98% in Lomé) (Le Barbé et al., 1993). The present-day infiltration rate is assumed to vary from year to year, with a mean value of 63 mm (Le Barbé et al., 1993).

2.2 Hydrology

From a hydrological point of view, the plateau is drained by the tributaries of the Zio River (176 km), which is a tributary of Lake Togo (Figure 2.2). The river is characterised by a seasonal variation, with high water levels occurring between July and October and an average annual flow at the mouth estimated at 9.9 m^3/s (with inter-annual flow varying between 26.3 m^3/s during wet decadal years and 3.9 m^3/s during dry decadal years) (Avumadi, 2019).

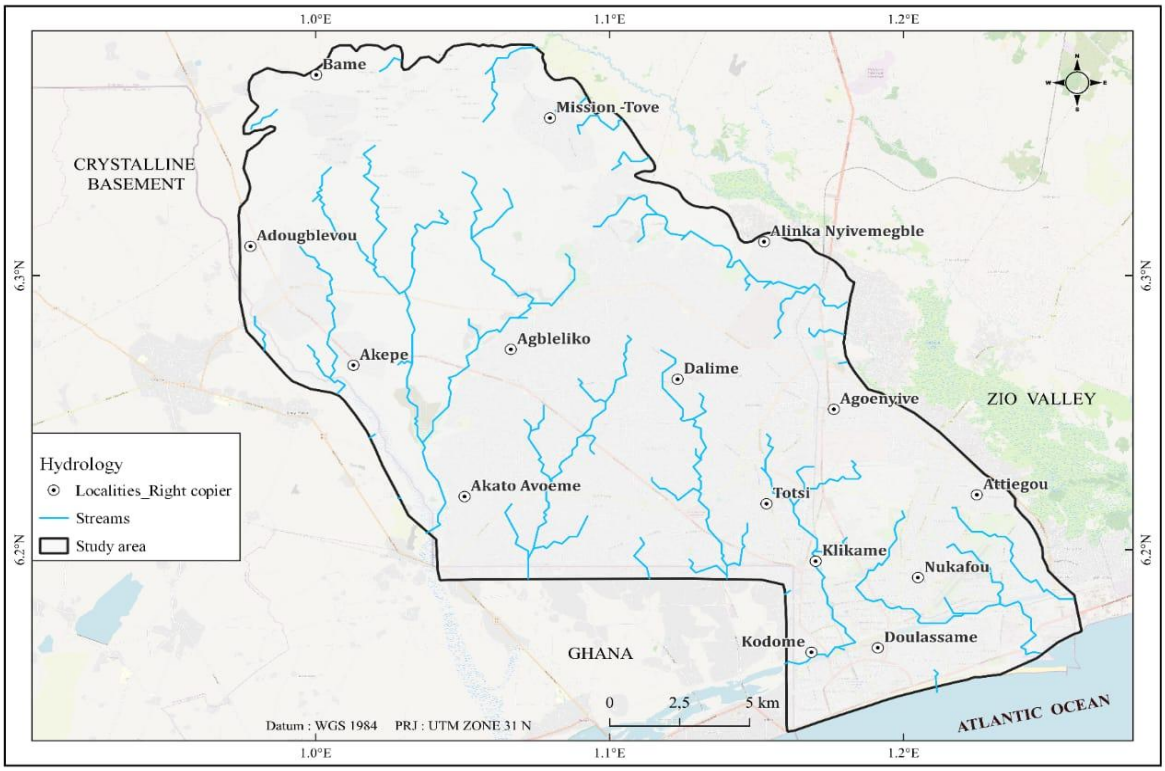

Figure 2.2: Hydrographic Network Map of the AP (Source: https://usgs.gov, Accessed on 05/07/2020)

There is also a need to highlight the presence of wetlands covering the entire Togolese coastline

(MERF/WACA-TOGO, 2017). The river and its floodplain represent a great agricultural asset for the riparian populations.

2.3 Geology and Hydrogeology

The geology of the Togolese portion of the Sedimentary Coastal Basin in general and the geology of the Agoènyivé plateau (Figure 2.3 and Figure 2.4) have been reconstructed through numerous exploratory works done in the area (Gnazou et al., 2015a; Gnazou et al., 2015b; Johnson, 1987; Sylvain et al., 1986; Monciardini et al., 1986). The reconstructed post-Palaeozoic sedimentary series is known from the Maastrichtian/Eocene marine series (mainly made up of sand, marly limestone, marl, and clay dipping toward the south) to the Quaternary series of continental and coastal origin formations resting horizontally and discordantly on the marine series (mainly made up of sand, gravel, and sometimes clay with a great number of lateral facies variations) (Da Costa, 2005; Johnson, 1987; Slansky, 1962). The zone is presented in series and is entirely covered by the formations of the Continental Terminal, with formations outcropping more and more young towards the south except for the Quaternary deposits (alluvium). The area is characterised by Mesozoic, Xenozoic, Continental Terminal, and Quaternary deposits. The Mesozoic in the study area (the emerging part of the plateau) is characterised mainly by the Maastrichtian (with a thickness exceeding 60 m). The formation, covering approximately a total area of 79 km^2, is essentially made up of sand associated with pyretic black clays and woody and marly beds. For Xenozoic deposits, the Palaeocene and Eocene are the essential structures. The Palaeocene, covering an area of 78 km^2, is characterised by the predominance of biochemical deposits and presents in its upper part a series of small levels of glauconious phosphatic, followed by a series of finely laminated marly clays with attapulgite, and in its lower part clayey marls (base) and zoogenic limestone (Togocyamus seefridi limestone) (at the top**).** The Eocene, known as the "Ypresian" is structured (based on bio-stratigraphic and sedimentological characteristics) into the Lower Basal Eocene (149 km^2), the Lower Eocene Terminal to Middle (75 km^2), and the Middle Eocene-Bartonian (1 km^2), characterised by continuous flaky attapulgite clays and interspersed small levels of glauconious limestone with the Lutetan of a limestone nature at the base with conglomerates of coprolites, then finely phosphatic, chalky, or marly, and clayey-marly. The Continental Terminal (382 km^2), grouping the azo formations (transgressive in the SCBT from the NNE to SSE on the crystalline basement, the Maastrichtian, then the Eo-Palaeocene) between the Eocene and the alluvial or coastal deposits, is mainly characterised by clay-detrital deposits with varied granulometry, often with a variegated and reddish continental appearance.

These materials are organised in a lower part essentially made of fine or limno-marly sand, discordant on the Palaeocene and Cretaceous clays, and a coarser upper term constituting a discontinuous level of gravel and rolled quartz pebbles and located at the base of a discordant sand-clay formation at the underlying level (Da Costa, 2005; Johnson, 1987; Slansky, 1962). Finally, the quaternary deposits as described by Tastet (1979) comprise four lithological formations in the AP corresponding to different environments, including the continental formation of the lowlands or low plateaus (essentially clayey sand with a constant grain size, covering an area of 1 km^2 with a thickness ranging between 15 and 30 m over the SCBT), coastal marine formation (essentially medium to coarse sand more or less clayey and covering an area of 19 km^2), lagoon-marine formation (essentially clayey and sandy and covering an area of 12 km^2), and fluvio-lacustrine formations (essentially the undifferentiated alluvium covering an area of 9 km^2).

Considering the lithology of the basin, several hydrogeological structures can be observed, with the main ones described below:

- ***Sand Aquifer of the Coastal Rim/Coastal Marine Sand (MaS)*:** Two kilometres wide, this formation is mainly made up of sands that connect with the sea and the lagoon, thus being highly exposed to marine invasion and anthropogenic contamination. These formations contain a shallow water table aquifer with a thickness ranging between 10 and 30 m and are highly exploited at flow rates between 1 and 15 m^3/day (Gnazou, 2008).
- ***Continental Terminal Aquifer (CT)*:** Essentially sandy (with various sizes), the aquifer thickness varies depending on the sectors, with weaker power in the north compared to the south. The average thickness ranges between 10 m (Légbassito) in the north, 30 m (Gakli) in the centre, and 40 m (Amoutivé) in the south. The roof of the aquifer is represented by a shallow crown in areas such as Adjougba, Légbassito, and Sogbéssito (with a depth of 12 m), clay in sectors such as Lomé II, Atiémé, Mission Tové, Agomé, Zongo, and Nyamassi reaching a depth between 8 and 20 m, and clayey sand in areas such as Attiegou, Logopé, Madjikpéto, GTA, Avédji, Sagbado, Cacavelli, Adidomé, Sanguéra, Klémé, Agoè, and Kitidjan with a depth varying between 20 m (Agoènyivé) and 70 m (Amoutivé) (Bleza et al., 2020b; Gnazou et al., 2015a). The wall of the aquifer is represented by the sands of the Maastrichtian in the northern sector and the clay of the Eocene in the central part of the plateau. The depth of the wall varies between 20 m in the north and northwestern parts, 40 m in the central part, and 120 m in the southern part (Bleza et al., 2020b; Gnazou et al., 2015a). The northern part represents the recharge area, while the ocean and the Zio River

are the discharge areas (Bleza et al., 2020b; Gnazou et al., 2015a). The formation is transgressive over the marine formations, which it covers in discordance. It tops the sands and clayey sands of the Maastrichtian in the north and covers in the southern part the Marly Eocene series and Palaeocene. Highly productive and shallow, this aquifer is highly exploited (around 18 boreholes of the TdE in addition to private and rural water systems). The depth of the CT aquifer ranges from a depth of 0 m (Togblékopé) to above 80 m in Lomé (Bleza et al., 2020b).

- ***Palaeocene Aquifer (Pa)***: It covers the entire Coastal Sedimentary Basin (Gnazou et al., 2015b). The layers of the aquifer on AP show a monocline arrangement, weakly dipping towards the south with an increasing thickness towards the south (Akakpo, 2017). The aquifer Pa is recharged essentially in the northern part through the CT and Ma over the Sedimentary Coastal Basin (Gnazou, 2008) and in the AP mainly through the CT aquifer, where it lays directly on the clayey sands of the undifferentiated Pa (Akakpo, 2017). The roof of the aquifer varies between -20 m (observed at Légbassito) and -320 m (observed at Avépozo), with a western–northern decreasing trend. The wall of the aquifer varies between -40 m (observed at Légbassito) and -380 m (observed at Avépozo). The average thickness observed ranges between 10 and 40 m. In addition, it has been reported that there is a direct contact between the CT aquifer formation and the clayey sand of the undifferentiated Palaeocene, observed around certain boreholes (W11 and W2) where the Eocene formation is absent (Akakpo, 2017).
- ***Maastrichtian Aquifer (Ma)*:** Both unconfined (northern part) and confined (southern part), the sands of the aquifer extend continuously from the Mono to the Ghanaian border (including the AP). The aquifer presents a low productive layer in the north (6–10 km wide along the contact with the crystalline basement, as the result of the presence of a "dry interface" and dominant clayey formations) and a productive layer in the south, 2–20 m wide and characterised by the abundance of sandy formations with thicknesses varying between 5 and 25 m (PNUD, 1975). The aquifer is easily accessible in the northern part of the basin compared to the southern part, where it is deep and characterised by a rapid increase in thickness. The formation is reported to occur at depths ranging from above 100 m to more than 350 m in the southern part (Akakpo, 2017). All the existing deposits as well as the geological cross-section are presented in Figures 2.3 and 2.4.

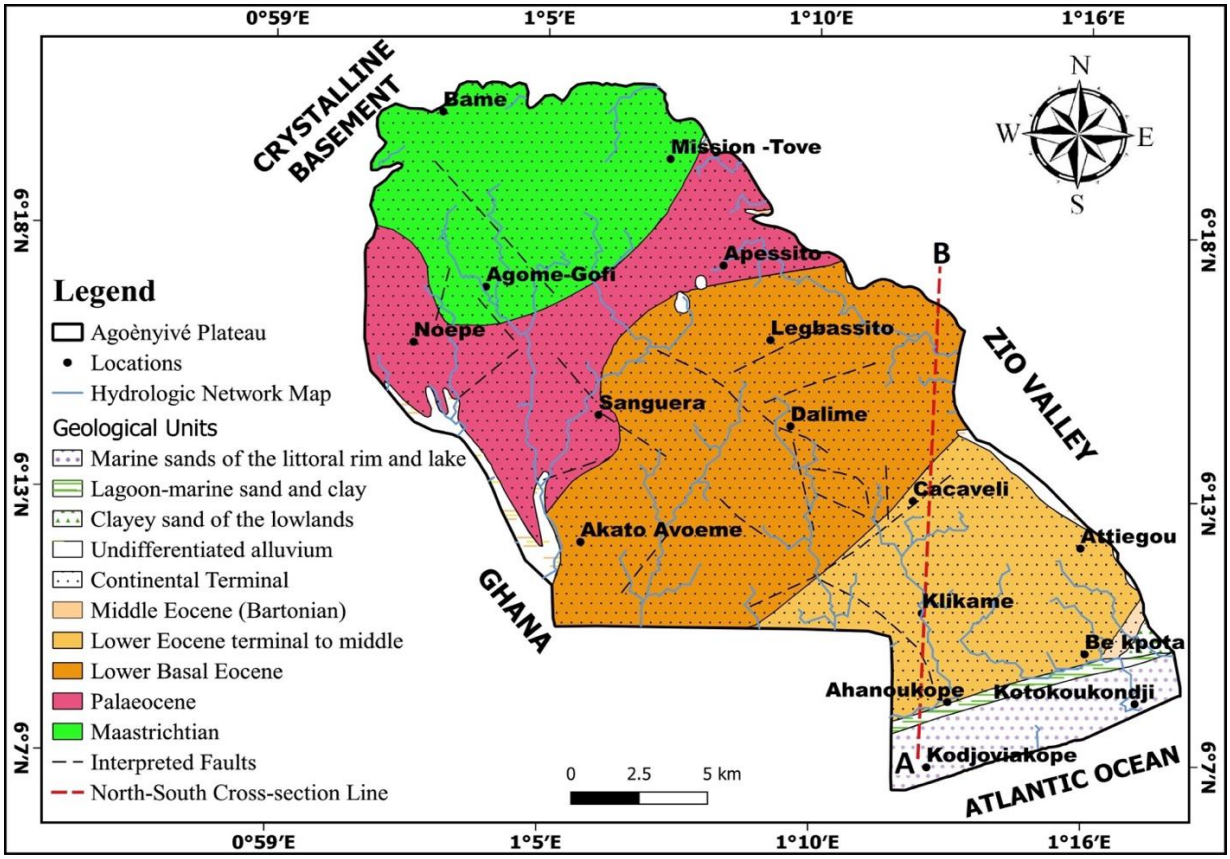

Figure 2.3: Geologic Map with North–South Cross-section line (Sylvain et al.,1986; Modified)

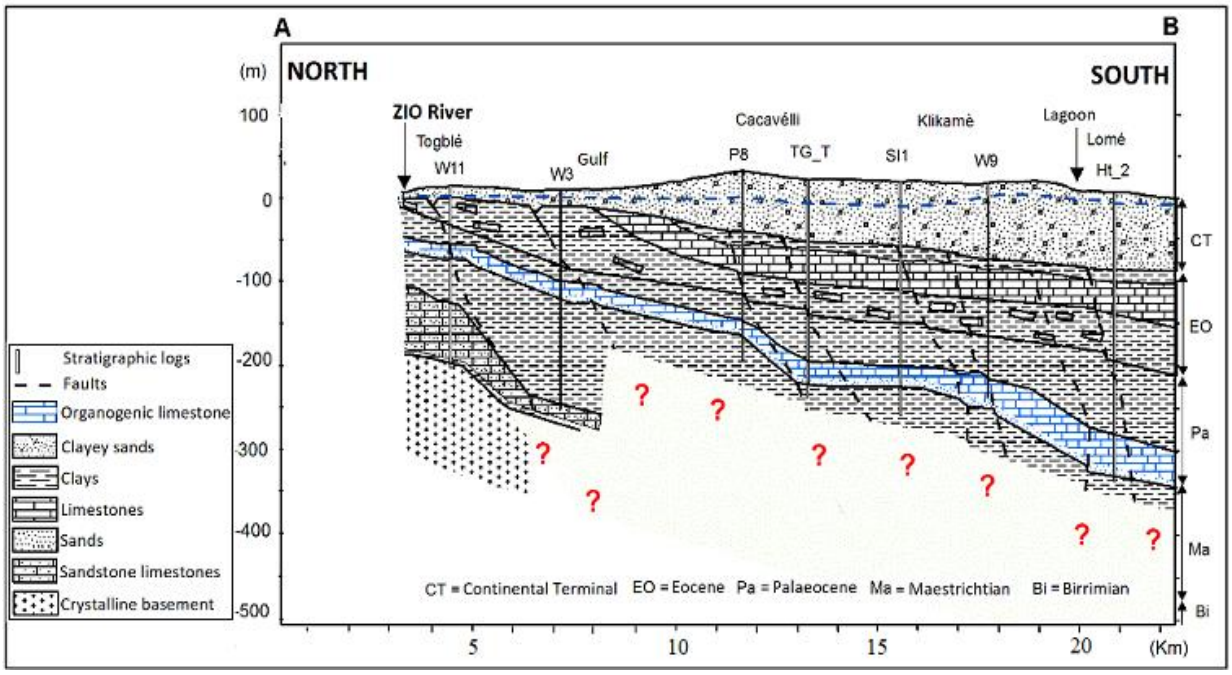

Figure 2.4: North–South Geological Cross-section in the AP (Akakpo, 2017; Modified)

2.4 Soils

The main soils in the AP include ferralitic soils, hydromorphic soils, and undeveloped soils (Figure 2.5):

- ***Ferralitic soils:*** Dominant and known as the "shallow crown," this type of soil is on clayey sediments and covers a total area of 308.99 km^2. This type of soil is considered a weakly ferrallitic, non-indurated soil (Lamouroux, 1969). Reported to be mainly sandy (75-90%) (Azontonde, 1994; 2000 in Gnazou 2008), and resulting from the extensive alteration of the sandy-clayey formations of the CT aquifer, they are characterised by destroyed structure (absence of stable aggregates), bedding in the form of humus horizons at the base of the surface anthropogenic horizon, and a very low organic matter content (less than 0.8%).
- ***Hydromorphic soils:*** Formed through gleying conditioned by the presence of excess water for a period year-round (Lamouroux, 1969), following a process, these grey soils are found at the bottom of the slope on sandy colluvium along the Zio River, covering an area of approximately 8.65 km^2. They are generally very poorly drained clay soils with highly developed grey-blue spots (pseudogley, characterised by grey and ocher spots appearing high in the profile).
- ***Undeveloped soils*:** Classified as poorly evolved contribution soils (related to the presence of a slightly humus-rich "A" horizon and a certain clayey gradient, appreciable in the soils located north of the lagoon depression), these soils, found on sandy alluvium along the coast or on recent alluvium or colluvium at the bottom of slopes or thalwegs are essentially sandy or sandy clay with poor water properties and cover a total area of 102.80 km^2.

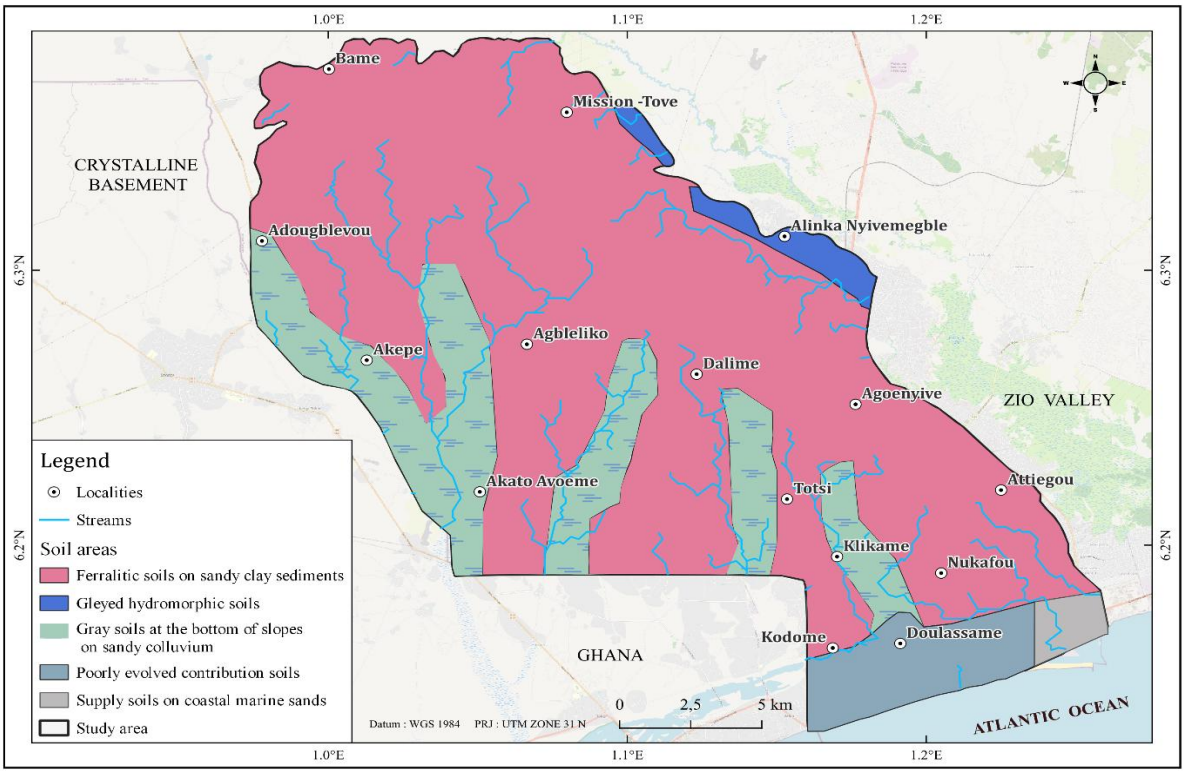

Figure 2.5: Soil Map of the Study Area (Lamouroux, 1969; Modified)

2.5 Vegetation and Land Use and Land Cover

The Agoènyivé Plateau is part of ecological Zone V with a landscape of wooded or shrub savannah (Ern, 1979) and was originally made up of gallery forests (because of its location on the banks of the Zio River) but has undergone a phenomenon of degradation associated with climate change and urbanisation resulting in the observed anthropogenic vegetation pattern. The main plant species encountered include coconut groves with thickets such as Chrysobalanus orbicularis, Fagara zanthoxyloides, Flacourtia Jiavescens, Azadirachta indica, and the carpet of grasses with Sporobolus virginicus and Paspalum vaginatum (along the coastal strip), depleted shreds of mangroves with Rhizophora racemosa, Avicennia sp, and Drepanocarpus lunatus (along the edge of the lagoons), and the carpet of grass with thickets of Mitragyna inermis, Eleaphorbia drupifera, and Capparis sp) (in the depressions with hydromorphic soils of Zio). In addition, cultivated lands are found, with the main crops being cassava and maize, but also gardens with vegetable crops including Daucus carota (carrot), Allium cepa (onion), Ocimum basilicum (basil), Capsicum annuum (pepper), and Solanum macrocarpum (spinach). The LULC (as of 2020) is characterised by built-up areas (261.87 km^2), mixed savannah (12.74 km^2), water bodies (2.35 km^2), cropland cropland/cultivated areas, bare areas (141.48 km^2), and wetlands (1.46 km^2) (Yomo et al., 2023).

2.6 Demography and Socio-Economic Activities

The Agoènyivé plateau includes partially the Golfe (Lomé, Aflao Sagbado, and Baguida cantons), Ave (Aképé and Noépé cantons), Agoènyivé (Légbassito, Togblékopé, Sanguera, and Agoènyivé cantons), and Zio districts (Mission Tové canton). The density of the population in 2010 was estimated at 9304.6 inhabitants, 3857.08 inhabitants, and 85.36 inhabitants per square kilometre for Lomé commune, Golfe and Ave districts, and the rest of the plateau, respectively (DGSCN, 2011). The total population in the plateau as of 2010 was estimated at 1627437 inhabitants (with an average density of 4415.77 inhabitants/km^2), representing 26.29% of the Togolese population. Based on the growth rate projected over the period of 2011–2030 (2.16%) by the DGSCN (2011), the population in the AP is expected to reach 2330489.784 inhabitants and 3033542.568 inhabitants by 2030 and 2050, respectively.

As part of the maritime region, the AP is endowed with high economic potential based on various goods production and service sectors, including the primary sectors (agriculture, livestock, fishing, and hunting), secondary (extractive industry, manufacturing industry, etc.), and tertiary (transport, service, trade, banking, in particular micro-credit, etc.):

- ***Farming*:** Essentially rain-fed, seasonal crops (corn, cassava, yam, sweet potato, taro, bean, rice, peanut, and soybeans) as well as perennial or commercial crops (coconut trees, palm oil trees., sugar cane, cotton, and pineapple) and gardens (vegetables, pepper, and okra) are found (MERF/WACA-TOGO, 2017; MERF/PANA, 2009). Irrigated agriculture is limited, with crops involved including rice, spices, and cassava crops.
- ***Livestock*:** Done in a mixed agro-pastoral system and representing the main supply of meat and eggs to the capital city. Livestock bred essentially include goats, sheep, cattle, pigs, and poultry. Indigenous are also involved in the breeding of small species such as agoutis, rabbits, and snails (MERF/WACA-TOGO, 2017).
- ***Fishing*:** is one of the main economic activities carried out in the Zio River, the lagoon (Be and East), and the sea. It includes both maritime fishing (artisanal and industrial) and inland fishing (artisanal) (MERF/WACA-TOGO, 2017). The coastal zone's contribution to the net country's annual fish production is estimated at more than 85 (MERF/WACA-TOGO, 2017).
- ***Industry*:** Part of the industrial zone, the AP is characterised by the presence of agri-food industries (Fan-Milk, Nioto, Uni-Food, Brewery, etc.) but also raw material processing industries such as CIMTOGO, mainly into cement production using clinker (HeidelbergCement, 2021). Other industries include the pharmaceutical (TONGMEI), chemical, and plastics industries.

CHAPTER THREE: DATA, MATERIALS AND METHODS

This chapter describes the various data collected, the tools and materials used, and the methodology adopted in both data collection and analysis. This section is organised into four parts: (i) LULC data collection, classification, and modelling; (ii) climate data (rainfall, temperature, evapotranspiration, and relative humidity) and RCM outputs data collection, trend analysis, and future projections; (iii) water samples and hydraulic head data collection and analysis; and (iv) resistivity data collection and analysis and future evolution in the groundwater lens response (hydraulic head, salinity, and intrusion extent) assessment. The overall analytical framework (Figure 3.1) includes LULC classification and modelling using the land change modeller, the climate trends analysis and regional climate models (RCMs) projections of future climate, characterisation of the multi-layered aquifer of the AP (physico-chemistry, isotopy, true resistivity distribution, and hydraulic head), and modelling groundwater lens response.

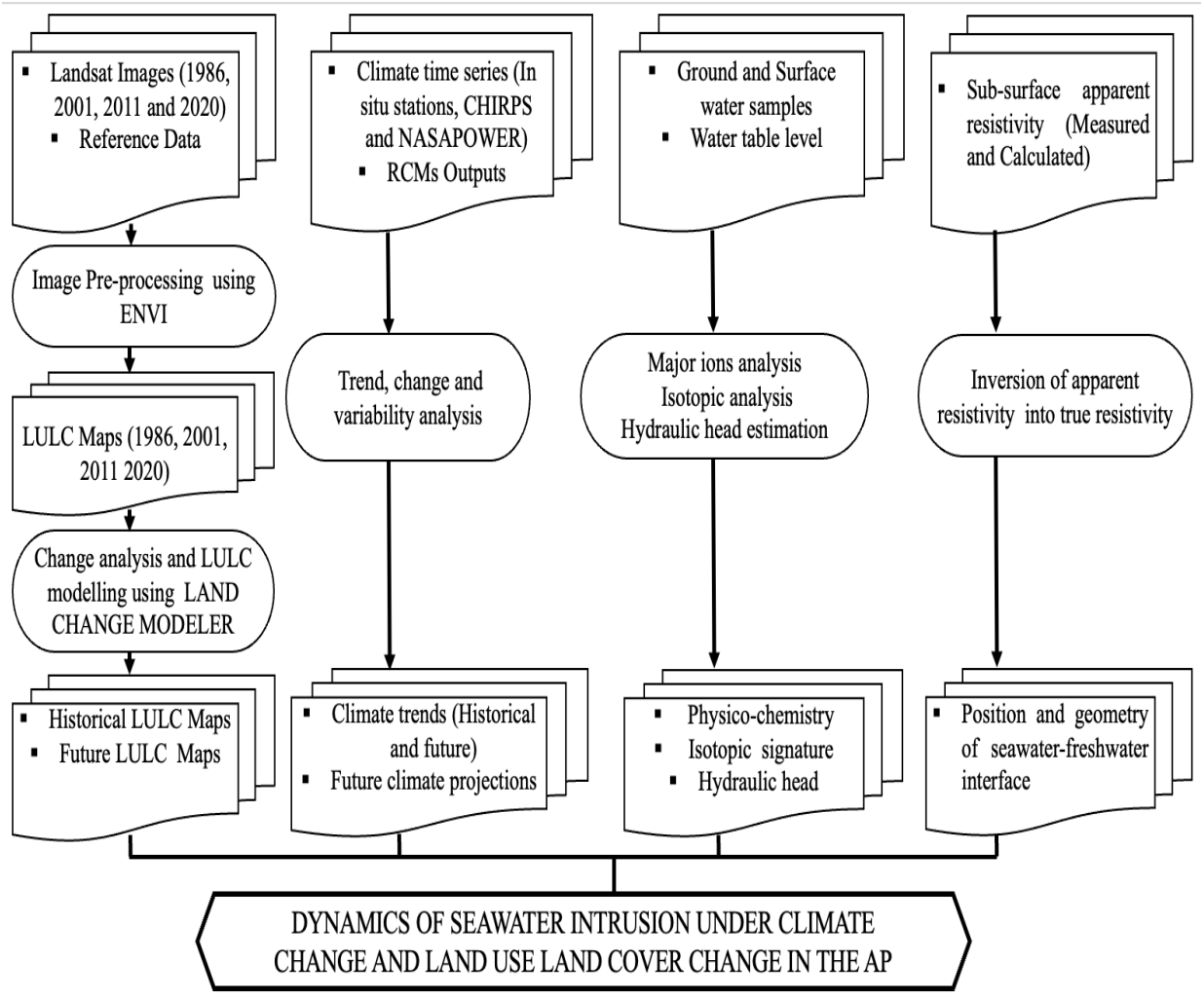

Figure 3.1: Overview of the General Research Work

3.1 Data

3.1.1 LULC Related Data

3.1.1.1 Landsat Images

30 m spatial resolution Landsat 5 and 7 (Enhanced Thematic Mapper and Thematic Mapper) images were selected (based on the quality of images and their availability over the study area for the selected time frame) and downloaded from the United States Geological Survey's Global visualisation (GloVis) viewer website (http://glovis.usgs.gov/) for the years 1986, 2001, 2011, and 2020. In addition, this choice of sensors was made to have the same pixel resolution for better comparison, as highlighted by several authors (Mama et al., 2013; Escadafal, 2007). Images of the late season (January–April), which represents the dry period, and a cloud cover criterion of less than or equal to 10% were considered to minimise the confusion between natural vegetation and agricultural lands and the interference of clouds, respectively (Zoungrana et al., 2015; Ruelland et al., 2008), with a slight constraint with images of 2001 (April image). Before usage, images from the ETM+ sensor (2011 and 2020) underwent a process of removal of scan line errors (stripes) using a null filling method in QGIS 3.10 representing a simple replacement method (Ali and Mohammed, 2013), which consisted of filling the no-data zones using validated pixels from the same scene but previous date, including the scenes of January 23, 2010 and December 26, 2019 for the images of 2011 and 2020, respectively. Beside the above, a radiometric correction has been considered for all the considered images using the Dark Object Subtraction (DOS) method on the blue, green, red, near infrared, and middle infrared bands to improve their quality.

The study area covers a single scene (scene path/row: 192/056) of a Landsat image (Table 3.1).

Table 3.1: Characteristics of Satellite Images

Year	Date of acquisition	Platform (Sensors)	Scene Cloud cover	Spatial Resolution	Projection
2020	2020/01/03	Landsat 7 (ETM+ C2 Level-2)	0/0	30m	WGS 84/ UTM Zone 31N
2011	2011/01/10	Landsat 7 (ETM+ C2 Level-1)	29/42	30m	
2001	2001/04/04	Landsat 7 (ETM+ C2 Level-1)	2/1	30m	
1986	1986/01/13	Landsat 5 (TM)	0/1	30m	

ETM: Enhanced Thematic Mapper, TM: Thematic Mapper, WGS: World Geological Survey

3.1.1.2 Reference Data

The reference data used as the basis for the classification (training), class validation, and accuracy assessment source from:

- ***Field Control Points:*** Control points were taken during a field campaign using a global positioning system over the period of January–March 2021 (dry season). A total of 177 points were taken across the 5 classes (built-up areas, mixed vegetation/savannah, water bodies, wetlands, croplands, and bare surfaces) across the AP to account for the year 2020.
- ***Topographic Map Control Points***: The 1989 topographic map (scale: 1:200000) (IGN/DCNC, 1980) and 2013 topographic map (including NB-31-XIV-1a LOME, NB-31-XIV-1b BAGUIDA, and NB-31-XIV-1c TSEVIE, realised at a scale of 1:50.000) were collected from the Directorate of National Cartography and Cadastre (Ministry of Equipment, Mines, Posts and Telecommunications) with 50 and 63 points considered to account for the years 1986 and 2011, respectively.
- ***Google Earth Imagery Control Points:*** Control points were taken from a high-resolution (10–15 m) digital globe and a SPOT satellite over the study area. In total, 50 points, 137 points, and 100 points were considered for the years 1986, 2001, and 2011, respectively.
- ***Classified Maps:*** A part of the points accounting for the year 1986 were collected from persistence areas (detected using the LCM) over the period of 1986–2001.

The dataset considered for classes validation is described in the Table 3.2.

Table 3.2: Summary of the Control Points for each LULC Class

CLASSES	1986	2001	2011	2020
Croplands/Bare surfaces	26	41	38	34
Built-up Areas	48	69	98	121
Savannah/Mixed vegetation	18	20	14	13
Wetlands	5	4	10	5
Water Bodies	3	3	3	4
Total	100	137	163	177

3.1.1.3 Local Perception on Land Use and Land Cover Dynamics

As part of the participatory approach, an interview was carried out during the period of January–March 2021 to capture the local community's (considered an agent of change) understanding of the dynamics of LULC in the AP. A total of 25 areas were considered in reference to the observed changes in the 1986 land use and land cover map. From there, 115 people were randomly selected and are mainly holders of houses, farmlands, and plantations. The investigation focused on (i) the drivers of changes in the study area, (ii) the causes of the change, and (iii) the past, current, and future LULC in the study area.

3.1.2 Climate Data

3.1.2.1 Station and Gridded Climate Data

Data considered for this study includes daily observations (temperature and precipitation) for stations in the AP (i.e., Lomé Aéroport, Mission Tové, and Sanguera) over a period of 1991–2020 obtained from the national meteorological agency (TogoMet). In addition, rainfall and temperature data (1991–2020) from the satellite-based products, including the Climate Hazards Group InfraRed Precipitation with Stations (CHIRPS) and the National Aeronautics and Space Administration Prediction of Worldwide Energy Resources (NASA POWER), were respectively considered as complementary datasets to deal with gaps found in the station observation datasets. Figure 3.2 and Table 3.3 depict, respectively, the spatial distribution of the grids considered and the characteristics of the satellite products.

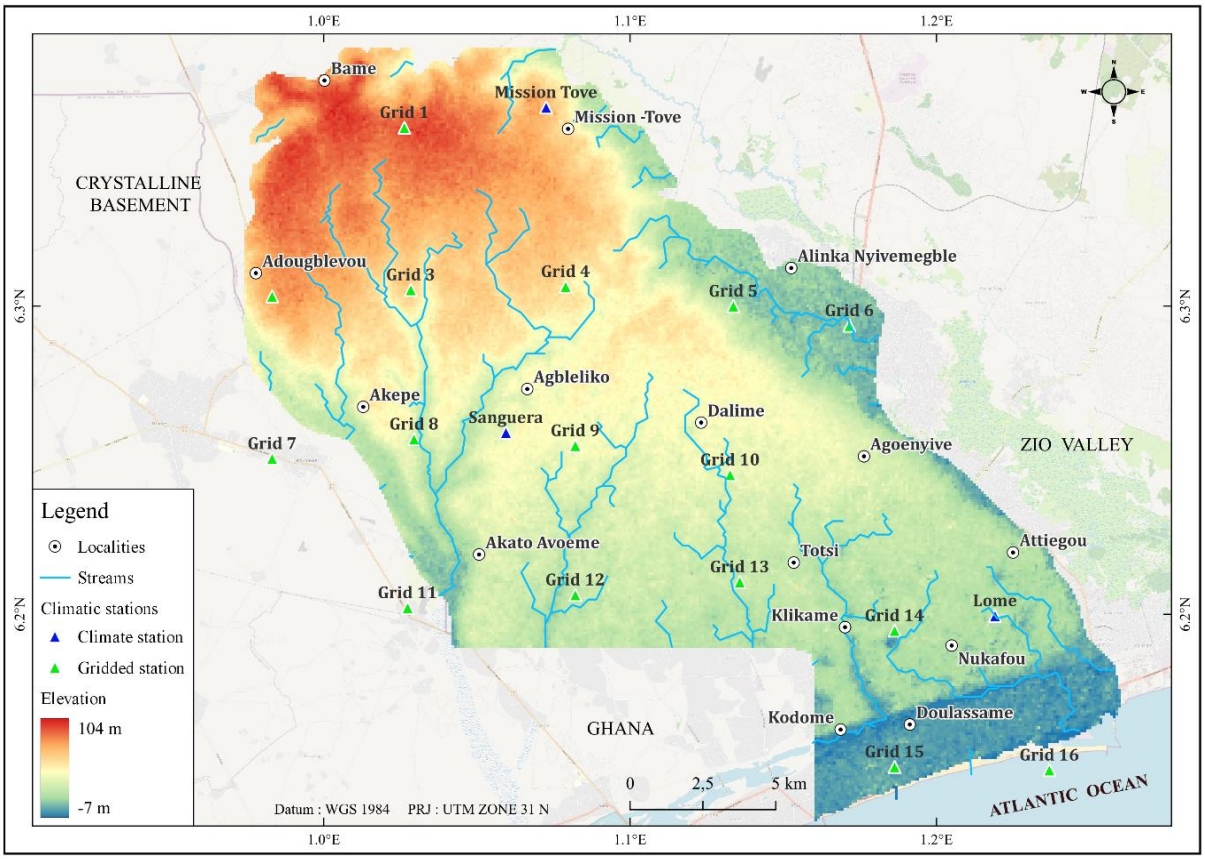

Figure 3.2: Map of the AP Showing Climatic Stations (https://usgs.gov, accessed on 05/07/2020)

Table 3.3: Rainfall and Temperature Satellite Products

Satellite Product	Temporal (Spatial) Coverage	Temporal (Spatial) Resolution	Institute	Website
CHIRPS	1981–Today (50˚ N–50˚ S)	Daily (0.05˚/~5 km)	UCSB and USGS	http://chg.geog.ucsb.edu/data/chirps

NASA POWER	1981–Today (0.5° N–0.5° S)	Daily (0.5°/~ 50 km)	NASA	http://power.larc.nasa.gov/data-access-viewer/

*UCSB, USGS, and NASA stand for the University of California/Sant Barbara (Climate Hazard Group), the United States Geological Survey, and the National Aeronautics and Space Administration, respectively.

3.1.2.2 Regional Climate Models (RCMs)

Daily climate variables (precipitation and temperature) datasets were obtained from the 50 km-resolution Coordinated Regional Climate Downscaling Experiment-Africa (CORDEX-Africa). The details of the selected CORDEX-Africa Regional Climate Models (RCMs), the various institutions that produced them, and their driven Global Climate Models (RCMs) are presented in Table 3.4. The Rossby Centre regional atmospheric model (RCA4) downscaled outputs, including CanESM2-RCA4 and NorESM1-RCA4, were selected based on prior studies that provide validation of the use of these resources in reproducing the climatology in West Africa, such as over the Volta River basin (Okafor et al., 2019), Tano River basin (Larbi et al., 2022), Oti River basin (Kwawuvi et al., 2022), and Kpong Irrigation Scheme area (Ashaley et al., 2020). Also, RACMO22T from the Royal Netherlands Meteorological Institute was considered for its ability to reproduce the precipitation in West Africa, including the Ouémé Basin River basin (M'Po et al., 2016) and the Senegal and Nakambe river basins (Karambiri et al., 2011), and more particularly for fairly simulating the Guinea Coast's rainfall (Akinsanola et al., 2015b). Finally, the CCLM4-8-17 from the Climate Limited-area Modelling Community was also considered. The RCMs outputs considered in this study covered a period of 45 years (1991–2005 and 2021–2050) for two Representative Concentration Pathways (RCP 4.5 and RCP 8.5). These datasets were downloaded from the World Data Centre for Climate (WDCC)/German Climate Computing Centre (DKRZ) website (https://cera-www.dkrz.de/WDCC/ui/cerasearch/info?site=IPCC-DDC-AR5-data).

Table 3.4: Selected CORDEX-Africa RCMs Characteristics

RCMs	GCMs	Spatial Resolution	Institution/Centre	Source
CanESM2-RCA4	CCCma-CanESM2	0.44°×0.44°	Canadian Centre of Climate Modelling and Analysis, Canada	https://esgf-data.dkrz.de/search/cordex-dkrz/
NorESM1-RCA4	NCC-NorESM1-M	0.44°×0.44°	The Norwegian Climate Center, Norway	
CCLM4-8-17	MPI-M-MPI-ESM-LR	1.9° × 1.9°	Climate Limited-area Modelling Community (CLM-Community)	
RACMO22T	ICHEC-EC-EARTH	1.25° × 1.25°	Royal Netherlands Meteorological Institute, The Netherlands	

3.1.3 Physicochemical, Isotopic, and Hydraulic Heads Data

Monthly water table-level data (2012–2020) from four piezometers tapping the CT aquifer (Campus Nord, USP Segbé, Lycée technique of Attiegou, and Peage Sanguera). In addition, punctual physicochemical data (2013 and 2020) for two piezometers (Campus Nord, Lycée technique of Attiegou) were obtained from the water resources directorate of the Ministry of Water and Rural Hydraulics. Furthermore, physicochemical and hydraulic head datasets from PRESAF (2015) were obtained from the LHAE (University of Lomé).

Apart from the secondary dataset, a total of 159 water samples and 110 water samples were collected in two single campaigns during the rainy season (RS) and dry season (DS), respectively. The RS covers the period of April–July 2021, while the DS covers the period February–March 2022. The sampling has considered the hydrogeology (MaS, CT, Pa, and Ma), the Lomé lagoon system (i.e., west lake, east lake, and Bè lake), and the ocean (Figures 3.3a-b) and was based on borehole or well accessibility during the campaigns (explaining why some water points were sampled over the two campaigns and others were not). Contrary to dug wells, water sampled in boreholes was pumped until stable values of key parameters (temperature, EC, and pH) were reached to get rid of impurities and allow the complete renewal of the water column. Then, 2 bottles of 1500 mL for each sample were collected for the physicochemical and isotopic analysis (49 water samples collected during the DS) as depicted in Figure 3.3c.

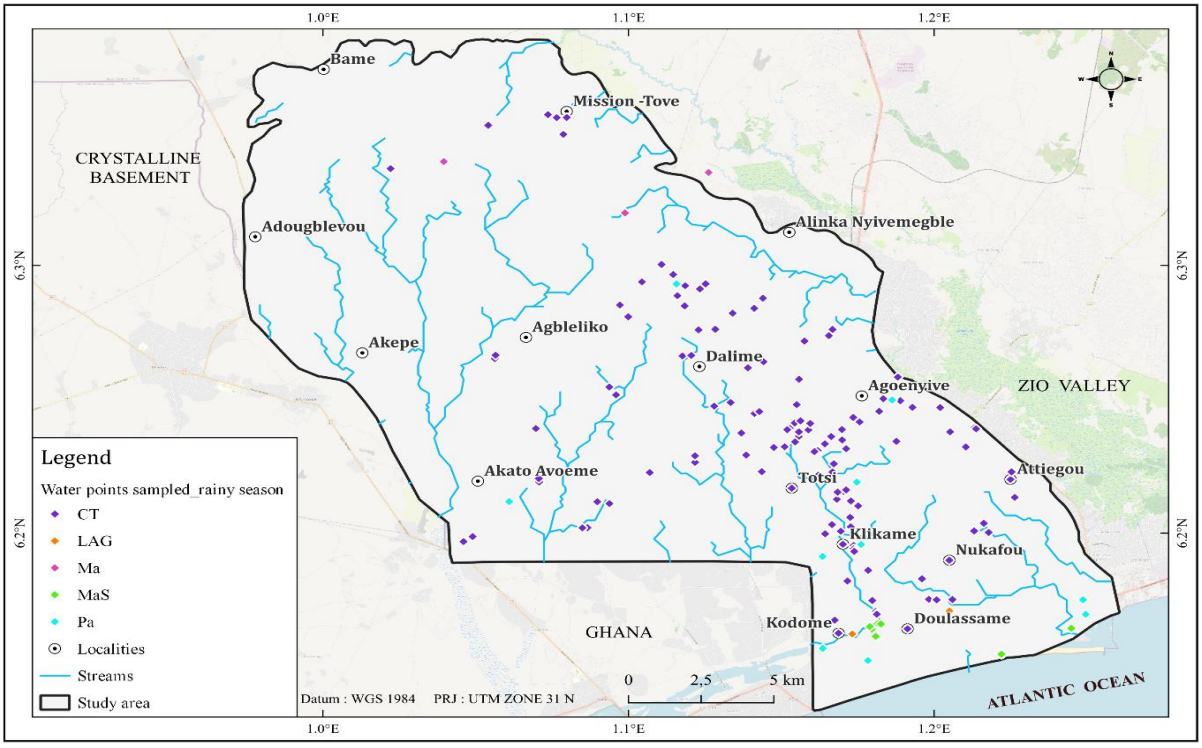

Figure 3.3a: Sampled Water Points for Physicochemical Characterisation (Fieldwork: RS 2021**)**

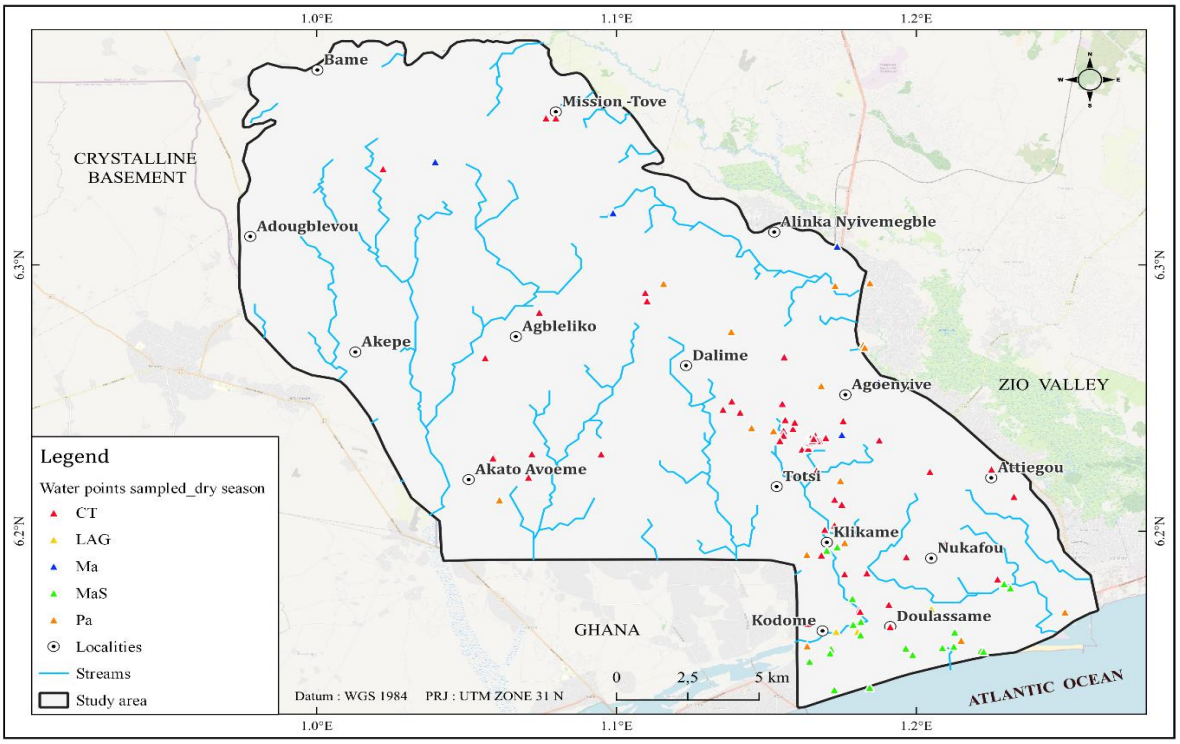

Figure 3.3b: Sampled Water Points for Physicochemical Characterisation (Fieldwork: DS 2022)

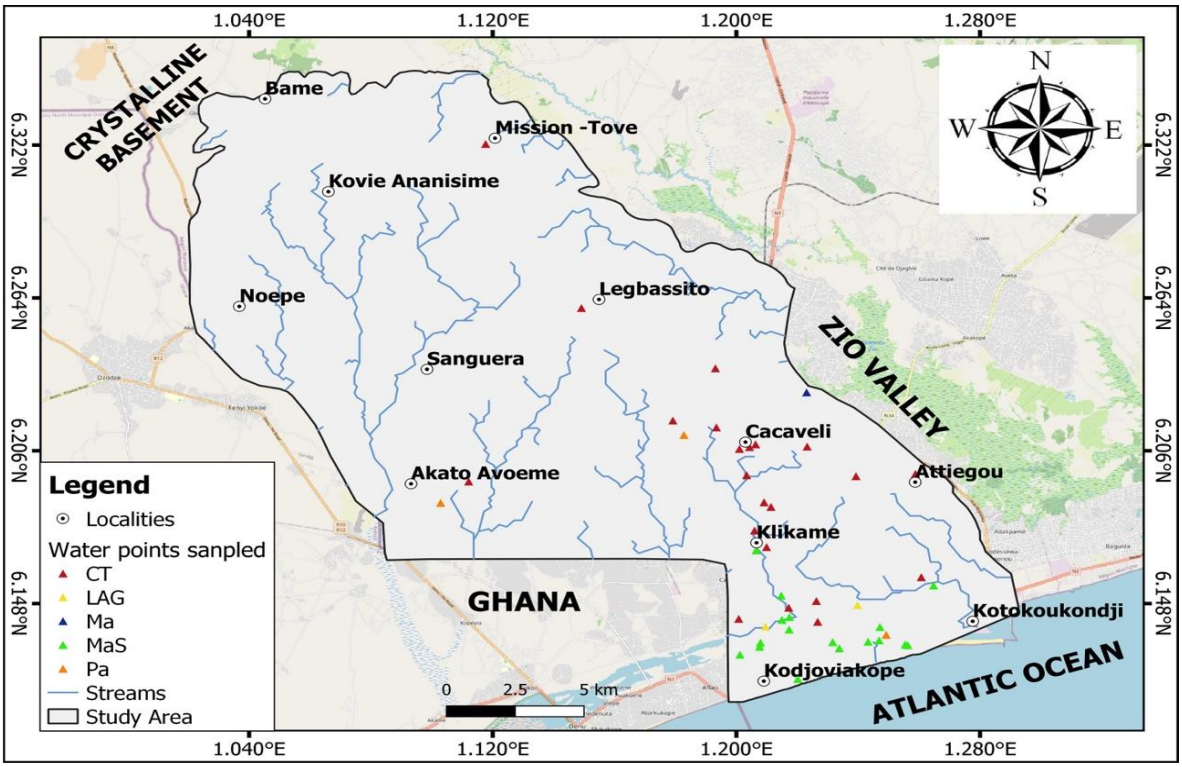

Figure 3.3c: Sampled Water Points for Isotopic Characterisation (Fieldwork: DS 2022)

On the other hand, water table levels were measured using a luminous probe. A total of 47 water points, including the MaS aquifer (11), CT aquifer (30), Pa aquifer (04), and Ma aquifer

(02), were considered for the RS, while 40 water points, including the MaS aquifer (14), CT aquifer (21), Pa aquifer (03), and Ma aquifer (02), were considered for the DS. These data were later used for aquifer characterisation, SEAWAT calibration, and validation.

3.1.4 Sub-surface Electrical Resistivity Data

The resistivity data were collected through the Electrical Resistivity Tomography (ERT), a geophysical approach highly considered in the context of seawater intrusion assessment. The choice of this method is based on its ability to depict a significant contrast between seawater electrical resistivity (0.2 Ωm) (Nowroozi et al., 1999; Loke, 1999) and saturated freshwater layers (> 10 Ωm) (Loke, 1999). This gives way to mapping out the subsurface groundwater salinity distribution (Najib et al., 2017; Werner et al., 2013). In addition, this method has been reported to be an ideal technique for mapping the position of the seawater-freshwater interface in coastal settings (Chabaane et al., 2018; Loke, 1999) because of its ability to deliver high-quality data (Batayneh et al., 2010; Dahlin, 2001).

A total of seven ERT profiles were carried out across the AP during the main RS (April–July 2021) using the ABEM Lund System (including SAS1000 resistivity). The ABEM Lund System consists of 64 electrodes distributed into 4 cables with a constant inter-electrode spacing of 5 m. The choice of ERT sites was based on a feasibility survey, considering the availability of space of 350 m (at least), the availability of borehole log data, or hydrogeological cross-sections as well as water points. Resistivity data was collected using the Wenner-Schlumberger (WS) and the Dipole-Dipole (DD) configurations. The choice of these two configurations is related to their keenest in imaging the geometry of the transition zone, including the embeddings, landings, and individualisation of intrusion cones. The Wenner-Schlumberger (WS) is a hybrid configuration resulting from the combination of the Wenner-alpha and Schlumberger arrays (Pazdirek and Bláha, 1996). Its adequacy for low resistivity environments, such as the sedimentary settings characterised by more porous and higher water content, is linked to its capacity to give results with adequate signal-to-noise ratio and resolution it provides (Ward, 1989). Used across the world (Bourhane, 2014; Rao et al., 2013) for its ability to better capture the geometrical characteristics of the interface or transition zone, including the immersion, the horizontal landings, and thickness (Comte, 2008; Comte and Banton, 2007), the configuration is also recommended for heterogeneous terrain with limited knowledge on the geometry of the structure to be studied (Bourhane, 2014). As for the dipole-dipole array, the choice was based on its ability to provide an adequate depth of investigation and its sensitivity to horizontal changes in resistivity associated with the lateral saline intrusion

(Reynolds, 2011). In addition, the configuration has been reported to be keen on capturing both the position and form of the rise cone if existing (Comte and Banton, 2007). Most of the profiles were carried out orthogonally to the coastline (Atlantic Ocean) and parallel to the Togolaise des Eaux (TdE) Cacaveli pumping field. The total length of these profiles ranges between 315 and 2395 m, while the depth of investigation ranges between 52.4 and 60 m. Further details of the profiles are summarised in Figure 3.4 and Table 3.5.

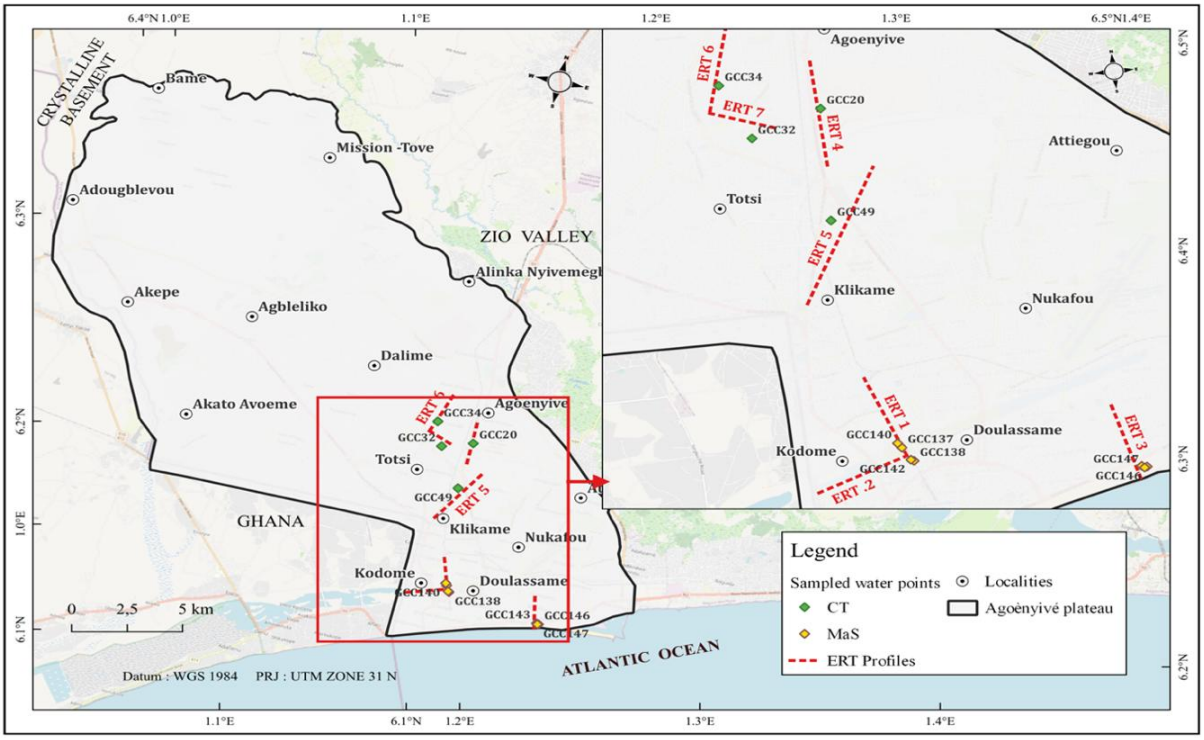

Figure 3.4: Map of AP Showing ERT Profiles (Fieldwork, 2021)

Table 3.5: ERT Profiles Characteristics

PROFILE	SITE	Direction	Electrodes Coordinates		N° of electrodes _ length	Array Configuration_ Number of datum points_Total number of data level_ Depth
			Electrode 1	Electrode 64		
ERT.1	Ahanoukopé	N (1-32) - S (33-64)	Long:1.216 Lat: 6.139	Long :1.213 Lat: 6.138	64_315	AHA2a_W-S64-2_177_17_50 AHA2b_D-D64-2_170_25_60
ERT.2	Ahanoukopé	E (1-32) - W (33-64)	Long:1.216 Lat: 6.139	Long:1.215 Lat: 6.142	64_315	HA1_W-S64 -2 _166_17_50 AHA1C_D-D64-2_163_24_60
ERT.3	Beach	N (33-64) - S (1-32)	Long: 1.254 Lat: 6.130	Long:1.254 Lat: 6.130	64_315	LPLAGE_ W-S64-2_148_17_50
ERT.4	État-Major General	N (33-64) - S (1-32)	Long: 1.209 Lat: 6.206	Long: 1.209 Lat: 6.211	144_715	CEMG_ W-S64-2_537_18_50
ERT.5	Université de Lomé	S (1-32) - N (33-64)	Long:1.203 Lat: 6.170	Long:1.213 Lat: 6.189	480_ 2395	YUL10_W-S 64_1855_18_50
ERT.6	Reserve_ Gendarme	S (1-32) - N (33-64)	Long:1.191 Lat: 6.209	Long:1.193 Lat: 6.215	144_715	LRYRES_W-S64-2_497_18_50
ERT.7	Togocom basement	N (1-32) - S (33-64)	Long:1.191 Lat: 6.209	Long:1.200 Lat: 6.206	64_555	LRYTGO_W-S64-2_365_18_50

NB: D-D and W-S stand for Dipole-Dipole and Wenner-Schlumberger, respectively.

3.1.5 Geological and Hydrogeological Data

The initial geological properties (hydraulic conductivity and storage coefficient) for the CT aquifer were essentially derived from the literature and existing works (Gnazou et al., 2018; DHE, 1983; PNUD, 1975) and from the SEAWAT calibration process. Nevertheless, because of the limited information available, vertical isotropy has been considered for hydraulic conductivity, while both vertical and horizontal isotropy have been considered for storage properties. Values of 10^{-2}–10^{-5} m/d were adopted as the hydraulic conductivity. For the storage coefficient values for the CT aquifer in the Sedimentary Coastal Basin in Benin, the estimated CT aquifer has also been taken into consideration (Agossou et al., 2022). Based on the above, values of 0.21, 0.25, and 0.3 were considered for the specific yield, effective porosity, and total porosity, respectively.

Quite unavailable, the parameters considered, including the screen ID and screen (top and bottom), were taken from PRESAF (2015) and the work of Bleza et al. (2020b). Parameters such as the depth of the wells have been defined under the hypothesis that all the boreholes considered cover the entire thickness of the aquifer, knowing the thickness and the depth of the lower confining bed of the CT aquifer across the study area.

3.1.6 Lithological, Soil and Topographic Data

The succession of geological materials in the study area was collected from existing studies, with the most including those of Akakpo (2017) and Bleza et al. (2020b). As for soil data, a soil map (scale: 1:500.000/1:1.000.000) was obtained from the National Geographic Institute-Togolese Republic (1960). Finally, for the topographic-related data, due to the lack of a topographic map, the Digital Elevation Model (accessible at https://gdex.cr.usgs.gov/gdex/) has been considered in the context of this study.

3.2 Methods and Tools

3.2.1 LULC Classification and Modelling

3.2.1.1 Image Pre-processing and LULC Classes Identification

A nomenclature of the different classes has been adapted from the national nomenclature established by the Ministry of Environment and Forest Resources for the development of databases on land use and Reducing Emissions from Deforestation (as of 2002) and forest Degradation (REDD+) nomenclature linked to the Togolese forestry code (as of 2018). Reference data (field observations, topographic maps, and Google Earth maps) and field expertise were used for the visual interpretation of acquired images (distinguishing spectral signatures). A total of five (05) classes were considered (Table 3.6).

Table 3.6: LULC Typology and Classes

Classes	Colour	Description
Built-up areas (1)		All areas of artificial construction, housing, roads, and human settlements (urban and rural) and urban plantations.
Savannah/Mixed vegetation (2)		Variant of savannah in which trees and shrubs are scattered among the grass carpets, with a slight dominance of either trees reaching the dimensions of trees in the forest (wooded) or only shrubs among the grass carpets (shrubby s) or grasses (grassy).
Water bodies (3)		Areas permanently covered with standing or moving water including rivers, lakes, water retention and Ocean.
Wetlands/Swamp formations (4)		Areas with forest/shrubs/grass/built-up standing on permanently waterlogged soil.
Cropland and Bare Surfaces (5)		Farmlands with trees (agroforestry parks and plantations) or without trees (cultures etc.), pastureland and bare surfaces (areas without vegetation: bare soil, rocky areas or mining quarries and beaches)

Source: MERF, 2018a (Modified)

3.2.1.2 Image Classification

The supervised classification was adopted along with the Maximum Likelihood Algorithm (MLA). This algorithm was considered as for: (i) its robustness in handling heterogenous settings like urban and semi-urban areas characterised by the co-existent of multiple classes including residential areas, water, farmland, and bare lands (Li et al., 2014), (ii) its keenest in representing medium-resolution images settings like the coastal areas (Heydarian et al., 2013), (iii) its ability to classify images' pixels on a probabilistic basis (Girard and Girard, 1999), (iv) its capacity to classify both spectrally unimodal and multimodal classes (Alshari and Gawali, 2021; Larbi et al., 2019; Folega et al., 2017), and finally (v) its highest accuracy with limited training samples (Li et al., 2014).

A part of the reference data and expert field knowledge were considered to guide the creation of Regions of Interest (ROI) for erroneous polygons and re-labelling, while the remaining part was used to validate the classification. The recognition of the different classes has been done considering the false colour composite (red, near infrared, and middle infrared bands) and Gaussian stretching in ENVI.

3.2.1.3 Accuracy Assessment

Accuracy assessment is an evaluation of the quality of the information derived for change detection. The assessment of each classification against the reference data is carried out statistically (Owojori and Xie, 2005). The error or confusion matrices, including the errors of commission (pixels being mistakenly included in a particular class) and omission (pixels being

mistakenly excluded from a particular class), were used. In addition, the non-parametric Kappa test, which accounts for all the elements in the error or confusion matrix, including the diagonal elements (Rosenfield and Fitzpatirck-Lins, 1986), was considered. The associated Kappa coefficient captures the agreement between model predictions and reality (Congalton, 1991). The classification accuracy and the Kappa coefficient calculation are depicted in Table 3.7.

Table 3.7: Algorithms for Accuracy Scores and Kappa Coefficient

User Accuracy	$\frac{Number\ of\ Correctly\ Classified\ Pixels\ in\ each\ Category}{Total\ number\ of\ Classified\ Pixels\ in\ that\ Category\ (\ row\ total)} X100$
Producer Accuracy	$\frac{Number\ of\ Correctly\ Classified\ Pixels\ in\ each\ Category}{Total\ number\ of\ Classified\ Pixels\ in\ that\ Category\ (columns\ total)} X100$
Overall Accuracy	$\frac{Number\ of\ Correctly\ Classified\ Pixels\ (\text{Diagonal})}{Total\ number\ of\ Reference\ Pixels} X100$
Kappa Coefficient	$\frac{(\text{TS xTCS}) - \sum(Column\ Total\ X\ Row\ Total)}{TS^2 - \sum(Column\ Total\ X\ Row\ Total)} X100$

TS = Total Sample, TCS = Total Corrected Sample

3.2.1.4 Scenarios Development

For LULC change projection over the study area by 2030 and 2050, four (04) different scenarios were considered, namely the Business-As-Usual (BAU) scenario, the afforestation scenario, the building policy scenario, and the wetland restoration scenario defined considering the existing policy targets. The choice of these scenarios is mainly based on the local knowledge obtained through key informants' interviews on the causes of LULC change and observed changes in classes. These scenarios (as described in Table 3.8) were developed through an alteration of the probability matrices for the main classes to be converted into built-up areas, croplands/bare surfaces, wetlands, and savannah/mixed vegetation produced from the Markov chain analysis. The afforestation scenario was built based on the National Reduction of Emission from Deforestation and Forest Degradation (REDD+) strategies (which consist of reducing emissions from deforestation and forest degradation, including the protection and sustainable management of forests and reinforcement of forest carbon stock) derived from the National Forestry Policy forestry coverage targets (MERF, 2018b). The wetland policy scenario is developed based on the country's commitment to conserve wetlands, ensure their rational use and restoration, and acknowledge and appreciate their advantages, as defined through the RAMSAR strategic plan (2016–2024). The building policy scenario was derived from the national policy for housing and urban development (MUH, 2013), with the second

pillar aiming at ensuring harmonious and balanced spatial development of the Togolese urban centres and their integration into the sub-regional urban network for the period of 2015–2019.

Table 3.8: LULC Change Scenarios (Baseline: 1986–2020)

Scenario's type	Description
Business-As-Usual (BAU)	The future 2030 and 2050 LULC maps will be produced considering the expansion of built-up areas at the expense of croplands and the expansion of croplands at the expense of savannah or missed vegetation and wetlands.
Afforestation	Increase in natural vegetation (savannah or mixed vegetation) by 10% and 30% by 2030 and 2050, respectively, by limiting the expansion of cropland.
Wetland Restoration Policy	Increase in wetlands areas by 5% and 15% by 2030 and 2050, respectively, by limiting the expansion of croplands and built-up areas.
Building Policy	Decreasing the spatial expansion of built-up areas by 5% and 15% by 2030 and 2050, respectively, by increasing the expansion of croplands and savannah or mixed vegetation.

3.2.1.5 Future Land Use and Land Cover Analysis in the AP

For future LULC predictions, the Land Change Modeller (LCM) for Ecological Sustainability is considered. Developed by Clark Labs, the LCM is an integrated machine learning software (Van Soesbergen, 2016) embedded in IDRISI Selva GIS (Terrset Geospatial Monitoring and Modelling System). It uses, respectively, the Markov Chains analysis (Markov chain model) and the automatic Multi-Layer Perceptron for time prediction and spatial allocation of simulated land cover scores (Eastman, 2012). The choice of the LCM is based on its: (i) ability to carry out decadal assessments but also to provide high accuracy LULC change analysis (Roy et al., 2014; Mithun et al., 2022), (ii) its ability to integrate various transitions involving same explanatory variables into a single sub-model, characteristic of urban and coastal settings (Regmi et al., 2017; Nahib et al., 2018), (iii) its ability to reproduce LULC in West Africa (Vea catchment in Ghana) with a good overall Crammer's V value and accuracy (Larbi et al., 2019), (iv) its limited cost, and (v) its usefulness and viability for smaller projects (Van Soesbergen, 2016) but also (vi) its ability to inform/produce key knowledge/information in support to projects aimed at Reducing Emissions from Deforestation and Forest Degradation (REDD).

Explanatory Variables

Biophysical and socio-economic factors known as "explanatory variables" are reported to be key in shaping a particular area's LULC (especially the causal relationships of its dynamics). This makes them paramount for developing a model that captures the realities on the ground (Christensen and Arsanjani, 2020). The potential explanatory variables considered in the

context of this study were identified based on the literature (Bawa, 2017) and local perceptions of drivers of change in the study area, as summarised in Table 3.9. From there, the Land Change Modeller's projective power and the influence order of the explanatory driver variables considered were assessed using the accuracy scores. These scores are included in the Parameters and Performance session of the LCM (average skill measure and average accuracy rate) and the sensitivity of the model to forcing independent variables to be constant outputs. These tests are reported to be the strongest (Eastman, 2016).

Table 3.9: Description of Potential Explanatory Variables

Driver variable	Spatial/Temporal Resolution	Implication for LULC Change	Source
Digital Elevation Model (DEM)	30 m	Determines the hydrological process in a basin and shapes the spatial croplands development.	SRTM Digital Elevation Database
Slope	30 m	Shapes the spatial croplands development	
Distance from Urban Center	Scale: 1:50.000/1986	With potential to influence future built-up areas sprawl.	Directorate of National Cartography and Cadastre
Distance from Urban Center	Scale: 1:200000/2013	With potential to influence future built-up areas sprawl.	
Distance from main Road	Scale: 1:50.000/1986	With potential to influence future built-up areas sprawl.	

Change Detection – Transition Potential Modelling – Model Validation – Change Prediction

The analysis and scenario map development for the AP include processes such as change detection, transition potential modelling, model validation, and change projection.

Change detection in LULC for the considered years was performed by the post-classification comparison technique, a widely used approach for LULC change detection (Mahmoud and Alazba, 2016), through the change analysis module of the LCM (including gain and loss, net change, and contributors to the change). In addition, to capture the change pattern between periods of different LULC classes, the percentage of change and the rate of change were considered as expressed in Equations 3.1 and 3.2 (Hassen and Assen, 2018):

$$Percent\ of\ change = \frac{(LULC_{t2} - LULC_{t1})}{LULC_{t1}} * 100 \quad \text{(Eq.3.1)}$$

$$Rate\ of\ change = \frac{(LULC_{t2} - LULC_{t1})}{T} \quad \text{(Eq.3.2)}$$

With $LULC_{t2}\ and\ LULC_{t1}$ standing for the area of the late and earlier image classified, respectively and T, the time interval between 2 images considered.

Change prediction was carried out using the historical rate of change and transition potential maps (Müller et al., 2010).

The major transitions were created using the change analysis module along with the historical LULC maps of the years 1986, 2001, 2011, and 2020 (2001 t_1–2011 t_2 and 1986 t_1–2020 t_2) as the inputs to the model and capture the transition that has occurred from one class to the other, considering two sets of images of different dates but the same legend and spatial characteristics (Megahed et al., 2015). In addition, the likelihood of transformation (evidence likelihood image) from one class to the others (transition from savannah/mixed vegetation and wetlands to croplands and transition from croplands/bare surfaces to built-up areas) was created using the variable transformation utility module with the re-classed transition maps (RECLASS module) and classified maps as inputs. From there, the transitions were created for areas less than 22 square kilometres (2200 hectares). At the end, the Multi-Layer Perceptron (MLP) neural network, one of the algorithms of the LCM, is employed for transition potential modelling and transition potential maps produced using the transition potentials module. A total of two sub-models were run, including the cropland sub-model (transition from savannah or mixed vegetation and wetland to croplands) and the built-up areas sub-model (transition from croplands and bare surfaces to built-up areas). Finally, the transition potentials for the period 2001–2011 were created using the transition sub-models.

The Land Change Modeller's (LCM) projective power and the influence order of the explanatory driver variables considered (slope, DEM, distance from the main road, distance from urban areas 1986, and distance from urban areas 2013) were assessed using the accuracy scores and the SENSITIVITY OF MODEL TO FORCING INDEPENDENT VARIABLES TO BE CONSTANT outputs, respectively. The accuracy scores are embedded in the PARAMETERS AND PERFORMANCE section and include the average skill measure and the average accuracy rate. As a matter of fact, the detailed analysis of the power of explanatory variables provided after the completion of the training stage (in the case of the MLP model) was reported to be the strongest test (Eastman, 2016). The skill measures account for the number of correct predictions minus those attributable to random guessing to that of a hypothetical perfect prediction (Gibson et al., 2018). They are scaled between -1 and 1, with values below 0 indicating worse model performance (compared to expected random guessing), 0 implying model performance as random guessing, and finally, values between 0 and 1 indicating performance exceeding expectation by pure chance.

For the validation of the LCM projection (for the year 2020), a statistical approach with the aptitude to examine the agreement between a pair of maps that show any categorical

variable and can have any number of categories (Pontius and Chen, 2006) was considered. As a result, the simulated map (as of 2020) was compared with the classified map of the same year using the validation module to evaluate the accuracy of the model using two well-known methods, including the Kappa Index/statistics/scores (K_{scores}) (Langley et al., 2001; Pontius, 2000) and the Relative Operating Characteristics (ROC) (Mishra et al., 2014). The K_{scores} considered include the K_{no} (which gives the overall simulation run), the $K_{location}$ (level of agreement of location, given a specified quantity), the $K_{quantity}$ (level of agreement of quantity, given the model's ability to specify location), and the overall Kappa ($K_{standard}$). Following the validation and assessment of the model's performance, the LCM was used to project the future LULC scenario maps for the years 2030 and 2050 based on the same driving variables and the historical LULC change between 1986 and 2020, going through the previous process.

The entire process and the adopted steps are summarised in Figure 3.5.

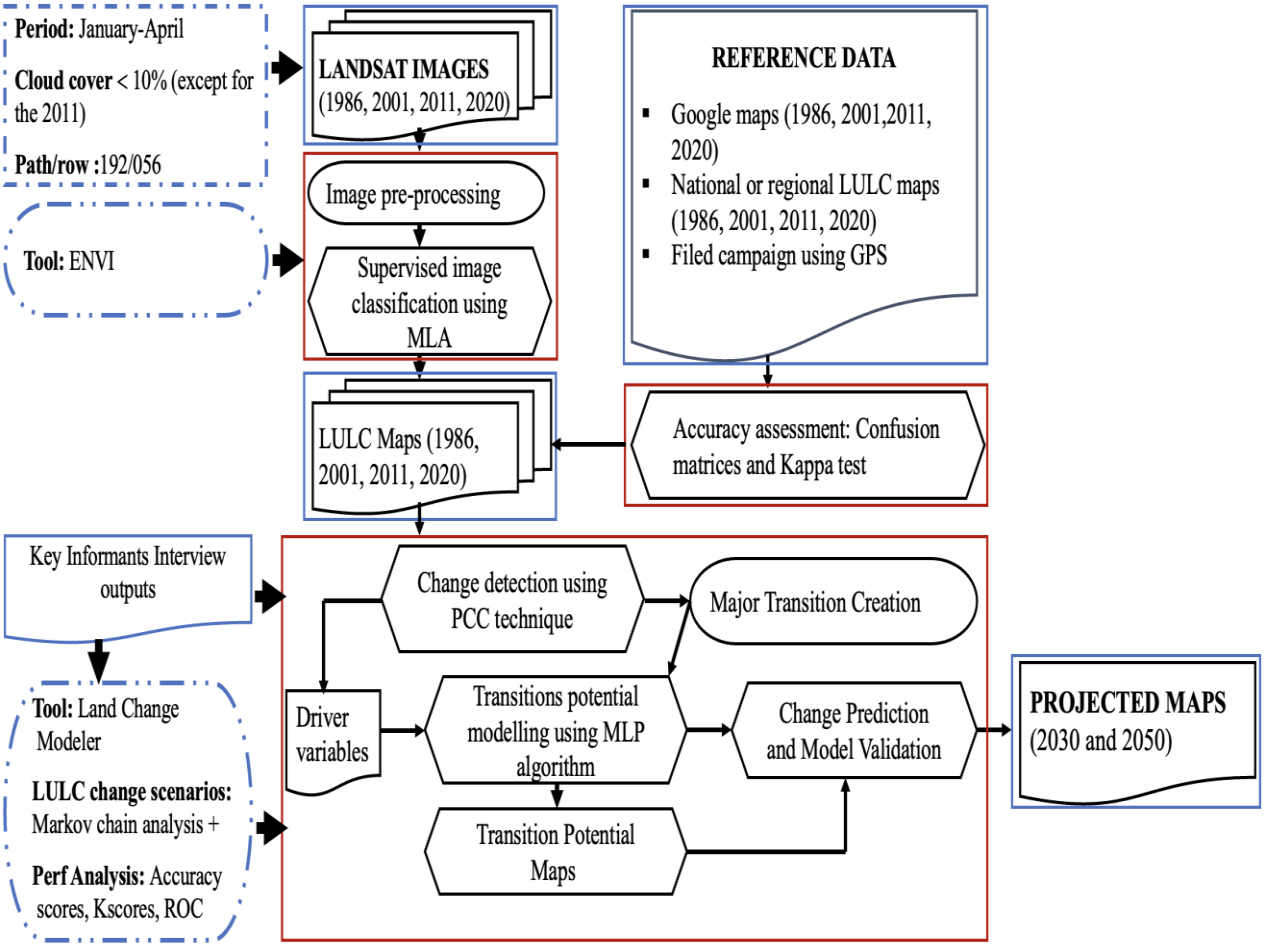

Figure 3.5: Methodological Sketch Diagram

*LCM, MLP, MLA, LULC, Blue boxes and red boxes stand Land Change Modeler, Multi-Layer Perceptron, Maximum likelihood Algorithm, and Land Use Land Cover, Data and tools, and processes, respectively.

3.2.2 Analysis of Climatic Trends and Future Projections

3.2.2.1 Data Mining Data Mining and Quality Control

The data mining and quality control were realised for three stations (Lomé, Mission Tové, and Sanguera stations) using Microsoft Excel and the Rclimdex Tydiverse (Wickham et al., 2019), gridExtra (Auguie, 2017), VIM (Kowarik and Templ, 2016), and Knitr (Xie, 2014) packages of R (version 4.1.0). The quality control consisted of detecting and replacing erroneous values (mainly negative rainfall values and daily rainfall values greater than 200 mm) with missing values (−999 in this case).

3.2.2.2 Bias Correction of the Regional Climate Models' Outputs

Teutschbein and Seibert (2010) highlighted the need for bias correction of RCMs in the context of climate impact studies to palliate the bias representation associated with raw RCMs in producing the monthly mean considering current climate conditions (Minville et al., 2009). In this study, statistical downscaling has been considered with the bias in the RCMs selected (Gudmundsson et al., 2012) corrected using the Climate Model data for hydrologic modelling (CMhyd) (Rathjens et al., 2016), a widely used extraction and bias correction tool in the context of climate change assessment (Yeboah et al., 2022; De Carvalho et al., 2021; Larbi et al., 2019). The distribution mapping (quantile mapping) was considered for the bias correction of the temperature, while the power transformation method was considered for the precipitation based on their performance as depicted by existing research (Gunavathi and Selvasidhu, 2021; Teutschbein and Seibert, 2012).

Power Transformation of Precipitation (PTR)

Essentially accounting for correction in monthly mean and variance, the PTR applies an exponential correction factor aP^b (Mendez et al., 2020; Kim et al., 2020) with 'b' estimated with a monthly (b_m) distribution-free approach using a 90-time steps window. Initially, 'b' is determined by equalising the coefficient of variation (CV) of corrected RCM precipitation (P^b) and observed precipitation (P_{obs}) for each month (m) using the root-finding algorithm based on Brent's method (Brent, 1971). Then, 'bm' and 'CV_m' are estimated using Equations 3.3–3.4, respectively. In addition, Equations 3.5–3.6 were used for equalising the datasets.

$$f(b_m) = 0 = \mathrm{CV}_m\left(P_{obs}(t)\right) - \mathrm{CV}_m\left(P^{b_m}{}_{\boldsymbol{Contr}}(t)\right) \quad \text{(Eq.3.3)}$$

$$\frac{\sigma_m\left(P_{obs}(t)\right)}{\mu_m\left(P_{obs}(t)\right)} - \frac{\sigma_m\left(P^{b_m}{}_{\boldsymbol{Contr}}(t)\right)}{\mu_m\left(P^{b_m}{}_{\boldsymbol{Contr}}(t)\right)} \quad \text{(Eq.3.4)}$$

$$P^{*1}{}_{\boldsymbol{Contr}}(t) = P^{b_m}{}_{\boldsymbol{Contr}}(t) \quad \text{(Eq.3.5)}$$

$$P^{*1}{}_{\boldsymbol{Scenario}}(t) = P^{b_m}{}_{\boldsymbol{Scenario}}(t) \quad \text{(Eq.3.6)}$$

Thereafter, the long-term monthly mean of observed precipitation (P_{obs}) is matched with the monthly mean of the intermediate series precipitation using the standard linear scaling method. At the end, corrected control and scenario precipitation datasets were derived using Equations 3.7 and 3.8.

$$P^{*1}{}_{\boldsymbol{Contr}}(t) = P^{*1}{}_{\boldsymbol{Contr}}(t) * \left[\frac{\sigma_m\left(P^{b_m}{}_{\boldsymbol{Contr}}(t)\right)}{\mu_m\left(P^{b_m}{}_{\boldsymbol{Contr}}(t)\right)}\right] \quad \text{(Eq.3.7)}$$

$$P^{*1}{}_{\boldsymbol{Scenario}}(t) = P^{*1}{}_{\boldsymbol{Scenario}}(t) * \left[\frac{\sigma_m\left(P^{b_m}{}_{\boldsymbol{Contr}}(t)\right)}{\mu_m\left(P^{b_m}{}_{\boldsymbol{Contr}}(t)\right)}\right] \quad \text{(Eq.3.8)}$$

Distribution Mapping of Temperature (DM)

The DM method matches the distribution functions of both the RCM outputs and the observed data, thus correcting the mean, standard deviation, and quantiles. It is assumed that the bias may result from a particular frequency of distribution followed by the simulated RCM and observations (Themeßl et al., 2011). In addition, the Gamma distribution is considered for effective temperature distribution (Equation 3.9).

$$\mathrm{f_y}\left(\chi \,|_{\alpha,\beta}\right) = \chi^{\alpha-1} * \frac{1}{\Gamma(\alpha) * \beta^{\alpha}} * e^{\frac{-\chi}{\beta}} \quad \chi \geq 0;\ \alpha,\beta > 0 \quad \text{(Eq.3.9)}$$

With **Γ**(.), **α**, **β** standing for the Gamma function, shape parameter, and scale parameter, respectively. Before the application of the DM method, the local intensity scaling (LOCI) method is applied to determine the wet days using the specific threshold. Thereafter, RCMs' outputs are corrected in terms of the Gamma cumulative distribution function (F_γ) and its inverse function ($F^{-1}{}_{\boldsymbol{\gamma}}$) as expressed in Equations 3.10 and 3.11, respectively.

$$P^{*1}{}_{\boldsymbol{Contr}}(t) = F^{-1}{}_{\boldsymbol{\gamma}}\left(F_\gamma\left(P_{Control}(t)\,|_{\alpha_{Control,m},\beta_{Control,m}}\right)\,|_{\alpha_{Control,m},\beta_{Control,m}}\right) \quad \text{(Eq.3.10)}$$

$$P^{*1}{}_{\boldsymbol{Scenario}}(t) = F^{-1}{}_{\boldsymbol{\gamma}}\left(F_\gamma\left(P_{Scenario}(t)\,|_{\alpha_{Control,m},\beta_{Control,m}}\right)\,|_{\alpha_{Control,m},\beta_{Control,m}}\right) \quad \text{(Eq.3.11)}$$

3.2.2.3 Satellite Data and Climate Models Evaluation and Validation

Satellite-based products (CHIRPS and NASA POWER) and RCMs evaluation and validation accuracy statistics were performed in R software using the hydroGOF package, considering some key metrics including the Root Mean Square Error (RMSE), the Coefficient

of Determination (R^2), Percent Bias (PBIAS), and Nash-Sutcliffe Efficiency (NSE) through Equations 3.12–3.15. The acquired data (satellite and RCMs) are basically validated against the in-situ observations (Larbi et al., 2018; Akinsanola et al., 2015b). PBIAS measures the average tendency of the simulated values to be larger or smaller than their observed values. The optimal value is 0, while low values imply high accuracy of the model simulation. In addition, the obtained values are either positive or negative, indicating an overestimated or underestimated bias, respectively. NSE (Nash and Sutcliffe, 1970) values range from 1 to -∞, with values equal to 1, ≥ 0.7, and ≥ 0.5 indicating the best, very good, and satisfactory fit between simulated and measured data, respectively (Nash and Sutcliffe, 1970). The R^2 gives information about the goodness of fit between the simulated data and the observed data. It ranges from 1 to 0, with 1 being the best fit between the simulated and observed data, and typical values greater than 0.5 are considered acceptable (Santhi et al., 2001).

$$NSE = 1 - \left[\frac{\sum_{i=1}^{N}(y_{obs} - y_{sim})^2}{\sum_{i=1}^{N}(y_{obs} - \bar{y}_{obs})^2}\right] \quad \text{(Eq.3.12)}$$

$$PBIAS = 100\frac{\sum_{i=1}^{N}(y_{obs} - y_{sim})}{\sum_{i=1}^{N}(y_{obs})} \quad \text{(Eq.3.13)}$$

$$RMSE = \sqrt{\frac{1}{N}\sum_{i=1}^{N}(y_{obs} - y_{sim})^2} \quad \text{(Eq.3.14)}$$

$$R^2 = 1 - \frac{\sum_{i=1}^{N}(y_{obs} - y_{sim})^2}{\sum_{i=1}^{N}(y_{obs} - y_{obs})^2} \quad \text{(Eq.3.15)}$$

Where y_{obs} , $\bar{y}_{obs}$ and N standing for observed data, predicted/simulated data and the average of observed data and the number of observations, respectively.

3.2.2.4 Trend Analysis

The change detection and the autocorrelation in the time series were carried out using the Khronostat software. Statistical tests embedded in the software, including the Pettitt test (Pettitt, 1979), the Buishand test (Buishand, 1982 and 1984), and the Lee and Heghinian test (Lee and Heghinian, 1977), were considered for break or change point detection. At the same time, the auto-correlogram and auto-correlation Rang test have been used at the 5% significance level to check the time series independence.

Based on the results obtained from the change detection and auto-correlation results, the analysis of the climate parameters (rainfall and temperature) was performed using both the Mann-Kendall (MK) and Modified Mann-Kendall (MMK) tests along with the Sen Slope test.

The Mann-Kendall (MK) test is recognised as a non-parametric test that does not require series to be normally distributed and is considered in various studies for climatic trend analysis (Fofana et al., 2022; Adeyeri et al., 2019). Each value is related to the other values in the series sequentially. The Mann-Kendall statistics are given in Equations 3.16–3.20.

$$S = \sum_{k=1}^{n-1} \sum_{j=k+1}^{n} Sgn(x_j - x_k) \quad \text{(Eq.3.16)}$$

With x_j and $x_k$representing sequential data values for the time series data of length n. The sum of the Sgn series is defined as below:

$$Sgn(x_j - x_k) = \begin{cases} 1 \ \ if \ \ x_j > x_k \\ 0 \ \ if \ \ x_j = x_k \\ -1 \ \ if \ \ x_j < x_k \end{cases} \quad \text{(Eq.3.17)}$$

The statistic S is approximately normally distributed, with the mean E (S) and the variance V (S) computed as follows:

$$E(S) = 0 \quad \text{(Eq.3.18)}$$

$$V(S) = \frac{1}{18}\left\{n(n-1)(2n+5) - \sum_{i=1}^{n} t_i[(t_i - 1)(2t_i + 5)]\right\} \quad \text{(Eq.3.19)}$$

With t representing the extent of any given tie and Σti denoting the summation over all ties, only used if the data series contains tied values.

The standard normal variate Z is calculated as follows:

$$Z = \begin{cases} \frac{S-1}{\sqrt{V(S)}} & if \ \ S > 0 \\ 0 \ \ if \ \ S = 0 \\ \frac{S+1}{\sqrt{V(S)}} & if \ \ S < 0 \end{cases} \quad \text{(Eq.3.20)}$$

The trend is evaluated at the 5% significance level (corresponding to the threshold value of ±1.96) with the null hypothesis (Ho), stipulating no trend is rejected when /Z/ ≥ Zα/2 at the α = 0.05 level of significance. The positive and negative values of Z implicate a rising trend and a decreasing trend, respectively.

The slope test is carried out using Theil-Sen's estimator, which estimates the slope of n pairs of data points (Sen, 1968) and was modified by Hirsch et al. (1982) in order to assess the magnitude of the trend. The formula is depicted in Equations 3.21–3.23.

$$\boldsymbol{Q_i} = \frac{(\boldsymbol{x_j} - \boldsymbol{x_k})}{(\boldsymbol{j} - \boldsymbol{k})} \quad \text{for i = 1, ……N} \tag{Eq.3.21}$$

With $\boldsymbol{x_j}$ ***and*** $\boldsymbol{x_k}$ being values at times j and k, respectively. Note, j >k. Qi is Sen's estimator of slope, which is the median of these N values.

If only one piece of data is present each time, the Equation 3.22 below will be considered :

$$\boldsymbol{N = n\,(n-2)/2} \tag{Eq.3.22}$$

With n being the number of time periods along with N values of Qi ranked by Q1 ≤ Q2 ≤⋯ ≤ QN-1 ≤ QN

$$\boldsymbol{Q_{med}} = \begin{cases} \boldsymbol{Q_{\frac{(N+1)}{2}}} \quad \boldsymbol{if} \quad \boldsymbol{N\ is\ \ odd} \\ \boldsymbol{(1/2)\left(Q_{N/2} + Q_{\frac{(N+2)}{2}}\right) if\ N\ \ is\ even} \end{cases} \tag{Eq.3.23}$$

Recommended to correct the effect of autocorrelation in time series, the MMK is considered in addition to MK for trend analysis. This method consists of (i) calculating the trend using the Sen slope estimator (Equation 3.24); (ii) removing the trend in the time series (Equations 3.25–3.28); (iii) subtracting the calculated lag-1 autocorrelation coefficient from the trendless time series (Equation 3.29) and adding the trend to the independent time series (Equations 25–26); and then the trend in the independent time series is calculated using the MK method.

$$S_{SSE} = median\left(\frac{Z_j - Z_i}{j - i}\right) \text{ for } \forall\ j>i;\ i=1:\ n\text{-}1 \text{ and } j=2:\ n, \tag{Eq.3.24}$$

$$Z^d{}_{\mathbf{SSE}} = Z_k - S_{SSE}.k; for\ k = 1{:}n, \tag{Eq.3.25}$$

$$Z^d{}_{\mathbf{ITA}} = Z_k - S_{ITA}.k, \tag{Eq.3.26}$$

$$Z^i = Z_k - \varphi 1.Z_k - 1, \tag{Eq.3.27}$$

$$Z^t{}_{\mathbf{SSE}} = Z^i{}_{\mathbf{k}} + S_{SSE}.k, \tag{Eq.3.28}$$

$$Z^t{}_{\boldsymbol{ITA}} = Z^i{}_{\mathbf{k}} + S_{ITA}.k. \tag{Eq.3.29}$$

With S_{SSE} and S_{ITA} standing for trend values calculated using SSE and Sen_ITA methods
$Z^d{}_{\text{ITA}}$ and $Z^d{}_{\text{SSE}}$ representing time series without trend.
Z^i indicates the independent time series without correlation effect.
$Z^t{}_{\text{SSE}}$ and $Z^t{}_{ITA}$ represent independent time series including the trend value calculated.
.

3.2.2.5 Spatial Analysis of Rainfall and Temperature

To generate spatially continuous data in order to appreciate the spatial distribution of climate parameters both in the past and the future, the Inverse Distance Weighting (IDW) method was considered in the context of the AP. Belonging to the deterministic interpolation methods (Qu et al., 2017), the IDW was considered based on (i) the characteristics of the study

area (flat zone with the elevation varying between -7 and 104 m and a small size with a scale of 5 km) and (ii) its accuracy in representing spatial distribution patterns (le Roux et al., 2023).

The IDW is a non-linear interpolation technique based on the principle that the value of a considered parameter in an unmeasured location can be defined by leveraging the measured values in neighbouring points or locations. The overall weight assigned is a function of the distance between data points and the interpolated location. The method is built on the assumption that the value at the interpolated location will be closer to the value at a data point closer to it than the one distant, thus making weights proportional to the inverse of the distance. The value at the interpolated location is calculated using Equation 3.30.

$$\hat{v}_i = \frac{\sum_{i=1}^{n} \frac{1}{dp_i} v_i}{\sum_{i=1}^{n} \frac{1}{dp_i}} \qquad \text{(Eq.3.30)}$$

With $v_i, dp_i \ldots . dp_n, n$, p standing for the known value, the distances from n data points and the power of p of the point estimated, respectively.

Figure 3.6 summarizes the methodology for climate trend analysis and future projections.

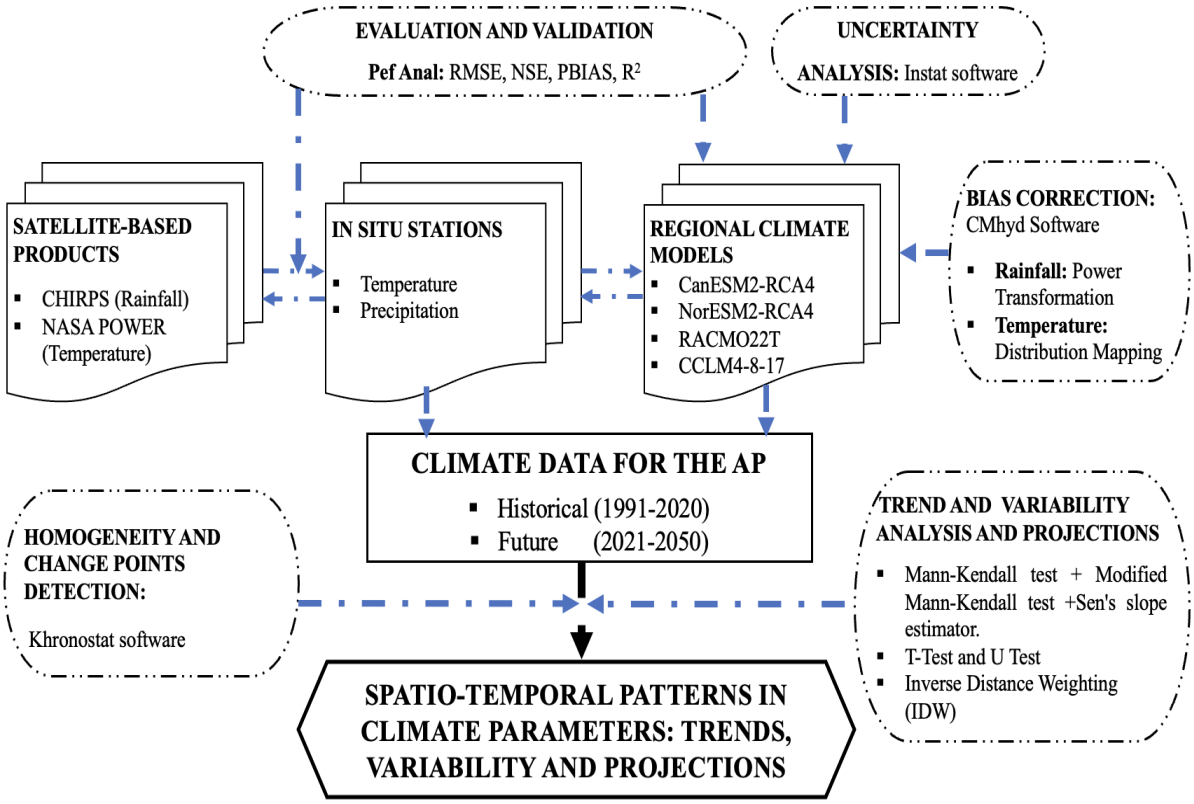

Figure 3.6: Flowchart of Climate Trend Analysis and Future Climate Projections

RMSE, R^2, PBIAS, and NSE stand for Root Mean Square Error the Coefficient of Determination, Percent Bias and Nash-Sutcliffe Efficiency, respectively.

3.2.3 Characterisation of the Multi-Layered Aquifer in the AP

3.2.3.1 Geochemical Characterisation of the Multi-Layered Aquifer

Physical parameters (temperature, pH, and EC) were measured *in situ* using a portable multiparameter type HANNA. The major ions (cations and anions) were analysed at the LHAE (University of Lomé, Togo) using the French Association of Standardisation (AFNOR) methods (AFNOR, 1997). These major ions considered, along with the measuring apparatus and methods, are summarised in Table 3.10. At the end, the water ionic balance of each sample was checked and validated for a charge balance error of ±5% using the "Diagrams" software (Simler, 2005).

Table 3.10: Measuring Apparatus and Methods for Physicochemical Characterisation

Parameters	Methods/Measuring Apparatus	Accuracy
Temperature	Conductimetry (NFT90-111)	±0.5 °C
EC	Conductimeter WTW	±1%
pH	Electrometry (NFT90-017) / Hanna portable pH/EC meters, pHmeter WTW pH330i	±0.1
Mg^{2+}, Ca^{2+}	Complexometric with EDTA titration (NFT90-003)	Ca^{2+} = ±0.5 $mg.L^{-1}$ Mg^{2++} = ±0.24 $mg.L^{-1}$
Oxydability to the KMnO4	Hot acid medium / Glassware and reagents	-
K^{+}, Na^{+}	Flame photometry (NFT 90-20) / Perkin Elmer model 2380 spectrophotometer	Limit of Detection = 0.2 $mg.L^{-1}$
Cl^{-}	Volumetric analysis (NFT 90-014) / Glassware and reagents	±0.5 $mg.L^{-1}$
HCO_3^{-}	Volumetric analysis (NFT 90-036) / Glassware and reagents	±3 $mg.L^{-1}$
$NH4^{+}$, $NO2^{-}$, Fe2+, Mn2+, PO43-, $NO3^{-}$,$SO4^{2-}$	Molecular absorption spectrophotometry (NFT 90-009, NFT 90-012, NFT 90-013, NFT 90-01, NFT90-045, NFT90-013, NFT900175) / Digitron Elvi 675 spectrophotometer	$NO2^{-}$, $NO3^{-}$, $SO4^{2-}$ = 1–2%

Multiple approaches, including conventional methods such as descriptive statistics (minimum, maximum, average, standard deviation, and spatial variation), bivariate plots, indexes/indicators (including the Revelle Index, cation-anion ratios, and saturation indices), and diagrams (Piper diagram and Hydrochemical Facies Evolution Diagram), were used for hydro-chemical result interpretations. In addition, statistical methods such as the Principal Components Analysis (PCA) and the Ascendent Hierarchic Classification (AHC) were

considered for mineralization origin detection. Furthermore, the spatial distribution of the salinity and state of water saturation with respect to carbonated and evaporitic minerals was also considered to illuminate natural sources of mineralisation (dissolution of minerals) and base exchange, as saturation indices are considered to capture mineral dissolution and precipitation contributions in the evolution of the hydro-chemical composition of groundwater (Gao et al., 2019; Liu et al., 2017). Both saturations with respect to the evaporitic and carbonate minerals were considered. In the sedimentary context, minerals such as Dolomite [(Ca, Mg) (CO3)2], Aragonite (CaCO3) and Calcite (CaCO3) on the one hand, and Gypsum (CaSO4) and Anhydrite (CaSO4.2H2O) on the other hand, were selected to present the carbonates and evaporitic minerals, respectively. These indices were computed using the "Phreeq" in Diagrammes software (Equation 3.31) and displayed using the R software. Values equal to 0, inferior to 0, and superior to 0 imply equilibrium, under saturation (minerals tend to dissolve), and oversaturation (minerals tend to precipitate) states, respectively.

$$\mathrm{SI} = \lg\left(\frac{IAP}{K}\right) \qquad \text{(Eq.3.31)}$$

With IAP and K standing for the ionic activity product and solubility product, respectively.

Finally, some metrics, including Ascendant Hierarchic Clustering (AHC), chloride-related metrics (Revelle index, Cation Exchange Value, Sodium-Chloride Ratio), Stiff, and the Hydrochemical Facies Evolution diagrams, were used to assess the potential for seawater intrusion in the plateau. With regards to the geological characteristics of the considered aquifers (CT, Pa, Ma, and MaS), the Base Exchange Indices (BEX) and the calcium enrichment were not considered for this study because of the dolomite nature of the CT aquifer and the limestone and dolomite nature of the Pa aquifer, respectively, in order to avoid the interference resulting from the dissolution of these rocks. The metrics considered for the seawater intrusion potential are summarised in Table 3.11.

Table 3.11: Seawater Intrusion Potential Assessment Metrics

Metrics	Description and implications	Calculation/Tools	Sources/References
Piper Diagram	It pictures the relative concentrations of the major ions on ternary diagrams and thus depicts the groundwater facies present and the mineralisation pathways, thus helping in capturing the common pathway for salinization in an area.	Diagrammes software	Custodio and Bruggeman (1987)
Principal Components Analysis (PCA) and Ascendant Hierarchic Clustering (AHC)	Entirely based on the eigenvalue analysis of a correlation or covariance matrix. It aims at reducing the information stocked in many variables into a set of weighted linear combinations of those variables without differentiating between common and unique variance. Water samples clustered with the water samples from the ocean are considered to be severely impacted by marine intrusion (1), while the rest of the samples are clustered into slightly impacted samples (2) and unaffected samples (3).	R software version 4.1.1 (along with Car, Scales, Cluster, FactoMineR and Factoextra packages)	-
Revelle Index (RI)	Part of the chloride-related metrics, RI gives the degree of contamination of freshwater by saltwater and is based on the contrast of chloride (Cl) and bicarbonate content in seawater and freshwater. 0.1–5 = Inland water 20–50 = Seawater < 0.5 = Unaffected samples 0.5–6.6 = Slightly affected samples > 6.6 = Strongly affected samples		Revelle (1941)
Cation Exchange Value (CEV)	As a chloride-related metric, CEV gives an idea related to seawater intrusion. (+)1.2 – (+)1.3 = Seawater ≥ 0.2 = Seawater intrusion ~ 0 = Inland water		Custodio and Bruggeman (1987)
Sodium - Chloride Ratio (Na/Cl)	Water in aquifers intruded by seawater shows a Na-Cl ratio lower compared to that of the ocean. 0.86 = Seawater		Sherif et al. (2011)

	< 0.86 = Seawater intrusion > 1 = Anthropogenic pollution		
Stiff Diagram	Water in aquifers intruded by seawater shows a Na/Cl ratio lower compared to that of the ocean. The diagram is a polygon whose geometry depends on the samples' chemical element contents, with the axes being Na^{+}, Cl^{-}, Ca^{2+}, $HCO3^{-}$, Mg^{2+}, and $SO4^{2-}$, and which gives an idea of the dominant species of a sample and the chemical relationships between species. Unaffected samples (3) = freshwater geometry Slight intrusion (2) = Altered freshwater geometry (high Na-Cl content, high HCO3) Strong/severe intrusion (1) = Seawater geometry	Diagramme software	Sherif et al. (2011)
Hydrochemical Facies Evolution Diagram (HFE-D)	It provides a way to identify the state of an aquifer (determine the dynamics of saline/saltwater intrusion) with respect to intrusion/freshening phases, based on the distribution of major cations (Ca^{2+} and Na^{+}) and anions ($HCO3^{-}$, $SO4^{2-}$ and Cl^{-}) percentages. The diagram accounts for facies evolution sequence during recharge and intrusion events. The HFE-D outputs (water facies) were translated to the Piper Diagram and organized in tree classes: Unaffected samples (3) = Ca-HCO3 facies, MixCa-MixHCO3 facies, MixNa-MixHCO3 facies, MixCa-HCO3 facies and MixNa-HCO3 Slight intrusion (2) = MixNa-MixCl, MixNa- Cl, Na-MixCl, MixCa-MixCl, MixCa-Cl Strong/Severe intrusion (1) = Na-Cl	HFE-D Excel Macro	Giménez-Forcada (2010) (Accessible at https://hidrologia.usal.es/HFE-D.htm, for more information see Giménez-Forcada and Sánchez San Román, 2014)

3.2.3.2 Isotopic Signature Characterisation

Additional classic methods such as the environmental tracers, especially the couple $^{18}O/^{2}H$ (correlation between the two isotopes and the excess of ^{2}H and their spatial distribution), were considered to confirm the processes contributing to the mineralisation of groundwater in the study area. The two stable isotopes were analysed using the laser spectrometer PICARRO 2140-i (accuracy of ±0.2‰ and ±1‰ for the ^{18}O and ^{2}H, respectively).

As part of the water molecules, ^{18}O and ^{2}H are reported to be useful in capturing the origins of water, the recharge zones, and the processes defining their mineralisation (including their salinization). The isotopic signature is a function of the prevailing processes in the water phase, with the most important being evaporation and condensation. Waters that have been subjected to condensation are characterised by a depleted composition of heavy isotopes and an enriched composition of light isotopes. The isotopic composition of precipitation is a function of factors such as the temperature, topography (altitude and latitude), distance from the evaporation source (ocean or sea), etc. For this process, an increase in the heavy isotopes (^{18}O and ^{2}H) of water is associated with a high temperature, low altitude, or latitude, and closeness to the evaporation source. These waters are captured by the Global Meteoric Water Line (GMWL) or Craig's line, characterised by a slope of 8 and an excess in ^{2}H of 10 (Craig, 1961a). On the other hand, waters that have undergone an evaporation process tend to be enriched with heavy stable isotopes (^{18}O and ^{2}H) and low light isotopes (^{16}O and ^{1}H) (Etcheverry, 2002), explaining the enrichment of these waters. The slope of these waters is quite low compared to those that have not undergone the process and is reported to be between 3 and 5 (Fontes, 1976), and it still depends on the kinetics of the basin (speed of evaporation, temperature, and atmospheric water content). Above all, the paleoclimate also plays a key role in the groundwater isotopic signature, as an aquifer can contain fossilised (very old) water that was recharged in the distant past, with a highly depleted composition of heavy isotopes (^{18}O and ^{2}H). Besides all this, ^{18}O is considered important for its capacity to inform the origin and movement of water masses and thus the physical processes (evaporation and mixing) that can affect these masses. The basic principle of the isotopic approach is that mineralisation (chloride content) resulting from the dissolution of minerals or rocks is associated with no or insignificant change in the isotopic composition of the considered water samples (IAEA, 1981), while mineralisation resulting from other processes such as mixture with seawater or brackish water and evaporation is associated with a significant change in isotopic composition (Payne and Halevy, 1983).

The concentration of the isotopes was measured using a laser spectrometer in terms of the difference from a standard in parts per thousand, both at the LHAE (University of Lomé, Togo) and at the Laboratory of Radio-Analysis and Environment (National Engineering School of Sfax, Tunisia). Isotope composition is reported in terms of a normalised difference from global standards and is normally reported in parts per thousand (symbolised as 0‰). The reference commonly used is the Standard Mean Ocean Water (SMOW), representing the mean isotopic composition of the oceans (Craig, 1961a), or the Vienna Standard Mean Ocean Water (V-SMOW), standing for a value of 0‰ as expressed in Equation 3.32.

$$\delta\ (‰) = \left(\frac{\text{R sample} - \text{R standard}}{\text{R standard}}\right) \text{x } 1000 \qquad \text{(Eq.3.32)}$$

The $\delta\ ^{18}O$ versus $\delta\ ^{2}H$ plot was plotted considering the GMWL (Craig, 1961a), characterised by the equation: $\delta\ ^{2}H = 8\ \delta^{18}O + 10$, the Local Meteoric Water Line of the plateau region (Akpataku et al., 2019), having the same climate as the study area and characterised by the equation: $\delta^{2}H = 7.67\ \delta^{18}O + 11$, and the Mixing Sea Water Line (MSWL), characterised by a slope lower than 0 and heavy isotope content around 0‰ (Craig, 1961a, 1961b; Fontes, 1976). Finally, the Evaporation Line (EL), characterised by the equation $\delta^{2}H = 3.94\ \delta^{18}O\text{-}3.68$, is considered. In addition, the evolution of Cl^- concentrations against $\delta^{18}O$ and the EC against $\delta^{18}O$ were considered to discuss the process of groundwater salinisation in the AP.

3.2.3.3 Hydraulic Head Characterisation

The collected water table levels of the various aquifers considered were first readjusted to a reference level, which is the ground at the location of the water point (elevation in reference to the mean sea level defined based on the Digital Elevation Model). From there, hydraulic heads for each water point considered were calculated using Equation 3.33.

$$H = z - Hp \qquad \text{(Eq.3.33)}$$

With H, z and Hp standing for hydraulic head, altitude or Elevation of the water point and water table level, respectively.

3.2.3.4 Characterisation of Seawater-Freshwater Interface

The obtained datum points obtained from the ERT were inverted (iteration number = 3) using the RES2DINV software (Loke, 2006) and, by default, the smoothness-constrained Gauss-Newton least-squares algorithm (Loke and Barker, 1996) along with finite difference modelling. The algorithm divides the subsurface into rectangular blocks, and then there is an

adjustment of the block resistivity to minimise iteratively the difference between the computed and measured apparent resistivity values. Additional inversion parameters that were considered include the convergence limit (with a percentage RMS error of 5), the contour interval option (user-defined linear contour intervals), robust inversion (standard constraint for the data and model inversion), and changing display settings (contour lines displayed). Furthermore, a range of resistivity values (0–700 Ωm) was adopted based on the values displayed for each profile to allow easy comparison between profiles. As an outcome, the measured and calculated apparent resistivities are converted into true resistivities. The quality of the outcome is assessed using the root mean square (RMS) error, which measures the difference between the computed and measured apparent resistivity values. The obtained ERT profiles are interpreted by correlating and cross-validating the true resistivity distribution with the occurrence of the geological formations with depth (lithological data), the Total Dissolved Solids (TDS), and the chloride concentration (physicochemical data) of boreholes close to the profiles, previously presented.

3.2.4 Dynamics of Seawater Intrusion

3.2.4.1 Recharge Estimation over the Agoènyivé Plateau

Aquifer or groundwater lens recharge was considered as the amount of rainfall reaching the water table, taking into consideration rainfall as water intake while evaporation (from land surface, plant leaves, and soil), vegetation transpiration (essentially by shallow-rooted plants occurring at soil and unsaturated zone levels), and runoff were considered as water uptake or removal. Current and future recharge over the study area was estimated considering the water balance method. In the context of the AP, knowing the depth of the CT aquifer (reaching up to 80 m in Lomé), the groundwater uptake (below the water table by deep-rooted plants taking water within the saturated zone) was neglected; thus, the input parameters considered for this model include precipitation, actual evapotranspiration, and runoff (Equation 3.34).

$$P = AET + Q + I + \Delta S \quad \text{(Eq. 3.34)}$$

With AET, Q, I, and ΔS standing for actual evapotranspiration (mm), surface runoff (mm), recharge or infiltration (mm), and change in soil water storage (mm), respectively.

Daily Mean Areal Precipitation Estimation

The daily mean areal precipitation has been estimated using the Thiessen polygon method (Equation 3.35). This method is reported to be good for flat areas like the AP, where the topography only varies between -7 and 104 m (based on the Digital Elevation Model) with a linear rainfall distribution. In addition, the uniformity and density of the climatic station

network have been highlighted as keys to successful results. In the case of the AP, a total of 19 stations (both in situ and grid) were considered for this purpose.

$$P_{\text{Average}} = \frac{\sum_{n}^{i=1}(P_i A_i)}{\sum_{n}^{i=1}(A_i)} \quad \text{Eq.3.35}$$

With P_i and A_i standing for the precipitation at a station and the area of land representing the station (Voronoi polygon), respectively.

Actual Evapotranspiration (AET)

Known as one of the key factors in land-atmosphere interactions, actual evapotranspiration represents the actual total amount of water evaporated over a surface. It can be measured or estimated (Rose and Sharma, 1984) using analytical and micrometeorological approaches. Measurement methods include eddy covariance and lysimeters, among others, while estimation methods include the water balance method, the energy balance method, calibrated evapotranspiration equations, and models. For micrometeorological approaches, this parameter accounts for climatic factors (including parameters such as precipitation, temperature, insolation, wind speed, etc.), land use and land cover characteristics, as well as soil types and the useful soil reserve (Pidwirny, 2006). In the context of the AP, the Coutagne method (Coutagne, 1954) and the Turc method (Turc, 1961) were considered among the panoply of existing empirical methods across the world to estimate the AET. Salazar and Poveda (2006) explored the use of the Coutagne and Turc methods, among others, in computing the actual evapotranspiration over the Amazon River basin. They reported that these two methods show opposite estimates, where one underestimates while the other one overestimates the actual evapotranspiration. In addition, Gassama-Jallow (2021) considered several methods (Penman, Turc, and Thornthwaite) in application to the Greater Banjul area and concluded that the Turc method provided the best approximation of the AET. Finally, based on part of the objectives of the current study (the estimation of actual ET), the Turc and Coutagne methods were considered viable based on their low data requirements, limited primary to annual precipitation, and the average annual temperature. At the end, to reinforce the quality of the results and reduce the amount of uncertainty, the average value of the calculated actual evapotranspiration for the two methods was considered for the recharge calculation.

The Coutagne method (Coutagne, 1954) is expressed in the Equation 3.36.

$$\text{AET} = P_{annual} \text{ for } P_{annual} < l/8 \quad \text{Eq.3.36}$$

$$\text{AET} = P_{annual} * \frac{1 - P_{annual}}{l} \quad \text{for } l/8 \leq P_{annual} \leq l/2$$

AET= 200 + 35T_{mean} for $P_{annual} > l/2$

Where: $l = 140 * T_{mean} + 800$ and AET (mm) represents the actual evapotranspiration and P_{annual} the total annual precipitation (mm) and T_{mean} (°C) the annual average temperature. In the context of AP, $l/8 \leq P_{annual} \leq l/2$, thus, the formula derived for the AET calculation is expressed in the equation below:

$$AET = P_{annual} * \frac{1 - P_{annual}}{l}$$

Turc method (Turc, 1954) has also been considered with the formula in the Equation 3.37.

$$AET = \text{P for } \frac{\text{P}}{l_T} \leq 0.316$$

$$AET = \frac{\text{P}_{annual}}{\sqrt{0.9 + \frac{\text{P}_{annual}{}^2}{l_T{}^2}}} \quad \text{for } \frac{\text{P}}{l_T} > 0.316 \qquad \text{Eq.3.37}$$

Where: $l_T = 300 + 25T + 0.05T^2$ while AET, P, and T represent the actual evapotranspiration, the total annual precipitation, and the average annual temperature, respectively.

In the context of the AP $\frac{\text{P}}{l_T} > 0.316$, thus the derived formula for the estimation of the actual evapotranspiration is expressed in the equation below:

$$AET = \frac{\text{P}_{annual}}{\sqrt{0.9 + \frac{\text{P}_{annual}{}^2}{l_T{}^2}}}$$

Surface Runoff Depth Estimation

LULC maps over the AP for the years 2001, 2011, 2020, 2030, and 2050 (see chapter four), along with daily rainfall data over the period of 1991–2020 and 2021–2050 (see chapter five), the slope (defined based on the DEM), and soil characteristics (sandy, sandy clayey, and clayey standing for ferralitic soils, poorly evolved contribution soils, and hydromorphic soils, respectively) were considered for the surface runoff depth estimate. The Soil Conservation Service Curve Number (SCS-CN) method, a product of the USDA SCS (Rallison, 1980), was considered for potential runoff depth estimation (Muthu and Santhi, 2015). For this purpose, the Antecedent Moisture Condition (AMC) classes (Table 3.12) were defined considering a computed five-day rainfall (these days being successive and preceding a storm) while the hydrological soil groups were defined based on the infiltration capacity of the existing soil types (Table 3.13). Finally, these two datasets were superimposed with LULC maps to define the curve number using the standard SCS-CN table.

Table 3.12: Antecedent Moisture Condition Classes

AMC-Class	5-day antecedent rainfall (mm)		Conditions
	Dormant season	Growing season	
I	< 13	< 36	Dry soil but not the wilting point
II	13–28	36–53	Average condition
III	> 28	> 53	Saturated soils, heavy or light rainfall

Source: Soil Conservation Service (1972)

Table 3.13: Hydrological Soil Group and their Characteristics

Group	Infiltration rate (mm/hour)	Soil texture
A	High > 25	Sand, loamy sand or sandy loam
B	Moderate 12.5–25	Silt loam or loam
C	Low 2.5–12.5	Sandy clay loam
D	Very low < 2.5	Clay loam, silty clay loam, sandy clay, silty clay or clay

Source: Chow et al. (1988)

From the above, the monthly potential maximum retention (S), the initial abstraction (I_a) and the monthly surface runoff (Q_i) was computed using Equation 3.38 - 3.40 (P standing as the total precipitation). Finally, the recharge was estimated considering scenarios (Table 3.14).

$$S = \frac{1000}{CN} - 10 \qquad \text{Eq.3.38}$$

$$I_a = 0.2 * S \qquad \text{Eq.3.39}$$

$$Q_i = \frac{(P - I_a)^2}{(P - I_a + S)}, \quad If \ P > I_a \qquad \text{Eq.3.40}$$

$$Q_i = 0, \quad If \ P > I_a$$

Table 3.14: Recharge Estimation Scenarios

Scenario type	Temperature (T)	Rainfall (P)	LULC
LULCC_CC_Recharge 2001	T_2001	P_2001	LULC 2001
LULCC_CC_Recharge 2011	T_2011	P_2011	LULC 2011
LULCC_CC_Recharge 2020	T_2020	P_2020	LULC 2020
LULCC_CC (RCP 4.5) _Recharge 2030	T_2030 (RCP 4.5)	P_2030 (RCP 4.5)	LULC 2030
LULCC_CC (RCP 8.5) _Recharge 2030	T_2030 (RCP 8.5)	P_2030 (RCP 8.5)	LULC 2030
LULCC_CC (RCP 4.5) _Recharge 2050	T_2050 (RCP 4.5)	P_2050 (RCP 4.5)	LULC 2050
LULCC_CC (RCP 8.5) _Recharge 2050	T_2050 (RCP 8.5)	P_2050 (RCP 8.5)	LULC 2050
CC (RCP 4.5) _Recharge 2030	T_2030 (RCP 4.5)	P_2030 (RCP 4.5)	LULC 2020
CC (RCP 8.5) _Recharge 2030	T_2030 (RCP 8.5)	P_2030 (RCP 8.5)	LULC 2020
CC (RCP 4.5) _Recharge 2050	T_2050 (RCP 4.5)	P_2050 (RCP 4.5)	LULC 2020
CC (RCP 8.5) _Recharge 2050	T_2050 (RCP 8.5)	P_2050 (RCP 8.5)	LULC 2020
LULCC_Recharge 2030	T_2020	P_2020	LULC 2030
LULCC_Recharge 2050	T_2020	P_2020	LULC 2050

* T: Temperature, P: Rainfall, CC: Climate change, and LULC: land use and land cover.

The overall methodology for estimating recharge is summarized in the Figure 3.7.

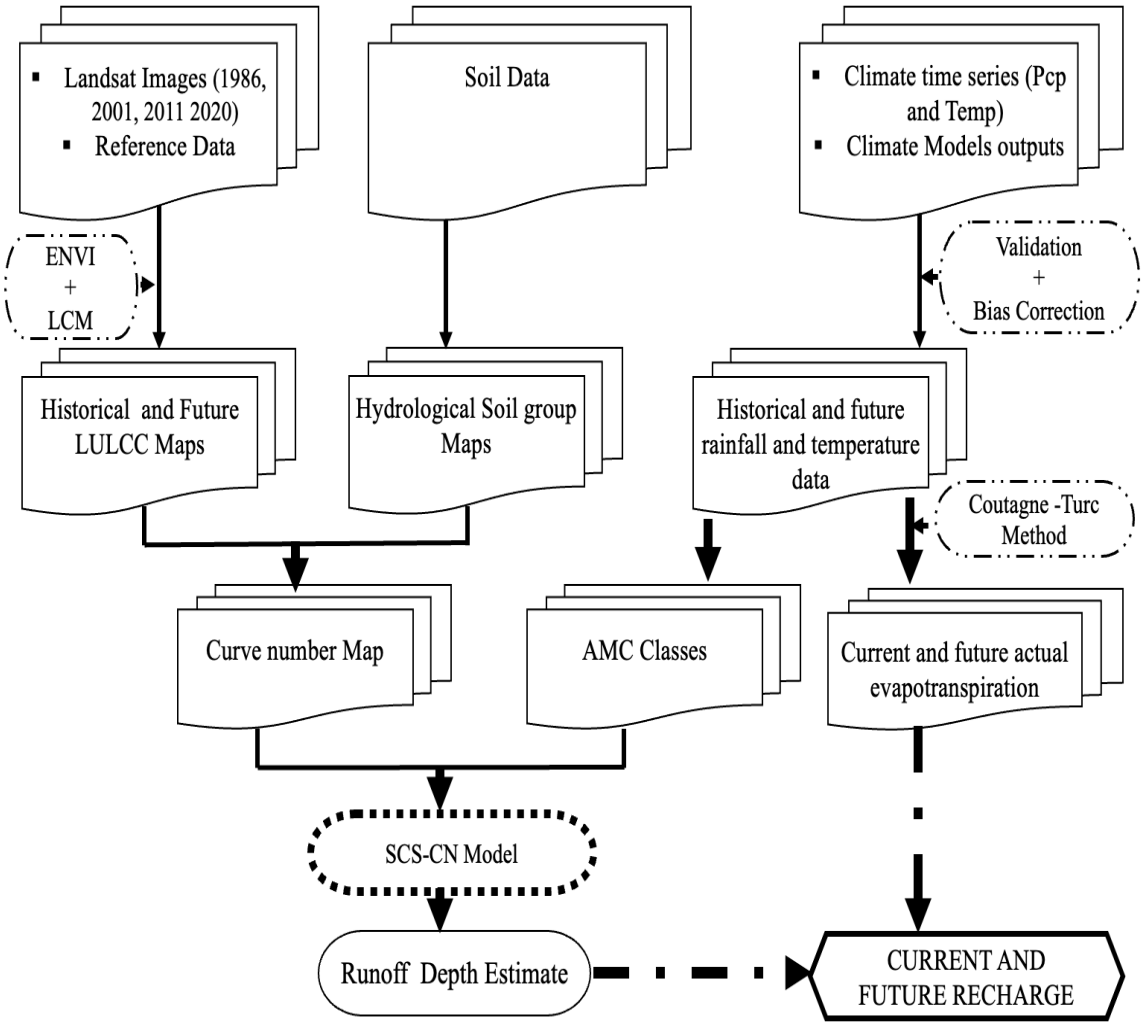

Figure 3.7: Recharge Estimation Methodology Flow Chart: USDA (1972, Modified)

3.2.4.2 Seawater Intrusion Dynamics Modelling

SWI dynamics modelling included the development of the conceptual model (based on AP realities), the conversion of conceptual to the numerical model, and scenario development.

3.2.4.2.1 Conceptual Model

Representing a key step in the modelling process for giving an idealized, simplified, but accurate representation of the system to be modelled (Mutasa, 2011), the conceptual model includes the spatial distribution of the geologic and hydrogeologic conditions, the physical location of system boundaries (rivers, drains, aquifers, and boundary types), values on aquifer parameters, and hydrogeological stresses (Van Der Heiden and Lithén, 2011). In the context of the AP, the conceptual model was built to predict the response of the upper aquifers (in terms

of the hydraulic head, salinity concentration, and the intrusion extent) to future changes. It follows the following steps:

Defining Modelling Objectives

The modelling objectives include the starting date (defined based on the data such as observed field head and concentration, pumping data, etc.), the units of the parameters, and the geographical coordinates. In the context of the AP, 01 March 2015 (available data for the initial heads and concentration from PRESAF) and the UTM 31 N as geographic coordinates were considered.

Definition of the Model Area and Conceptual Model Development

The total area considered for the modelling includes the entire Agoè plateau, located between Togo and Ghana. It stops at the first stream encountered to the west of this plateau and covers a total area of 867 km^2. The model considers the shallow/upper aquifers of the SCBT in the AP, including the Continental Terminal and the Coastal Marine Sand (considered as the continuity of the CT aquifer). Collected data was essentially imported as points, polylines, polygons, surfaces (created in the Modflow flex using the Kriging technique and the inverse distance), time schedules, and wells. From there, the model surface area, the layers and structure of the model (with two layers including the ground level and the lower confining bed of the Continental Terminal defined as erosional and base, respectively), as well as the initial and boundary conditions were defined.

Layer development is done through a vertical discretisation of the model area. Because of the lack of a topographical map, a 30 m-resolution digital elevation model (obtained from the USGS) has been considered to represent the ground level. In addition, the lower confining bed of the CT aquifer, based on the work of the BRGM geological synthesis (Monciardini et al., 1986), was adopted. The upper layer (ground level) represented by the SRTM/DEM data depicts values ranging between -0.13 and 82.89 m, while the lower layer (lower confining bed of the CT aquifer) depicts values ranging between -105.01 and 22.10 m. Then, the defined layers were converted into horizons and positioned based on their vertical occurrence. For the structure building, the upper layer and the lower layer were assigned as the erosional and base layers, respectively.

The groundwater flow pattern follows the topography in the direction of the Zio River and the Atlantic Ocean, representing the natural discharge areas. The aquifer is recharged in the northern part of the study area, with an average annual recharge estimated to be 62.21 $mm.year^{-1}$ (as of 2020) and water samples are characterised by low EC. The details of the conceptual model for the AP are depicted in Figures 3.8a-b.

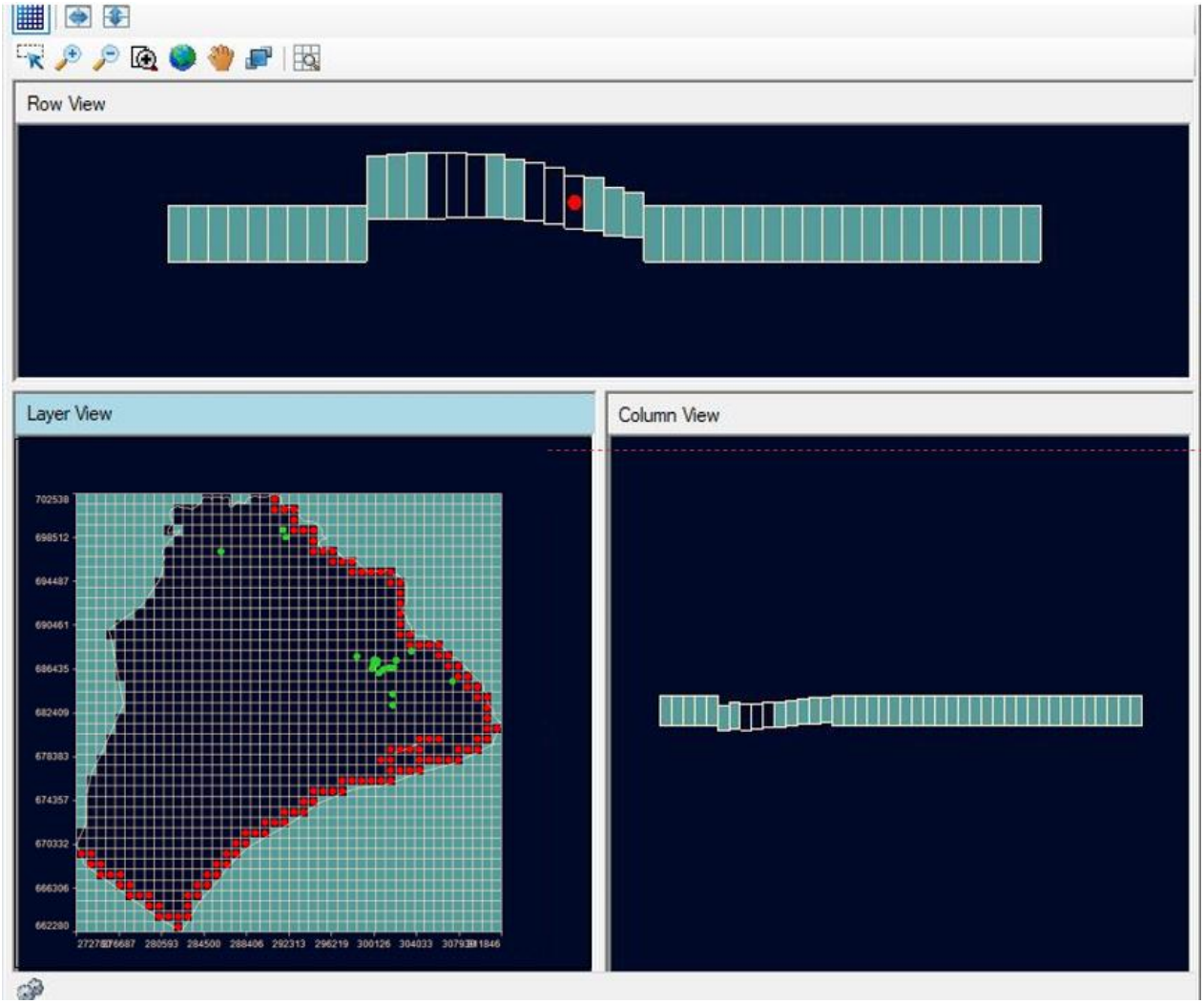

Figure 3.8a: Conceptual Model Showing the Discretized Domain (Layer, Row and Column views) with Boundary Conditions (Red Dots) and Observation Data (Green dots), Extended AP

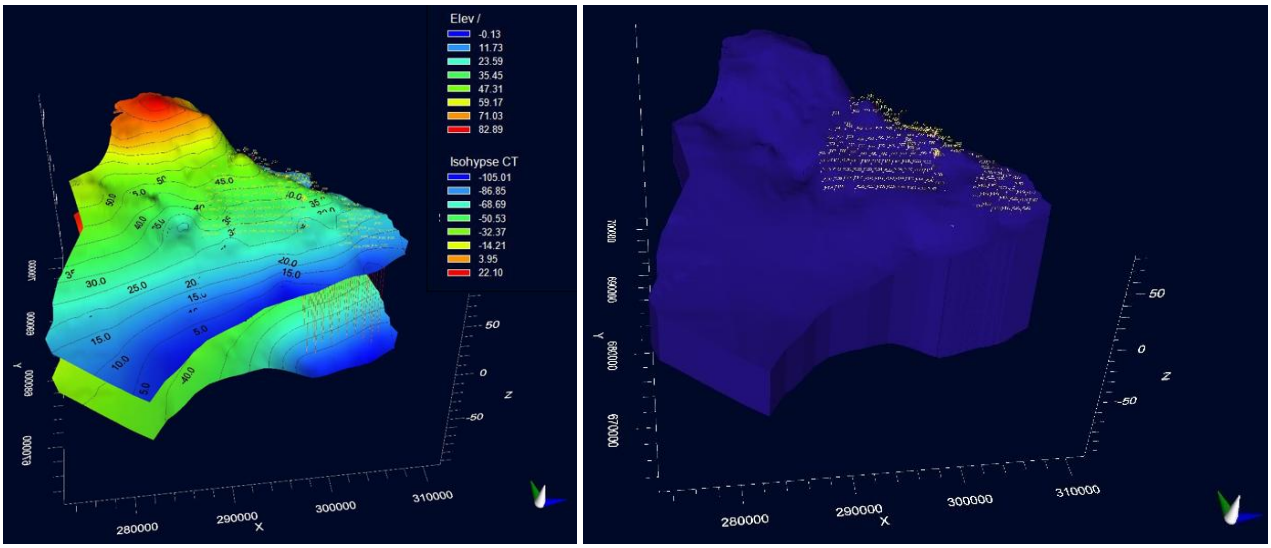

Figure 3.8b: Conceptual Model Showing the Composite Elements (Top layer: Ground Surface and Bottom Layer: Lower Confining Bed of the CT) and the zone view, extended AP

Properties Zones Definition

It concerns hydraulic parameters such as hydraulic conductivity, storage, and dispersivity, as summarised in Table 3.15. It also includes the initial conditions (head and concentration).

Table 3.15: Groundwater Model Hydraulic Parameters for the CT Aquifer

PARAMETERS	UNITS	CT AQUIFER	SOURCE
K	$m.s^{-1}$	15.10^{-5}-2.10^{-2}	Calibrated considering values in BNRM (1986); DHE (1982, 1983).
n_e	-	0.25	Calibrated considering values between the sandy clayey and sandy formations in Johnson (1967)
n_T	-	0.3	Calibrated
Sy		0.21	Calibrated considering values for sandy clayey and sandy formations in Johnson (1967).
α_L	m	10–200	Calibrated
α_L/α_v	-	0.1	Default value
α_L/α_h		0.01	Default value
K_d	$m^2.day^{-1}$	10^{-2}–10^{-7}	Calibrated

K: hydraulic conductivity; S_y: storage coefficient or specific yield; n_e: effective porosity, n_T: total porosity α_L: longitudinal dispersivity; α_v: vertical dispersivity; α_h: horizontal dispersivity; K_d: hydraulic conductance at the seafloor

3.2.4.2.2 Numerical Model

The SEAWAT model was chosen as the mathematical model to better understand the seawater intrusion process in the AP but also predict the aquifer response both in terms of hydraulic head and salinity concentration. The Visual MODFLOW Flex (VMOD flex) version 8.0 (Waterloo hydrogeologic product) was used as the graphical user interface, incorporating the SEAWAT (Version 4.00.05), which combines the MODFLOW-2005 (Version 1.18.01) and the MT3DMS (Version 5.20) as model codes. The MT3DMS is a modular 3-D multi-species transport model developed at the University of Alabama for the U.S. Department of Defense, while the MODFLOW-2005 is a U.S. Geological Survey modular finite-difference groundwater flow model. The SEAWAT model has been chosen for this project because, beyond its reasonable computational resource request, it gives room for : (i) the prediction of the future (Gopinath et al., 2016) and quantifying uncertainty through the inversion code/modelling linked to it; (ii) the use of the method of characteristics (known to be ideal in reducing numerical dispersion) by the MT3DMS model in solving the transport equation; (iii) the characterisation of various types of time-dependent boundary conditions; and (iv) the

simulation of steady-state and long-term transient flow and solute transport with the least numerical instability.

The governing equation (Equation 3.41) for density-dependent groundwater flow in terms of freshwater head is solved by MODFLOW routines in SEAWAT code (Guo and Langevin, 2002).

$$\frac{\partial}{\partial\alpha}\left\{\rho K_{\mathrm{f}\alpha}\left[\frac{\partial h_{\mathrm{f}}}{\partial\alpha}+\frac{\rho-\rho_{\mathrm{f}}}{\rho_{\mathrm{f}}}\frac{\partial Z}{\partial\alpha}\right]\right\}+\frac{\partial}{\partial\beta}\left\{\rho K_{\mathrm{f}\beta}\left[\frac{\partial h_{\mathrm{f}}}{\partial\beta}+\frac{\rho-\rho_{\mathrm{f}}}{\rho_{\mathrm{f}}}\frac{\partial Z}{\partial\beta}\right]\right\} \quad \text{Eq.3.41}$$
$$+\frac{\partial}{\partial\gamma}\left\{\rho K_{\mathrm{f}\gamma}\left[\frac{\partial h_{\mathrm{f}}}{\partial\gamma}+\frac{\rho-\rho_{\mathrm{f}}}{\rho_{\mathrm{f}}}\frac{\partial Z}{\partial\gamma}\right]\right\}=\rho S_{\mathrm{f}}\frac{\partial h_{\mathrm{f}}}{\partial t}+\theta\frac{\partial\rho}{\partial C}\frac{\partial C}{\partial t}-q_{\mathrm{s}}\rho$$

Where α, β, and γ are orthogonal coordinate axes aligned with the principal directions of permeability; Kf_{α}, Kf_{β}, and Kf_{γ}, are equivalent freshwater hydraulic conductivities in the three coordinate directions, respectively [LT^{-1}]; ρ and ρ_f represent the density of the fluid [ML^{-3}] and the density of fresh water [ML^{-3}], respectively. h_f and Z stand for the equivalent freshwater head [L] and the elevation above datum of the center of a model cell [L], respectively. S_f is the equivalent freshwater specific storage [L^1]; θ is the effective porosity (dimensionless); C is the solute concentration [ML^{-3}]; ρ is the density of water entering from a source or leaving through a sink [ML^{-3}]; q_s is the volumetric flow rate of sources or sinks per unit volume of aquifer [T^{-1}]; and t is time [T].

The solute-transport governing equation of the SEAWAT code uses MT3DMS routines (Zheng and Wang, 1999), as expressed in Equation 3.42.

$$\frac{\partial C}{\partial t}=\nabla.(D.\nabla C)-\nabla.(\tilde{\upsilon}C)-\frac{q_s}{\theta}\mathrm{C}_s+\sum_{k=1}^{N}(R_k) \quad \text{Eq.3.42}$$

Where D is the hydrodynamic dispersion coefficient [$L2T^{-1}$]; ῡ is the fluid velocity [LT^{-1}]; C_s is the solute concentration of water entering from sources or leaving through sinks [ML^{-3}]; and R_k (k = 1,..., N) is the rate of solute production or decay in reaction k of N different reactions [$ML^{-3}T^{-1}$].

For a coupled variable-density flow and solute-transport simulation, fluid density is assumed to be a function only of solute concentration, with the effects of pressure and temperature on fluid density ignored (Guo and Langevin, 2002). A linear equation of state is used by the SEAWAT code to convert solute concentration to fluid density (Langevin et al., 2007; Guo and Langevin, 2002) (Equation 3.43).

$$\rho=\rho_f+\frac{\partial\rho}{\partial C}\mathrm{C} \quad \text{Eq.3.43}$$

Where ∂ρ/∂C is the slope of the equation. The value for ∂ρ/∂C is a dimensionless constant having an approximate value of 0.7143 for salinity concentrations ranging from zero to 35 kg/m^3 of seawater.

3.2.4.2.3 Discretization

A finite difference of 888 m x 959 m, well adapted to the density of available data, was adopted, resulting in 44 columns and 42 rows, making a model domain of 1848 total cells. Finally, the deformed grid option was considered for depicting a model with layers following the elevation.

3.2.4.2.4 Pumping Wells

Pumping wells considered in the frame of this study include those from the water supply society (the withdrawal by the Togolaise Des Eaux based on the available daily withdrawn volumes is estimated at 540–2660 m^3), from industries (Lomé Brewery considering continuous nominal rates on a daily basis is estimated at 367.92 m^3), and from privates (household use, pure water producers, and tap level sellers with an estimation of a daily withdrawal of 0.3 m^3, 0.3 m^3, and 1 m^3, respectively).

The projection for the years 2030 and 2050 was estimated by considering the increase in withdrawal from individuals with a ratio of 1.43 and 1.86 by 2030 and 2050, considering the DGSCN (2011) projection of a population growth rate of 1.26% over the period. Due to the limited data on the technical characteristics of the boreholes, boreholes have been moved to the centre of the grid and considered to cover the entire thickness of the aquifer, thus reaching the wall of the aquifer.

3.2.4.2.5 Initial and Boundary Conditions

The model area is assumed to be an open system, with the inflow water being mainly recharged from rainfall and the outflow through natural discharge areas such as the Zio River (the eastern part) and the ocean (the southern part). In addition, artificial discharge has also been considered and represented by pumping wells. The model area is limited in its northern part by an impermeable crystalline basement and in its western part by the first river encountered in Ghana. The bottom of the aquifer is assumed to be permeable, with plausible exchange with lower aquifers such as the Palaeocene and the Maastrichtian.

For the groundwater flow model and solute transport model boundary conditions, a constant head boundary condition, also termed "Dirichlet" (which represents a specified head or concentration boundary condition, used to fix the head or concentration value in selected grid cells regardless of the system conditions in the surrounding grid cells, thus acting as a potentially infinite source of water or solute entering the system or as an infinite sink for water or solute leaving the system), was considered for the western (first river encountered in Ghana representing the western limit of the basin), eastern (Zio River), and southern (Ocean) limits. A value of 0 m as a constant head has been assigned for the ocean because of the water head

observed in one of the boreholes close to the ocean and a concentration of 35 kg.m^3. Finally, a no-flow boundary, also termed "Neumann," was attributed to the northern limit where the CT aquifer is in contact with the impermeable crystalline basement.

On the other hand, the hydraulic head and salt concentrations (TDS) obtained from PRESAF (2015) were considered the initial conditions in setting the model.

The discretisation, the pumping wells, and the observation wells considered, as well as the initial and boundary conditions, are depicted in Figure 3.9.

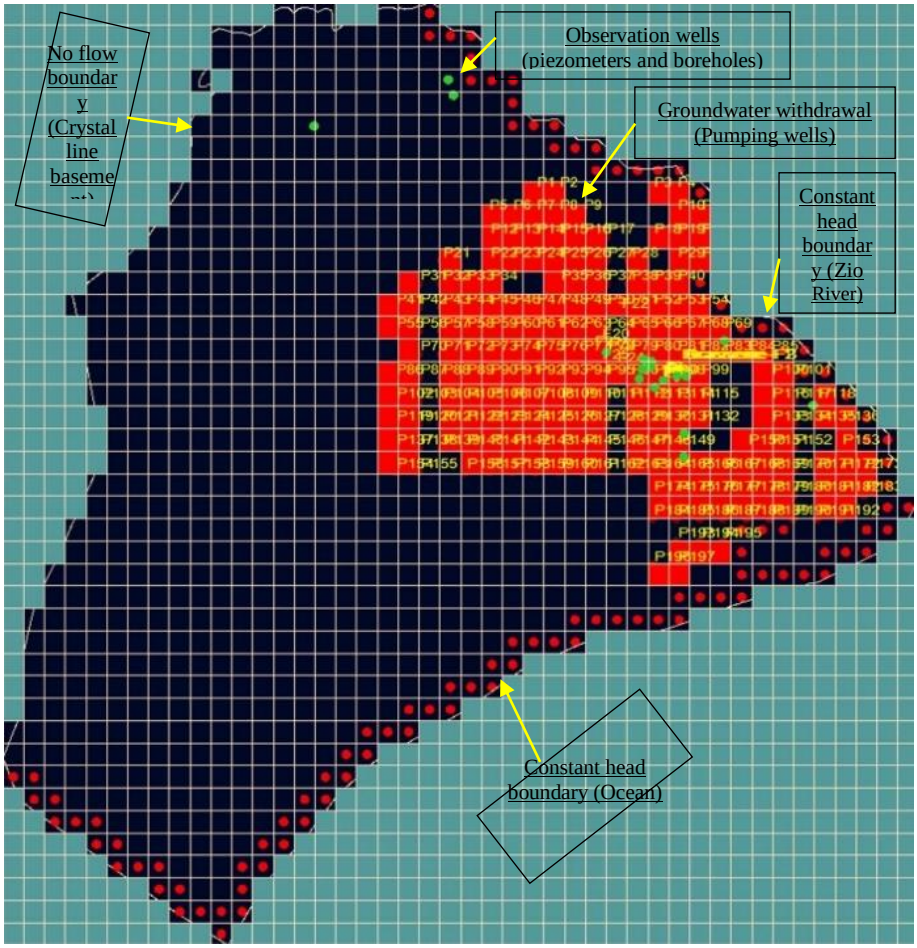

Figure 3.9: Model Boundary Conditions with Locations of Boreholes/wells (Pumping and Observation), extended AP

3.2.4.2.6 Calibration and Validation of the Model

Model calibration consists of adjusting selected model input parameters within reasonable limits to produce simulation results that best match the measured values, while model validation is the next step to check the robustness using another set of data. Though subjective, these steps are key to setting up a reliable model and leaning on its outputs for conclusions and recommendations for sustainability. In the context of the AP, the focus has been on parameters such as the hydraulic conductivity and the specific yield for the

groundwater flow model, the longitudinal dispersion, and the hydraulic conductance at the seafloor. Trial-and-error calibration was considered in this context to build the system based on the user's expertise and knowledge to better understand the behaviour of the system being modelled (Deslauriers and Mahdi, 2018) but also leverage the limitation of data availability in the study area, which was successful in several cases (Abd-Elaty and Zelenakova, 2022; Nasiri et al., 2021). The calibration process was carried out for both the steady and transient states, where the parameters are considered steady (same starting and ending values) with observations or field data from the RS 2021 (both hydraulic head and TDS), with stress periods defined based on the recharge parameter. Then the validation was carried out using observations or field data from the DS 2022.

Key settings considered for the run of SEAWAT code in the AP are summarised in Table 3.16.

Table 3.16: SEAWAT Model Run Settings

RUN ENGINES	SECTION	SETTINGS
SEAWAT-FLOW	SETTINGS	Property package = LPF (Time step = 10; Multiplier = 1.2)
	SOLVER	PCG (HCLOSE = 10^{-7}; RCLOSE = 10; IPRPCG = 5)
	LAYER	3: Confined/Unconfined, variable S, T
SEAWAT-TRANSPORT	GENERAL	Porosity option: Effective Courant number = 0.75 Min step = 0.01
	SOLVER SOLUTION	Advection method = CFD (Implicit GCG; Relative convergence = 10^{-8}; Concentration change printing interval = 5; Preconditioner = Modified Incomplete Cholesky; DTO = 3; Max step size = 3)
	OUTPUT CONTROL	Max number of transport steps = 2000 (for calibration and validation) and 5000 (for the projections)

The robustness of the model has been pinned out based on the Visual MODFLOW flex analysis tools (calculated vs. observed scatter graphs and calibration residuals histograms) but also using accuracy statistics performed in R software using the hydroGOF package, including the RMSE, R^2, PBIAS, NSE with the equations presented in section 3.3.2.

3.2.4.2.7 Scenarios Development

The response of the groundwater lens to future changes was captured considering changes in the recharge rate, changes in the groundwater withdrawal (with a focus on the individual or informal withdrawal), and sea level rise (SLR). The scenarios considered in the context of the AP are summarised in Table 3.17.

Table 3.17: Groundwater Lens Response Simulation Scenarios

Scenarios	Description
Scenario A: groundwater withdrawal	In this case, the recharge rate and sea level were kept unchanged (as of 2021), whereas the groundwater withdrawal has been increased (focus on the informal or individual boreholes) at an increase in water withdrawal rate of 1.43 and 1.86 by 2030 and 2050 in reference to the expected increase of the population by 2.16% over the considered period.
Scenario B: Change in groundwater recharge (LULCC, CC, and LULCC-CC)	In this case, three options are considered as recharge results based on the climate (rainfall and temperature), and land use and land cover. Meanwhile, the other parameters are kept unchanged (as of 2021). Three sub-scenarios are then considered: • B1: Recharge values considering land use and land cover change only. • B2-1 (B2-2) / B2-1' (B2-2'): Recharge values considering changes in rainfall and temperature for the RCP 4.5 (RCP 8.5) for the year 2030/2050 only. • B3-1 (B2-2) / B2-1' (B2-2'): Recharge values considering combined changes in land use and land cover, rainfall, and temperature for the RCP 4.5 (RCP 8.5) for the year 2030/2050.
Scenario C: SLR	While other parameters were kept unchanged, changes in sea level were considered for the year 2030 and 2050 (estimated to increase by 0.22 m, 0.24 m for RCP 4.5 and RCP 8.5, respectively by 2030 and 2050) *: • C1: 2030/2050 sea level rise under the RCP 4.5 • C2: 2030/2050 sea level rise under the RCP 8.5
Scenario D: Recharge + SLR + groundwater withdrawal (the most realistic scenario)	This scenario considers all the changes in parameters over the study area by 2050 Thus includes: • D1: Recharge (LULC-CC for the RCP 4.5, groundwater withdrawal ratio: 1.86, SLR: 0.22 m). • D2: Recharge (LULC-CC for the RCP 8.5, groundwater withdrawal ratio: 1.86, SLR: 0.24 m).

*Source: Trisos et al., 2022

3.3 Partial Conclusion

This chapter gives a description of the different types of data collected as well as tools and methods used in analyzing the data to achieve the objectives set in the framework of this study and thus includes:

- Data : This includes (a) primary data including land use and land cover reference data and local population perceptions on land cover dynamics; the physicochemical parameters (pH, EC, temperature, major anions, and cations) of groundwater and surface water sampled and hydraulic heads for two seasons (DS and RS); isotopic

results ($\delta\ ^{2}H$ and $\delta\ ^{18}O$) of the considered aquifers for the DS; and sub-surface electrical resistivity and (b) secondary data such as Landsat images, climate data (stations and grids), outputs from regional climate models (CORDEX-Africa), soil map, hydraulic heads time series, hydrodynamic properties of the CT aquifer, and borehole characteristics.

- Methods : different models and softwares were considered for the analysis of the data considered, including ENVI, Land Change Modeler (LCM), QGIS, ArcGIS, R-software, CMhyd, Khronostat software, DIAGRAMME, Hydrochemical Facies Evolution Diagram (HFE-D), SURFER, RES2DINV software, Turc-Coutagne-SCS-CN, and finally the SEAWAT model.

CHAPTER FOUR: LAND USE LAND COVER ASSESSMENT AND PROJECTIONS

This chapter includes LULC assessment outputs for the AP. A 34-year LULC (1986–2020) and future LULC (2030 and 2050) were assessed using a supervised classification along with the MLA and MLP-Markov chain approaches of the LCM, respectively. The future LULC projection considered four scenarios, including the BAU, afforestation, wetlands policy, and building policy. The simulated 2020 map was considered for model validation and accuracy assessment, while those of 2030 and 2050 account for the near and far futures, respectively. Past LULC change trends in the study area were captured through a cross-tabulation of four (04) sets of time periods: t_1 (1986–2001), t_2 (2001–2011), t_3 (2011–2020), and t_4 (1986–2020). The results are organised into (i) local perceptions of land use and cover dynamics, (ii) LULC mapping and change detection, (iii) model validation, and (iv) future LULC projection.

4.1 Local Perception on LULC: Dynamics, Drivers, and Causes

Results have shown that the local population (more than 80% of the respondents) is aware of the changes in land use and land cover in the study area but also has a perception of the causes and drivers of these changes as well as their dynamics.

The population-based perceptions of the main causes of the transition from one class to another are found to be direct and indirect. Direct causes include deforestation (19%, n = 98), agricultural expansion (7%, n = 98), and rainfall variability (9%, n = 98), while indirect causes include urbanization (34%, n = 98) and population growth (31%, n = 98). The dynamics of LULC in the study area were painted out, highlighting the past, present, and plausible future of LULC. In fact, respondents (n = 104) highlighted a predominance of agricultural land and plantations and forest/mixed vegetation, representing 38% and 33%, respectively, in the study area in the past, compared to a current state (n = 109), characterised by the predominance of housing, agricultural land, and forest/mixed vegetation representing 48%, 29%, and 23%, respectively. These observations depict an increase in built-up areas at the expense of agricultural lands and mixed vegetation, such as forests and plantations. Nevertheless, only 6% (n = 103) reported that the future LULC in the study area will follow a different pattern than the current status and will be characterised by more housing, less agricultural land, and less vegetation or forest. Some of the respondents predict the future LULC to be characterised by more housing, more agricultural land, and less vegetation or forest (44%, n = 103), while others

paint a very pessimistic picture characterised by agricultural land and housing (46%, n = 103) only or housing only (5%, n = 103).

Drivers of change in LULC in this context are considered factors that increase or decrease the value of land for certain purposes (building, farming, etc.), thus driving the change in classes. The highlighted drivers for past changes are reported to be the same for future changes. Found to be essentially based on the LULC class, these drivers' variables include mainly the distance from the road, the distance from the urban area, the slope, and topography (DEM), standing for 32%, 41%, 18%, and 9% (n = 56), respectively.

These insights drove the definition of the LULC scenarios and the choice of the explanatory or driver variables for the LULC modelling.

4.2 Land Use and Land Cover Mapping and Change Detection

4.2.1 Accuracy Assessment and Land Use and Land Cover Change Analysis

The error or confusion matrices of the classified images depicted overall classification accuracies of 87% (1986), 88% (2001), 90% (2011), and 92% (2020) and a kappa coefficient slightly above 0.8 (Table 4.1). Reproduction of the wetland class demonstrated significant prediction error (reproduction rates of 57%, 50%, 79%, and 67% for the four LULC maps, respectively). Assessment of these results indicates that this error can be attributed to erroneous pixels that were inaccurately classified as built-up, cropland, or bar surface pixels. These inaccuracies can be explained by the pattern of the occupation of wetlands for agricultural and pasturing purposes (including patches in Ahanoukopé, Adéwi, Hédzranawoé, and Nyékonakpoé/Kodomé along the lagoon) and housing purposes. In addition, some mixed vegetation areas are found to be built-up areas (based on the reference data), as in the case of reserve infirmerie (Agoè) and Méolite Next (Cacaveli), which were found to be sites currently under construction during the reference data collection. These results highlight the role played by ground reference data collection.

Table 4.1: LULC's Accuracy Statistics for the AP

(a) 1986 LULC MAP

Classified Data	**Reference Data**							**Users' Accuracy (%)**
	LULC Classes	Wetlands	Mixed vegetation/ Savannah	Croplands/ bare Surfaces	Built-up Areas	Water bodies	Reference Total	
	Wetlands	4	1	0	0	0	5	**80**
	Mixed vegetation/Savannah	0	14	4		0	18	**78**
	Croplands/bare Surfaces	0	1	24	1	0	26	**92**
	Built-up areas	3	0	3	42	0	48	**88**
	Water bodies	0	0	0	0	3	3	**100**
	Classified Total	7	16	31	43	3	100	
Producer Accuracy (%)		**57**	**88**	**77**	**98**	**100**		
Overall Accuracy (%)								**87**
Kappa Coefficient								**0.81**

(b) 2001 LULC MAP

Classified Data	**Reference Data**							**Users' Accuracy (%)**
	LULC Classes	Wetlands	Savannah/Mixed vegetation	Croplands/ bare Surfaces	Built-up Areas	Water bodies	Reference Total	
	Wetlands	3	0	0	1	0	4	**75**
	Mixed vegetation/Savannah	0	17	3	0	0	20	**85**
	Cropland/bare Surfaces	0	3	35	3	0	41	**85**
	Built-up areas	3	0	4	62	0	69	**90**
	Water bodies	0	0	0	0	3	3	**100**
	Classified Total	6	20	42	66	3	137	
Producer Accuracy (%)		**50**	**85**	**83**	**94**	**100**		
Overall Accuracy (%)								**88**
Kappa Coefficient								**0.81**

(c) 2011 LULC MAP

Classified Data	Reference Data							Users' Accuracy (%)
	LULC Classes	Wetlands	Savannah/Mixed vegetation	Croplands/ bare Surfaces	Built-up Areas	Water bodies	Reference Total	
	Wetlands	7	0	1	2	0	10	**70**
	Mixed vegetation/Savannah	0	12	2	0	0	14	**86**
	Croplands/bare Surfaces	0	4	34	0	0	38	**89**
	Built-up areas	3	0	5	90	0	98	**92**
	Water bodies	0	0	0	0	3	3	**100**
	Classified Total	10	16	42	92	3	163	
Producer Accuracy (%)		**70**	**75**	**81**	**98**	**100**		
Overall Accuracy (%)								**90**
Kappa Coefficient								**0.82**

(d) 2020 LULC MAP

Classified Data	Reference Data							Users' Accuracy (%)
	LULC Classes	Wetlands	Savannah/Mixed vegetation	Croplands/ bare Surfaces	Built-up areas	Water bodies	Reference Total	
	Wetlands	4	0	0	1	0	5	**80**
	Mixed vegetation/Savannah	0	11	2	0	0	13	**85**
	Croplands/bare Surfaces	0	2	28	4	0	34	**82**
	Built-up areas	2	0	3	116	0	121	**96**
	Water bodies	0	0	0	0	4	4	**100**
	Classified Total	6	13	33	121	4	177	
Producer Accuracy (%)		**67**	**85**	**85**	**96**	**100**		
Overall Accuracy (%)								**92**
Kappa Coefficient								**0.84**

Producer Accuracy: error of omission (%), Users' accuracy: error of commission

The AP LULC historical dynamics results and the area under each LULC class for the period of 1986–2020 are represented in Figure 4.1 and Tables 4.2a-b, respectively. Cropland and bare surfaces were found to be dominant for the years 1986 (56.58%) and 2001 (48.97%); the built-up areas have overtaken the trend (47.1% in 2011 and 62.35% in 2020) from 2011. As for wetlands, both an increasing (1986–2001) and decreasing trend (since 2001) have been observed.

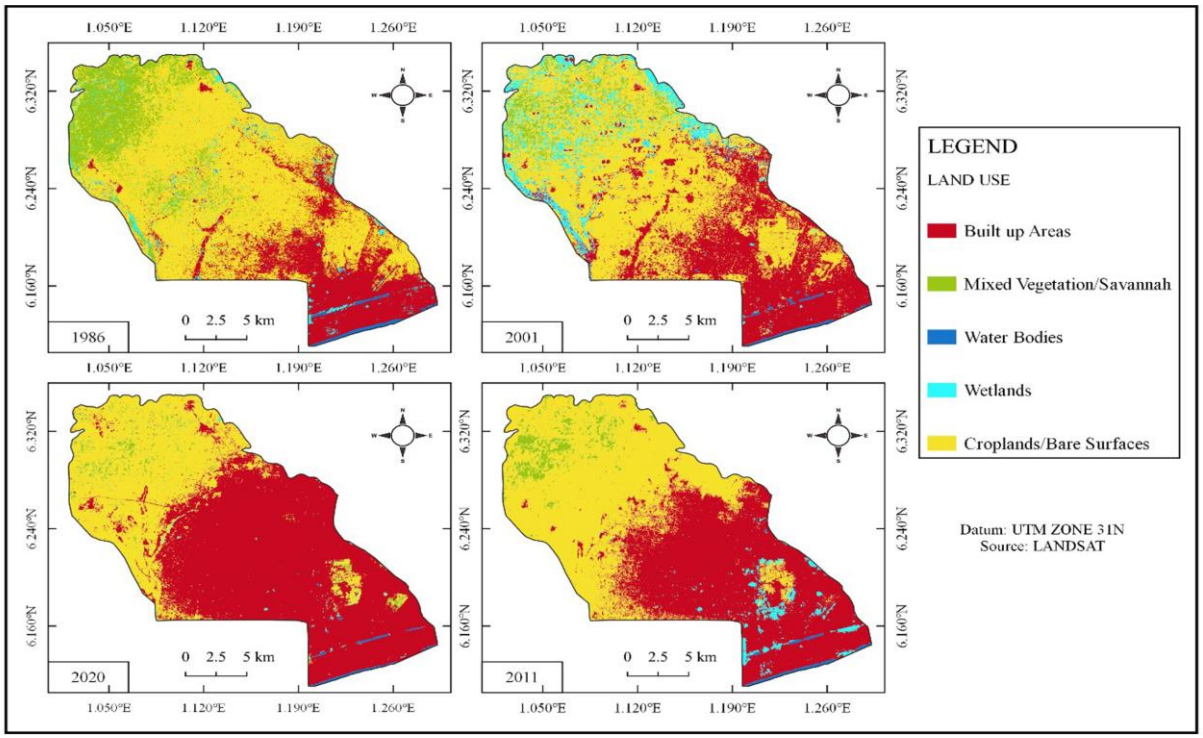

Figure 4.1: LULC Dynamics Maps of the AP: 1986, 2001, 2011 and 2020

The analysis of the 34 years of LULC in the AP considering the timeframes of 1986–2001, 2001–2011, and 2011–2020 in terms of the net change of the LULC classes considered shows that the main classes that have undergone changes are the built-up areas, croplands/bare surfaces, savannah/mixed vegetation, and wetlands, with the most dominant change being the conversion from cropland/bare surfaces to built-up areas, followed by the conversion from savannah/mixed vegetation and wetlands to croplands/bare surfaces. Over the period of 1986–2001, built-up areas increased by 45.32 km^2 (10.79%), while croplands and mixed vegetation decreased by 31.96 km^2 (7.6%) and 31 km^2 (7.4%), respectively. The rate of change over the period considered depicted an increase in LULC classes such as built-up areas at an annual rate of 4.78% against a decrease in croplands/bare surfaces and savannah/mixed vegetation at an annual rate of 1.48% and 2.83%, respectively. Though the mixed vegetation class follows a decreasing pattern, there is also a need to highlight the decreasing pattern of deforestation. The deforestation rate dropped from 2.07 (1986–2001) to 0.45 (2011–2020).

Table 4.2a: Historical LULC Classes: Rate (**%)** and Coverage (km^2)

Class Name	**Statistics**							
	1986		**2001**		**2011**		**2020**	
	km^2	**%**	**km^2**	**%**	**km^2**	**%**	**km^2**	**%**
Built-up Area	99.3	23.64	144.62	34.43	197.83	47.1	261.87	62.35
Mixed Vegetation/Savannah	62.99	15	31.99	7.62	16.83	4.01	12.74	3.03
Water Bodies	4.4	1.05	2.99	0.71	2.9	0.69	2.35	0.56
Wetlands	15.57	3.71	34.61	8.24	10.26	2.44	1.46	0.35
Croplands/Bare Surface	237.64	56.58	205.68	48.97	192.07	45.73	141.48	33.69

Table 4.2b: Change in the Historical LULC Classes: Rate (%) and Coverage (% and km^2)

Class Name	**Statistics**											
	1986–2001			**2001–2011**			**2011–2020**			**1986–2020**		
	km^2	**%**	**Rate**	**km^2**	**%**	**Rate**	**km^2**	**%**	**Rate**	**km^2**	**%**	**Rate**
Built-up Area	45.32	45.64	3.02	53.21	36.79	5.32	64.04	32.37	7.12	162.57	163.72	4.78
Mixed Vegetation/Savannah	-31	-49.21	-2.07	-15.16	-47.39	-1.52	-4.09	-24.30	-0.45	-50.25	-79.77	-1.48
Water Bodies	-1.41	-32.05	-0.09	-0.09	-3.019	-0.01	-0.55	-18.97	-0.06	-2.05	-46.59	-0.06
Wetlands	19.04	122.29	1.27	-24.35	-70.36	-2.44	-8.8	-85.77	-0.98	-14.11	-90.62	-0.415
Croplands/Bare Surface	-31.96	-13.45	-2.13	-13.61	-6.62	-1.36	-50.59	-26.34	-5.62	-96.16	-40.46	-2.83

4.2.2 Contributors to the Changes in Land Use and Land Cover in the AP

Over 34 years (Figure 4.2), the main contributing classes to the expansion of built-up areas are croplands (~140 km^2/34.59%), savannah/mixed vegetation (~10 km^2/2.04%), and wetlands (~8 km^2/1.84%), while the main contributors to the croplands/bare surfaces are savannah/mixed vegetation (~45 km^2/10.15%) and wetlands (~1.40%).

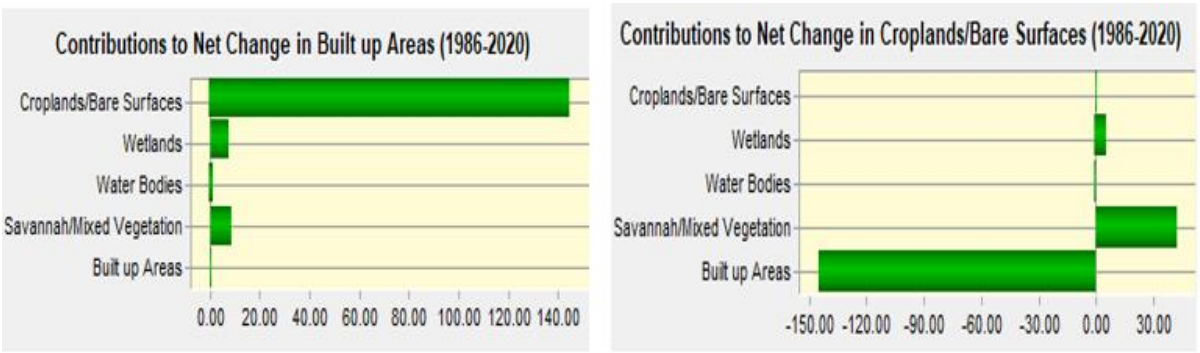

Figure 4.2: Contribution to Net Change in Built-up Areas and Cropland (km^2): 1986–2020

4.3 Model Validation and Future Land Use and Land Cover Projection

4.3.1 Model Validation

A comparison of the simulated and classified 2020 LULC map areas (Figure 4.3 and Table 4.3) shows minor differences, including the overestimation of built-up areas, croplands, and bare surfaces and the underestimation of the savannah or mixed vegetation.

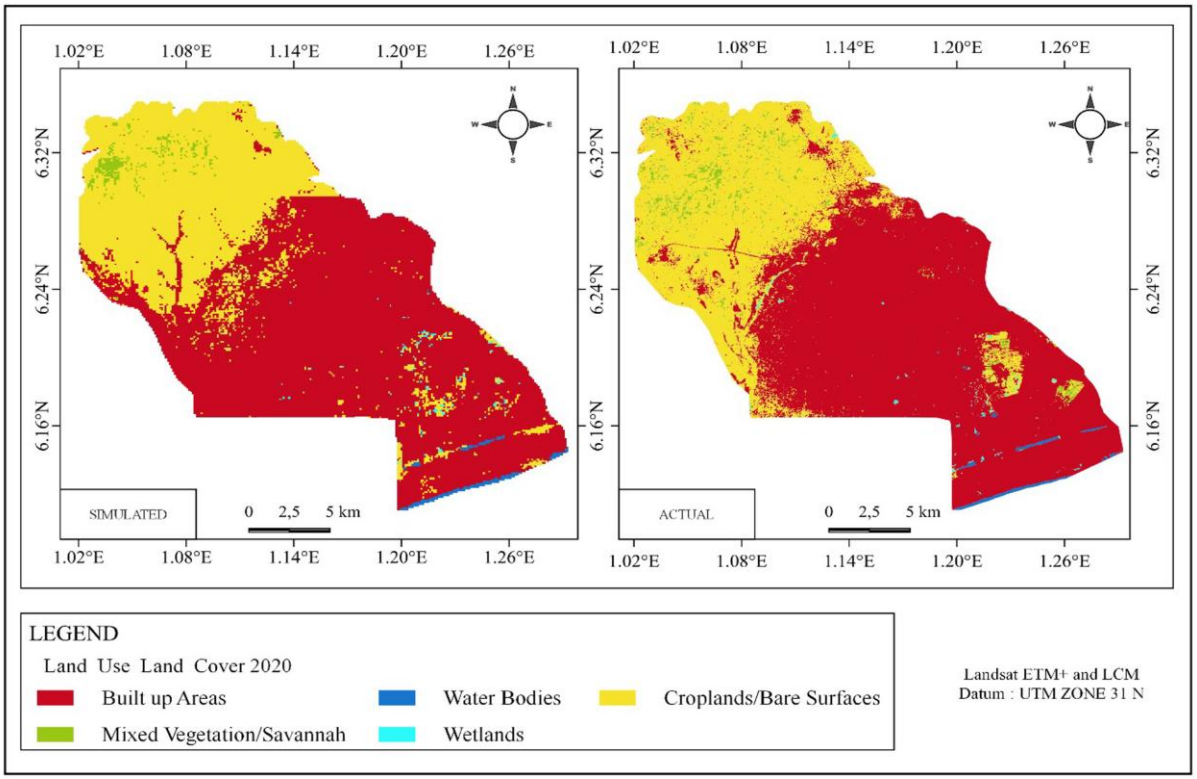

Figure 4.3: Simulated and Actual LULC Maps: 2020

Table 4.3: Area Comparison between Actual and Simulated 2020 LULC (km^2 / %)

LULC Classes	Actual Map	Simulated Map	Simulation Error
Built-up Area	261.87/62.35	264.6/63	2.73/0.65
Mixed Vegetation/Savannah	12.74/3.03	4.90/1.17	-7.84/1.87
Water Bodies	2.35/0.56	2.92/0.70	0.57/0.14
Wetlands	1.46/0.35	1.45/0.35	-0.01/0.002
Croplands/Bare surfaces	141.48/33.69	145.8/34.72	4.35/1.04

The output of the detailed analysis of the power of explanatory variables provided after the completion of the training stage shows an average skill measure (ASM) of 0.56 and an average accuracy rate (AAR) of 72.29%, with details presented in Table 4.4. A value of the ASM ranging between 0 and 1 depicts a performance exceeding expectation through pure change (Gibson et al., 2018). In addition, the variations of the kappa index of agreement between the 2020 simulated map and the 2020 actual map, including the K_{no} (gives the overall simulation run), the $K_{location}$ (level of agreement of location, given a specified quantity), the $K_{quantity}$ (level of agreement of quantity, given the model's ability to specify location), and the overall Kappa ($K_{standard}$), are 0.89, 0.87, 0.99, and 0.85, respectively. Furthermore, the obtained ROC value for the area is 0.74. In sum, the high value of the ASM (ranging between 0 and 1), overall Kappa (close to 90% or 0.9), and ROC (with the area under the curve estimate at 0.74), and values of the remaining Kscores being above 85% or 0.85 show a perfect agreement (Pontius, 2000) with only minor quantification and location errors between the actual and simulated maps, implicating that the LCM was capable of projecting the 2020 LULC map, hence showing the robustness of the model to predict reasonable outputs for the years 2030 and 2050. In addition, the MLP has fairly captured the wetland class and can be used to trace the dynamics of wetlands, which are essential for artificial recharge of aquifers to palliate overexploitation or seawater intrusion.

Table 4.4: Land Change Modeler's Power Test

2001–2011 (ASM = 0.53, AAR = 69.22%); 1986–2020 (ASM = 0.43, AAR = 71.42%)

Period	Sub-Model	Accuracy rate (%)	Skill measure	Training RMS	Testing RMS
2001–2011	Croplands/Bare surfaces	58.43	0.45	0.31	0.36
	Built-up Areas	80	0.60	0.41	0.38
1986–2020	Croplands/Bare surfaces	59.85	0.20	0.50	0.50
	Built-up Areas	83	0.66	0.36	0.36

NB: Croplands/bare surfaces sub-model stands for all LULC converted to croplands/bare surfaces while built-up Areas sub-model stands for all LULC converted to built-up areas.

4.3.2 Future Land Use and Land Cover Projections over the AP

The outputs of the 2030 and 2050 LULC projections using the Markov chain for the four (04) scenarios, including the BAU, afforestation, wetlands policy, and building policy scenarios, are depicted in Table 4.5 and Figures 4.4a-b. They project a general decreasing trend for croplands and bare surfaces, savannah or mixed vegetation, and an increasing trend for built-up areas under all the scenarios. Under the BAU scenario, an expansion of built-up areas at the expense of croplands/bare surfaces and savannah/mixed vegetation is expected. The built-up areas will potentially expand from 261.87 km^2 (62.35%) in 2020 to 294.57 km^2 (70.14%) in 2030 and 344.97 km^2 (82.14%) in 2050, while the croplands, bare surfaces, and savannah or mixed vegetation are expected to shrink from 141.48 km^2 in 2020 to 113.87 km^2 (27.11%) in 2030 and 70.17 km^2 (16.71%) in 2050, and from 12.74 km^2 (3.03%) in 2020 to 8 km^2 (1.90) in 2030 and 2.04 km^2 (0.49%) in 2050, respectively. The afforestation scenario, which considered limitation in cropland expansion by promoting vegetation growth, also depicts an expansion of built-up areas from 261.87 km^2 (62.35%) in 2020 to 294.57 km^2 (70.14%) in 2030 and 344.58 km^2 (82.04%) in 2050 against an expected shrink of the croplands/bare surfaces and savannah/mixed vegetation from 141.48 km^2 (33.69%) in 2020 against 113.44 (27.01%) in 2030 and 67.48 (16.07%) in 2050 and from 12.74 km^2 (3.03%) in 2020 to 8.43 km^2 (2.01) in 2030 and 5.12 km^2 (1.22) in 2050, respectively. Apart from the observed doubling of the wetland areas, especially in the long run (2050), the wetland policy has induced a long-term decrease in built-up areas (0.03% in 2050) and croplands (0.02% in 2050), compared to the BAU scenario. Finally, the building scenario, which considered the limitation of urban sprawl by promoting "ecological apartments," apart from inducing a decrease in the built-up areas (79.02% against 82.04% for the BAU), induces an increase in the croplands (27.49% in 2030 against 27.11% for the BAU and 19.59% against 16.71% in 2050 for the BAU) and an increase in savannah or mixed vegetation in the long term (0.69% against 0.49% in 2050). Slight changes are accounted for in the wetlands and the water bodies areas, plausibly related to the consideration of only the major transitions.

Table 4.5: Statistics of the Projected (2030 and 2050) LULC in the AP (km^2)

Classes	BASELINE	BAU		Afforestation		Wetland Policy		Building Policy	
		2030	2050	2030	2050	2030	2050	2030	2050
Built-up Areas	261.87 (62.35)	294.57 (70.14)	344.97 (82.14)	294.57 (70.14)	344.58 (82.04)	294.57 (70.14)	344.86 (82.11)	292.94 (69.75)	331.89 (79.02)
Savannah/Mixed Vegetation	12.74 (3.03)	8 (1.90)	2.04 (0.49)	8.43 (2.01)	5.12 (1.22)	8 (1.90)	2.04 (0.49)	8.034 (1.91)	2.89 (0.69)

Water Bodies	2.35 (0.56)	2.36 (0.56)	2.36 (0.56)	2.36 (0.56)	2.36 (0.56)	2.36 (0.56)	2.36 (0.56)	2.36 (0.56)	2.36 (0.56)
Wetlands	1.46 (0.35)	0.92 (0.22)	0.18 (0.043)	0.92 (0.22)	0.18 (0.043)	0.94 (0.22)	0.37 (0.09)	0.93 (0.22)	0.29 (0.07)
Croplands/Bare Surfaces	141.48 (33.69)	113.87 (27.11)	70.17 (16.71)	113.44 (27.01)	67.48 (16.07)	113.85 (27.11)	70.08 (16.69)	115.46 (27.49)	82.29 (19.59)

*Values in the parenthesis represents the percentage of land in refence to the total area of AP

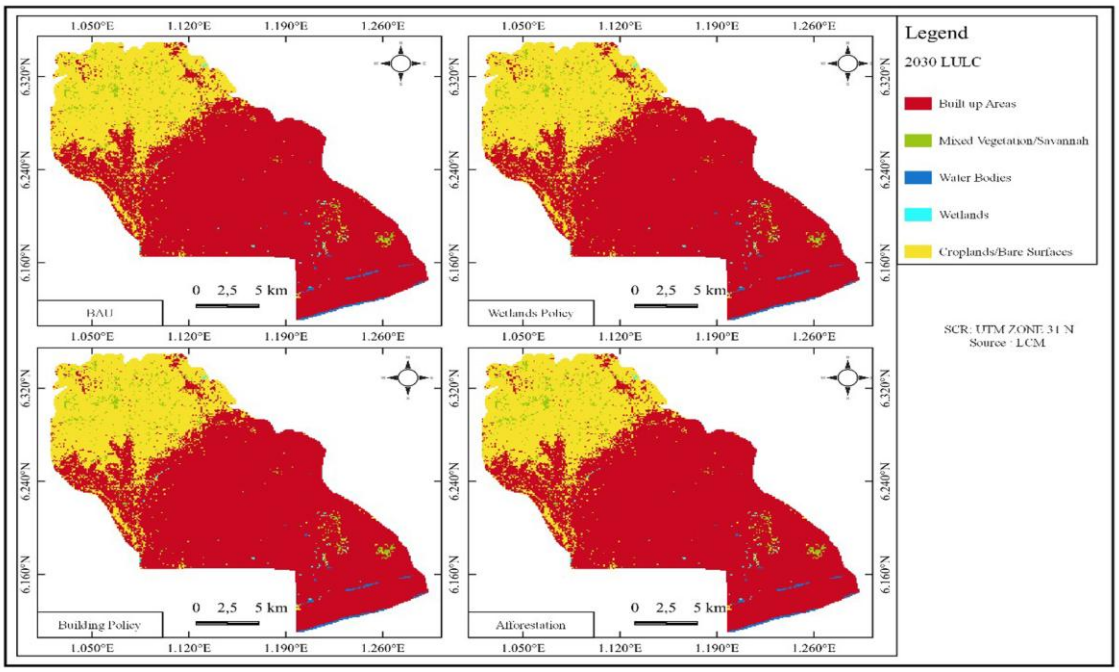

Figure 4.4a: Predicted 2030 LULC in AP under Various Scenarios

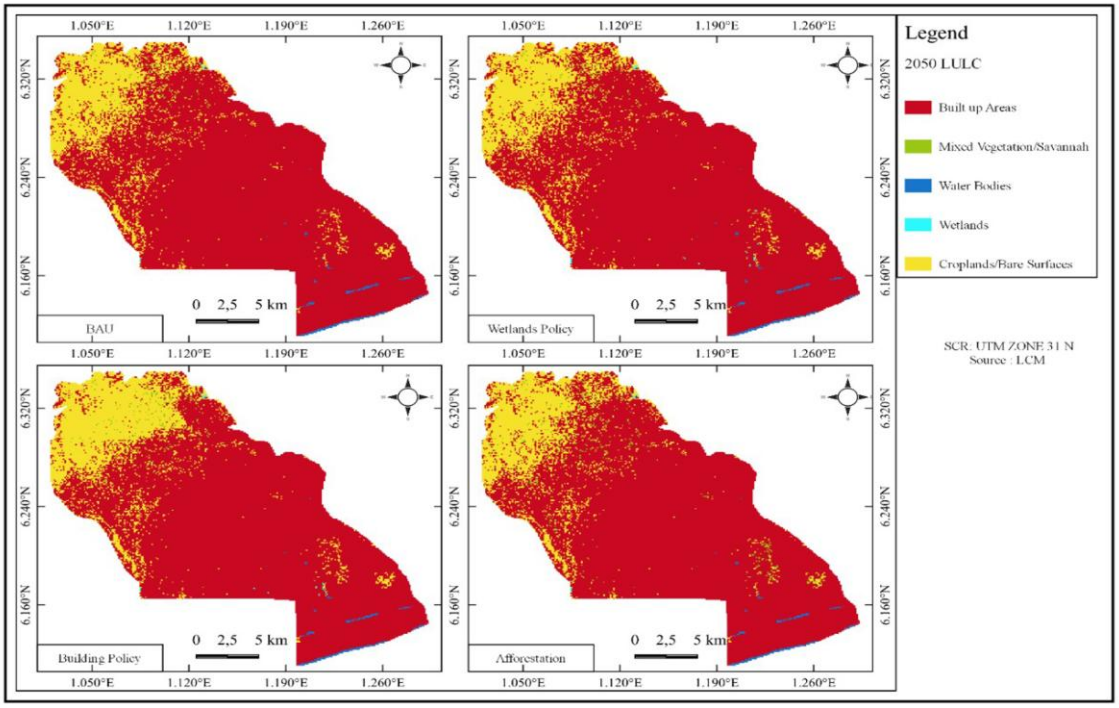

Figure 4.4b: Predicted 2050 LULC in AP under Various Scenarios

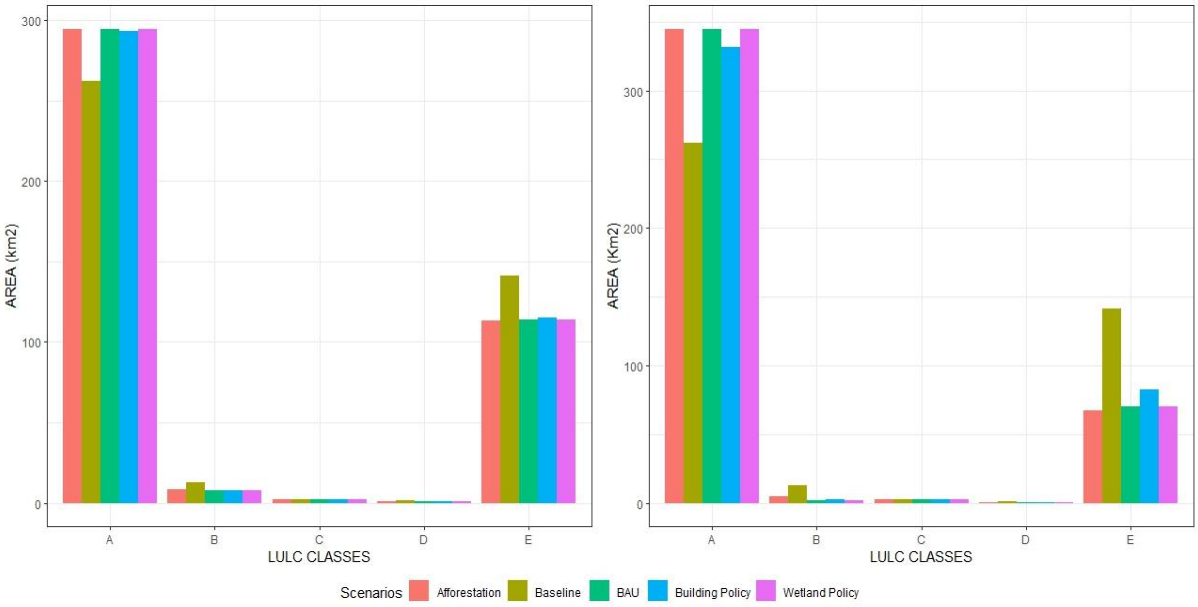

Figure 4.4c: Projected LULC over the AP for the year 2030 (Left) and 2050 (Right) under Various Scenarios
A, B, C,D and E stand for built-up area, Savannah/Mixed vegetation, water body, wetland, cropland and bare surface, respectively.

4.4 Discussion

A 34-year past LULC (1986–2020) assessment was carried out using the MLA in ENVI, and a future LULC (2020, 2030, and 2050 accounting for the near future and far future, respectively) was projected using the MLP-Markov chain approach embedded in the LCM (scenarios: BAU, afforestation, wetlands policy, and building policy). The LCM has been validated for the year 2020, and the predictive power of the model has been evaluated.

4.4.1 Agoènyivé Plateau Land Use and Land Cover: Accuracy Assessment, LCM Model Projection and Validation

The accuracy level of the classified maps can be attributed to both the heterogeneity linked to the intermixture of grasses and trees with harvested croplands as observed in the Vea catchment in Ghana (Larbi et al., 2019; Forkuor, 2014) and farming parcels found in buildings, around and in the midst of houses and buildings, or croplands in wetlands. The likely confusion between the savannah/mixed vegetation and croplands is related to the use of the mono-temporal data (January-April, representing the late season in the study area) (Zoungrana et al., 2015), while the confusion between buildings or croplands with wetlands (i.e., areas such as Adéwi, Ahanoukopé, and Hédzranawoé) is found to be a practice in the country related to poverty where people find themselves building in wetlands. In addition, agriculture is found to be promising in wetlands because of the associated humidity.

As for the validation of the LCM for this study, the 2020 classified (actual) map was compared with the simulated map. The comparison highlighted a slight overestimation of built-up areas and croplands with a simulation error of 2.73 km^2 (0.65%) and 4.35 km^2 (1.04%), respectively, along with an underestimation of mixed vegetation with a simulation error of 7.84 km^2 (1.87%). This result can be explained by the algorithm behind the MLP, which better captures the wetlands in the study areas at the expense of built-up areas, mixed vegetation, and croplands (chosen with the purpose of enabling future groundwater recharge through wetlands). It is also observed that some unrealistic changes were captured (false alarms and missing LULC classes), which can be attributed to changes that might have occurred in the reference year but were not shown during the calibration period (Olmedo et al., 2015). In addition, the lack of stationarity in changes during the calibration (2001–2011) and validation (2011–2020), associated with extrapolation from the calibration interval to the validation interval, may result in systematic errors that will affect the accuracy of the projection (Robertson and Swinton, 2005). Furthermore, the implication of complex processes (shaped by dynamic, non-linear human-nature interactions) in LULC dynamics can also be the root of the observed differences between the simulated and actual LULC maps and the reported Kappa statistics (Kolb et al., 2013). The projective power of the LCM in AP is shown through an average skill measure of 0.53 (2001–2011), ranked as the value for a model's performance, exceeding expectancy by pure chance (Gibson et al., 2018), along with high Kscores (with the overall Kappa estimated at around 0.90) and ROC (with the AUC estimated at 0.74).

4.4.2 Past Land Use and Land Cover and Future Projections in the AP

The LULC assessment in the AP revealed that the most common LULC class conversions in the AP are croplands to built-up areas and savannah/mixed vegetation to croplands. The urban areas have sprawled over the years (1986–2020) with a net gain in built-up areas of 162.57 km^2 (which almost doubled) as reported in the national strategy of greenhouse gas emissions due to deforestation and forest degradation (MERF, 2018a) and fit the projected urban expansion along the Gulf of Guinea, among others (Seto et al., 2012). This sprawl, following a northward trend (from the coast towards the peri-urban areas in the north), was found to be mainly at the expense of croplands and bare surfaces (contributing at 34.59%). The increasing trend of built-up area at the expense of other classes has also been observed in the Kanyakumari coastal zone in India (Kaliraj et al., 2017). Nevertheless, there is a need to highlight that, contrary to the AP, LULC in most of Togo depicts rather an expansion of savannah and agricultural land (Houteta

et al., 2019; Diwediga et al., 2015) or forest and savannah (Koglo et al., 2018) as the main classes.

Another pattern observed in the study area is the shrinking of the savannah or mixed vegetation at the expense of the croplands and bare surfaces. In total, mixed vegetation areas were reduced by 79.77% (50.25 km^2 lost), confirming a general decreasing trend of forest cover or savannah over the entire country (Akodéwou et al., 2020; Polo-Akpisso et al., 2020; Houteta et al., 2019; MERF, 2018a; Koglo et al., 2018; Kpedenou et al., 2016) and also observed in the coastal zone of Greater Accra, Ghana (Boampong, 2020). In addition, the 2016 National Forestry Inventory showed a predominance of built-up areas and agricultural lands over other LULC classes (MERF/IFN, 2016). The LULC spatial dynamic in the AP over the period of 1986–2020 follows the national LULCC pattern observed over the period of 2005–2017 (MERF, 2018b), expressed through an increase in built-up areas at the expense of croplands and bare surfaces (contribution of an area of 145.27 km^2), which on the other side expands at the expense of savannah or mixed vegetation (contribution of an area of 42.65 km^2). The most significant mixed vegetation loss occurred in the northern part of the study area and follows a northward pattern. Besides these observed changes in the savannah or mixed vegetation and wetlands, there is a need to highlight the decreasing rate of change in these classes over the years. The change rate has evolved from 2.07 (1986–2001) to 1.52 (2001–2011), then to 0.45 (1986–2020) for the savannah or mixed vegetation, while the rate of change in the wetlands has evolved from 2.44 (1986–2001) to 0.98 (2001–2011) to 0.42 (1986–2020). This finding is in line with the MERF report (MERF, 2018a), which found a lower rate of forest cover loss (0.4% annual deforestation rate over the period of 1990–2000 against 0.2% annual deforestation rate over the period of 2000–2015). The observed decreasing rate of these LULC types might be attributed to national and regional efforts to protect and restore wetlands, forests, and savannah.

Above all, the AP is found to be characterised by a transitional LULC class, which is the croplands and bare surfaces in the conversion from the savannah/mixed vegetation to built-up areas, making the urbanisation through the built-up areas class an underlying driver of the savannah conversion. This is in line with the report of the MERF (2018a), which highlighted the population growth associated with urbanisation and expansion of agricultural lands as the underlying cause of deforestation at the national level and in the maritime region. While at the regional level (maritime), the expansion of croplands and urban sprawl were key drivers of LULC change over the period of 2005–2017 (MERF, 2018b), in the AP, the key driver of LULC change is urban sprawl, with croplands and bare surfaces being the transitional LULC

class. This regional LULC trend (including the AP) is attributed to the absence of a land use plan, shifting agriculture, and population growth (MERF, 2018b). As the study area is the beneficiary of an agricultural project like the Rural Development Project of Agricultural Land in the Mission Tové area (PARTAM), covering an area of 600 hectares to strengthen the rice sector in an area that still hosts remaining savannah or mixed vegetation, there is a need to promote smart agriculture (productive agriculture along with sound agricultural practices) and avoid shifting agriculture in the region.

Another pattern observed in the AP, contrary to the overall pattern, is the shirking of the agricultural land area. These results are opposite to most of the findings (Akodéwou et al., 2020; Houteta et al., 2019; Kpedenou et al., 2016). Besides, the decrease is found to be sharper over the period 2011–2020 and can be explained by the lack of compensation for conversion from other classes to agricultural lands, plausibly as a result of the reinforcement of wetlands protection and afforestation laws. AP is currently in a shocking situation that can lead to land degradation and food insecurity in the long term. As a matter of fact, loss (145.77 km^2) and gain (48.54 km^2) in the croplands class show a strong reduction in croplands and bare surfaces in the AP that may result in more pressure on the remaining savannah areas but also hinder food security as a result of the potential scarcity of agricultural lands, which may be associated with the necessity to import foodstuffs from other parts of the country with the resulting increase in transport fees on the overall food staff price. This situation can also be a source of conflict as a result of competition between various users (i.e., agricultural, water resources, etc.). Furthermore, the link between LULC and the hydrological response to the water cycle needs to be highlighted, as does its ability to affect water resources (in terms of quality and quantity). This pattern is quite different from the pattern observed in other urban areas, such as Abidjan, where agricultural lands are reported to increase over time (Abdelaziz et al., 2020).

Above all, the evolution of LULC classes over the considered period in the AP shows a northward expansion of built-up areas, cropland, and bare surface. This pattern is found to follow the urbanisation pattern.

Under the BAU scenario, either for the near future (2030) or the far future (2050), the built-up areas are expected to sprawl (occupying up to 82.14%), while mixed vegetation or savannah area is expected to shrink (to 0.49%) compared to the baseline (2020). These results confirm the report of the MERF, which highlights an expected regional (maritime) decline in savannah by 2028 under the BAU scenario (MERF, 2018a). Nevertheless, there is still hope, as scenarios taking into account the afforestation, wetland policy, and building policy give insight into the long-term impacts of policies on the overall LULC outputs (mixed vegetation:

0.49% under BAU against 1.22% under the afforestation scenario and 0.69% under the building policy; croplands and bare surfaces: 16.71% under BAU against 16.07% under the afforestation scenario and 19.59% under the building scenario). Nevertheless, the results show that by focusing only on the afforestation policy, the vegetated areas may improve, but the area will still be subject to food insecurity as a result of a continuous decrease in croplands and bare surfaces. As a matter of fact, the building policy, which consists of limiting the horizontal expansion of built-up areas by 5% and 15% by 2030 and 2050 by promoting state-built apartments, will decrease the area being lost for all the different classes.

In summary, the assessment of LULC has brought into light the importance of long-term policy on LULC dynamics. On one hand, the urban sprawl in the AP is associated with reduced cropland and mixed vegetation/savannah, which in turn may induce the degradation of key ecosystems, thus reducing their capacity to render their services and sustain long-term development. The above-cited changes may potentially impact the national economy, as agriculture in Togo accounts for 40% (as of 2015) of the country's GDP and employs up to 65% of the active population (MAEH/PNIASAN, 2018). On the other hand, the link between LULC change and the hydrological response to the water cycle needs to be taken into consideration in order to minimise future impacts of this component on water resources (both its quality and quantity). In fact, existing studies have reported that changes in LULC are associated with impacts on the hydrological processes, especially through the changes in the proportions of impervious areas (Veldkamp and Lambin, 2001). It is the case of the observed increase in the peak discharge in the Dano watershed as a result of the expansion of agricultural lands and savanna degradation, which represents a huge flood risk to the population (Yira et al., 2016). In addition, water balance components (including surface runoff, evapotranspiration, and water yield) in the Mono River basin and Vea catchment were found to be influenced by many factors, including land use and land cover change (Larbi et al., 2021; Houteta et al., 2019). Furthermore, the increase in agricultural lands and built-up areas at the expense of forest areas was linked to the increase in runoff and a decrease in recharge in Abidjan (Abdelaziz et al., 2020).

4.5 Partial Conclusion

This chapter covered the assessment of LULC dynamics over the Agoènyivé Plateau in Togo, including the historical (1986–2020) and future (2030 and 2050) LULC trends using the ENVI software along with the Maximum Likelihood Algorithm and the LCM along with the Multilayer Perceptron Neural network—Markov Chain approach, respectively. Key drivers or

explanatory variables were derived, and LULC scenarios were built based on the drivers and causes of the observed changes highlighted by the local population and included in the literature. The results of the assessment include:

- The historical LULC trend: observed increase in built-up areas (38.71% land gain) at the expense of croplands and bare surfaces (22.89% land loss), which in turn grow from the conversion of mixed vegetation/savannah areas (22.69% land loss) and wetlands (3.36% land loss).
- Future LULC trend: LULC is expected to follow the same pattern as in the past under the BAU scenario, while the building policy scenario is found to be associated with a long-term increase in croplands and bare surfaces (2.88% by 2050 compared to the BAU scenario), wetlands (0.027% by 2050 compared to the BAU scenario), and mixed vegetation/savannah (0.2% by 2050 compared to the BAU scenario), key in protecting both the forest and wetland but also in ensuring food security in the study area.

CHAPTER FIVE: CLIMATIC TRENDS AND FUTURE PROJECTIONS

This chapter covers the analysis of climate time series (rainfall and temperature) for the historical (1991–2020) and future (2021–2050) periods for the AP. The results consist of (i) climate data quality control; (ii) validation of satellite-based products (CHIRPS and NASA POWER); (iii) regional climate model outputs bias correction; (iv) historical and future climatic trend analysis; and (v) future projections (RCP 4.5 and RCP 8.5).

5.1 Climate Data Quality Control

The obtained climate time series (stations) have been evaluated to account for their quality and quantity (missing data). The temporal and spatial distribution of missing data, as well as the percentage of missing values, are depicted in Figure 5.1. Gaps at both temporal and spatial scales are observed, with missing values in the rainfall time series reaching 10% at the Sanguera station and above 10% at the Mission Tové station. It can also be observed that data for variables such as temperature is only available for the Lomé station. The above realities justify the consideration of satellite-based data to complement the existing dataset.

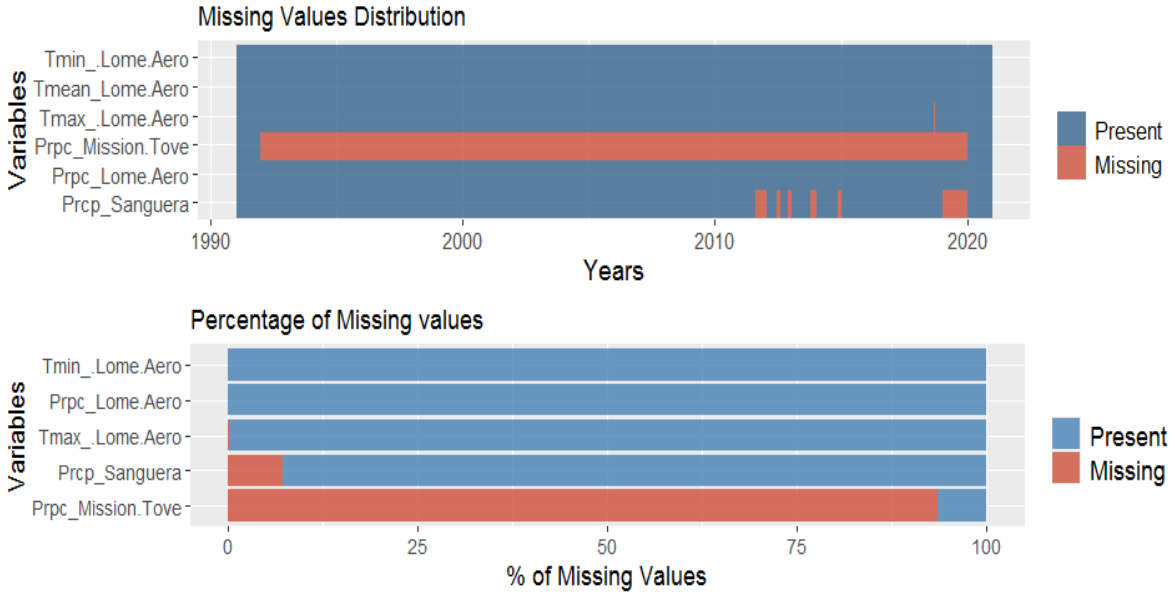

Figure 5.1: Temporal and Spatial Rainfall and Precipitation Distribution in the AP

5.2 Performance Evaluation of Satellite Based Products and Regional Climate Models

The performance of the CHIRPS product (rainfall dataset) has been evaluated at a monthly scale. for the Lomé-Aéroport station and Sanguera station over the period of 1991–2012 and 1991–2010, respectively, while the performance of the NASA POWER product (temperature dataset) has been evaluated over the Lomé-Aéroport station for the period of

1991–2012. The evaluation statistics, including the RMSE, R^2, PBIAS, and NSE, were considered using the hydroGOF package in R. The evaluation was basically done by comparing the satellite products with the observations (stations). The results show that both the CHIRPS and NASA POWER datasets capture the rainfall and the temperature temporal pattern in the study area (Figures 5.2-5.3). The CHIRPS data for the 2 stations show a bimodal rainfall pattern with the peak observed in June and October.

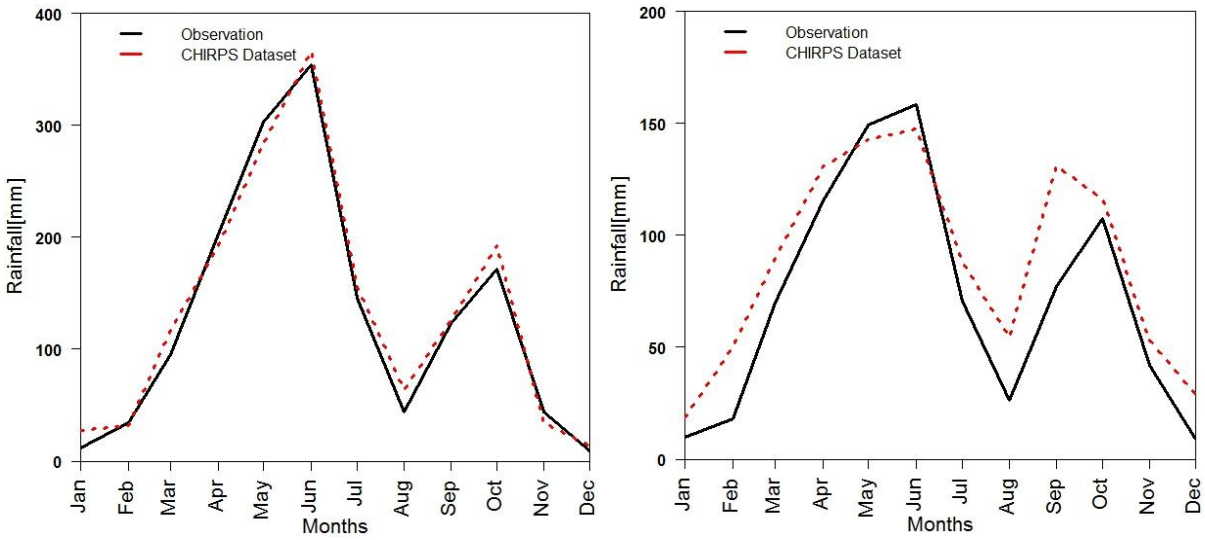

Figure 5.2: Annual Rainfall Cycle at Lomé (Left) and Sanguera (Right) Stations: In situ Observation Vs. CHIRPS Dataset

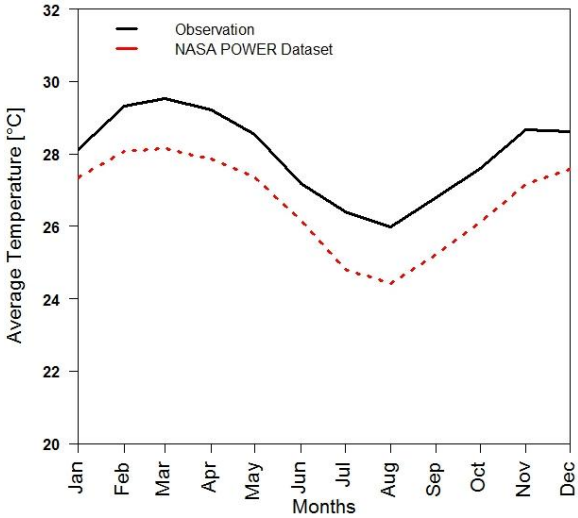

Figure 5.3: Annual Average Temperature Cycle for Lomé Station: In Situ Observation Vs. NASA POWER Dataset

The evaluation results (Table 5.1) show a very high agreement with a high coefficient of determination ($R^2_{Lomé} = 0.99$, $R^2_{Sanguera} = 0.90$) and good Nash-Sutcliffe efficiency ($NSE_{Lomé} = 0.98$, $NSE_{Sanguera} = 0.79$). Nevertheless, there is a need to highlight the overestimation of the October peak (Lomé Aéroport and Sanguera stations) and the underestimation of the June peak

(Sanguera station), which can be false alarms in dealing with extremes in general over the study area. On the other side, though the mean monthly temperature is slightly underestimated, the NASA POWER data evaluated for the Lomé Aéroport station show a high agreement with the station data in capturing the seasonal pattern with a high correlation coefficient (r = 0.98) but poor Nash-Sutcliffe efficiency (NSE = -0.39) (Table 5.1). The PBIAS of both the CHIRPS and the NASA POWER datasets fall within the range of ±25 (Table 5.1), proving that the data is acceptable and thus can be used for future analysis (Liechti et al., 2012).

Table 5.1: Validation Statistics for the CHIRPS and NASA POWER datasets

	Rainfall (CHIRPS)		**Temperature (NASA POWER)**
	Lomé	**Sanguera**	**Lomé**
RMSE	14.27	23.25	1.33
PBIAS (%)	4.3	23.2	-4.7
NSE	0.98	0.79	-0.36
R^2	0.99	0.90	0.97

A comparison of the selected CORDEX RCMs (CanESM2-RCA4, NorESM1-RCA4, CCLM4-8-17, and RACMO22T) over the period of 1991–2005 shows that, despite having the same resolution (50 km), these RCMs have different performance in simulating the mean monthly rainfall and temperature over the Agoènyivé plateau (Table 5.2, Figures 5.4a-b, and Annex 1). As for the rainfall in the study area, the two rainy season patterns (March–July and September–November) are best captured by RACMO22T ($PBIAS_{MAMJJ}$ = 0%, $PBIAS_{SON}$ = -0.01%) and CCLM4-8-17 ($PBIAS_{MAMJJ}$ = 0%, $PBIAS_{SON}$ = 0%). Unlike the rainfall parameter, the temperature is quite well captured by most of the RCMs and the ensemble mean (with R^2~1). It has also been observed that the bias in the monthly mean temperature is greater in the DS compared to the RS for almost all the RCMs.

Table 5.2: RCMs Performance Statistics in Simulating the Mean Monthly Rainfall and Temperature at Annual Basis: 1991–2005

	Raw RCMs				**Bias Corrected RCMs (DM)**			
	PBIAS (%)	R^2	**RMSE**	**NSE**	**PBIAS (%)**	R^2	**RMSE**	**NSE**
CanESM2	-54.1 (8.6)	0.01 (0.53)	69.07 (2.51)	-1.92 (-2.73)	0 (1.4)	1 (1)	3.44 (0.38)	1 (0.91)
NorESM1	-19.4 (5.7)	0.04 (0.63)	71.52 (1.7)	-1.11 (-0.72)	0 (1.4)	1 (1)	3.3 (0.39)	1 (0.91)
RACMO22T	36.2 (-7.5)	0.59 (0.51)	41.79 (2.19)	0.28 (-1.84)	0 (0.39)	1 (1)	0 (0.38)	1 (0.91)
MPI-ESM-LR	106.4 (3.9)	0.26 (0.67)	128.72 (1.72)	-5.84 (-0.75)	0 (1.4)	1 (1)	0 (0.38)	1 (0.91)
ENS-MEAN	17.3 (2.7)	0.24 (0.74)	56.01 (0.98)	-0.29 (0.43)	0 (1.4)	1(1)	1.49 (0.38)	1 (0.91)

NB: Where values in parentheses represents statistics for temperature.

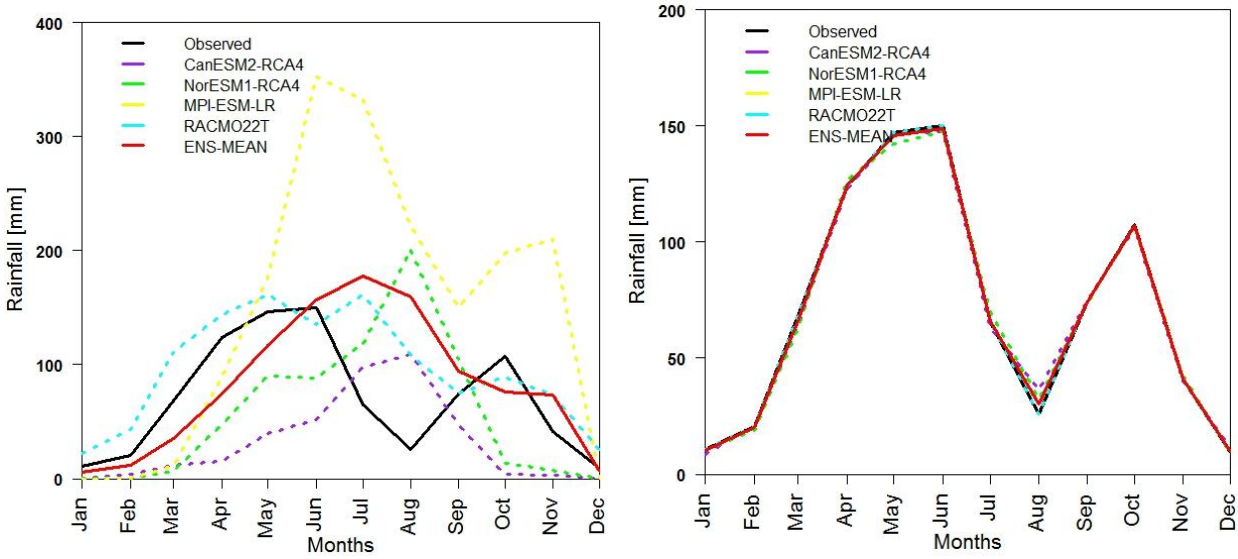

Figure 5.4a: Observed Vs. Raw (Left) and Bias Corrected (Right) RCMs Mean Monthly Rainfall Outputs in the AP: 1991–2005

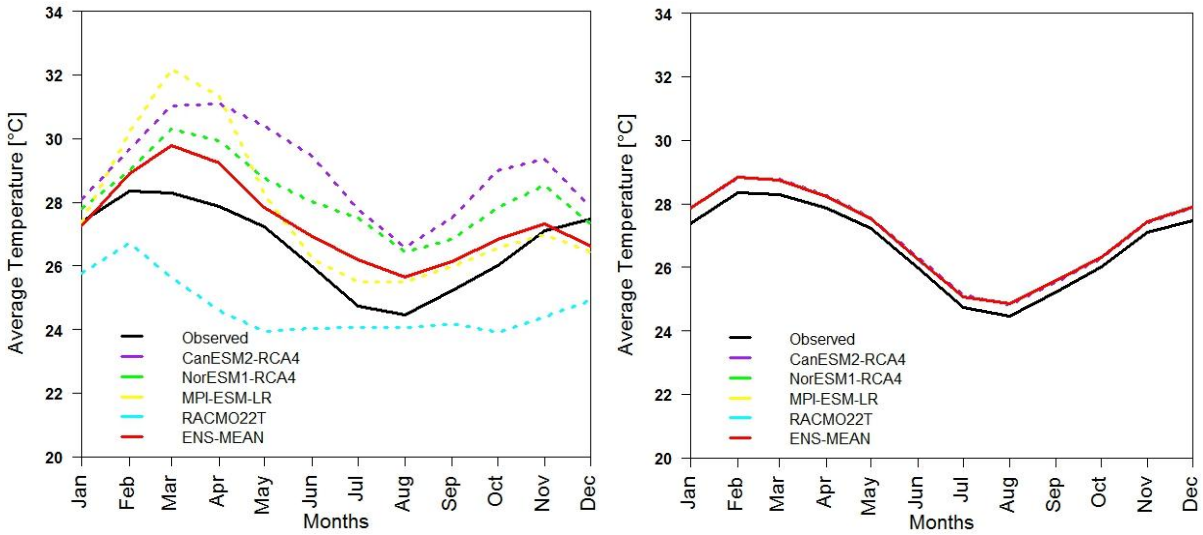

Figure 5.4b: Observed Vs. Raw (Left) and Bias Corrected (Right) RCMs Average Temperature Outputs in the AP: 1991–2005

5.3 Climate Trend Analysis in the Agoènyivé Plateau

This section captures the trend in rainfall and temperature for the historical (1991–2020) and the future (2021–2050) periods after the existence of change points and autocorrelation in the acquired time series is checked.

Table 5.3 depicts an independent and stationary rainfall time series over the entire AP, with no break point significant at 5%. At grid level, almost all the grids follow the same pattern, except for Grid 15, which showed a probability of a breakpoint in 2016, with a probability value of 0.74 significant at 1% (Scheffe test as part of Hubert segmentation). Contrary to the

previous variable, an auto-correlated temperature time series (Auto Correlation-Rang value > 1.96) over the AP with break points in 1997 and 2004 (Lomé station), 199 and 2015 (Mission Tové, Grid 7–16), 2012 (Sanguera, Grid 1–6), and 2012 and 2020 (AP) is also observed. Based on the above, both the modified Mann-Kendall (MMK) and Mann-Kendall (MK) tests were considered for the trend analysis in the AP.

Table 5.3: Summary of Rainfall and Temperature Statistical Test

STATIONS	TEMPERATURE				RAINFALL			
	PT	BT	LEE and HEGHINIAN-HUBERT (Scheffe test: 1%)	AUTO CORRELATION-RANG	PT	BT	LEE and HEGHINIAN-HUBERT (Scheffe test: 1%)	AUTO CORRELATION-RANG
Lomé	-		+ (1994 and 2004)	(+)***	-	-	-	(-)***
Mission Tové	-		+ (1997 and 2015)	(+)***	-	-	-	(-)***
Sanguera	-	-	+ (2012, P = 0.71)	(+)***	-	-	-	(-)***
Grid1	-	-	+ (2012, P = 0.71)	(+)***	-	-	-	(-)***
Grid2	-	-	+ (2012, P = 0.71)	(+)***	-	-	-	(-)***
Grid3	-	-	+ (2012, P = 0.71)	(+)***	-	-	-	(-)***
Grid4	-	-	+ (2012, P = 0.71)	(+)***	-	-	-	< 1.96 only at 95% and 99%
Grid5	-	-	+ (2012, P = 0.71)	(+)***	-	-	-	(-)***
Grid6	-	-	+ (2012, P = 0.71)	(+)***	-	-	-	(-)***
Grid7	-	-	+ (1997 and 2015)	(+)***	-	-	-	(-)***
Grid8	-		+ (1997 and 2015)	(+)***	-	-	-	(-)***
Grid9	-		+ (1997 and 2015)	(+)***	-	-	-	(-)***
Grid10	-		+ (1997 and 2015)	(+)***	-	-	-	(-)***
Grid11	-		+ (1997 and 2015)	(+)***	-	-	-	(-)***
Grid12	-		+ (1997 and 2015)	(+)***	-	-	-	(-)***
Grid13	-		+ (1997 and 2015)	(+)***	-	-	-	(-)***
Grid14	-		+ (1997 and 2015)	(+)***	-	-	-	(-)***
Grid15	-		+ (1997 and 2015)	(+)***	-		+ (2016, P = 0.74)	<1.96 only at 95% and 99%
Grid16	-		+ (1997 and 2015)	(+)***	-		-	(-)***
AP	-	+	+(2012 and 2020)	(+)***	-	-	-	(-)***

NB: PT and BT stands for PETTITT test and BUISHAND test, respectively.
(+): Presence of correlation; (-):No autocorrelation, ***: $\alpha = 0.001$; **: $\alpha = 0.01$; *: $\alpha = 0.05$

Historical (1991–2020) average temperature analysis statistics (Table 5.4) depict on a monthly scale a significant increasing trend for almost all the months, except for the months of February, June, October, and December. At the same time, all the seasons, including March–July (MAMJJ), September–November (SON), December–February (DJF), and August (A), show a significant increase in temperature, with an average seasonal warming accounting for

0.02 °C. The AP has experienced a significant increase ($p < 0.05$) in temperature estimated to be 0.02 °C annually (1991–2020: cumulative total of 0.6 °C), with twelve (12) stations (Lone, Mission Tové and Grid 7–16) depicting a significant increasing trend with an average annual warming rate of 0.02 °C. In the future (2021–2050), in reference to the period of 1991–2020, a significant increase ($p < 0.05$) in the average temperature is expected under both scenarios in the AP (estimated annually at 0.01/0.02 °C under RCP 4.5/RCP 8.5), including all the stations (ranging annually between 0.003–0.01 and between 0.02-0.03 °C under RCP 4.5 and RCP 8.5, respectively), and the two rainy seasons (estimated annually under RCP 4.5/RCP 8.5 to be 0.02/0.03 °C and 0.01/0.03 °C for the MAMJJ and SON, respectively). In fact, the increase in temperature during the rainy season, which represents the crop-growing season, can be fatal to agricultural activities as associated with an increased evapotranspiration.

On the other hand, rainfall trend analysis statistics for the period 1991–2020 (Table 5.4) reveal a non-significant ($p > 0.05$) increase over AP estimated at 0.81 mm annually (with a cumulative total of 24.3 mm over the period of 1991–2020). As a matter of fact, almost all the stations considered agree with this increasing pattern. Besides, there is a need to highlight the decreasing trend in the rainfall during the main rainy season (MAMJJ), which depicts a decrease in rainfall (0.89 mm annually), while the remaining seasons show an increase in rainfall, reaching 2.13 mm annually. In the future (2021–2050), a non-significant ($p > 0.05$) slight annual increase of 0.05 mm (with a cumulative total of 1.5 mm over the period of 2021–2050) and a decreasing trend estimated at 0.69 mm annually (with a cumulative total of 20.7 mm) are expected at the AP level under RCP 4.5 and RCP 8.5, respectively (Table 5.4). Above all, stations such as Sanguera, Grids 1–3, and Grid 7 are expected to experience a significant ($p < 0.05$) increase, while stations such as Grid10 and Grids 12–16 are projected to undergo a significant decreasing trend under the RCP 4.5. Contrary to the RCP 4.5, most of the stations in AP are expected to experience a significant ($p < 0.05$) decrease in rainfall under the RCP 8.5. Finally, it has been observed that the two main rainy seasons are expected to experience a non-significant ($p > 0.05$) decrease in rainfall under both scenarios.

Table 5.4: Trend Analysis Statistics: Historical (1991–2020) and Future (2021–2050)

STATION	TEMPERATURE						RAINFALL					
	Historical		RCP 4.5		RCP 8.5		Historical		RCP 4.5		RCP 8.5	
	Z-Value	Sen's slope	Z-Value	Sen's slope	Z-Value	Sen's slope	Z-Value	Sen's slope	Z-Value	Sen's slope	Z-Value	Sen's slope
Lomé	4.26***	0.02	2.21*	0.003	9.02***	0.03	0.93	4.6	-1.28	-1.08	-1.97*	-1.87
M. Tové	5.46***	0.02	7.17***	0.01	7.30***	0.02	1.32	4.25	2.5	1.99	1.36	1.10
Sanguera	1.44	0.01	5.39***	0.01	7.26***	0.02	-0.64	-3.51	4.79***	5.41	4.04***	4.45

Grid1	1.44	0.01	5.51***	0.01	6.47***	0.02	0.79	2.36	3.63***	2.98	2.34*	1.9
Grid2	1.44	0.01	5.51***	0.01	6.49***	0.02	0.43	1.96	4.10***	3.71	3.20**	2.85
Grid3	1.44	0.01	5.51***	0.01	6.49***	0.02	0.61	2.01	2.97**	2.44	1.96	1.56
Grid4	1.44	0.01	5.87***	0.01	6.50***	0.02	1.64	3.94	0.91	0.68	-0.12	-0.10
Grid5	1.44	0.01	5.87***	0.01	6.49***	0.02	1.14	2.54	-0.18	-0.14	-1.31	-0.97
Grid6	1.44	0.01	5.87***	0.01	6.49***	0.02	0.93	2.44	-1.17	-0.84	-2.06*	-1.76
Grid7	5.46***	0.02	6.16***	0.01	9.17***	0.02	-0.39	-1.44	3.39***	2.81	2.30*	1.84
Grid8	5.46***	0.02	6.16***	0.01	9.12***	0.02	0.32	0.69	1.56	1.13	0.44	0.35
Grid9	5.46***	0.02	6.42***	0.01	9.04***	0.02	0.25	0.62	-1.24	-0.89	-2.03*	-1.69
Grid10	5.46***	0.02	6.42***	0.01	9.08***	0.02	0.071	0.2	-2.57*	-2.04	-3.07**	-2.93
Grid11	5.46***	0.02	6.16***	0.01	9.17***	0.02	-0.89	-2.9	1.18	0.83	0.16	0.15
Grid12	5.46***	0.02	6.42***	0.01	9.04***	0.02	0.11	0.32	-2.06*	-1.67	-2.67**	-2.46
Grid13	5.46***	0.02	6.42***	0.01	9.08***	0.02	0.61	1.19	-3.8***	-3.37	-4.2***	-4.06
Grid14	5.46***	0.02	6.42***	0.01	9.08***	0.02	1.53	0.32	-4.7***	-4.84	-5.1***	-5.60
Grid15	5.46***	0.02	6.42***	0.01	9.08***	0.02	1.89	1.19	-3.9**	-3.68	-0.76	-0.78
Grid16	5.46***	0.02	6.42***	0.01	9.08***	0.02	1.32	3.12	-3.3**	-2.88	-3.9***	-3.64
AP	3.85***	0.02	6.37***	0.01	7.81***	0.02	0.39	0.81	0.06	0.05	-0.92	-0.69
January	2.00*	0.02	1.37	0.004	7.43**	0.05	-0.18	-0.04	0.61	0.03	0.71	0.04
February	2.11	0.02	4.00***	0.01	6.34***	0.03	0.82	0.33	-0.52	-0.05	-0.92	-0.09
March	2.57*	0.02	5.66***	0.02	6.47***	0.03	0.75	0.49	-0.55	-0.09	-2.09*	-0.35
April	2.91**	0.02	6.34***	0.02	8.29***	0.04	-1.57	-1.4	0.01	0.00	1.03	0.23
May	3.03**	0.02	6.08***	0.02	8.07***	0.03	-0.25	-0.17	-2.26*	-0.44	-2.51*	-0.59
June	1.82+	0.01	6.87***	0.017	7.17***	0.02	0.03	0	-1.12	-0.42	-0.99	-0.36
July	2.64**	0.01	7.53***	0.018	8.42***	0.03	0.03	0.01	2.39*	0.56	1.64	0.44
August	2.28*	0.02	6.60***	0.02	7.46***	0.03	0.11	0.02	3.92***	0.68	3.13**	0.45
September	3.36***	0.03	6.62***	0.015	7.30***	0.023	1.61	1.68	1.44	0.37	-0.10	-0.04
October	2.46	0.0	4.74***	0.01	7.87***	0.03	0.82	0.61	-1.14	-0.28	-1.35	-0.31
November	2.46*	0.02	-1.05	0.002	7.17***	0.02	1.57	0.65	-0.25	-0.03	0.53	0.06
December	1.75	0.01	0.51	0.001	6.88***	0.03	-0.14	-0.01	1.91+	0.08	1.83	00.08
MAMJJ	4.00***	0.02	8.46***	0.019	8.44***	0.025	-0.5	-0.89	-1.35	-0.91	-1.42	-1.02
SON	3.25**	0.02	3.99***	0.005	8.71***	0.03	1.5	2.13	-0.10	-0.04	-0.68	-0.30
DJF	2.75**	0.02	3.021**	0.005	6.62***	0.02	2.11	1.86	-0.04	-0.01	-1.03	-0.31
A	2.28*	0.02	6.60***	0.02	8.46***	0.02	1.03	1.43	3.77***	1.80	2.37**	1.06

*MAMJJ: March–July, SON: September–November, DJF: December–February and A: August
***: $\alpha = 0.001$; **: $\alpha = 0.01$; *: $\alpha = 0.05$

5.4 Changes in Climate Parameters over the AP: Historical and Future Projections

5.4.1 Temporal Pattern

A comparison of RCMs' projections of the average annual rainfall unveiled that while some RCMs (NorESM1 and RACMO22T and the ensemble mean), projected an increase in the average annual rainfall, others (CanESM2 and CCLM4-8-17) depict an expected decrease pattern under the RCP 4.5 (Table 5.5). For the RCP 8.5, except for RACMO22T, which is still showing an expected increase in average annual rainfall, the remaining RCMs, including the ensemble mean, agree on a projected decrease in rainfall over the AP (Table 5.5). On the other hand, a comparison of the projected average temperature under the various RCMs considered

revealed that quite all the RCMs, as well as the ensemble mean project an increase in the temperature under both scenarios, except for the CanESM2 under the RCP 4.5 (Table 5.5).

The average annual rainfall (Table 5.5, Figures 5.5a-b, and Figures 5.6a-b) observed in the AP is estimated at 875.41 mm (1991–2020). Based on the ensemble-mean, this value is expected to reach 862.39 mm (non-significant decrease estimated at 1.49%) and 848.04 mm (non-significant decrease estimated at 3.13%) in the future (2021–2050) under RCP 4.5 and RCP 8.5, respectively. On the other hand, the recorded average temperature for the period of 1991–2020 is 26.8 °C (Table 5.5, Figures 5.7–5.8). Based on the ensemble mean, this value is expected to reach 27.11 °C (with an increase estimated at 0.31 °C) and 28.09 °C (with an increase estimated at 1.29 °C) under the RCP 4.5 and RCP 8.5, respectively. These observed changes in the average temperature are found to be significant ($p < 0.05$) for both RCPs.

Table 5.5: Long-term Changes in Rainfall and Temperature over the AP

Variable	Baseline (1991–2020)	RCP 4.5 (2021–2050)				
		CanESM2	NorESM1	CCLM4-8-17	RACMO22T	ENS MEAN
Tmean	26.8	25.04 (-1.76)	27.79 (0.99)	27.77 (0.97)	27.84 (1.04)	27.11 (0.31)
Tmin	24.67	23.29 (-1.38)	25.18 (0.51)	25.43 (0.76)	25.58 (0.92)	25.32 (0.65)
Tmax	28.41	26.33 (-2.09)	29.92 (1.51)	29.53 (1.12)	29.75 (1.33)	28.74 (0.33)
Rain	875.41	799.81 (-8.64)	877.81 (0.27)	856.71(-2.14)	915.25 (4.55)	862.39 (-1.49)
		RCP 8.5 (2021–2050)				
		CanESM2	NorESM1	CCLM4-8-17	RACMO22T	ENS MEAN
Tmean	26.8	28.47 (1.67)	27.99 (1.19)	27.89 (1.09)	28 (1.2)	28.09 (1.29)
Tmin	24.67	25.86 (1.19)	25.36 (0.70)	25.59 (0.93)	25.69 (1.03)	25.63 (0.96)
Tmax	28.41	30.61 (2.19)	30.20 (1.79)	29.54 (1.13)	29.88 (1.46)	30.02 (1.61)
Rain	875.41	821.36 (-6.17)	826.9 (-5.54)	812.05 (-7.24)	931.82 (6.44)	848.04 (-3.13)

* Tmean/Tmin/Tmax and rain are expressed in °C and mm, respectively while values in the parenthesis represent the changes expressed in °C (temperature) and % (rain).

When it comes to the seasonality of rainfall (Figures 5.5a-b and Table 5.6), the ensemble mean (in reference to the period 1991–2020) projects a decrease in rainfall during the two rainy seasons (MAMJJ and SON), estimated to reach 6.6% and 7.8% under RCP 4.5 and RCP 8.5, respectively. In addition, the peaks during the two rainy seasons are expected to undergo a reduction both under RCP 4.5 (estimated at 10.59% and 19.2% for the June peak and October peak, respectively) and RCP 8.5 (estimated at 10.64% and 17% for the June peak and October peak, respectively). Furthermore, though the June rainfall peak has been captured for both the observation and future periods, a shift has been observed for the October peak under the RCP 4.5 (the peak is rather expected in September). Contrary to what has been

highlighted so far, it has been observed that the rainfall is expected to increase during the month of August, which represents the small dry season.

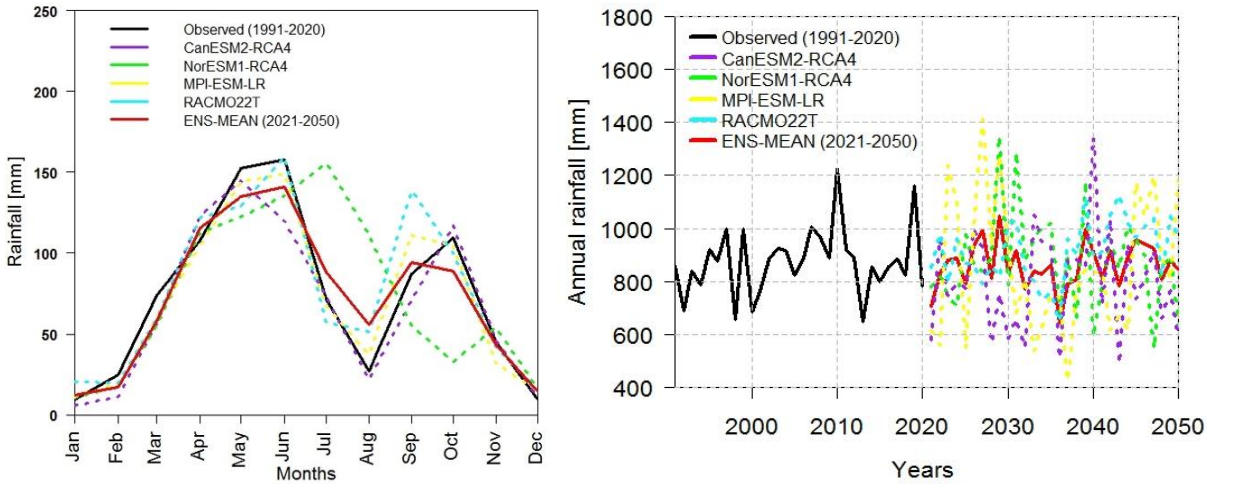

Figure 5.5a: Monthly (Left) and Annual (Right) Average Rainfall over the AP : Individual RCMs and Ensemble-mean Projection under RCP 4.5

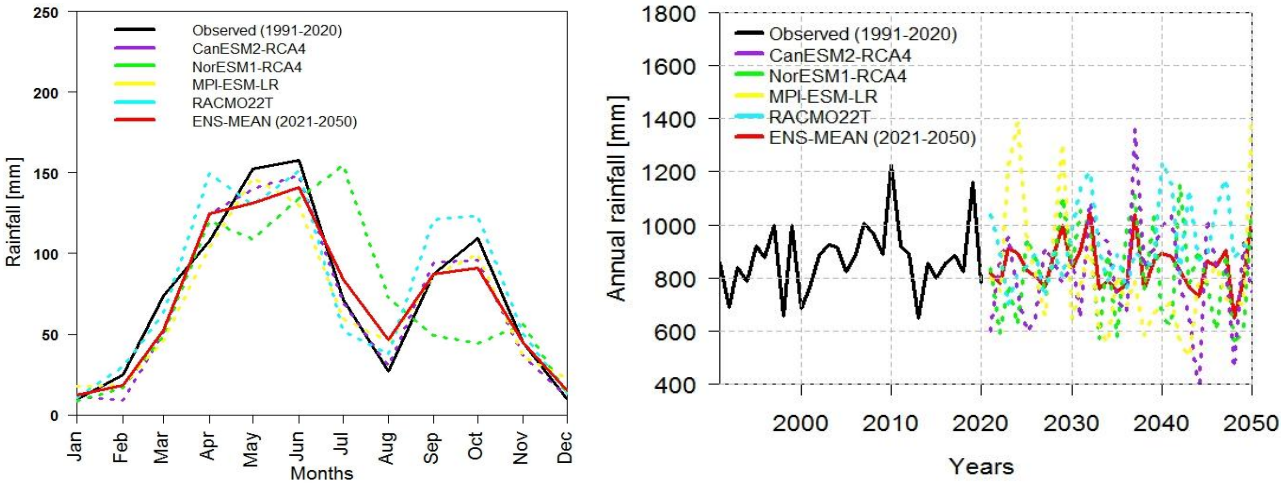

Figure 5.5b: Monthly (Left) and Annual (Right) Average Rainfall over the AP : Individual RCMs and Ensemble-mean Projection under RCP 8.5

Table 5.6: Monthly and Seasonal Average Rainfall over the AP

Months/Seasons	Periods		
	1991–2020	2021–2050	
	Observation	RCP 4.5	RCP 8.5
January	9.80	12.01(22.55)	12.06 (23.06)
February	24.80	16.94 (-31.69)	18.41 (-25.77)
March	73.82	57.69 (-21.85)	52.35 (-29.08)
April	107.58	115.45 (7.32)	124.69 (15.90)
May	152.23	135.11(-11.25)	131.38 (-13.70)
June	157.67	140.98 (-10.59)	140.90 (-10.64)
July	71.44	88.36 (23.68)	83.81 (17.32)

August	26.74	55.49 (107.52)	46.39 (73.49)
September	87.38	94.06 (7.64)	87.45 (0.08)
October	109.66	88.58 (-19.22)	90.95 (-17.06)
November	44.84	43.28 (-3.48)	44.73 (-0.25)
December	9.44	14.44 (52.97)	14.91(57.94)
MAMJJ (March–July)	562.74	537.59 (-4.47)	533.13 (-5.26)
SON (September–November)	241.88	225.92 (-6.60)	223.13 (-7.75)
DJF(December–February)	44.04	43.39 (-1.50)	45.38 (3.07)
A (August)	26.74	55.49 (107.52)	46.39 (73.49)

*Rainfall values are in mm, while values in brackets are changes expressed in percentage.

For the seasonality of the average temperature, the highest increase in temperature is expected during the dry seasons under both scenarios (Table 5.7 and Figures 5.6a-b). Nevertheless, the concern is the expected increase in the average temperature during the crop growing seasons with an estimate of 0.5/1.3 °C (RCP 4.5/RCP 8.5) and 0.2/1.1 °C (RCP 4.5/RCP 8.5) for MAMJJ and SON, respectively. In a setting where agriculture is essentially rainfed, these changes will be associated with increased evapotranspiration, thus threatening the crop growth.

Table 5.7: Monthly and Seasonal Average Temperature over the AP

Months/Seasons	Periods		
	1991–2020	2021–2050	
	Obs	RCP 4.5	RCP 8.5
January	27.49	27.45 (-0.04)	29.12 (1.63)
February	28.41	28.38 (-0.03)	30.02 (1.61)
March	28.35	28.74 (0.39)	29.97 (1.62)
April	28.00	28.34 (0.34)	29.30 (1.3)
May	27.38	27.81 (0.43)	28.66 (1.28)
June	26.09	26.75 (0.66)	27.34 (1.25)
July	24.95	25.64 (0.69)	25.98 (1.03)
August	24.67	25.32 (0.65)	25.63 (0.96)
September	25.40	25.92 (0.52)	26.27 (0.87)
October	26.15	26.52 (0.37)	27.26 (1.11)
November	27.17	26.90 (-0.27)	28.43 (1.26)
December	27.53	27.52 (-0.01)	29.08 (1.55)
MAMJJ (March–July)	26.95	27.46 (0.51)	28.25 (1.3)
SON (September–November)	26.24	26.45 (0.21)	27.32 (1.08)
DJF(December–February)	27.81	27.80 (-0.01)	29.33 (1.52)
A (August)	24.67	25.63 (0.96)	25.96 (1.29)

*Both the average temperature as well as the changes (in bracket) are expressed in °C.

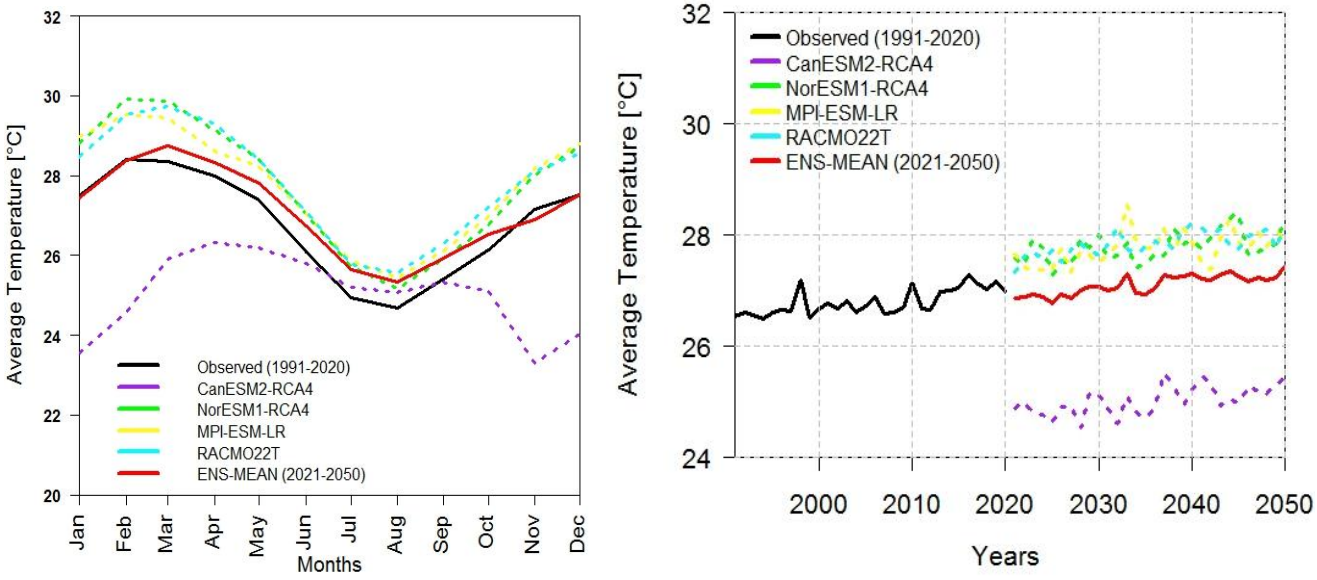

Figure 5.6a: Monthly (Left) and Annual (Right) Average Temperature over the AP : Individual RCMs and Ensemble-mean Projection under RCP 4.5

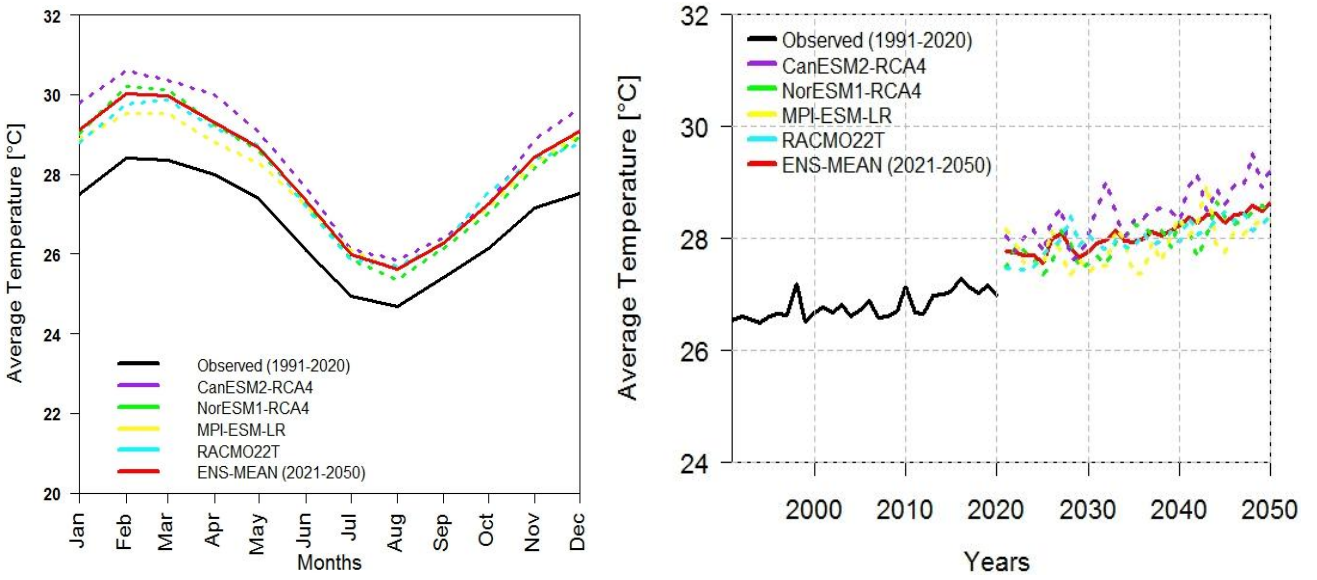

Figure 5.6b: Monthly (Left) and Annual (Right) Average Temperature over the AP : Individual RCMs and Ensemble-mean Projection under RCP 8.5

5.4.2 Spatial Pattern

The spatial distribution of the expected change in rainfall and temperature in the AP (reference period: 1991–2020) is captured by Table 5.8 and Figures 5.7a-b and 5.8a-b.

For the period of 1991–2020, the average annual rainfall ranges between 697.57 mm (Grid 14) and 1005.21 mm (Sanguera station and Grid 2) (Figure 5.7a and Table 5.8) with an expected decrease in the value, respectively ranging between 0.2 and 7% and between 1 and 9% under RCP 4.5 and RCP 8.5 (Figure 5.7b and Table 5.8). For both RCPs, the highest decrease in the annual rainfall is expected in the southern and central parts of the AP.

Table 5.8: Spatial Annual Rainfall and Average Temperature: 1991–2020 and 2021–2050

Stations	RAINFALL			TEMPERATURE		
	1991–2020	2021–2050		1991–2020	2021–2050	
	Obs	RCP 4.5	RCP 8.5	Obs	RCP 4.5	RCP 8.5
Lomé	837.77	810.57 (-3.25)	805.75 (-3.82)	28.12	28.27 (0.15)	29.35 (1.23)
M. Tove	983.34	942.81 (-4.12)	923.32 (-6.10)	26.77	27.12 (0.35)	28.43 (1.66)
Sanguera	1005.21	1075.7 (7.02)	1083.25 (7.76)	26.65	27.02(0.37)	27.78 (1.13)
Grid 1	995.08	979.29 (-1.59)	961.63 (-3.36)	26.65	27.07 (0.42)	28.41 (1.76)
Grid 2	1005.18	1009.8 (0.46)	993.31 (-1.18)	26.65	27.07 (0.42)	28.38 (1.73)
Grid 3	962.67	960.48 (-0.23)	946.00 (-1.73)	26.65	27.07 (0.42)	28.38 (1.73)
Grid 4	926.57	892.74 (-3.65)	877.96 (-5.25)	26.65	27.12 (0.47)	28.40 (1.74)
Grid 5	886.09	856.32 (-3.36)	836.76 (-5.57)	26.65	27.12 (0.47)	28.43 (1.78)
Grid 6	856.44	828.64 (-3.25)	810.18 (-5.40)	26.65	27.12 (0.47)	28.43 (1.78)
Grid 7	953.59	973.64 (2.10)	958.96 (0.56)	26.77	26.99 (0.21)	27.78 (1.00)
Grid 8	912.66	909.31 (-0.37)	896.35 (-1.79)	26.77	26.99 (0.21)	27.75 (0.98)
Grid 9	844.91	826.56 (-2.17)	809.05 (-4.25)	26.77	27.02 (0.24)	27.75 (0.98)
Grid 10	794.28	778.98 (-1.93)	761.59 (-4.12)	26.77	27.02 (0.24)	27.78 (1.01)
Grid 11	875.83	897.36 (2.46)	885.20 (1.07)	26.77	26.99 (0.21)	27.78 (1.00)
Grid 12	807.20	794.98 (-1.51)	779.43 (-3.44)	26.77	27.02 (0.24)	27.75 (0.98)
Grid 13	749.08	726.21(-3.05)	712.57 (-4.87)	26.77	27.02 (0.24)	27.78 (1.01)
Grid 14	697.57	665.26 (-4.63)	649.28 (-6.92)	26.77	27.02 (0.24)	27.78 (1.01)
Grid 15	763.86	710.73 (-6.95)	692.00 (-9.41)	26.77	27.02 (0.24)	27.78 (1.01)
Grid 16	775.48	746.04 (-3.80)	730.14 (-5.85)	26.77	27.02 (0.24)	27.78 (1.01)
AP	875.4	862.39 (-1.49)	848.03 (-3.13)	26.80	27.11 (0.31)	28.09 (1.29)

*Values in bracket are changes in rainfall and temperature expressed in % and °C, respectively.

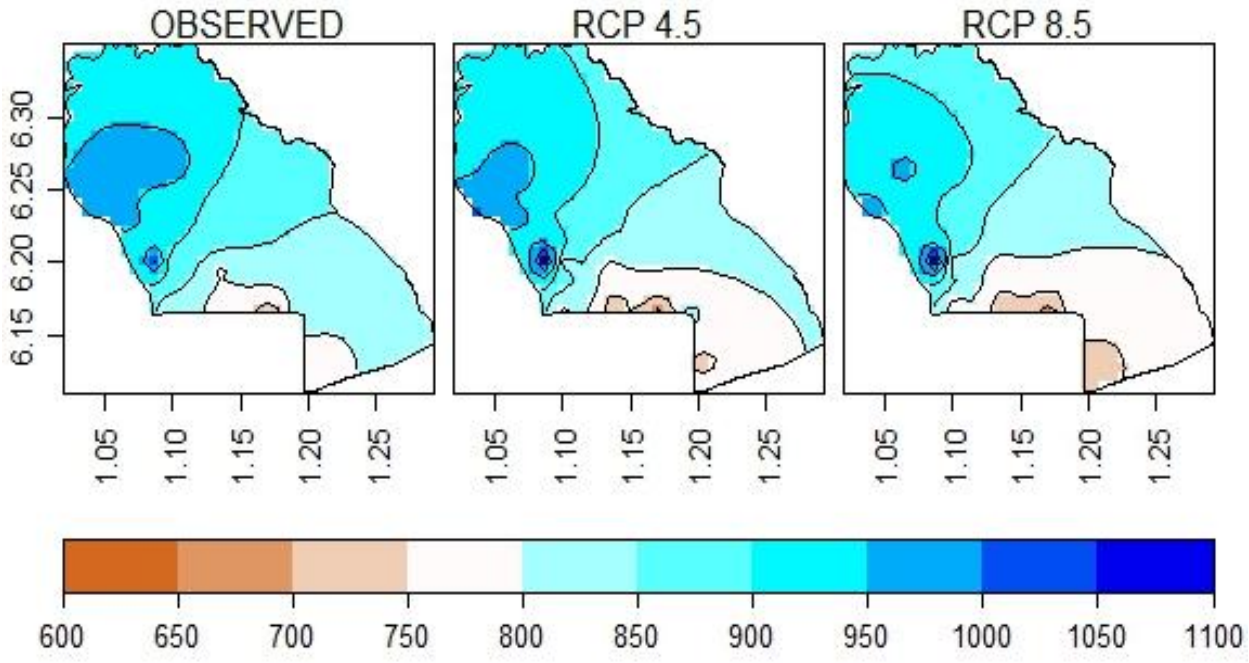

Figure 5.7a: Spatial Distribution of the Average Annual Rainfall (mm), AP

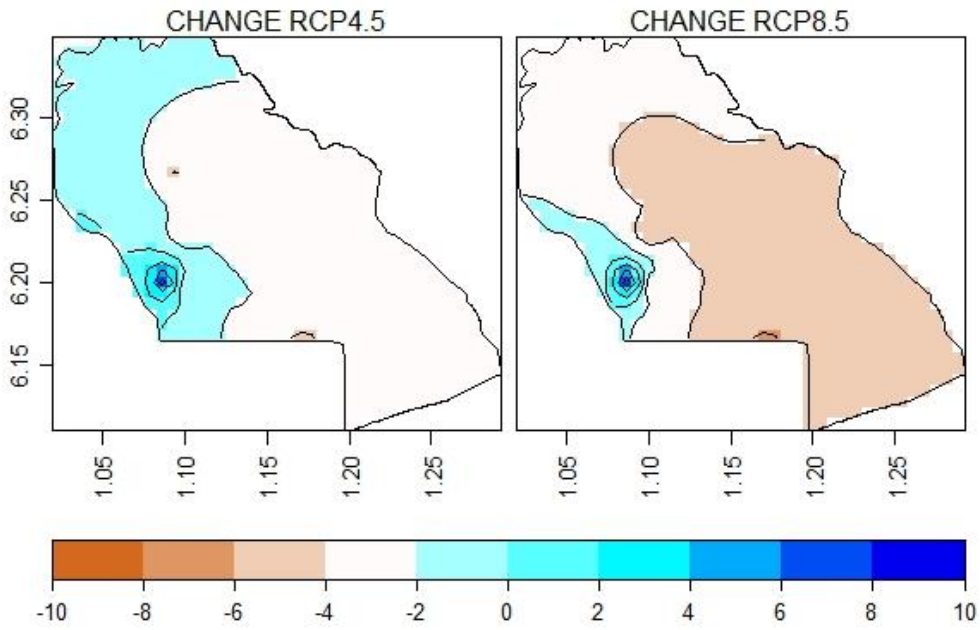

Figure 5.7b: Spatial Distribution of Projected Changes in the Annual Rainfall (%), AP

On the other hand, the average temperature is reported to range between 26.65 °C (Sanguera station and Grid 1–6) and 28.12 °C (Lomé) over the period 1991–2020 (Figure 5.8a and Table 5.8). The increase in temperature in the future (Table 5.8 and Figure 5.8b) over the AP is expected to range between 0.2 °C (Lomé and Grid 7–16) and 0.5 °C (Grid 4–6) under RCP 4.5. As for the RCP 8.5, the expected increase ranges between 1 °C (Lomé station, Sanguera station, Grid 7, and Grid 10–16) and 1.7 °C (Mission Tové station and Grid 1–6).

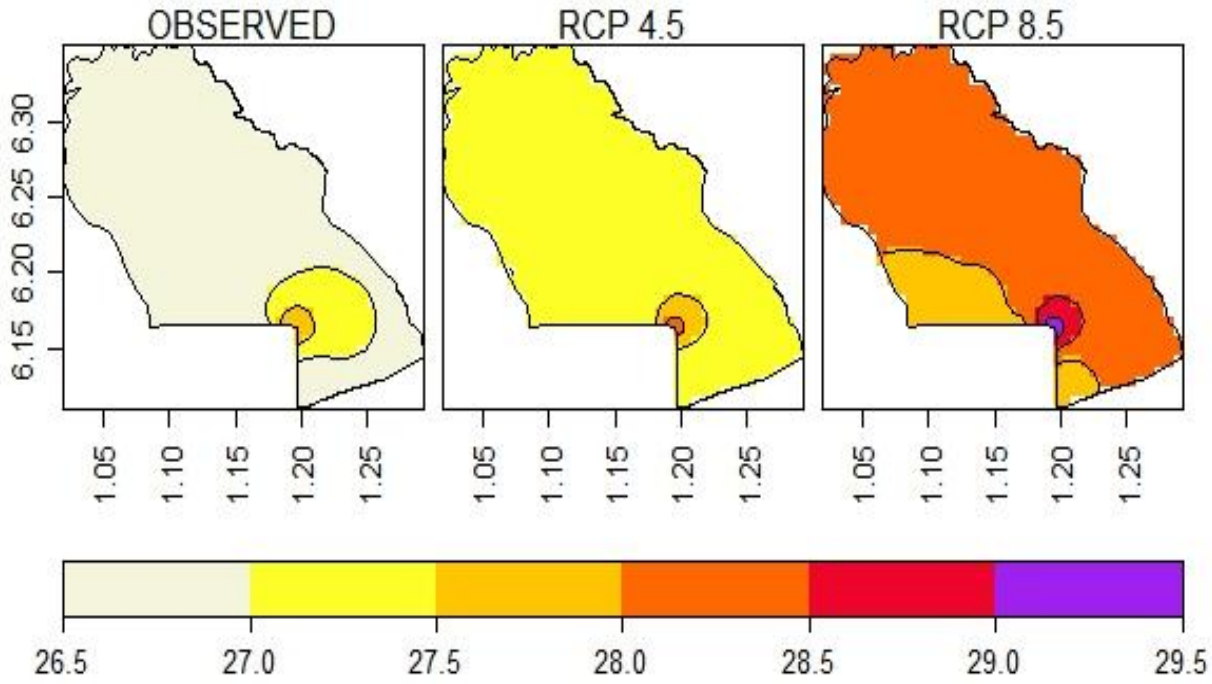

Figure 5.8a: Spatial Distribution of the Average Temperature (°C), AP

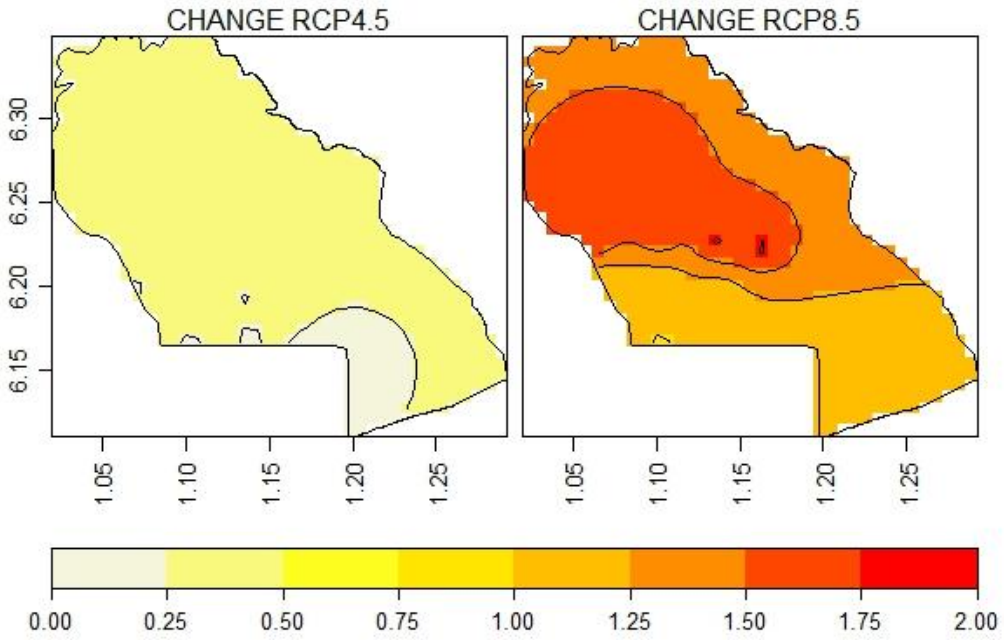

Figure 5.8b: Spatial Distribution of Projected Changes in the Average Temperature (°C), AP

5.4.3 Assessment of RCMs' Projective Performance

The uncertainties in the RCMs' projections (rainfall and temperature) are found to vary from one RCM to the other (Figures 5.9a-b).

These results confirm that RACMOT is the most reliable among the RCMs considered for both the projection of rainfall and temperature (rainfall: -22.75/-16.46% to 33.70/46.89% under RCP 4.5/RCP 8.5; temperature: 0.28/0.4 °C to 1.13/1.41 °C under RCP 4.5/RCP 8.5). Nevertheless, there is a need to highlight that the ensemble mean gives a comprehensive output with averaged uncertainties (rainfall: -23.34/-23.02% to 24.43/24.38% under RCP 4.5/RCP 8.5; temperature: -0.25/0.56 °C to 0.43/1.62 °C under RCP 4.5/RCP 8.5).

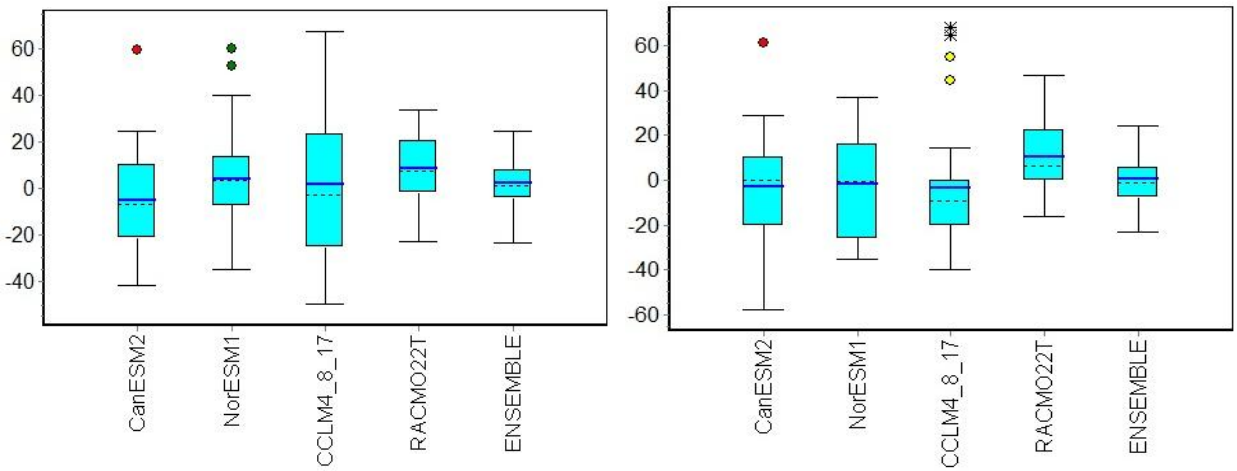

Figure 5.9a: Rainfall Projection Uncertainty Boxplot: RCP 4.5 (Left) and RCP 8.5 (Right)

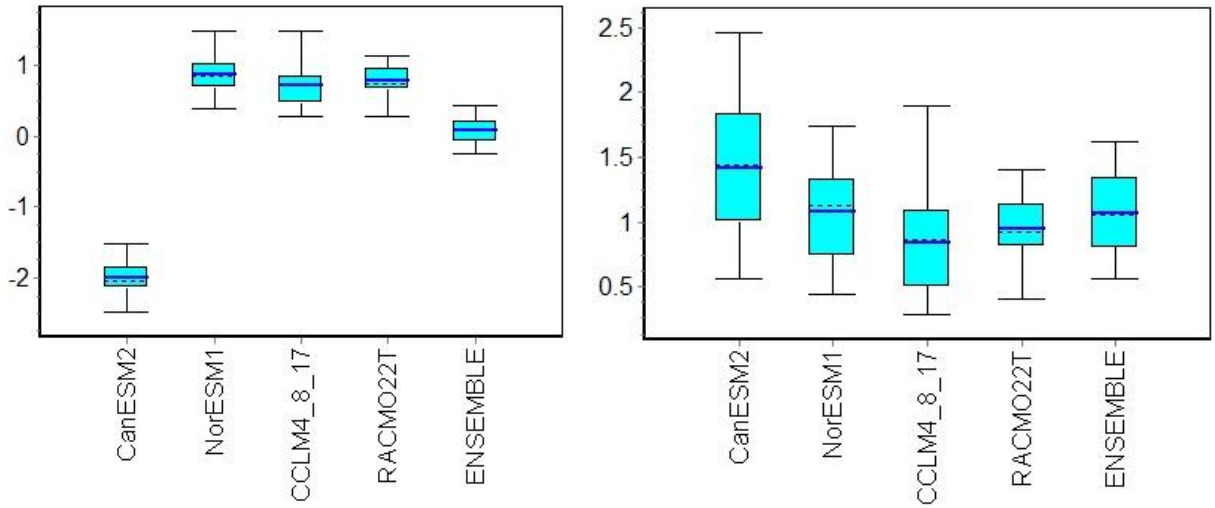

Figure 5.9b: Temperature Projection Uncertainty Boxplot: RCP 4.5 (Left) and RCP 8.5 (Right)

5.5 Discussion

To overcome challenges associated with the quality and quantity of existing climate time series as well as the adequate distribution of in situ observation stations for sound long-term time series analysis in the AP, satellite-based products, including rainfall and temperature datasets from CHIRPS and NASA POWER, respectively, were considered. These datasets were validated with the existing observations from the in-situ station for two-time frames, including 1991–2012 and 1991–2010 for the rainfall and the period of 1991–2012 for the temperature, depicting their ability to reproduce the climate of the AP. This result confirms the reported ability of the CHIRPS data in reproducing climate over West Africa, including the coastal settings (Larbi et al., 2018; Ogbu et al., 2020). On the other hand, the NASA POWER data also captured the climate of the AP with very low PBIAS and RMSE and high R^2, as reported in Brazil ($R^2 > 0.70$) with reasonable confidence for regional and national spatial scales (Monteiro et al., 2017).

Regional climate models' performance evaluation has shown that while some models underestimate climate variables, others overestimate them. Nevertheless, it is also observed that the ensemble mean gives a better and more reasonable result with low uncertainties as it captures all the limits of each individual model. Besides, the results of the comparison of the raw and the bias-corrected RCMs, either for rainfall or temperature, support the need for bias correction for a realistic projection of future climate or further climate impact studies, as highlighted in the literature (Teutschbein and Seibert, 2012).

Temperature trend analysis statistics for the period of 1991–2020 depicted a significant ($p < 0.05$) increase in the average temperature estimated at 0.02 °C (with a cumulative total of 0.6 °C over the period). The reported increasing trend in the AP confirms the findings of

Koudahe et al. (2017) and Houteta et al. (2020), who reported a significant warming trend for most of the stations in southern Togo (1970 to 2014) and over the Mono River basin (1961–2016). In addition, these results are in line with Padgham et al. (2015) and Daron's (2014) findings, reporting a warning ranging between 0.3 and 1 °C over West Africa (recent decades) and an increase ranging between 0.4 and 1.4 °C along the coastal regions of West Africa (1963 to 2012), respectively. Furthermore, Sylla et al. (2016) reported a decadal increase of 0.1 °C in the southern part of the Gulf of Guinea using data from UDEL, CRU, and ARC. Furthermore, the World Bank (2020) and Akpegnon (2021) findings reported a 0.5 °C increase in mean annual temperature at Lomé station over the period of 1979–2016 and a decadal increase of 0.4 °C at Lomé station considering the Zio River basin (south Togo) over the period of 1960–2019, respectively. In the future (2021–2050), in reference to the period of 1991-2020, AP is expected to undergo a decadal increase in temperature estimated at 0.1 °C and 0.2 °C under RCP 4.5 and RCP 8.5, respectively (with a cumulative total of 0.3/0.6 °C over the period, under the RCP 4.5/RCP 8.5). The increasing pattern in temperature expected under both RCPs over the AP agrees with the findings of MERF/TNC (2015) using SimCLIM2013 and Patchali et al. (2020) using the HadGEM and NorESM models (2031–2060). The Togolese Third National Communication on Climate Change (TNC) projected an increase ranging between 1.6 and 1.8 °C by 2050 under the RCP 8.5 in reference to the period of 1986–2005. Patchali et al. (2020) also reported an expected increase in temperature of 3.6 °C at Lomé station (2031–2060). In all, there is a need to highlight the convergence in the trend's nature but also the divergence in the magnitude of the change across these studies.

On the other hand, rainfall trend analysis statistics for the period of 1991–2020 show a non-significant ($p > 0.05$) increase in rainfall over the AP (almost all the stations) estimated annually at 0.81 mm annually (with a cumulative total of 24.3 mm over the period). These results confirm the findings from Akinsanola and Ogunjobi (2015a) and the World Bank (2020), unveiling an increasing trend in rainfall over the vast majority of Nigeria (over the period of 1971–2000) and Lomé (estimated at 0.3 mm annually for the period of 1979–2016), respectively. Nevertheless, some other parts of West Africa are expected to experience quite different trends in rainfall. These studies include Djaman et al. (2017) and Houteta et al. (2020), which respectively reported a decrease in annual precipitation in the maritime region and a non-significant decreasing trend in rainfall over the Mono River Basin (1961–2016). In the future (2021–2050), the expected non-significant ($p > 0.05$) changes in rainfall (slight increase estimated at 0.05/1.5 mm annually/cumulative under the RCP 4.5 against a decrease in rainfall

estimated at 0.69/20.7 mm annually/cumulative under RCP 8.5) over the study area support some of the findings obtained in West Africa but also in southern Togo. Sylla et al. (2016) reported that Togo is expected to experience a change in precipitation ranging between -5 and 5% for both RCP 4.5 and RCP 8.5 over the period of 2036–2065 and 2071–2100. In addition, Larbi et al. (2022) found a non-significant increase of 0.5% under RCP 4.5 and a decrease of 3.2% under the RCP 8.5 scenario in the Tano river basin (2021–2050 in reference to the period of 1986–2015). Furthermore, the TNC has reported an expected decrease in rainfall of 3% in the southern part of the country by 2050 in reference to the period of 1971–2000 (MERF/TNC, 2015). The divergence observed in both the nature (increasing or decreasing) and magnitude of change for both temperature and rainfall, both in the past and the future, can be attributed to the divergence in time series temporal and spatial resolution but also the RCMs considered. As an example, when it comes to rainfall, several research works in West Africa depicted a decreasing trend in rainfall since the 1970s (Yao et al., 2018; Servat et al., 1998), which was later reported to have resumed since the 1990s (Amoussou et al., 2015), though these latter precipitation events are recognized to be less compared to the precipitation observed during the pre-drought period. Finally, contrary to the decreasing pattern for most of the seasons, the small dry season (August) is expected to experience an increase in rainfall. This situation can be attributed to an expected occurrence of a punctual or single intense rainfall event, which may be the result of climate change (USAID, 2018) or the forcing of rainfall from the extra tropics, as experienced in 2004 by some countries in West Africa, including Togo (Knippertz and Fink, 2008).

While the temporal datasets projected the magnitude changes (long-term decrease in rainfall against increase in average temperature), the spatial datasets provided the direction of the observed changes. The highest increase in temperature is expected in the northern and northeastern parts of the study area. As for the annual rainfall, the highest decrease in the parameter is expected in the southern and central parts of the study area under both scenarios.

These current and future changes will probably have huge impacts on natural resources, ecosystems, and activities, especially those that are climate-dependent, and will potentially lead to human insecurity. So, the obtained results can serve as inputs to biophysical models (i.e., groundwater lens response to climate change and land use and land cover) for: (i) a sound formulation and implementation of the national and local climate change adaptation and mitigation measures as regards the degradation of coastal environments (especially the Togolese Coastal National Action Plan for development and adaptation to climate change); and

(ii) the attainment and monitoring of the United Nations' sustainable development goals (especially the SDGs 3, 6, and 13).

5.6 Partial Conclusion

This study sought to identify and quantify long-term changes, the trend, and future projections of climate variables (rainfall and temperature), considering historical climate time series (CHIRPS, NASA POWER, and in situ observation station datasets), RCMs outputs (CanESM2-RCA4, NorESM1-RCA4, RACMO22T, CCLM4-8-17, and the ensemble mean based on the Representative Concentration Pathways 4.5 and 8.5). To achieve the set objective, the Mann-Kendall test and the Modified Mann-Kendall test (along with the Sen' slope test) were considered for the trend analysis while the basis statistics were the long-term change analysis. The results revealed:

- Historical trend (1991–2020): A non-significant ($p > 0.05$) increasing trend in rainfall (estimated at 0.81 mm annually) against a significant ($p < 0.05$) increasing trend in temperature (with an annual warming rate of 0.02 °C) is observed in the AP.
- Future projections (2021–2050): In reference to the period of 1991-2020, the ensemble mean depicts an expected non-significant ($p > 0.05$) increasing trend in annual rainfall (accounting for 0.05 mm annually) under the RCP 4.5 against a decreasing trend (accounting for 0.69 mm annually) under RCP 8.5. As for the average temperature, the ensemble mean depicts an expected increasing trend, accounting for 0.01 °C and 0.02 °C annually under the RCP 4.5 and RCP 8.5, respectively.
- Long-term change in temperature and rainfall: Considering the period of 1991–2020 as a baseline, a non-significant ($p > 0.05$) decrease in the annual rainfall estimated at 1.49/3.13% under the RCP 4.5/RCP 8.5 against a significant ($p < 0.05$) increase in the average temperature estimated at 0.31/1.29 °C under the RCP 4.5/RCP 8.5 is expected over the period of 2021–2050.

CHAPTER SIX: CHARACTERISATION OF THE MULTI-LAYERED AQUIFER IN THE AP: PHYSICO-CHEMICAL, ISOTOPIC OF GROUNDWATER AND HYDRAULIC HEAD AND SUB-SURFACE TRUE RESISTIVITY DISTRIBUTION

The overall purpose of this chapter is to understand the processes governing the mineralisation of existing aquifers in the AP, identify the most affected aquifers by the SWI, and define the position and geometry of the seawater-freshwater interface, if any. It gives the physicochemical and isotopic characteristics of water samples from various aquifers considered in the AP, including the MaS aquifer, CT aquifer, Pa aquifer, and Ma aquifer. In addition, the hydraulic heads of these aquifers and the true resistivity value of the sub-surface of these formations. At the end, the resulting data (salinity and hydraulic heads) were used as inputs for the calibration and validation of the SEAWAT model (Chapter seven).

6.1 Physicochemical Characterisation of Groundwater

6.1.1 Major Ions Contributing to the Salinity of Waters in the AP

This is based on the results of the Principal Components Analysis (PCA) and the plots of major cations (Ca^{2+}, Mg^{2+}, K^{+}, and Na^{+}) and anions ($HCO3^{-}$, $SO4^{2-}$, Cl^{-}, and $NO3^{-}$) against the sum of the cations (Σcations) and anions (Σanions).

Table 6.1a-b depicts the characteristics of water samples based on the PCA. The CT aquifer is characterised by parameters such as Ca^{2+}, Mg^{2+}, Na^{+}, Cl^{-}, and $SO4^{2-}$ (with their linear combination represented by dimension 1 and contributing at 61% of the total variance), K^{+}, and $HCO3^{-}$ (with their linear combination represented by dimension 2 and contributing at 17% of the total variance). For the MaS aquifer, parameters such as Ca^{2+}, Mg^{2+}, Na^{+}, Cl^{-}, $SO4^{2-}$, and K^{+} (with their linear combination represented by dimension 1 and contributing at 84% of the total variance), $HCO3^{-}$ (with their linear combination represented by dimension 2 and contributing at 15% of the total variance), and $NO3^{-}$ (with their linear combination represented by dimension 3 and contributing at 10% of the total variance) are the major ions. For the Pa aquifer, parameters such as Na^{+}, Cl^{-}, and K^{+} (with their linear combination represented by dimension 1 and contributing at 54% of the total variance) and $HCO3^{-}$ and $NO3^{-}$ (with their linear combination represented by dimension 2 and contributing at 25% of the total variance) are key to characterising this aquifer. Finally, parameters such as Ca^{2+}, Mg^{2+}, Na^{+}, K^{+}, Cl^{-}, $HCO3^{-}$, and $NO3^{-}$ (with their linear combination represented by dimension 1 and a contribution of 65% of the total variance) define the mineralisation level of the Ma aquifer.

Table 6.1a: PCA Characteristics for the RS (DS)

PCA characteristics	CT			Pa			Ma		MaS
	Dim.1	Dim.2	Dim.3	Dim.1	Dim.2	Dim.3	Dim.1	Dim.2	Dim.1
Eigenvalue	5.3 (6.2)	1.8 (1.5)	0.9 (1.1)	3.9 (6.4)	2.7 (2.1)	1.7 (1.2)	7.2 (5)	1.8 (3.2)	6.4 (17.6)
Percentage of variance	59.4 (62.1)	19.9 (14.7)	10.4 (11.4)	43.1 (64.1)	29.5 (20.8)	18.7 (11.7)	80.1 (49.9)	19.9 (32.2)	70.9 (97.9)
Cumulative % of variance	59.4 (62.1)	79.2 (76.8)	89.6 (88.3)	43.1 (64.1)	72.5 (85)	91.2 (96.7)	80.1 (49.9)	100 (82)	70.9 (97.9)

NB: Values in parentheses stand for the DS.

Table 6.1b: Correlation between Dimensions and Major Parameters

Parameters	CT			Pa			Ma		MaS
	Dim.1	Dim.2	Dim.3	Dim.1	Dim.2	Dim.3	Dim.1	Dim.2	Dim.1
c25°C	0.921 (0.933)	0.011 (0.021)	0.003 (0)	0.822 (0.957)	0.013 (0.015)	0.003 (0)	0.999 (0.913)	0.001 (0.02)	0.937 (0.984)
Ca^{2+}	0.729 (0.792)	0.121 (0.001)	0 (0.077)	0.276 (0.703)	0.035 (0.008)	0.560 (0.185)	0.949 (0.070)	0.051 (0.694)	0.832 (0.196)
Mg^{2+}	0.542 (0.849)	0.318 (0.010)	0.023 (0.059)	0.178 (0.925)	0.193 (0.007)	0.494 (0.008)	0.739 (0.850)	0.261 (0.009)	0.947 (0.797)
Na^{+}	0.858 (0.849)	0.041 (0.028)	0.004 (0.026)	0.866 (0.816)	0.025 (0.003)	0.079 (0.150)	0.792 (0.946)	0.208 (0.026)	0.885 (0.943)
K^{+}	0.425 (0.193)	0.455 (0.607)	0.065 (0.117)	0.720 (0.003)	0.025 (0.316)	0.174 (0.645)	0.811 (0.108)	0.189 (0.596)	0.504 (0.475)
$HCO3^{-}$	0.380 (0.164)	0.567 (0.680)	0.003 (0.023)	0.018 (0.196)	0.874 (0.736)	0.077 (0.044)	0.731 (0.007)	0.269 (0.968)	0.330 (0.225)
Cl^{-}	0.847 (0.895)	0.058 (0.047)	0.048 (0.033)	0.857 (0.881)	0.064 (0.049)	0.049 (0.061)	0.982 (0.843)	0.018 (0.102)	0.914 (0.881)
$SO4^{2-}$	0.598 (0.546)	0.062 (0.004)	0.003 (0.139)	0.100 (0.942)	0.607 (0.010)	0.241 (0.034)	0.607 (0.076)	0.393 (0.006)	0.932 (0.750)
$NO3^{-}$	0.042 (0.011)	0.156 (0.064)	0.786 (0.666)	0.038 (0.003)	0.816 (0.939)	0.007 (0.037)	0.601 (0.579)	0.399 (0.398)	0.103 (0.187)

NB: Values in parentheses stand for the DS.

Figures 6.1a-d, Figures 6.2a-d, and Annex 2a-b depict the correlation between major ions and the sum of cations and the sum of anions. A good correlation between cations such as Na^+, Ca^{2+}, and Mg^{2+} with the sum of cations and anions such as Cl^- and $SO4^{2-}$ with the sum of anions for the CT aquifer and the MaS aquifer has been observed. For the Ma aquifer, cations such as Na^+, Ca^{2+}, Mg^{2+}, and K^+ with the sum of cations and anions such as Cl^- and $HCO3^-$ with the sum of anions depict high correlation. Finally, the correlation between cations such as Na^+ and K^+ and the sum of cations and between anions such as Cl^- and the sum of anions is also found to be considerable for the Pa aquifer. Nevertheless, while considering the EC, it can be inferred that the main contributors to the mineralisation of waters in the AP are Na^+ and Cl^- for the CT aquifer and Pa aquifer, while Ca^{2+} and Cl^- account for the Ma aquifer. Finally, Mg^{2+}, Cl^-, and $SO4^{2-}$ are the main contributors to salinity in the MaS aquifer. Furthermore, though in general, a very bad correlation between the $NO3^-$ and the sum of anions is observed for all the aquifers, a rapid increase of the ions with a slight change in the sum of anions has been observed for the CT and MaS aquifers. This result suggests an anthropic source.

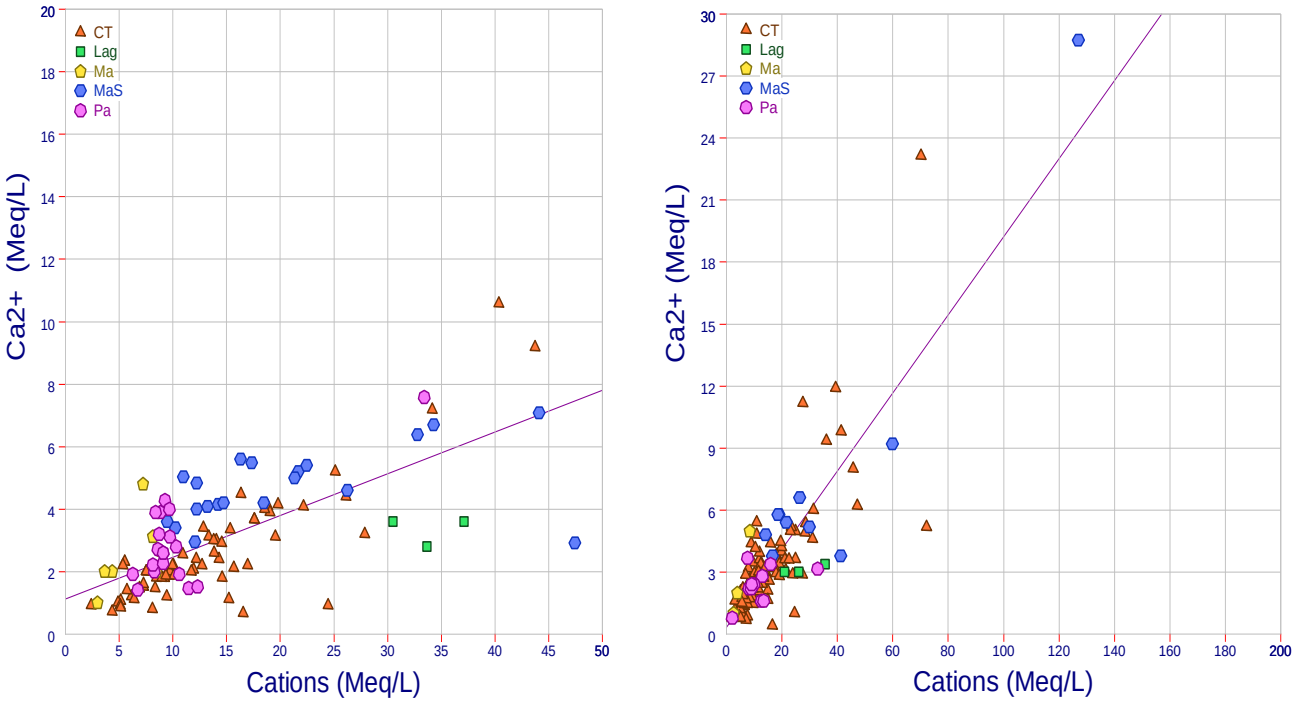

Figure 6.1a: Ca-ΣCations for the DS (Left) and the RS (Right)

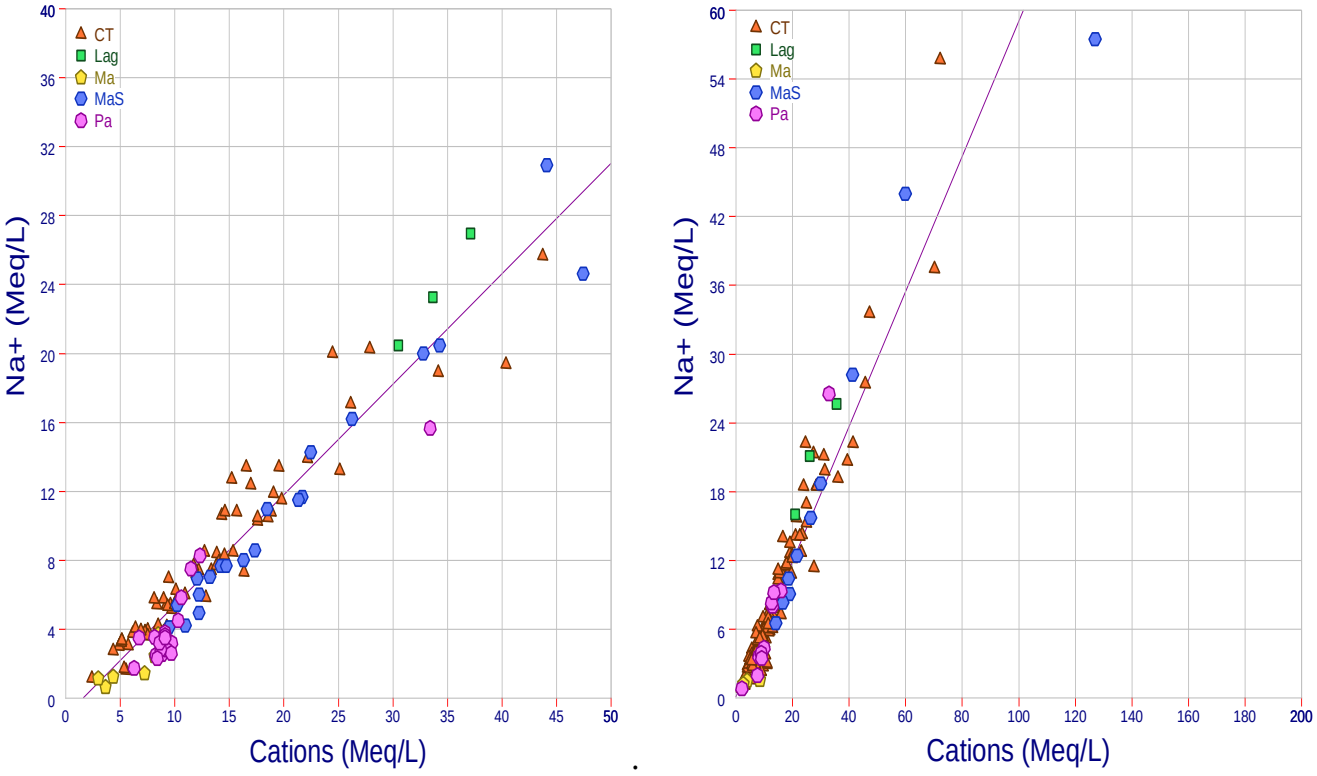

Figure 6.1b: Na-ΣCations for the DS (Left) and the RS (Right)

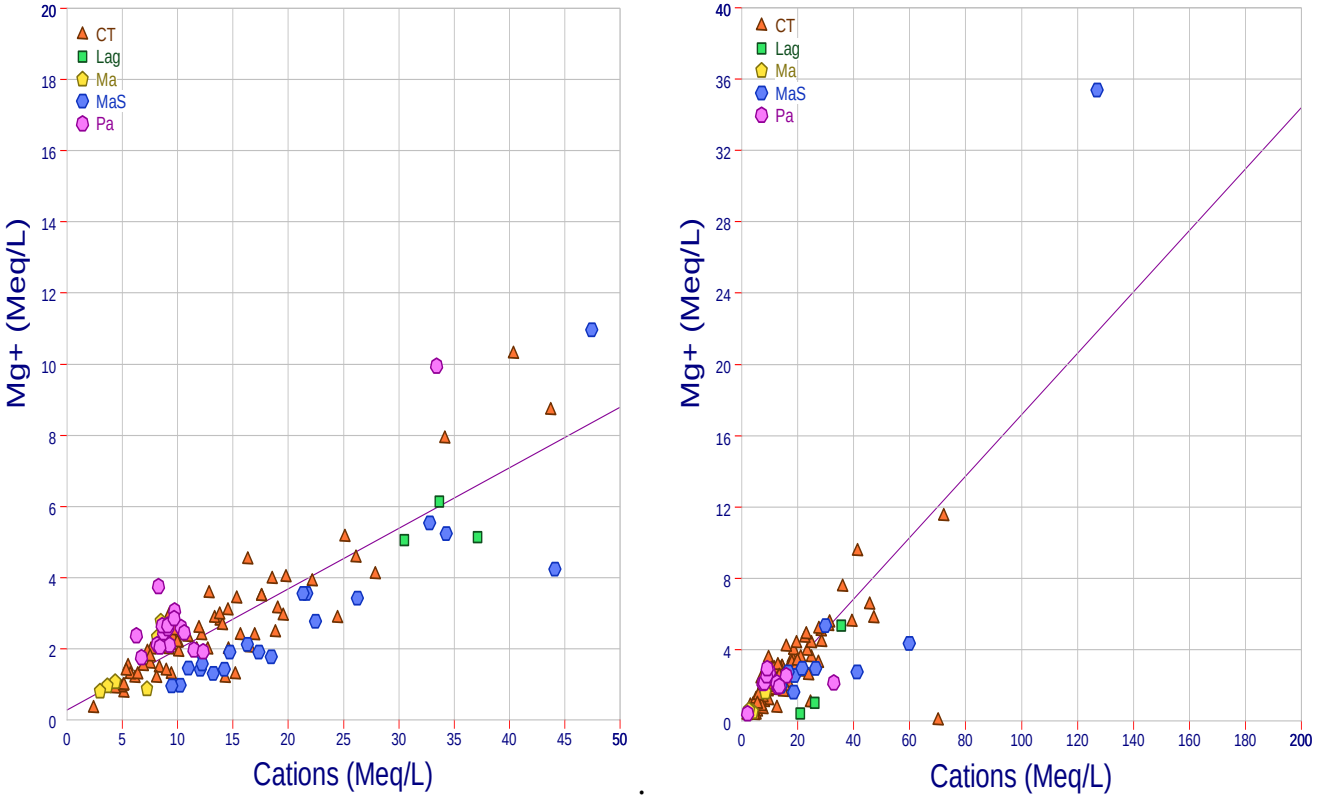

Figure 6.1c: Mg-ΣCations for the DS (Left) and the RS (Right)

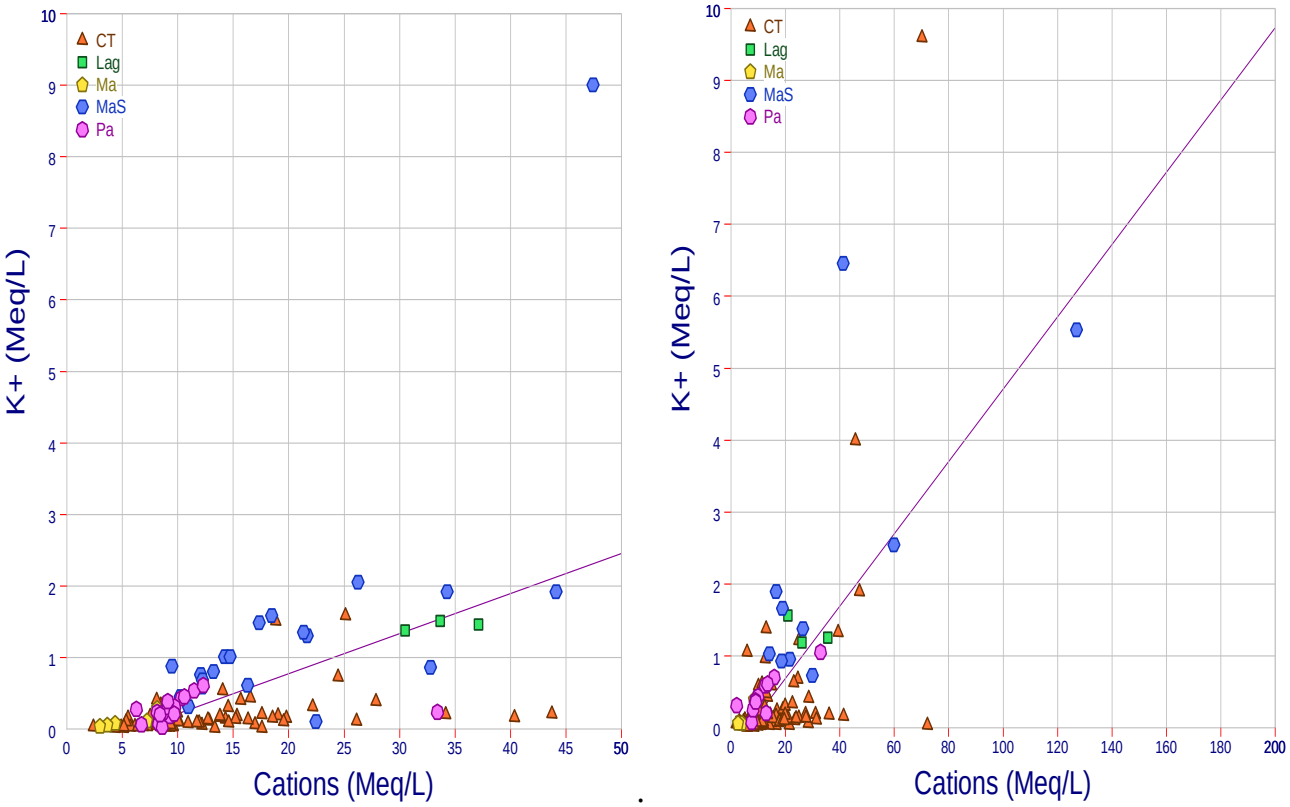

Figure 6.1d: K-ΣCations for the DS (Left) and the RS (Right)

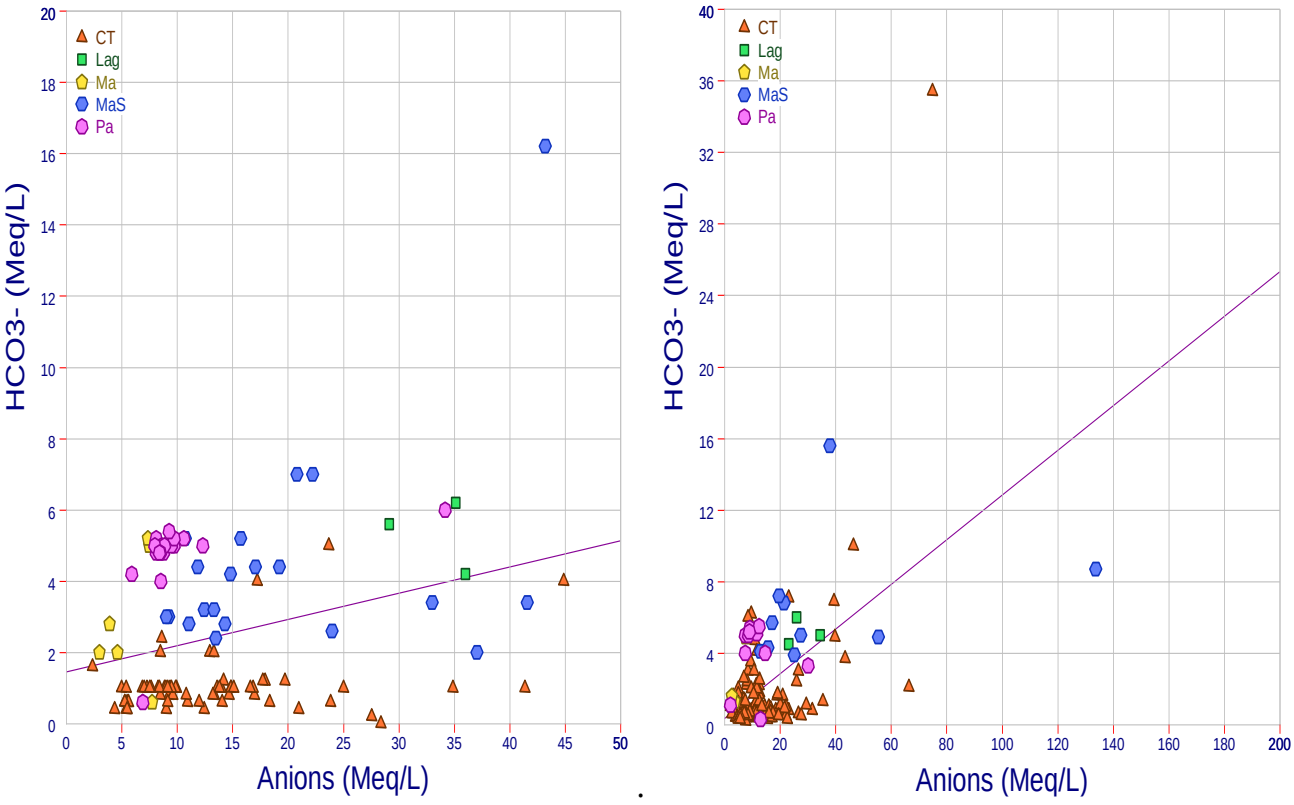

Figure 6.2a: HCO3-ΣAnions for the DS (Left) and the RS (Right)

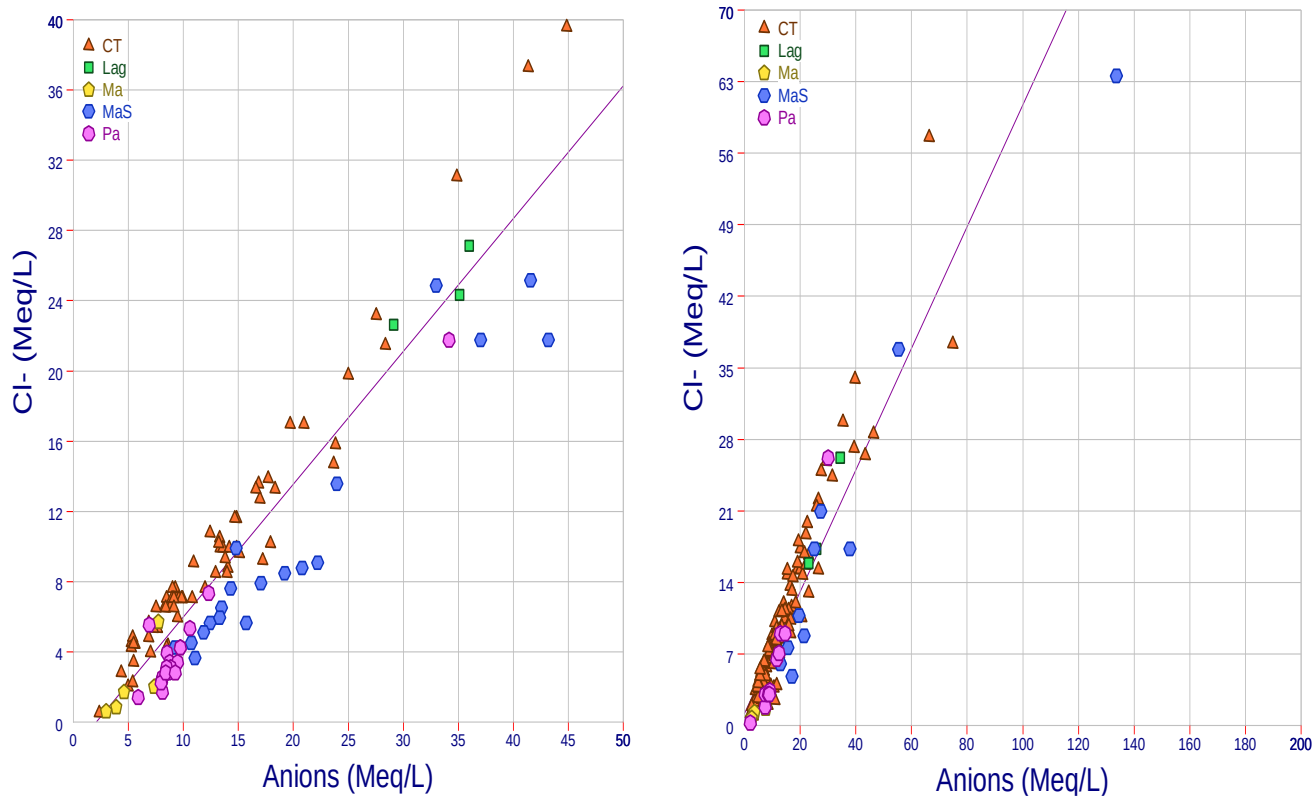

Figure 6.2b: Cl-ΣAnions for the DS (Left) and the RS (Right)

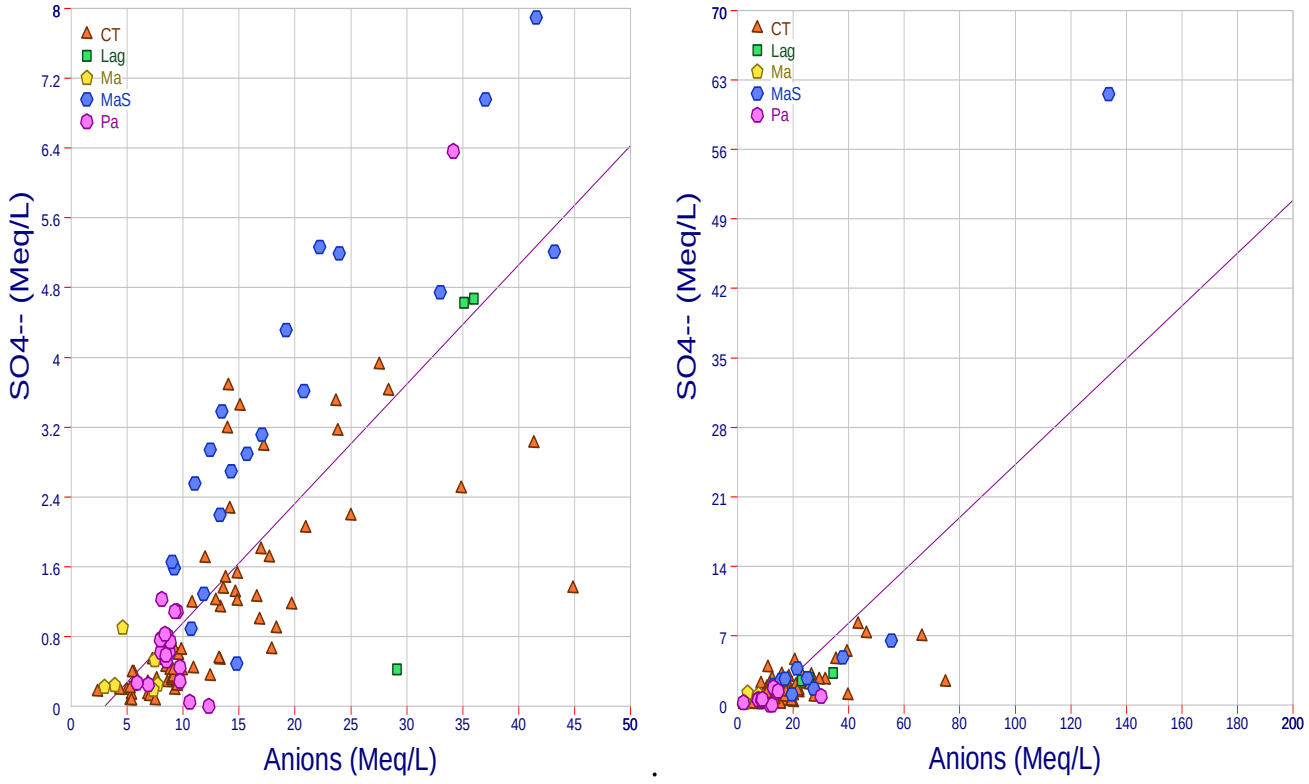

Figure 6.2c: SO4-ΣAnions for the DS (Left) and the RS (Right)

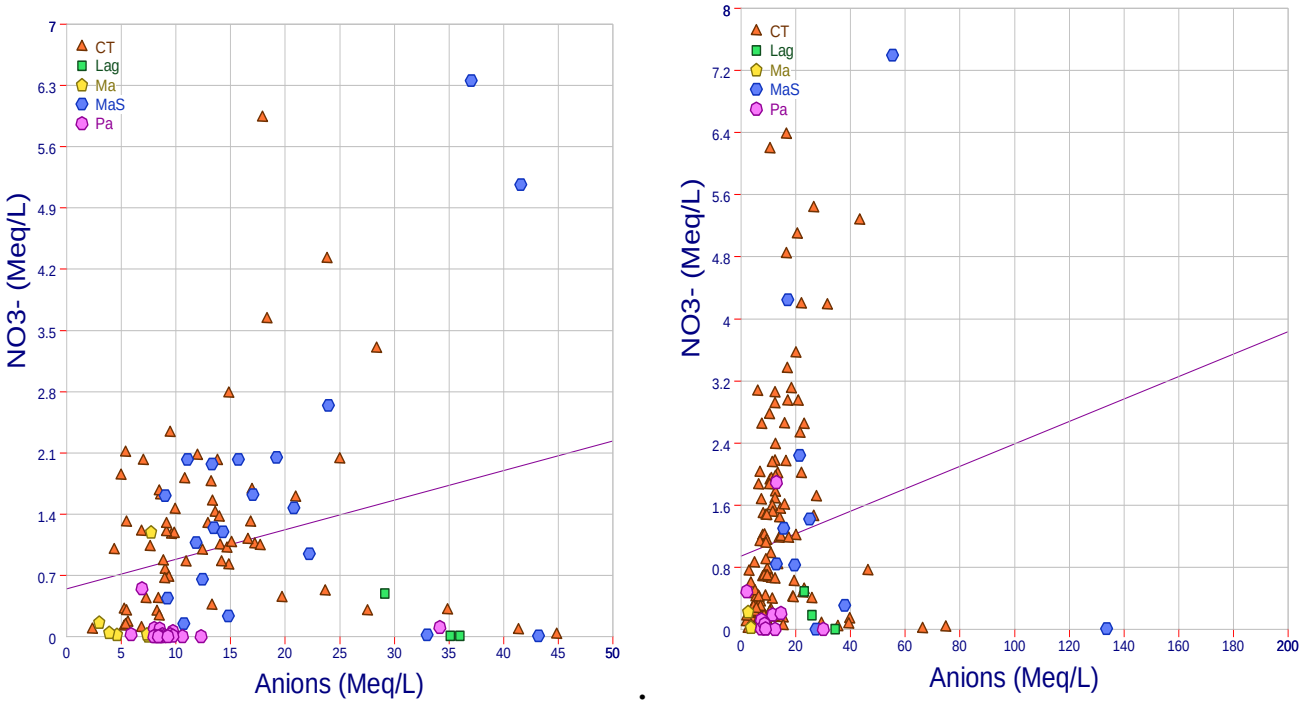

Figure 6.2d: NO3-ΣAnions for the DS (Left) and the RS (Right)

6.1.2 Temporal and Spatial Distribution of Key Parameters

Table 6.2 depicts the temporal evolution of various physicochemical parameters, while Figures 6.3a–6.3h show the spatial distribution of some key physicochemical parameters of the considered aquifers in the AP for the DS and RS. These parameters include the EC, TDS, as well as the main ions contributing to the mineralisation of the existing aquifers, including Ca^{2+}, Na^{+}, Mg^{2+}, Cl^{-}, $SO4^{2-}$, and $NO3^{-}$ (see section 6.1.1).

Though showing a southward increasing trend for all the aquifers, the EC in AP is observed to be high for the CT and MaS aquifers. The average values range, respectively, between 1480/1379 and 4853/1974 $\mu S.cm^{-1}$ for the CT aquifer (with the highest values found around Ahanoukopé, Attiegou, and Cacaveli) and the MaS aquifer (with high values found around Ahanoukopé located at a distance of 2.5 km from the ocean) for the RS/DS.

For the distribution of the TDS, no particular pattern is shown for all the aquifers and for the two seasons. Nevertheless, as the EC, the TDS values pin out the CT aquifer and the MaS aquifer to be characterised by the high values. Areas such as Attiegou (3049 $mg.L^{-1}$), Klikamé (4020 $mg.L^{-1}$), Gbadago, Kodomé (5291 $mg.L^{-1}$), and Cacaveli (3000 $mg.L^{-1}$) have been pinpointed as salinity hotspots for the CT aquifer. For the MaS aquifer, areas such as Gbadago (3717 $mg.L^{-1}$) and Ahanoukopé (8280 $mg.L^{-1}$) are counted as hotspots.

When it comes to the spatial distribution of the major cations, water samples from aquifers considered showed a southward (towards the ocean) increasing pattern of the sodium

ion (Na^+). For the CT aquifer and MaS aquifer, the Na^+ concentration is found to be very high in the Ahanoukopé area, suggesting seawater intrusion. In addition, the quite high values observed around areas such as Attiegou, Cacaveli, and Klikamé suggest plausible seawater intrusion through up coning. This inference is due to the distance of these areas from the ocean, which suggests a lateral intrusion. Another source of the Na^+ supply to the CT aquifer can be the cationic exchange with the matrix of the clayey roof of the aquifer. When it comes to the Pa aquifer, the high Na^+ content can be related to the supply from the CT aquifer. As a matter of fact, it has been reported that the CT aquifer recharges the aquifer in areas where it lies directly on the undifferentiated limestone (Akakpo, 2017). The obtained results for the Pa aquifer are in line with Akakpo's (2017) findings, who also reported a southwardly increasing pattern of sodium. Contrary to the three other aquifers, water samples from the Ma aquifer, all located in the northern part of the study area, depict low values (< 200 $mg.L^{-1}$). For magnesium ion (Mg^{2+}), though no particular spatial pattern is shown for all the aquifers, values beyond the guidelines are observed for the MaS aquifer. The highest values for this aquifer are observed around the Ahanoukopé area. Just as with Mg^{2+}, the spatial distribution of the calcium ion (Ca^{2+}) shows no particular pattern for all aquifers. Nevertheless, it has been observed that the CT aquifer and Pa aquifer depict high values. High concentrations of the ion are found in water samples from Agoè Télessou, Cacaveli, Attiegou, and Kegué for the CT aquifer, while water samples from Agoè Zongo stand for the Pa aquifer.

For the anions, though limited water points were sampled in the southern part of the study, the distribution of the chloride ion (Cl^-) across the entire area shows no particular pattern. Nevertheless, water samples from the CT aquifer (Ahanoukopé, Attiegou, and Cacaveli) and the MaS aquifer (Ahanoukopé) located in the central part and the southern part of the study area are found to record the highest values. The high concentration of the ion suggests pollution through sewage, brackish water, or seawater. For the sulphate ion ($SO4^{2-}$), no particular pattern can be observed for all the aquifers considered. High values are observed with water samples from the CT aquifer and MaS aquifer located in the southern part of the plateau (Kegué, Ahanoukopé, and Klikamé). The location of these hotspots corresponds to a highly urbanised part of the study area, suggesting pollution through sewage. Just as for the Cl^- and the $SO4^{2-}$, high values of nitrates ($NO3^-$) are observed for the CT aquifer and the MaS aquifer. Due to their unconfined and shallow nature, the potential source of this ion might be agricultural activities, as the area serves as the main source for the provision of vegetables and staple foods.

Table 6.2: Statistical Characteristics of the Ground and Surface Waters during RS (DS): April–July 2021 and February–March 2022

Parameters	WHO /EU	CT (n = 130/66)				Ma (n = 3/6)				MaS (n = 11/20)				Pa (n = 11/19)				Lag (n = 3)				Ocean
		Min	Max	Avg	St. Dev	Min	Max	Avg	St. Dev	Min	Max	Avg	St. Dev	Min	Max	Avg	St. Dev	Min	Max	Avg	St. Dev	-
TDS (mg.L^{-1})	500	149 (178)	3049 (2499)	795 (819.9)	541.1 (481.2)	204 (222)	584 (556)	351.7 (400.5)	203.66 (145.6)	925 (658)	10884 (3119)	3209 (1352)	3304.3 (708.1)	174 (412)	1912 (2091)	782.3 (698)	432.6 (351)	1476 (1851)	2159 (2273)	1785 (2097)	346.11 (219.5)	32300 (37212)
T (°C)	-	27.4 (25)	33.5 (32)	31.1 (28.98)	1.18 (1.7)	31 (28)	32.6 (29.9)	31.67 (28.77)	0.83 (0.73)	30 (28)	32.5 (31.5)	30.9 (30)	0.68 (0.81)	27.4 (27)	33.6 (32)	30.79 (29)	1.85 (1.35)	31.2 (30)	31.9 (30.4)	31.5 (30.2)	0.38 (0.2)	31 (29.8)
pH	6.5-8.5	4.78 (5.1)	7.1 (8.4)	5.67 (6.09)	0.52 (0.64)	6 (6)	6.68 (7.99)	6.27 (7)	0.36 (0.76)	4.98 (6.5)	7.6 (8.3)	6.5 (7.48)	1.01 (0.48)	5.23 (6.2)	7.59 (8.21)	6.85 (7.6)	0.86 (0.43)	7.98 (8.42)	9.2 (9.17)	8.56 (8.92)	0.61 (0.43)	8.04 (8.65)
c25°C (µS.cm^{-1})	500	198 (8.4)	6890 (4490)	1480 (1379)	1117 (888.8)	273 (270)	807 (934)	528 (554.7)	267.81 (264.2)	1405 (920)	15280 (4270)	4853 (1974)	4345.6 (1053)	221 (552)	3290 (3340)	1293 (972)	891.2 (592)	2530 (3200)	3610 (3590)	2973 (3417)	565.36 (198.6)	52800 (51900)
Ca++ (mg.L^{-1})	75	8 (14)	464 (212)	59.8 (51.81)	53.55 (35.69)	20 (20)	100 (96)	53.33 (49.73)	41.63 (26.34)	76 (58)	576 (142)	184 (94.9)	166.27 (23.28)	16 (29)	73.6 (152)	47.71 (58)	17.08 (28.8)	60 (56)	68 (72)	62.7 (66.7)	4.62 (9.24)	384 (440)
Mg++ (mg.L^{-1})	150	0 (3.8)	139 (125)	29 (31.53)	20.82 (21.09)	6.24 (9.6)	19.2 (33.6)	10.88 (17.76)	7.22 (10.42)	19.2 (12)	559.2 (133)	120 (35.2)	187.78 (28.29)	4.8 (21)	36 (121)	26.23 (35)	8.21 (21.6)	4.8 (61.4)	64.8 (74.4)	27.2 (66.1)	32.76 (7.22)	1209.6 (2064)
Na+ (mg.L^{-1})	200	18.6 (26)	1280 (590)	191 (183.8)	174.9 (118.2)	27.2 (15)	36 (85)	32.73 (40.8)	4.82 (25.47)	150 (94)	2520 (710)	669 (265)	718.4 (170)	19.6 (41)	610 (360)	166.2 (101)	162.3 (73.9)	368 (470)	590 (620)	481 (542)	111.05 (75.22)	9100 (9500)
K+ (mg.L^{-1})	12	0.5 (0.3)	375 (62)	12 (7.09)	37.12 (10.91)	2.2 (1.7)	15 (11.4)	6.57 (4.08)	7.31 (3.71)	28.4 (4)	252 (352)	96.3 (56.1)	77.84 (72.85)	2.7 (0.8)	41 (24)	17.57 (11)	10.68 (6.17)	46.5 (54)	61 (59)	52.2 (56.7)	7.75 (2.52)	320 (425)
HCO3^{-} (mg.L^{-1})	-	12.2 (0)	2159 (305)	100 (65.06)	204.3 (50.79)	79.3 (37)	299 (317.2)	158.6 (178.9)	121.85 (111.2)	238 (122)	951.6 (988)	430 (274)	220.62 (188.2)	18.3 (37)	336 (366)	243.5 (289)	108.2 (66.1)	274.5 (256)	366 (378)	315 (325)	46.59 (62.61)	170.8 (183)
Cl^{-} (mg.L^{-1})	250	13 (18)	2037 (1402)	346 (352)	297.4 (260)	25.03 (22)	60.1 (202.2)	43.38 (75.75)	17.57 (65.24)	170 (100)	3754 (891)	965 (359)	1109 (257)	10.01 (50)	926 (771)	233.8 (157)	251.4 (157)	560.6 (801)	926 (961)	699 (874)	198.1 (80.92)	18420.2 (22925)
SO4^{-}(mg.L^{-1})	400	1.51 (2.7)	389 (188)	52.5 (53.35)	71.99 (52.36)	10.78 (9.3)	57.6 (43.25)	40.29 (18.63)	25.69 (13.41)	49.4 (23)	2954 (379)	639 (165)	1098.2 (94.92)	0 (0)	82.8 (305)	30.29 (44)	25.66 (65.4)	116.4 (20.2)	156 (224)	134 (156)	20.03 (117.2)	2695.1 (1675)
NO3^{-}(mg.L^{-1})	50	0 (0.8)	436 (367)	78.9 (75.15)	90.54 (64.96)	1.25 (0)	13.7 (73.92)	5.87 (14.78)	6.79 (29.18)	0.14 (0.7)	458.4 (394)	105 (102)	140.15 (99.79)	0 (0)	117 (34.3)	16.89 (3.2)	34.5 (7.83)	0.1 (0.45)	30.6 (30.3)	13.9 (10.5)	15.43 (17.2)	0 (0)

*****EU and WHO stand for European Union and World Health Organisation, respectively.

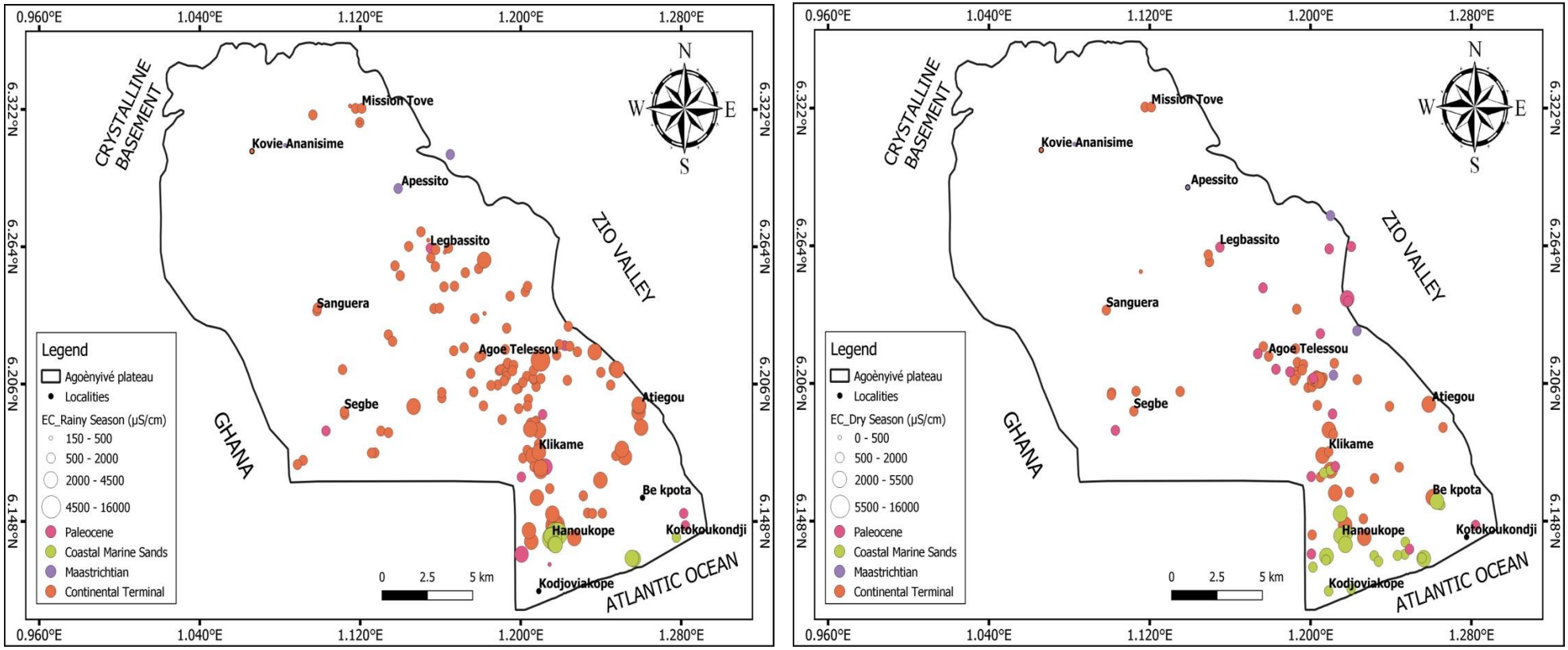

Figure 6.3a: Spatial Distribution of EC for the RS (Left) and the DS (Right) in the AP

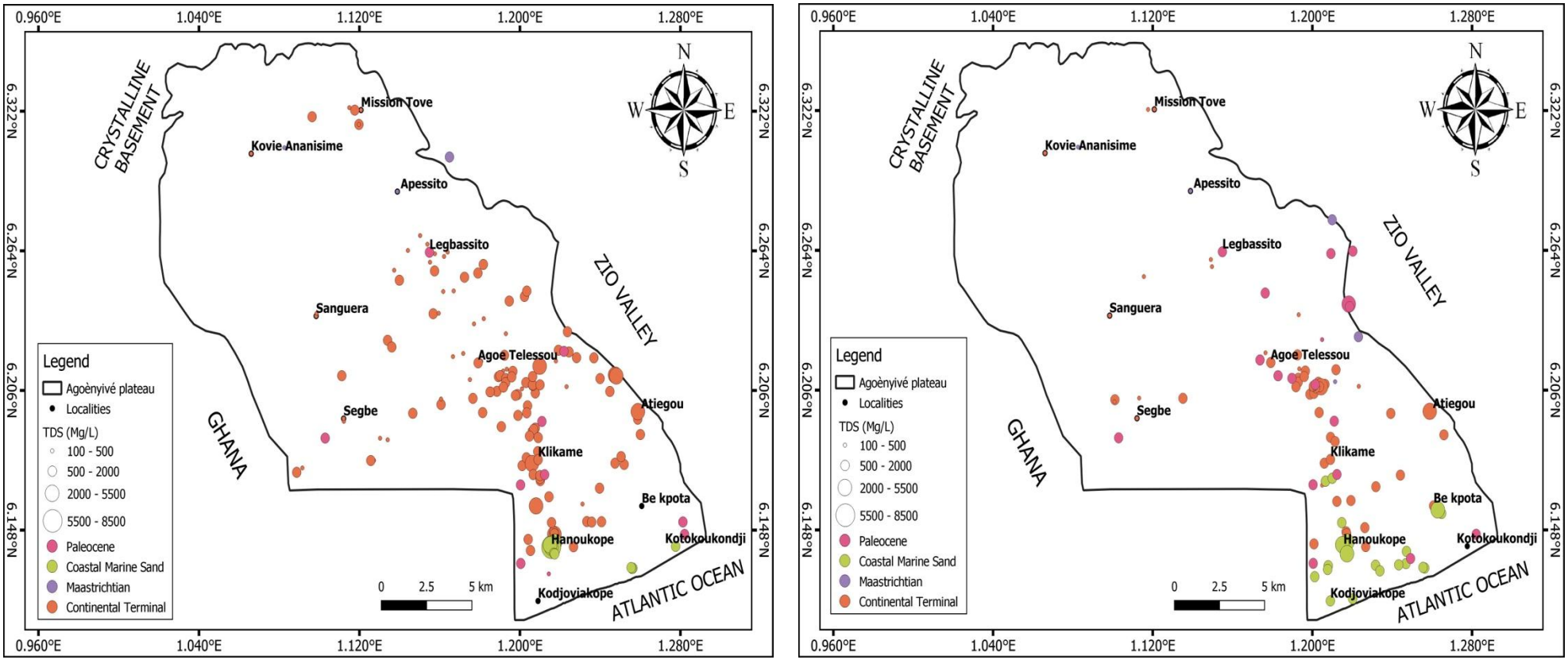

Figure 6.3b: Spatial Distribution of Salinity (TDS) for the RS (Left) and the DS (Right) in the AP

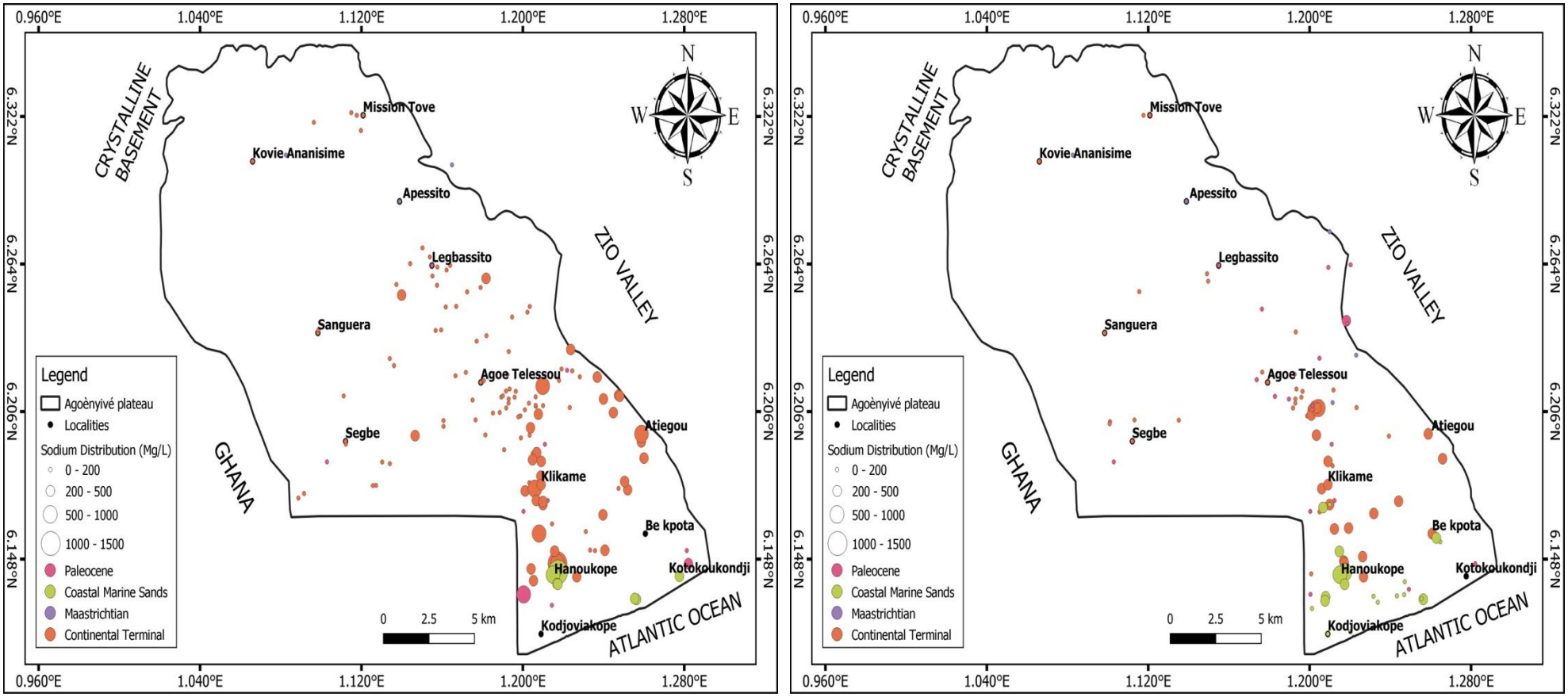

Figure 6.3c: Spatial Distribution of Sodium for the RS (Left) and the DS (Right) in the AP

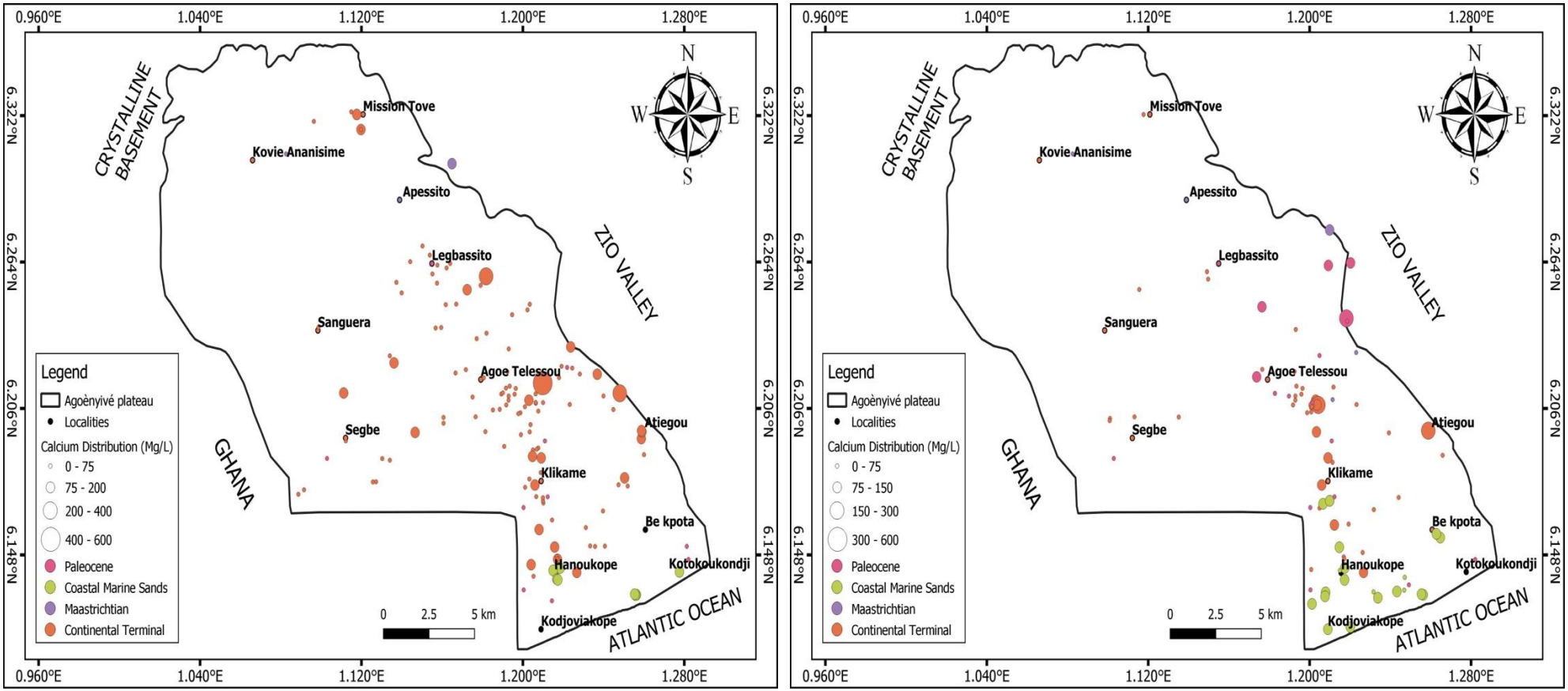

Figure 6.3d: Spatial Distribution of Calcium for the RS (Left) and the DS (Right) in the AP

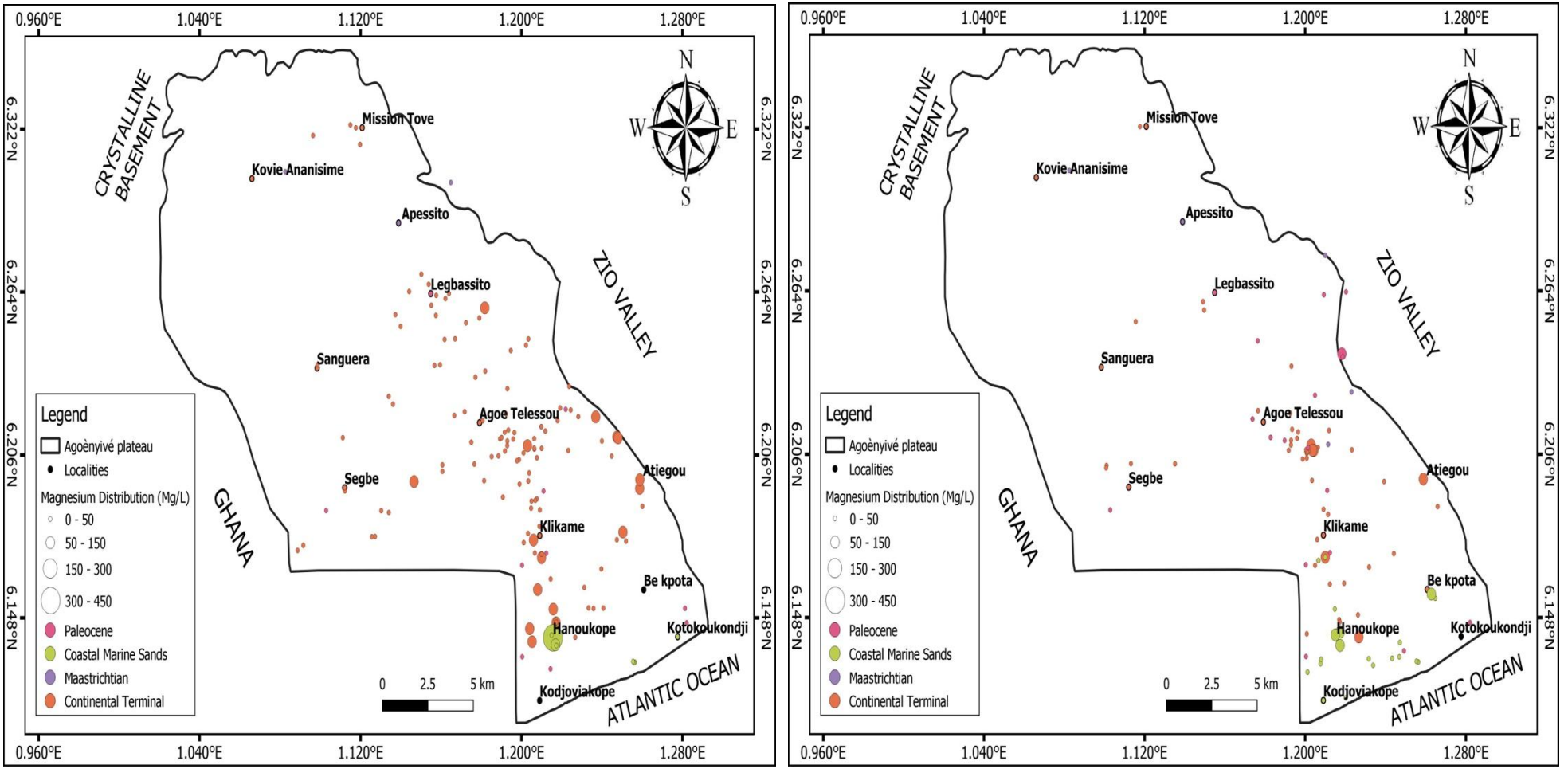

Figure 6.3e: Spatial Distribution of Magnesium for the RS (Left) and the DS (Right) in the AP

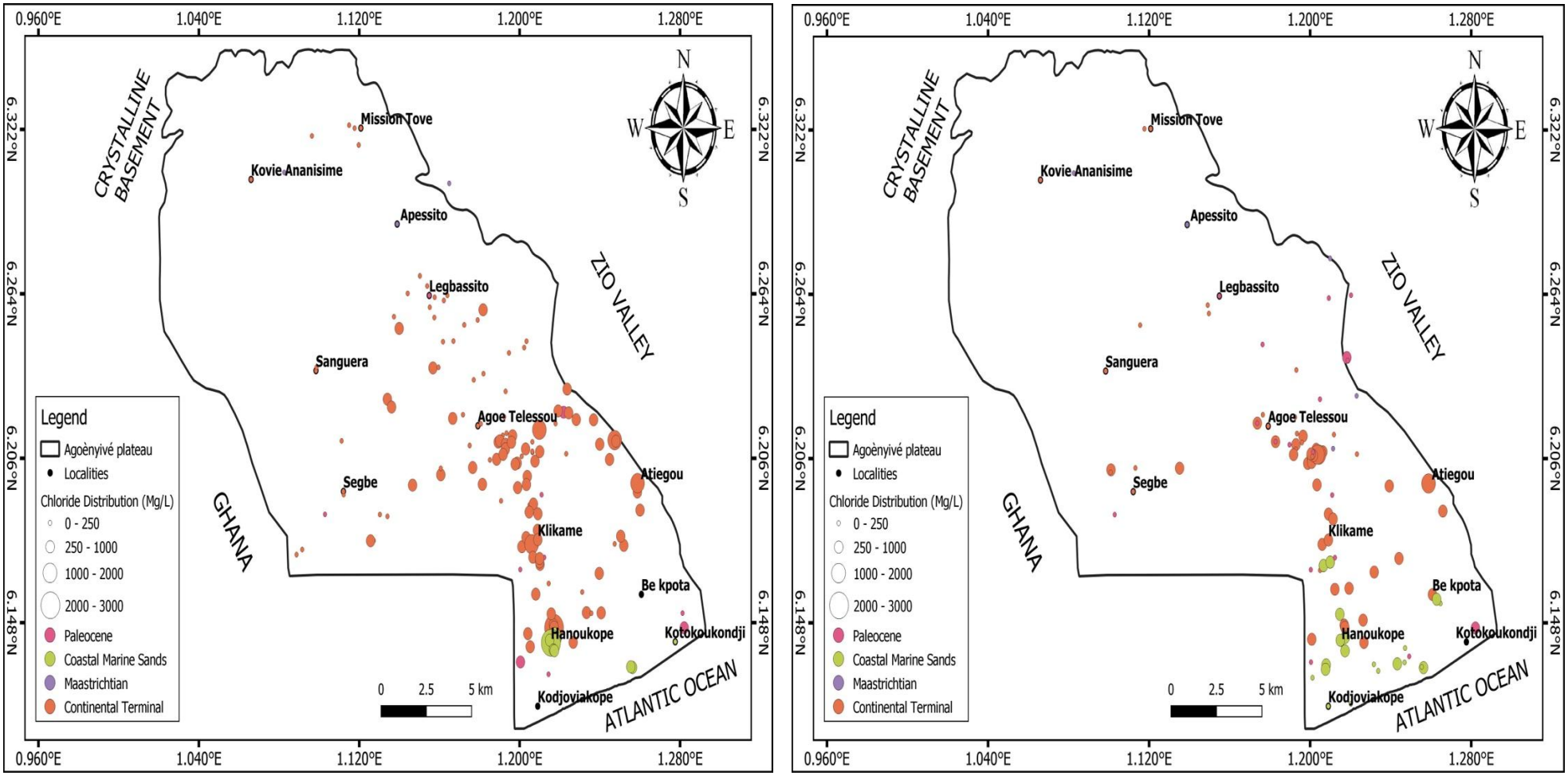

Figure 6.3f: Spatial Distribution of Chloride for the RS (Left) and the DS (Right) in the AP

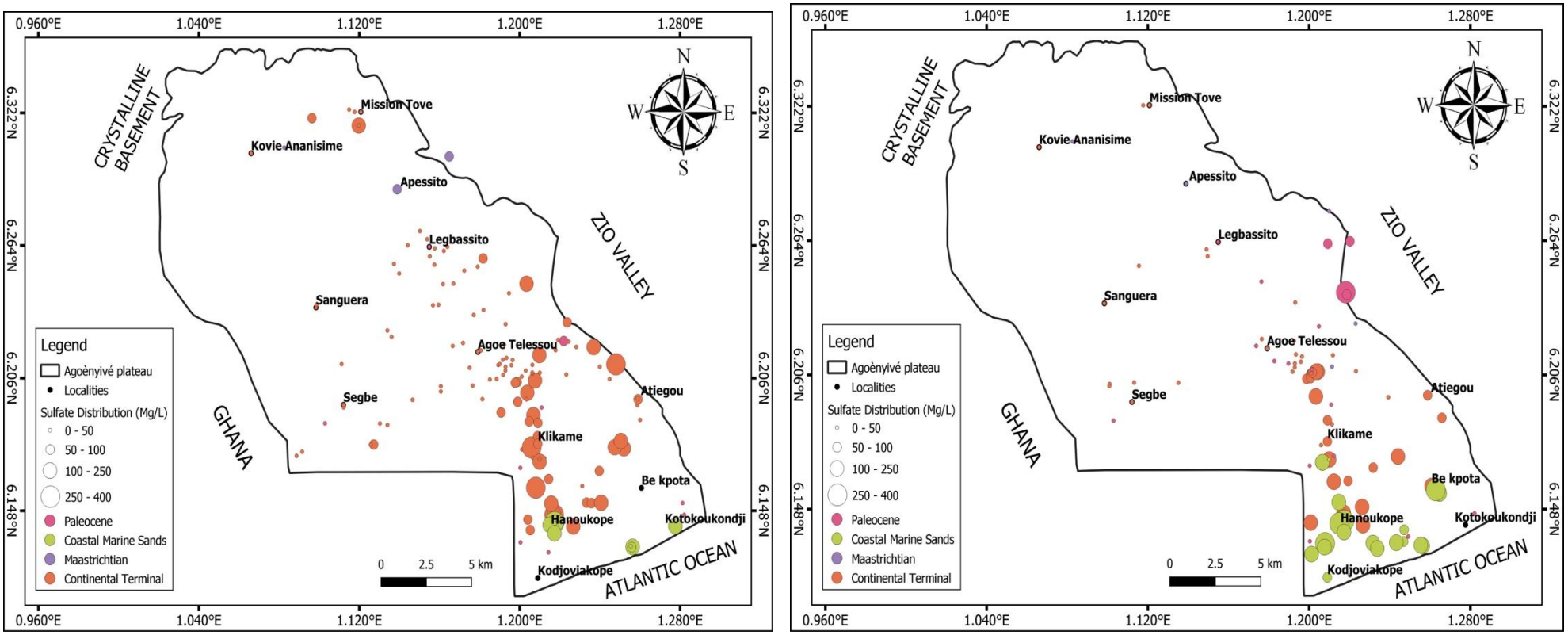

Figure 6.3g: Spatial Distribution of Sulfate for the RS (Left) and the DS (Right) in the AP

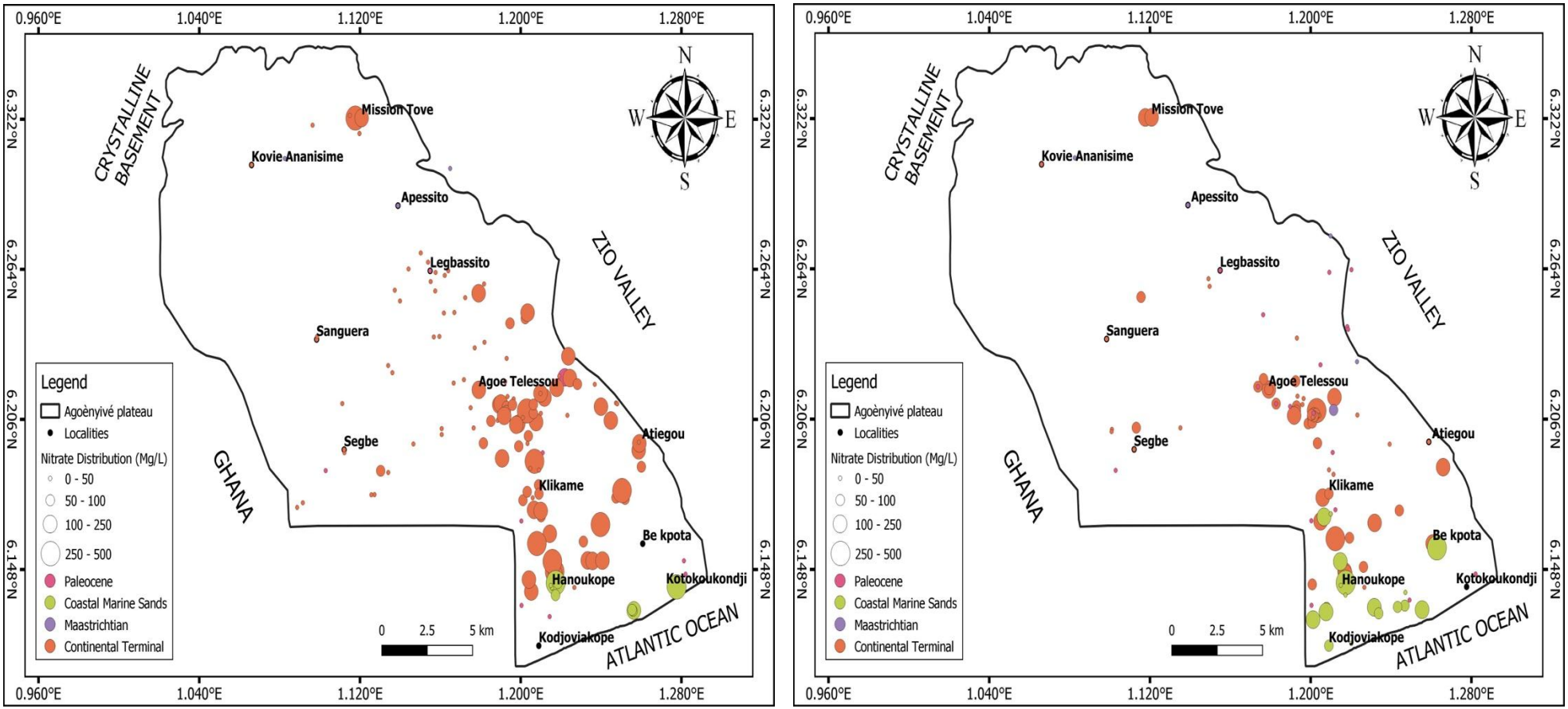

Figure 6.3h: Spatial Distribution of Nitrate for the RS (Left) and the DS (Right) in the AP

6.1.3 Water Facies of the Multi-layered Aquifer of the AP

6.1.3.1 Correlation between Major Anions and Cations

6.1.3.1.1 Correlation between Sodium and Chloride

The chloride has been considered in this context for its characteristics, including being a stable tracer and conservative element of the evaporites, absent in precipitations, non-affected by oxydo-reduction reactions, and non-influenced by bacteria. The ion is found to be highly correlated with Na^+ (Annex 2b and Figure 6.4a) during RS/DS. The coefficient of determination (R^2) for the RS/DS is 0.91/0.83, 0.99/0.91, 0.22/0.89, and 0.89/0.85 for the CT aquifer, Pa aquifer, MaS aquifer, and Ma aquifer, respectively. In addition, it has been observed that water samples from the Pa aquifer and Ma aquifer fall along the line, while most of the samples from the CT aquifer fall on the right side of the line. Furthermore, water samples from the MaS aquifer, the lagoon, and some samples from the CT aquifer fall on the left side of the line. The position of water samples from the CT aquifer suggests a common source of the two elements, while the space between sample points implicates a deficit of Na^+, thus suggesting a process of Na^+ fixation and Ca^{2+} liberation. On the other side, the position of the water samples from the MaS aquifer and lagoon and the remaining water samples from the CT aquifer imply an excess of Na^+, thus suggesting other sources of these elements, including the dissolution of halite, input from seawater, or other reactions.

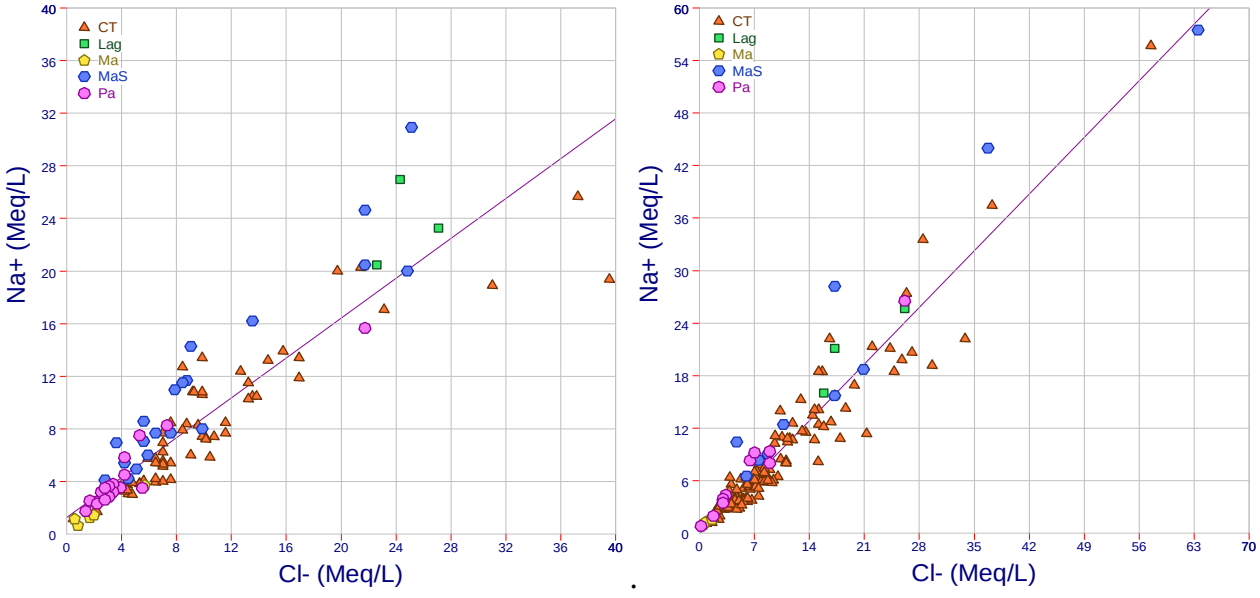

Figure 6.4a: $[Na^+]$ vs. $[Cl^-]$ for the DS (Left) and the RS (Right)

6.1.3.1.2 Correlation between Magnesium and Chloride

The coefficient of determination (R^2) between Mg^{2+} and Cl^- is found to be high for the CT aquifer (0.67/0.85), MaS aquifer (0.89/0.63), and Ma aquifer (0.61/0.67) for the RS/DS (Annex

2b and Figure 6.4b). In addition, it has been observed that except for the Ma aquifer, the remaining aquifers present either an excess of Cl^- (CT aquifer and MaS aquifer) or Mg^{2+} (Pa aquifer).

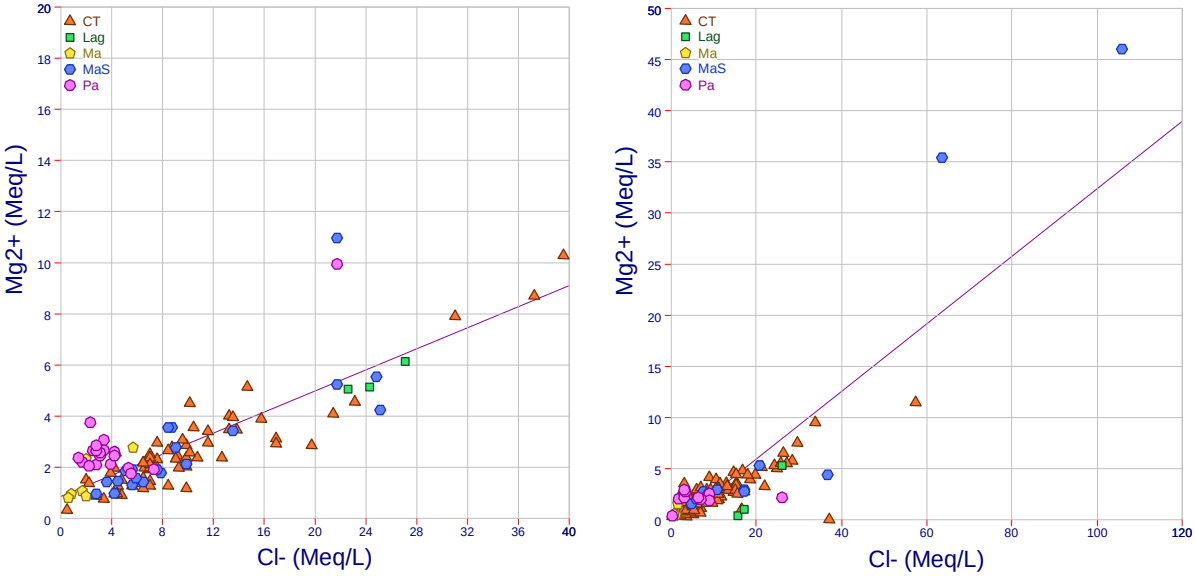

Figure 6.4b: [Mg^{2+}] vs. [Cl^-] for the DS (Left) and the RS (Right)

6.1.3.1.3 Correlation between Calcium and Sulfate

Contrary to the other formations, water samples from the MaS aquifer show a good coefficient of determination (R^2) between Ca^{2+} and $SO4^{2-}$ (Annex 2b and Figure 6.4c). The recorded coefficient of determination during the RS is 0.94. This result suggests sulfate supply from recharged runoff, as the MaS aquifer is very shallow and unconfined.

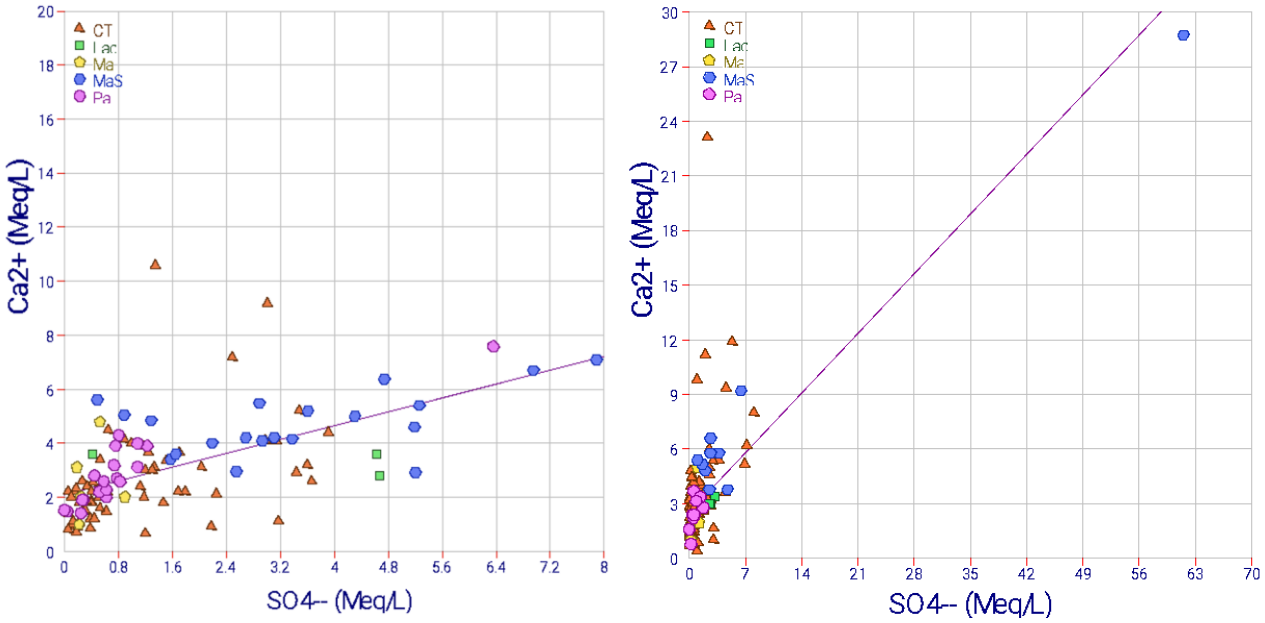

Figure 6.4c: [Ca^{2+}] vs. [$SO4^{2-}$] for the DS (Left) and the RS (Right)

6.1.3.2 Calculation of Saturation Indices

To further understand the sources of salinity in the considered aquifers in the AP, saturation indexes of the water samples collected with respect to the mineral phases of the evaporites and the carbonates have been considered (Figures 6.5a–d and Table 6.3).

A negative value (SI < 0) of the indices of saturation of the Halite (Figure 6.5a**)** has been obtained for water samples from all the aquifers and lagoons and for the two seasons. This result suggests the contribution of the dissolution of this mineral to the mineralisation of the waters of these aquifers. Nevertheless, it has also been observed that the increase in Na^+ and Cl^- is not proportionate to the increase in SI of the Halite for some samples, essentially from the CT aquifer and MaS aquifer, thus suggesting additional sources of these components.

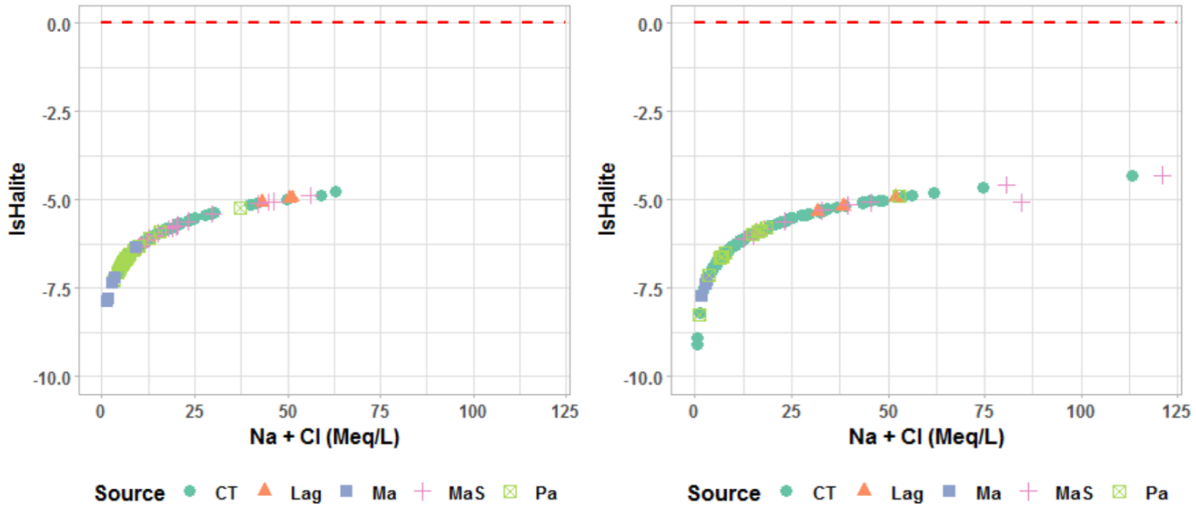

Figure 6.5a : [SI Halite] vs. [Na^++Cl^-] for the DS (Left) and the RS (Right)

Regarding water samples saturation to the carbonates, all water samples from the lagoon, a few water samples from the CT aquifer and MaS aquifer, and most of the water samples from the Pa aquifers show positive values of the SI (SI > 0). This indicates their oversaturation with respect to the dolomite, aragonite, and calcite (Figures 6.5b-d) and suggests the precipitation of these minerals. In addition, the remaining water samples from the CT aquifer and MaS aquifer and all water samples from the Ma aquifer show negative values of the SI (SI < 0). This result implies for these water samples an undersaturated state, thus suggesting the contribution of the dissolution of these minerals to the mineralisation of these aquifers. Nevertheless, the observed increase in magnesium and calcium concentrations (Ca^{2+} + Mg^{2+}), which is unproportionable to the increase in SI of the carbonate minerals for some water samples, essentially from the CT aquifer and MaS aquifer, suggests a plausible input from the sea (Wang et al., 2021).

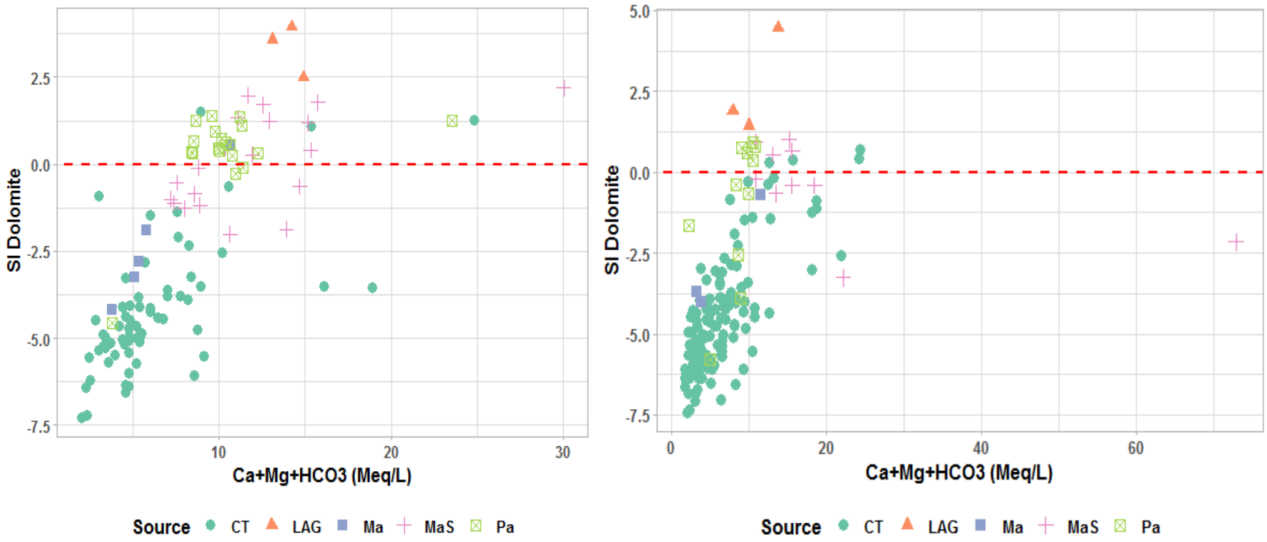

Figure 6.5b : [SI Dolomite] vs. [Ca^{2+}+Mg^{2+}+$HCO3^{-}$] for the DS (Left) and the RS (Right)

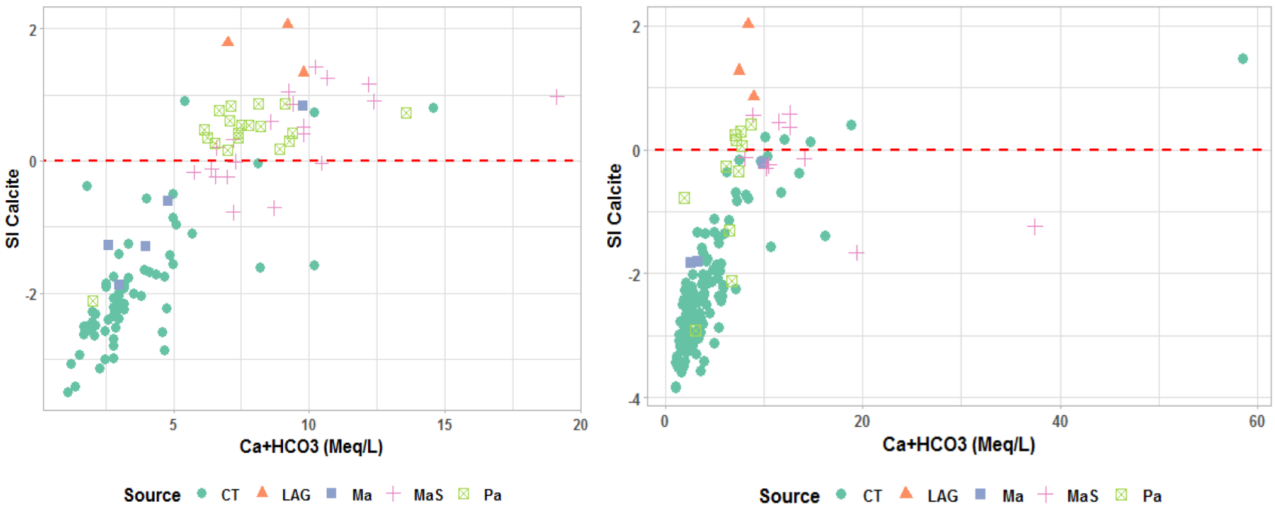

Figure 6.5c : [SI Calcite] vs. [Ca^{2+}+Mg^{2+}+$HCO3^{-}$] for the DS (Left) and the RS (Right)

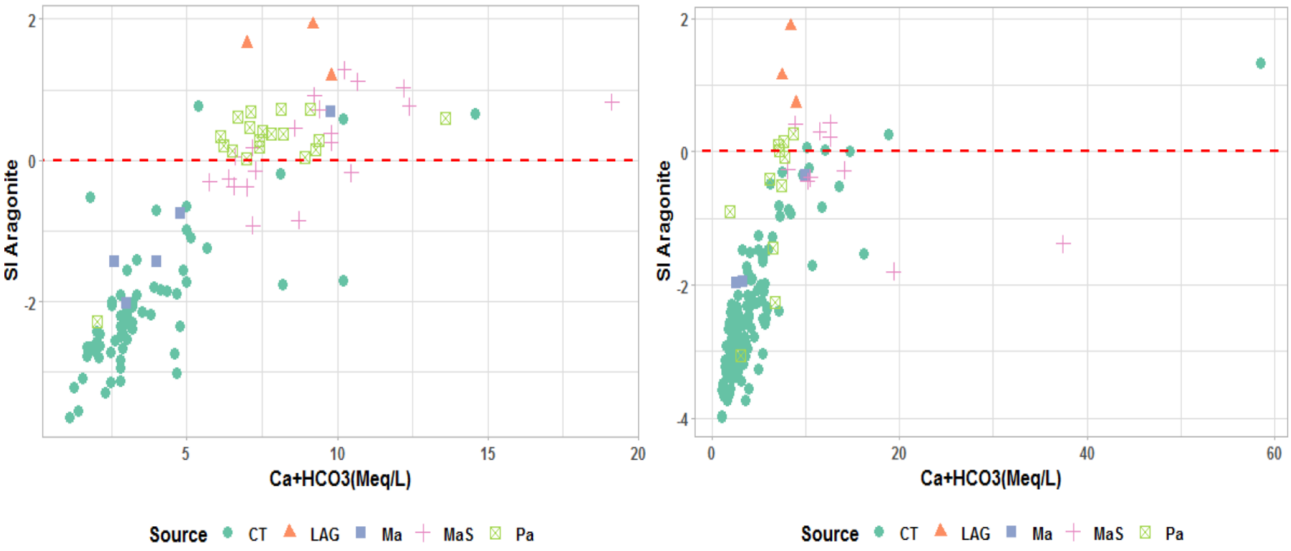

Figure 6.5d : [SI Aragonite] vs. [Ca^{2+}+Mg^{2+}+$HCO3^{-}$] for the DS (Left) and the RS (Right)

Table 6.3: Summary Saturation Indices (SI)

Aquifer		RS				DS			
		Halite	Aragonite	Calcite	Dolomite	Halite	Aragonite	Calcite	Dolomite
CT	Min	-9.09	-3.98	-3.84	-7.41	-7.87	-3.63	-3.49	-7.26
	Max	-4.3	0.26	0.4	0.68	-4.78	0.77	0.91	1.51
LAG	Min	-5.33	0.72	0.86	1.44	-5.08	1.19	1.33	2.49
	Max	-4.93	1.88	2.02	4.45	-4.94	1.92	2.06	3.94
Ma	Min	-7.73	-1.97	-1.83	-4.02	-7.9	-2.02	-1.88	-4.2
	Max	-7.27	-0.35	-0.21	-0.72	-6.36	0.69	0.83	0.55
MaS	Min	-6.11	-1.8	-1.66	-3.26	-6.63	-0.92	-0.78	-2.01
	Max	-4.3	0.44	0.58	1	-4.88	1.28	1.42	2.19
Pa	Min	-8.27	-3.05	-2.91	-5.79	-7.28	-2.27	-2.13	-4.55
	Max	-4.91	0.28	0.42	0.9	-5.23	0.73	0.87	1.39

*With the CT, LAG, Ma, MaS and Pa stand for the Continental Terminal, Lagoon, Coastal Marine Sand, Maastrichtian and Palaeocene.

6.1.3.3 Ionic Exchange Reaction: Base Exchange

The end water that reaches the aquifers has undergone a series of processes, including runoff and infiltration, phases during which these waters interact with solid materials (soil, rocks, and minerals). During these processes, the occurrence of a set of phenomena, among them the ionic/base exchange, is very plausible. For the aquifer systems characterised by the presence of organic colloids and clayey materials rich in Na^+, Ca^{2+}, and Mg^{2+}, the ionic/base exchange contribution to the chemical composition of the waters cannot be underestimated. This process consists of the fixing of monovalent cations (Na^+ and K^+) and the release of divalent cations (Ca^{2+} and Mg^{2+}), or the other way around, in the process of balancing their electrostatic charge. These exchanges have been captured by the relationship between [(HCO_3^- + $SO4^{2-}$)] and [Na^++ K^+- Cl^-] (Garcia et al., 2001), as presented in Figure 6.6. [(HCO_3^- + $SO4^{2-}$)] stands for the quantity of Ca^{2+} and Mg^{2+} lost or acquired compared to the supply from the dissolution of evaporitic minerals (gypsum and anhydrite) and carbonate minerals (calcite, aragonite, and dolomite), while [Na^++ K^+- Cl^-] stands for the quantity of Na^++ K^+ lost or acquired compared to the supply from the evaporitic minerals (Moussa et al., 2012; Fisher et Mullican, 1997).

The results show that most of the water samples from the CT aquifer, Ma aquifer, Pa aquifer, and lagoon fall along the line of slope -1 (Figure 6.6). More specifically, water samples from the Pa aquifer fall close to the origin point, showing rather a predominance of the dissolution process for water sample enrichment in Ca^{2+} and Mg^{2+} than base or ion exchange. The position of water samples from the Ma aquifer and most of the water samples from the CT

aquifer, far from the origin point (x = 0, y = 0), and mainly in the square of Na^+ absorption and Ca^{2+} release, suggests that the mineralisation of water samples from these aquifers is mainly governed by the base exchange, particularly the Na^+ absorption and Ca^{2+} release (direct cation exchange depicting a freshening process). Most of the water samples from the MaS aquifer and the remaining water samples from the CT aquifer depict the same pattern as the later aquifers, with the predominance of the base exchange, particularly the release of Na^+ and absorption of Ca^{2+} (reverse cation exchange suggesting SWI).

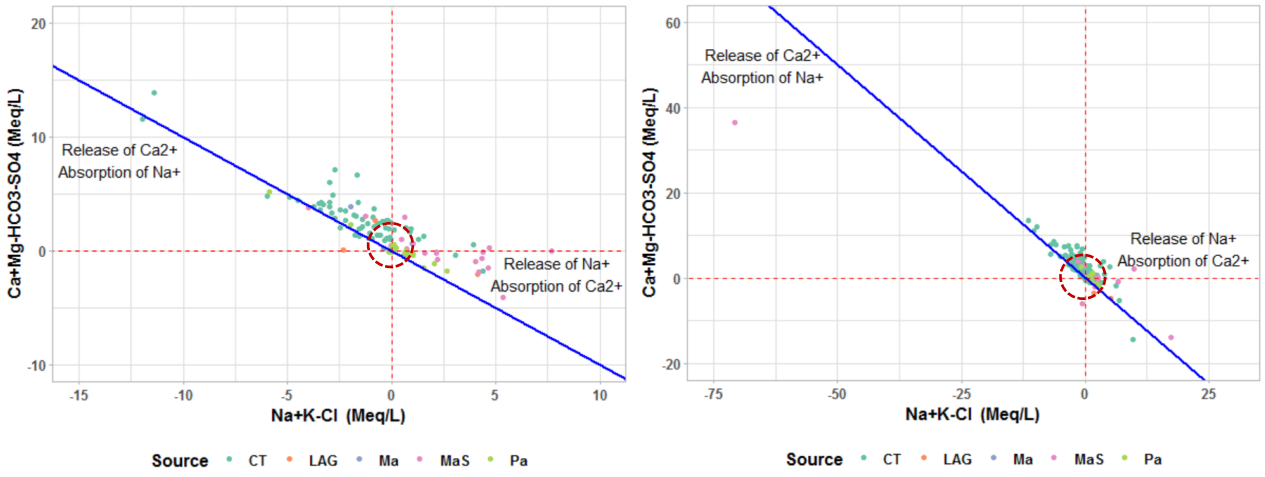

Figure 6.6: [Ca^{2+}+Mg^{2+} $HCO3^-$-$SO4^{2-}$] vs. [Na^++K^++Cl^-] for the DS (Left) and the RS (Right)

6.1.3.4 Piper Diagram and Mineralization Pathways

The dominant water facies for the considered aquifer in the AP (RS and DS) have been captured through the Piper diagram (Figure 6.7).

The diagrams show that water samples from the CT aquifer are prevalently chlorinated, with the two main facies observed including the chlorinated sodic-potassic (Na-K-Cl) waters (representing 86.94% of the samples) and the calcic and magnesia chlorinated (Ca-Mg-Cl) waters (16.32%). These results are in line with the results of PRESAF (2015) and Bleza et al. (2020a). Besides these two main facies, water samples from the CT aquifer can be hyperchlorinated sodic (case of GCC26 located at around 2 km from the ocean in the Gbadago area) or Magnesia and calcic bicarbonated (Ca-Mg-HCO3) (case of GCC12, GCC5, GCC62, GCC91, and GCC41 located at the centre and north of the study area). In addition, one thing that is obvious is the accumulation of most of the water samples in the chlorinated pole, especially around the water sample from the ocean. Furthermore, the position of water samples shows a gradual evolution from the bicarbonate pole to the chlorinated pole (from the Ca-Mg-HCO3 facies towards the Na-Cl facies via the Ca-Mg-Cl facies). This progressive evolution of the facies observed along with the occurrence of the Ca-Mg-Cl facies suggests a mixture of

two types of water characterised by varying concentrations of major ions (salinization Path 2 with a mixture of Ca-Mg-HCO3 facies with Na-Cl facies), thus allowing potential ion exchange (Howard and Lloyd, 1983). In the triangle of cations, an evolution of water samples from the calcium pole towards the sodium pole is observed, presenting a heterogeneous cloud with a relatively low content of Ca^{2+} and a great dominance of Na^{+}.

For the Pa aquifer, two main facies were found, including the magnesia and calcic bicarbonated facies (Mg-Ca-HCO3, 54.5%) and the sodic and potassic chlorinated facies (Na-K-Cl, 45.4%). The latter geochemical facies (including GCC149, GCC152, GCC153, and GCC159, which are large pumping boreholes located near the lagoon or ocean exploited by industries and the Togolese pumping society) is new. In fact, existing studies have rather prominently highlighted the magnesia and calcic bicarbonated facies (Mg-Ca-HCO3) (PRESAF, 2015; Akouvi et al., 2008) and the sodic and potassic bicarbonated facies (Akakpo, 2017). Therefore, the abrupt (without transit) occurrence of sodic and potassic chlorinated facies (Na-K-Cl) suggests isolated saltwater intrusion (salinization Path 2 with a mixture of Ca-Mg-HCO3 facies with Na-Cl facies). This occurrence can be attributed to the closeness of these water points to the ocean or lagoon as well as the pumping rate.

Water samples from the Ma aquifer are mainly calcic and magnesia bicarbonated (Ca-Mg-HCO3, 66.67%) and calcic and magnesia chlorinated (Ca-Mg-Cl, 33.33%) (case of GCC134 located in the northern part of the study area). The dominant cation is Ca^{2+}, while the dominant anion is $HCO3^{-}$. These results concur with the findings of Akouvi et al. (2008) and PRESAF (2015), except for the occurrence of the magnesia chlorinated water facies.

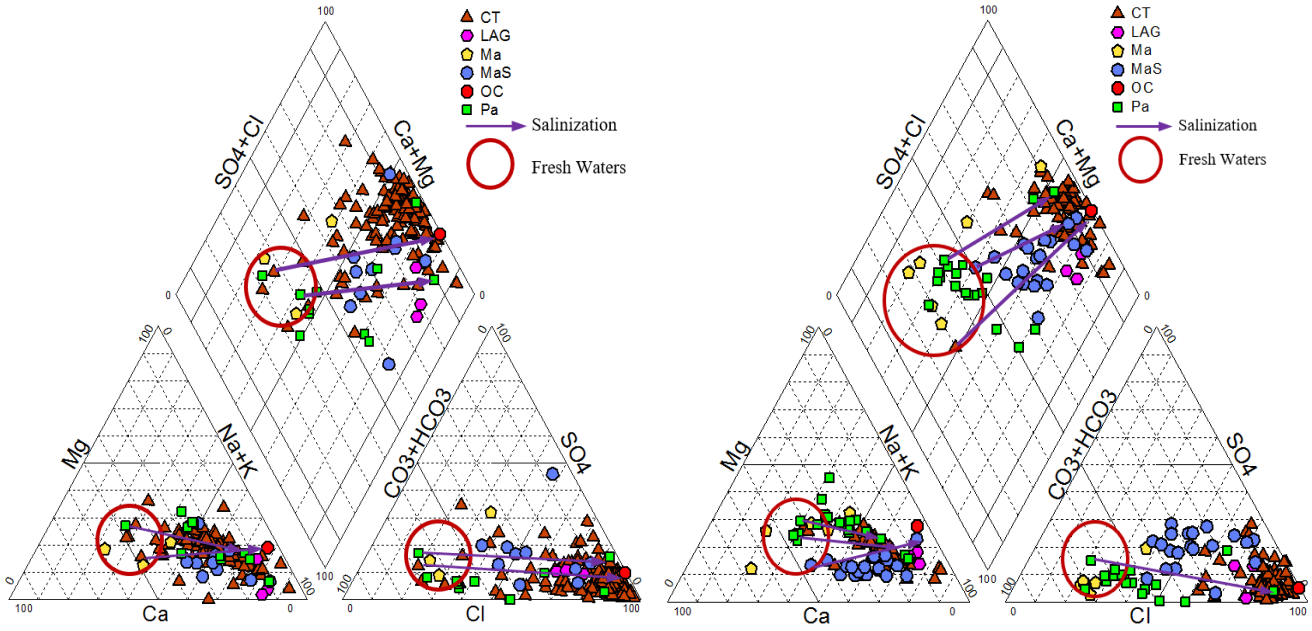

Figure 6.7: Piper Diagram showing mineralisation paths for the RS (Left) and the DS (Right)

6.1.3.5 Hydrochemical Facies Evolution Diagram

The hydrochemical Facies Evolution Diagram (HFE-D), as depicted in Figures 6.8a-d, shows four main facies, including Na-Cl (sea/saltwater), Ca-HCO3 (freshwater), Ca-Cl (salinised freshwater with reverse cation exchange), and Na-HCO3 (salinised freshwater with direct cation exchange). The square diagram is organised into three fields with regard to the conservative mixing line and is characterised by key facies. These fields stand for phases and include the freshening phase (located above and left of the conservative mixing line), the sea/saltwater intrusion phase (located below and right of the conservative mixing line), and the mixing phase (located at the centre or along the mixing line). The mixing line is defined considering the physicochemical parameters of the Atlantic Ocean (in Togo) for the DS and RS. These fields are also organised into sub-steps, including f_1, f_2, f_3, f_4, and FW representing the freshening fields, and i_1, i_2, i_3, i_4, and SW representing the intrusion fields.

Results show that most water samples from the CT aquifer (Figure 6.8a) fell in the intrusion phase (below the mixing line), with an increasing trend of salinity along the facies path MixCa-MixHCO3 / MixSO4 (10)-MixCa-MixCl (11)-MixCa-Cl (12)-MixNa-Cl (8) and Na-Cl (4) associated with the reverse cation exchange, showing MixCa-Cl facies. As a result, facies including Na-Cl, MixNa-Cl, MixCa-Cl, MixCa-MixCl, MixCa-MixCl, MixCa-HCO3 / SO4, Na-MixHCO3 / MixSO4, MixCa-MixHCO3 / MixSO4 and MixNa-HCO3 / SO4 are portrayed. In fact, water samples falling under the Na-Cl facies (4) support the hypothesis of a strong marine influence on the mineralisation of the aquifer. In addition, intermediary facies such as MixNa-Cl, MixCa-Cl, MixCa-MixCl, MixCa-MixCl are also observed (corresponding to the Ca-Na-Cl facies in the piper diagram), with an implication for a moderate marine or sea influence. Finally, the MixCa-HCO3 / SO4, Na-MixHCO3 / MixSO4 and MixCa-MixHCO3 / MixSO4 facies (corresponding to the Ca-Na-HCO3 facies in the piper diagram) correspond to late freshening stages (f_3, f_4) and early intrusion stages (i_1, i_2), with the ultimate end facies being the Ca-HCO3, suggesting a slight marine influence.

When it comes to the MaS aquifer (Figure 6.8b), water samples are found to fall under the Na-Cl (4), Na-MixCl (3), and MixNa-MixCl (8) facies. The Na-Cl facies (4) correspond to the Na-Cl facies in the Piper Diagram, thus supporting the hypothesis that the MaS is severely influenced by seawater. In addition, the presence of substage facies such as Na-MixCl and MixNa-MixCl (corresponding to Na-Cl) implies a moderate marine or sea influence on the aquifer. In sum, the observed facies paths show both freshening in its early stage and reverse cation exchange.

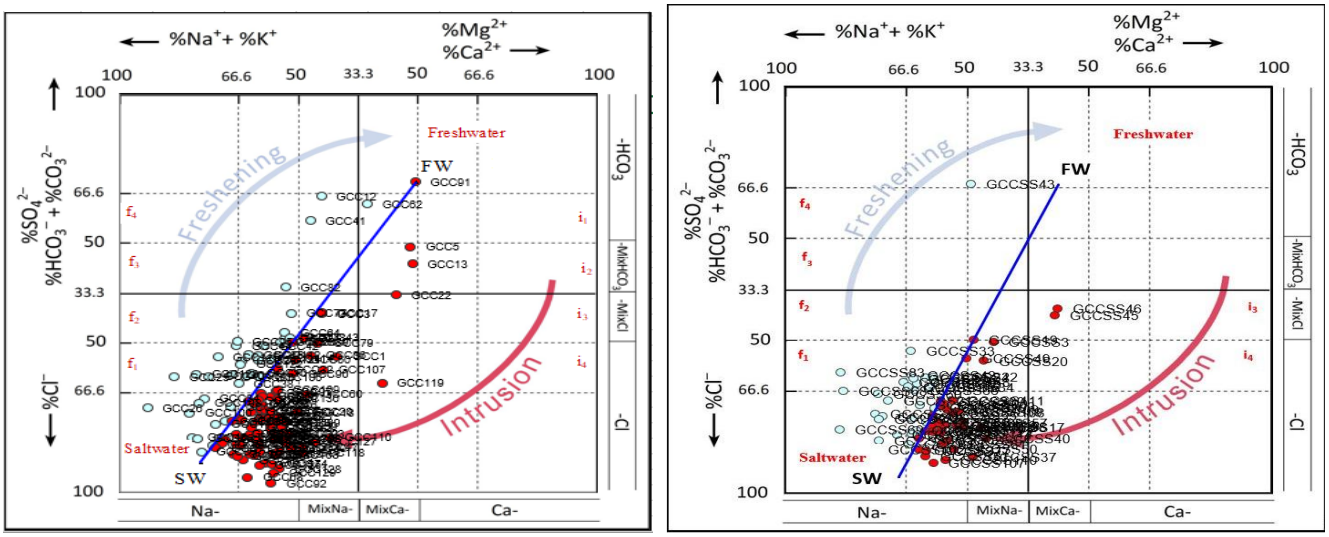

Figure 6.8a: HFE-D for the CT aquifer for the RS (Left) and the DS (Right), AP

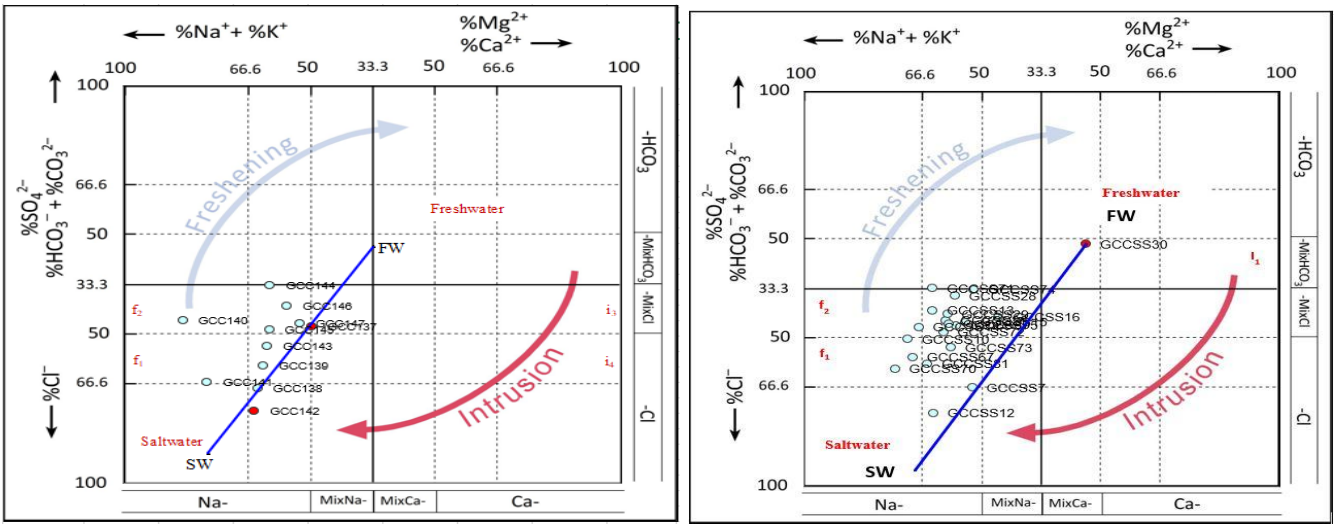

Figure 6.8b: HFE-D for the MaS aquifer for the RS (Left) and the DS (Right), AP

For the Pa aquifer (Figure 6.8c), it has been observed that only a few water samples fell along the mixing conservative line, portraying little to moderate marine influence. As a matter of fact, the facies observed include the Na-Cl facies (4) along with the MixNa-HCO3 (5) and MixCa-HCO3 (9) facies. The presence of the Na-Cl facies (corresponding to Na-Cl facies in the Piper diagram) suggests a severe marine influence with waters under the early freshening sub-stage. This pattern is observed with water samples close to the ocean or lagoon (GCC152, GCC153, GCC149, GCC159, and GCC154). On the other hand, the MixNa-HCO3 and MixCa-HCO3 facies correspond to late freshening (f_4) and early intrusion (i_1) sub-stages, suggesting that the aquifer where water samples were taken is freshwater going through a slight or no marine influence associated with direct cation exchange. These results confirm the work of Akouvi et al. (2008), which highlights plausible paleo-seawater intrusion in the Pa aquifer.

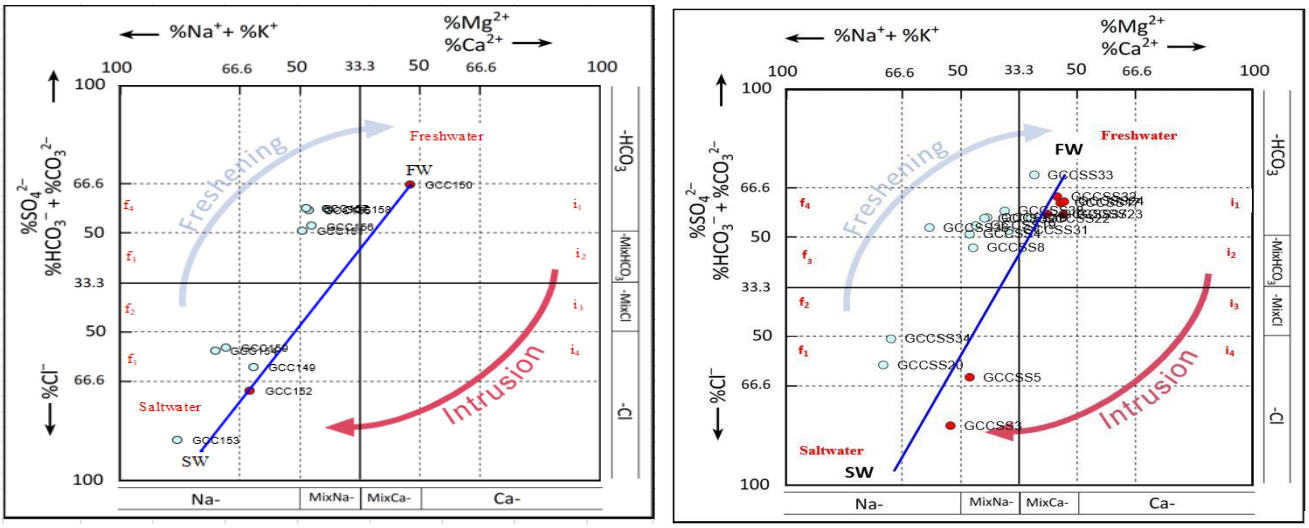

Figure 6.8c: HFE-D for the Pa aquifer for the RS (Left) and the DS (Right), AP

Figure 6.8d shows that water samples from the Ma aquifer fell under the Ca-HCO3 (13), MixCa-MixHCO3 / MixSO4 (10), and MixNa-HCO3 (5) facies. The Ca-HCO3 facies corresponds to Ca-HCO3 in the Piper diagram, thus representing the freshwater facies.

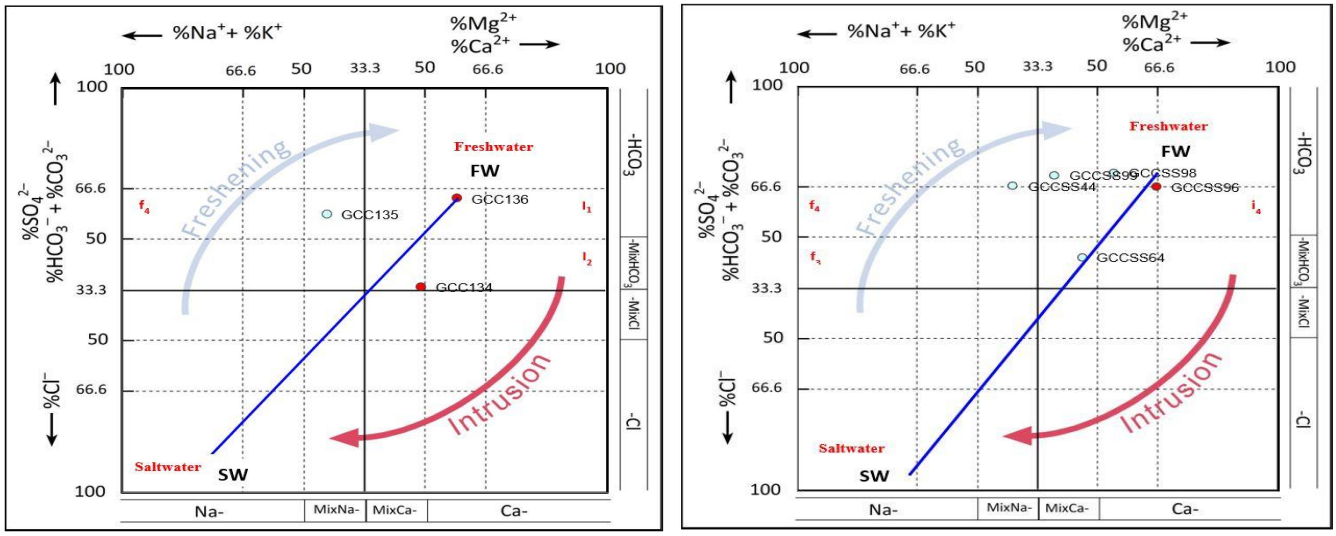

Figure 6.8d: HFE-D for the Ma aquifer for the RS (Left) and the DS (Right), AP

A seasonal comparison of the facies for the same points considered for the two seasons shows no (Ma and Pa aquifers) to little change (MaS and CT aquifers). For the CT aquifer, it is observed that the water sample GCC47 (GCCSS37) shows an intensification of the salinisation process with a shift from the MixNa-Cl facies in the RS to the Na-Cl facies in the DS. On the other hand, some other samples depict refreshing processes (found around Cacaveli). These latter changes include a shift from Na-MixCl facies to MixNa-MixCl facies and a shift from Na-Cl facies to MixNa-Cl facies from RS to DS for the samples GCC23 (GCCSS19) and GCC20 (GCCSS17), respectively. As for the MaS aquifer, a refreshing

process is observed occurring around Kotokoukondji with the water sample GCC143 (GCCSS28). The water point depicts a shift from Na-Cl in the RS to Na-MixCl facies during the DS.

6.1.4 Seawater Intrusion Potential Assessment

Several metrics (as described in section 3.2.3.1: Table 3.11), including the PCA and Ascendant Hierarchic Clustering (AHC), Revelle Index (RI), Cation Exchange Value (CEV), Sodium-Chloride Ratio (Na/Cl), and diagrams (Piper, HFE, and Stiff), have been considered for the potential SWI assessment. In addition, a physicochemical dataset obtained during the RS was considered. The overall classification was based on the "classification method agreement" (at least two methods) and expert knowledge of the study area.

The obtained results show that most of the water samples from the CT aquifer (n = 130) considered are severely affected by seawater intrusion (78.46%), while the slightly affected waters and freshwater (including water polluted with anthropogenic sources) represent 15.38% and 6.15%, respectively. As for the Pa aquifer (n = 11), the affected and freshwater water samples (including water polluted with anthropogenic sources) account for 45.45% and 54.55%, respectively. Water samples from the Ma aquifer (n = 3) are found to be mostly unaffected (including water polluted with anthropogenic sources) (66.67%). Finally, water samples from the MaS aquifer are found to range between severely affected samples (54.55%), slightly affected samples (36.36%), and unaffected samples (9.09%), including water polluted by anthropogenic sources.

When it comes to the spatial distribution of the water samples depicting the influence of the seawater on their mineralisation (Figure 6.9), it has been observed that most of the water samples affected are close to the coast. The second area that is accounted for in this process is low-lying areas characterise by low elevation (Gbadago, Hédzranawoé, Kégué, Kodomé, Kotokoukondji, Nukafu, Attiegou Ahanoukopé, Klikamé, and Habor Zone). From these results, it can be inferred that these parts of the aquifers are subjected to lateral seawater intrusion. This result is in line with the findings of Hounsinou (2020). The author reported a potential marine intrusion in the CT aquifer of the Coastal Sedimentary Basin of Benin with high EC and chloride content observed in the southern part (along the coast). In addition, Agossou et al. (2022) reported high EC along the coastal sedimentary basin of Benin using the SEAWAT model. Nevertheless, the presence of intruded samples from the CT aquifer inland (far from the coast) in areas such as Agoè and Cacaveli suggests an up coning of seawater into the aquifer.

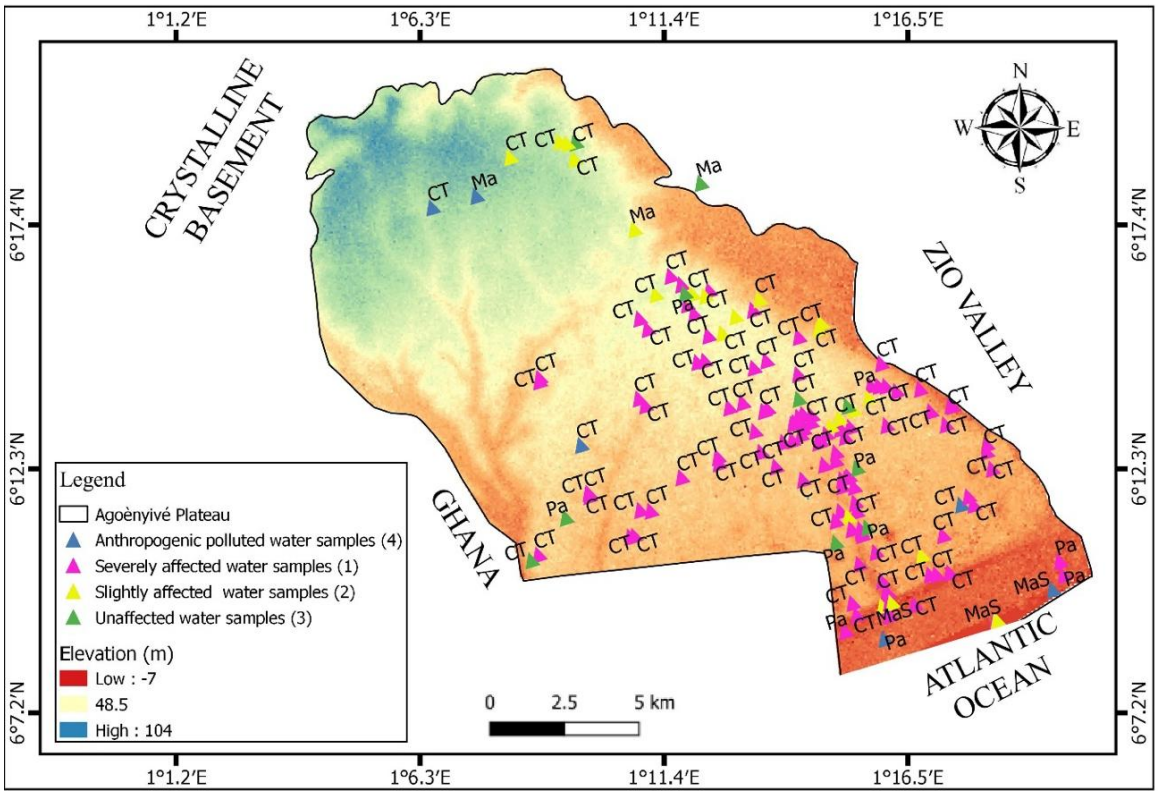

Figure 6.9: Water Samples Classes' Distribution across the AP

In terms of the metrics reliability (Table 6.4), it has been observed that all the metrics have captured the intrusion and freshening patterns, but the difference that stands out is the level of intrusion (slight or severe). However, it is found that there is a high agreement between the HFE-D diagram, the stiff diagram, and the AHC. This observed agreement can be explained by the multi-variable nature of these assessment tools, thus capturing all the stages (including those between main facies) compared to the remaining metrics, which are essentially bivariate. Nevertheless, the results reveal that RI+CEV+ (Na/Cl) can easily capture other sources of pollution apart from seawater intrusion compared to other metrics.

Table 6.4: Agreement Matrix between Metrics

Agreement (%)	RI+CEV+(Na/Cl)	HFE-D	Stiff-Diagram	AHC
RI+CEV+(Na/Cl)	100			
HFE-D	54.41	100		
Stiff-Diagram	60	95.48	100	
AHC	40.65	83.23	81.26	100

6.2 Isotopic Signatures of the Aquifers

As reported by Fritz and Fontes (1980), the consideration of isotopic signatures along the hydrochemistry has proven its importance in tracking the salinity origin. The isotopic

signature analysis is based on a dataset of 49 water samples (Annex 4) collected during the DS: CT aquifer (24), lagoons (2), MaS aquifer (19), Ma aquifer (1), and Pa aquifer (3).

Water samples from the CT aquifer display isotopic values between -3.32 and -2.09‰ (with an average of -2.7‰) and between -16.61 and -11.59‰ (with an average of -14.1‰) for δ^{18} O and δ^{2} H, respectively. On the other hand, water samples from the Pa aquifer depict values between -3.16 and -2.89‰ (with an average of -3.03‰) and between -17.42 and -14.92‰ (with an average of -16.2‰) for $\delta^{18}O$ and $\delta^{2}H$, respectively. Water samples from the lagoons (GCCSS 25 and GCCSS 9) depict very high isotopic values ranging between -0.09 and -0.02‰ (with an average of -0.06‰) and between -1.27 and -0.22‰ (with an average of -0.7‰) for the $\delta^{18}O$ and $\delta^{2}H$, respectively. The only water sample from the Ma depicts values of -2.98‰ and -15.45‰ for $\delta^{18}O$ and $\delta^{2}H$, respectively. Finally, water samples from the shallow MaS aquifer display values between -3.87 and -2.67‰ (with an average of -3.3‰) and between -19.98 and -12.74‰ (with an average of -16.4‰) for $\delta^{18}O$ and $\delta^{2}H$, respectively. The above results reveal that, except for lagoons, water samples from different aquifers have quite similar isotopic compositions. This suggests that a hydraulic connection exists between these aquifers, with plausible vertical recharge of the deep aquifers through the unsaturated soil zone. In fact, the recharge of the Pa aquifer by the CT aquifer has been reported, particularly in the area where the CT aquifer lay directly on the clayey-sand-orogenic limestone of the undifferentiated Palaeocene (P0) around the Adetikopé area (Akakpo, 2017).

The spatial variation of the stable isotopes, including oxygen 18 (^{18}O) and deuterium (^{2}H), over the AP for the considered aquifers is depicted in Figures 6.10a–b. The spatial distribution of the ^{18}O does not show any particular pattern (Figure 6.10a) but depicts high values for the CT aquifer around Cacaveli, Agoè (at the TdE pumping station), Klikamé, and Kovié Ananisimé. As for the Pa aquifer and Ma aquifer, the highest values are observed around Agoè (at the TdE pumping station). Finally, the highest values for the MaS aquifer are observed around Ahanoukopé.

Just as for the ^{18}O, the spatial distribution of the ^{2}H shows no particular pattern (Figure 6.10b). For the CT aquifer, high values are found in the northern part but also around Agoè, Cacaveli, Klikamé, and Amoutivé. Finally, for the MaS aquifer, the highest values of ^{2}H are around Ahanoukopé and Be Kpota. The observed enrichment in areas located in the southern part of the study area for the CT aquifer may be attributed to the contribution of lagoons and the ocean. As for the Pa aquifer, the highest values are reported around Cacaveli (the pumping station). Values of ^{2}H depicted by water samples from the MaS aquifer show enrichment around the lagoons (Ahanoukopé and Bé) and Gbadago. In addition, a decreasing pattern

toward the south is observed. Finally, the lagoons found in the southern part, around Ahanoukopé, Nyékonakpoé, and Be, also show an enrichment pattern of deuterium.

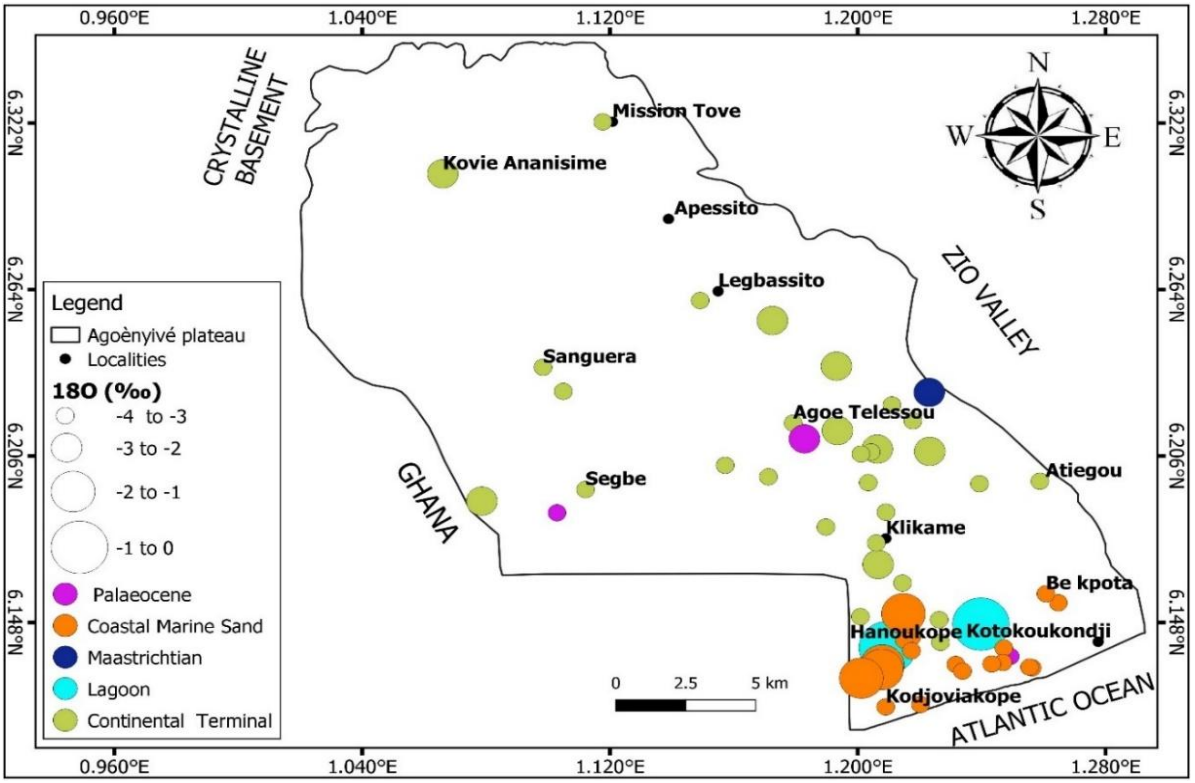

Figure 6.10a: Spatial Distribution of ^{18}O for the CT, Pa, Ma and MaS Aquifers over the AP

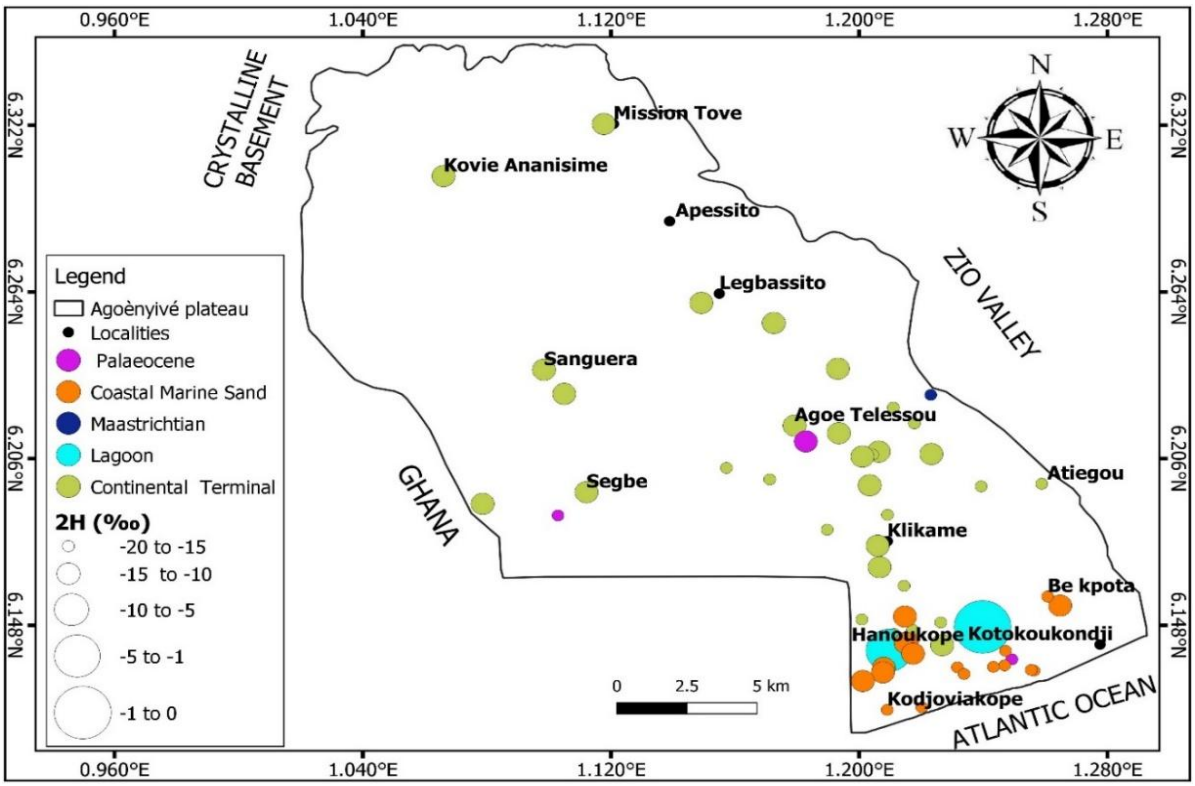

Figure 6.10b: Spatial Distribution of ^{2}H for the CT, Pa, Ma and MaS Aquifers over the AP

The distribution of water samples along the δ ^{2}H versus δ ^{18}O plot (Figure 6.11) shows that almost all the water samples fall close to the Global Meteoric Water Line (GMWL) and the Local Meteoric Water Line (LMWL), suggesting a meteoritic origin. Besides these points, another group of water points falls along the mixing seawater line (MSWL), suggesting a plausible mixture of these water samples with seawater or brackish water. It includes water points collected from the CT aquifer (Cacaveli: GCCSS17, GCCSS18, GCCSS48, and GCCSS93; Novissi: GCCSS7; Amoutivé: GCCSS22; Agoè Demakpoé/reserve: GCCSS53 and GCCSS59; and Segbé: GCCSS65), lagoons, and the MaS aquifer (Ahanoukopé: GCCSS10, GCCSS12, GCCSS13, GCCSS14, GCCSS15, GCCSS3, and Gbadago: GCCSS67). The third group of water samples is observed along the evaporation line (EL), depicting the role of evaporation in the mineralisation of these water points. Among them are water samples from shallow systems such as the CT aquifer (Attikoumé: GCC24) and the MaS aquifer. As a matter of fact, the hydraulic heads in the study area support this assertion, as the measured water table depth is on average 27 m for the CT aquifer (varying between 7 and 48 m) and 1.5 m for the MaS aquifer (varying between 0 and 3 m). The last group observed is made of water points (belonging to the Pa Aquifer) falling below all the lines considered above (LMWL, GMWL, MSWL, and EL), suggesting a paleo intrusion as reported by Akouvi et al. (2008).

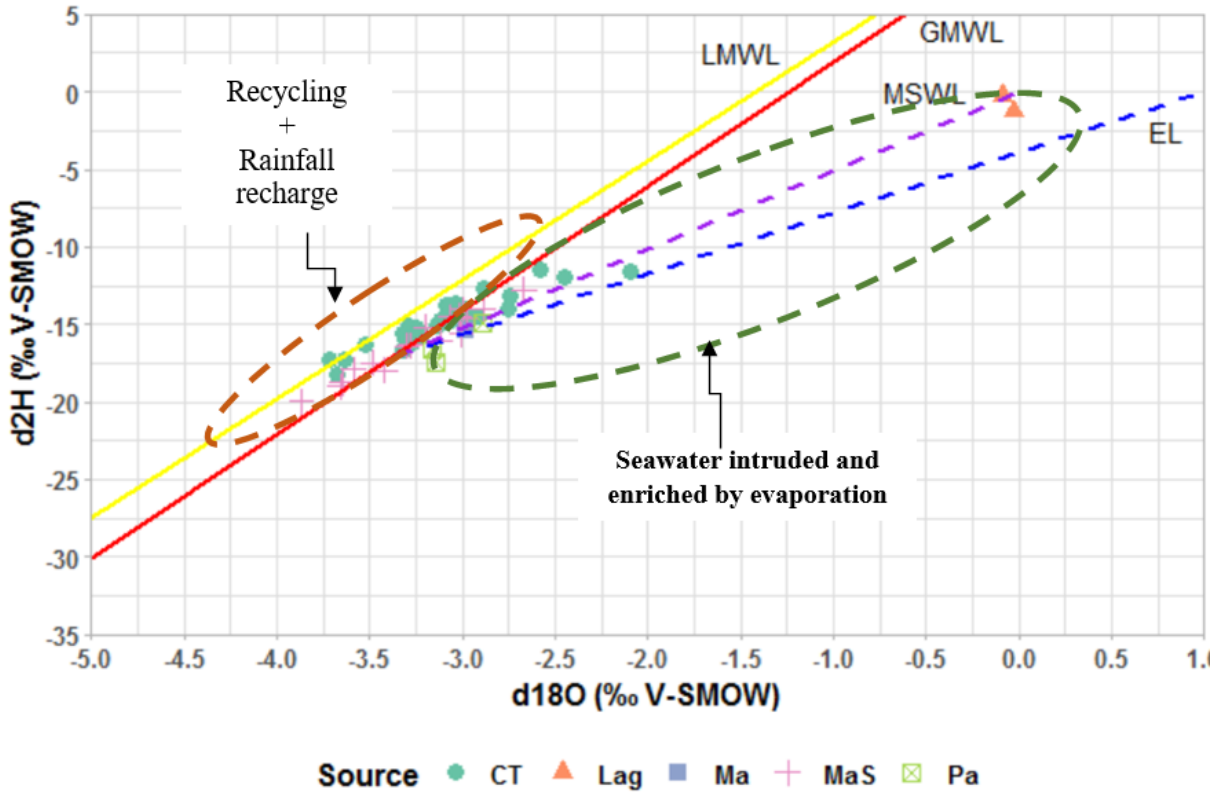

Figure 6.11: δ ^{2}H versus δ ^{18}O Plot

Over the period of 1970–1998/1999, no significant change has been reported in δ ^{18}O content over the AP (-3.88 and -2.91‰ as of 1998) (Akouvi et al., 2008). Nevertheless, these results were found to have significantly changed over the period 1998–2022. In fact, an enrichment process is shown, with values ranging between -3.87 and -2.09‰. These results imply that the exploitation of the resources during the last two decades has caused significant perturbations in the chemical characteristics of the system.

The effect of a possible seawater intrusion was also investigated by plotting the EC against δ ^{18}O. Three classes of water can be highlighted in Figure 6.12. The first group includes all the water samples from the Ma aquifer, the Pa aquifer, and some samples from the CT aquifer and the MaS aquifer. These water samples show depleted δ ^{18}O (range between -4 and -2.5‰) and low EC values (≤1500 µS.cm^{-1}), depicting freshwater as defined by Park et al. (2012). The second class consists of most of the water samples from the CT aquifer and MaS aquifer, depicting the same δ ^{18}O range as the previous class but associated with a parallel, non-linear increase in the EC (1500 µS.cm^{-1}). This pattern suggests plausible water mixtures with saline sources (including recent seawater, anthropogenic activities, or paleowater) or evaporated water. Finally, the third class includes water samples from the lagoons, characterised by an enriched δ ^{18}O close to 0‰ along with a high EC. The observed tendency suggests a mineralisation that results from water mixtures with seawater or brackish water.

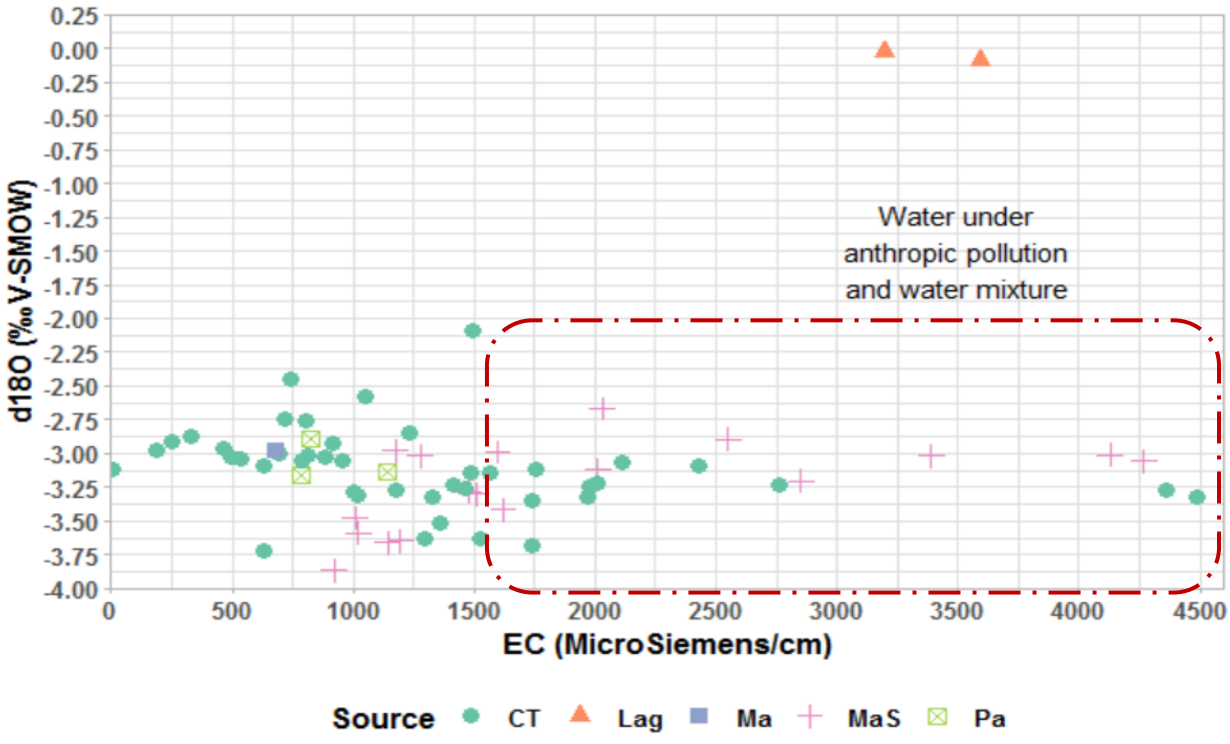

Figure 6.12: EC versus δ ^{18}O Plot

Finally, the plot of Cl^- content against $\delta\,^{18}O$ (Figure 6.13) has been considered to further explore the possible seawater intrusion in the AP. It has been observed that only water samples from lagoons and certain water samples from the CT aquifer and MaS aquifer, loaded with high chloride, are depicting a parallel and non-linear enrichment in $\delta\,^{18}O$. These results imply that the salinity of these water points does not originate mainly from the dissolution of salts in soils and rocks but from other sources, such as the evaporation process or the mixture with brackish or seawater. In fact, an excess of Cl^- has been observed in some water samples from the MaS aquifer (around Gbadago, Bè Kpota, and Ahanoukopé areas: GCCSS82, GCCSS10, GCCSS12, and GCCSS70) and CT aquifer (around Attiegou and Cacaveli areas: GCCSS 37 and GCCSS 107), confirming these sources.

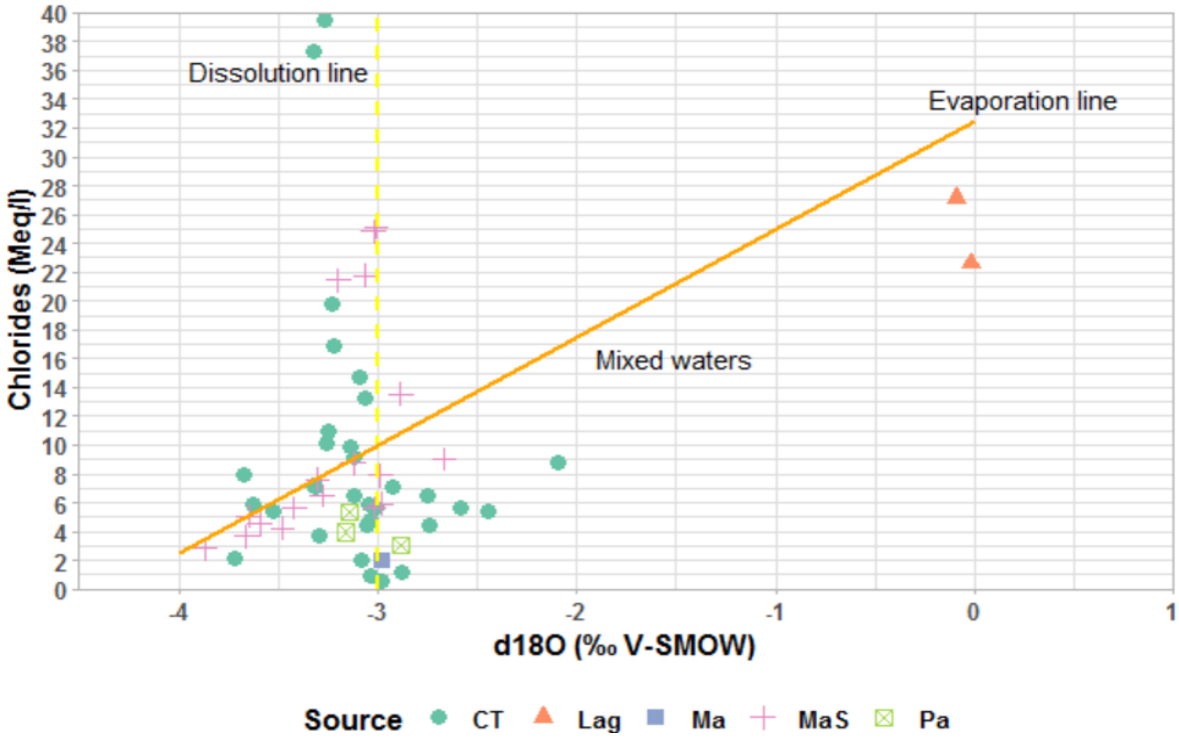

Figure 6.13: Chlorides ($Meq.L^{-1}$) Vs $\delta^{18}O$ (‰) Plot

6.3 Hydraulic Heads Pattern in the Agoènyivé plateau

6.3.1 Interannual and Inter-seasonal Evolution

The interannual evolution of the hydraulic heads for the CT aquifer, Pa aquifer, and Ma aquifer has been tracked for the period of 2016–2019 (Annex 5a–c).

Piezometers tapping the CT aquifer include those of Attiegou (located in the Lycée technique), Campus Nord (located within the University of Lomé), Segbé (located within the Segbé USP), Sanguera (located at the Peage of Sanguera), and Mission Tové (located within the EPP of Mission Tové). In addition, piezometers such as Légbassito (found within the CEG

Légbassito), Akato (found within the EPP Akato), and Campus Sud (located within the University of Lomé) tapping the Pa aquifer were considered. Finally, the Apéssito piezometer (located within the EPC Apéssito) was considered for the Ma aquifer.

A simultaneous analysis of rainfall and hydraulic head fluctuations (considering the 2017 annual cycle) in the AP (see annexes 5a) depicted that the increase in hydraulic head for the CT aquifer (i.e., Sanguera and Attiegou piezometers) reaches its peak in the RS (June). Nevertheless, the observed changes in the hydraulic head show that this increasing process started way before the RS. As a matter of fact, an increase in the hydraulic head is estimated to vary between 0.4 and 1 m and between 0.02 and 0.42 m for the period of January to June and March to June (RS), respectively. These results suggest multiple sources of the CT aquifer hydraulic head rise, including recharge from rainfall and potentially the influx from other water systems (i.e., rivers, adjacent groundwater basins, sewage, and the ocean). In addition, it is observed that the peak for both rainfall and hydraulic head of the CT aquifer is in June, implying a very short lag time (days) between rainfall and the aquifer response. Contrary to the CT aquifer, it is observed that the Pa aquifer (see Annex 5b) does not respond to the early rainfall up to the month of July (peak), where the aquifer shows an increase in its hydraulic head up to the month of August, after which the hydraulic head starts decreasing again. These results depict that rainfall contributes to a certain extent to the recharge of the aquifer. Furthermore, while comparing the piezometric peak and the rainfall peak, it can be inferred that the time lag until the response of the Pa aquifer is 1 month. Finally, for the Ma aquifer, barely any change in relation to the rainfall can be seen, inferring no or limited direct contribution of rainfall to the rise of the aquifer hydraulic head.

A general decrease in the hydraulic heads has been observed for all the aquifers considered, with the average values being 2.47 m (ranging between 0.05 m observed at the Mission Tové piezometer located in the northern part of the study area and 4.88 m observed at the campus Nord piezometer located in the central part of the study area), 3.36 m (ranging between 1.45 and 5.27 m), and 1.75 m (values ranging between 1.45 and 5.27 m) for the CT aquifer, Pa aquifer, and Ma aquifer, respectively. This observed pattern in hydraulic heads can be due to a decrease in recharge or an increased water withdrawal. Though the study area has been reported to be subject to a non-significant increase in rainfall over the period of 1991–2020 (with an estimated average value of 875.4 mm against 931.45 mm recorded over the period 2016–2019), the experienced increase in temperature estimated at 0.6 °C over this period (Chapter five: Tables 5.4 and 5.5) combined with the change in the LULC (characterised by an increase in built-up areas at the expense of mixed vegetation/savannah and agricultural areas

as depicted in Chapter four, Table 4.2) might change the overall recharge rate. In fact, the above-highlighted situation subjects the study area to increased evapotranspiration and runoff, which will eventually affect the recharge rate, especially for the unconfined and shallow aquifers such as the CT and MaS. As for the deep aquifers, including the Pa aquifer and the Ma aquifer (relying less on rainfall and occurring in high depths), the decrease in their hydraulic heads might be linked to continuous water withdrawal as the result of a growing population. As a matter of fact, a study carried out by the ANTEA (2013) reported that the estimated ratio of water withdrawal to water recharge amounts to 5%, 66%, and 43% for the CT aquifer, Pa aquifer, and Ma aquifer, respectively.

It has been observed for most of the piezometers tapping the CT aquifer, which is shallow and unconfined, that a decrease in their hydraulic heads occurs basically during the DS (July–August), which coincides with the period when deep aquifers (Pa aquifer) show a low decrease or increase in their hydraulic heads, suggesting a recharge of the Pa aquifer by the CT aquifer. These results are confirmed as the Pa and Ma aquifers are reported to be recharged by the CT aquifer in the northern part of the sedimentary coastal basin, where it lies directly on these formations (Gnazou et al., 2017; Akakpo, 2017; Gnazou, 2008; DHE, 1982).

6.3.2 2021/2022 Hydraulic Head in AP

The piezometric maps (see Figures 6.14a-c) of the aquifers considered, including the CT aquifer (combined with the MaS a continuity), Ma aquifer, and Pa aquifer, were established from the hydraulic heads collected across the AP (Annex 5d-f).

Heterogeneous hydraulic heads were found for the CT-MaS aquifer (Figure 6.14a), with a decreasing trend following the topography (towards the south), representing the flow direction. Based on the above, the ocean (located in the southern part), characterised by a lower hydraulic head, represents the natural discharge zone of the aquifer, while the northern part stands as the recharge zone. In fact, these results confirm the findings of Gnazou et al. (2018) and Bleza et al. (2020a), who gave more precision in reporting a north–west to south–east direction of the flow. The obtained hydraulic heads for the RS/DS vary between -0.74/-2.19 m (in the southern part) and 29.5/23 m in the northern part of the plateau (with a seasonal variation ranging between 0.01 and 2.63 m). The map also depicts a low hydraulic head around Cacaveli (TdE water pumping field), which represents a depression with a plausible contribution of the ocean in that area, as highlighted by Bleza et al. (2020b), comparing the field as a sink of secondary water flows. Though built based on a few water points located mainly in the southern and central parts of the study area, the hydraulic heads for the Pa aquifer are found to be below

sea level and range between -7.94/-9.24 and -13.61/-16.91 m for the RS/DS (with a season variation of 0.01 and 2.63 m). Typically, as for the CT aquifer, the flow of water for the Pa aquifer follows the topography (Figure 6.14b). Finally, water points from the Ma aquifer (Figure 6.14c), mainly located in the northern part of the study area, also depict piezometry that follows the topography, specifically a southeastward direction. The hydraulic heads obtained vary between 17.87/17.43 and 30/30.86 m for the RS/DS (with a seasonal variation ranging between 0.44 and 0.86 m).

There is a need to highlight that some observed seasonal differences in the hydraulic heads can be attributed to the seasonal fluctuation but also to the fact that some points were not considered for the two seasons due to limited access or refusal to access these points. In addition, the spatial distribution of the water points considered in the context of this study can be explained by the accessibility of these aquifers (in terms of their depth of occurrence) across the study area.

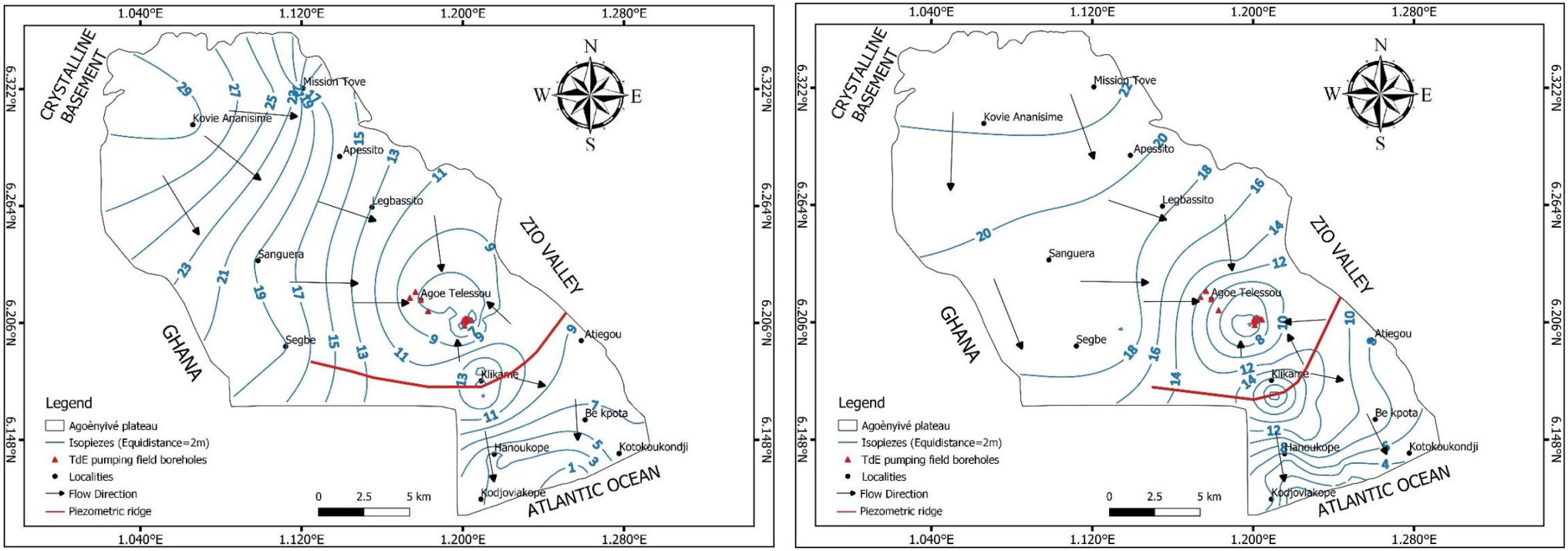

Figure 6.14a: Hydraulic Head Map of CT-MaS aquifer for the RS 2021 (Left) and the DS 2022 (Right)

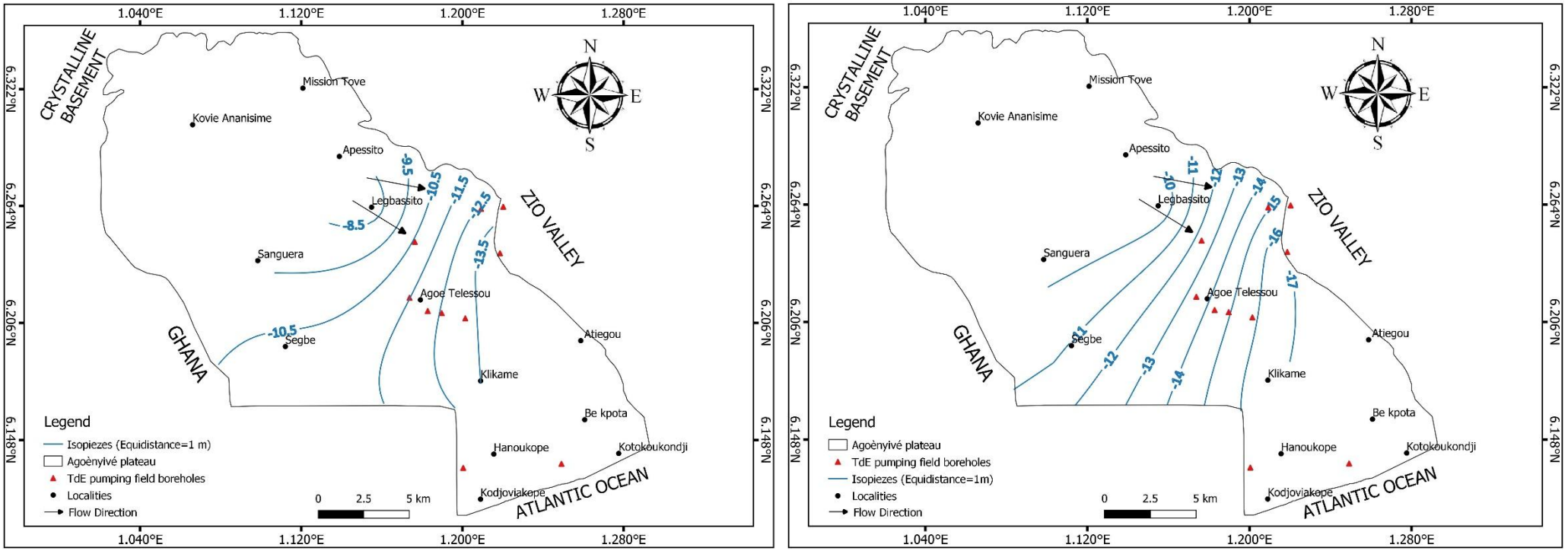

Figure 6.14b: Hydraulic Head Map of Pa Aquifer for the RS 2021 (Left) and the DS 2022 (Right)

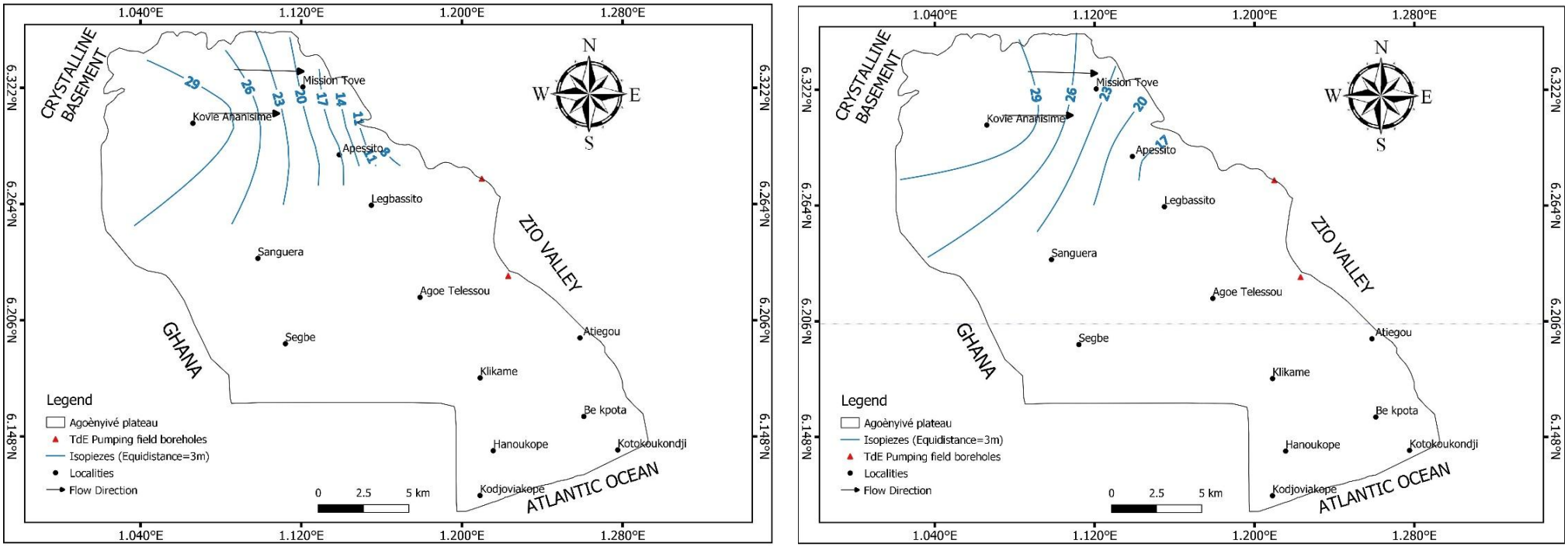

Figure 6.14c: Hydraulic Head Map of Ma Aquifer for the RS 2021 (Left) and the DS 2022 (Right)

6.4 Seawater-freshwater Interface Characterisation in the AP

The Electrical Resistivity Tomography (ERT) results presented as 2D electrical resistivity structures show a pattern of gradational colour representing a variation from a low resistivity to a high resistivity, indicating variation in the subsurface lithology as well as the fluid content. The interpretation of the resistivity results under this section is based on Section 2.3 and Table 6.5, describing the depth of occurrence of the aquifers considered and the lithology of the CT aquifer (geological materials depth of their occurrence presented from the top to the bottom) at the geophysical sites considered, respectively, but also the bulk resistivity range of natural materials proposed by authors as described in Table 6.6.

Table 6.5: Summary of the Geological Formation Occurrence with Depth in the CT Aquifer for the Selected Geophysics Sites

Formation	Klikamé	Cacaveli	Agoè	Ahanoukopé	Lagoon/beach
Shallow Crown	25 to10	30 to15	40 to 20	10 to 0	-
Clay	-	-	-	0 to -25	-
Clayey Sand	10 to -50	15 to 0	20 to 10	-25 to -45	5 to -70
Sand	-50 to -70	0 to -40	10 to -20	-45 to -110	-
Substratum	-70	-40	-20	-110	-70

* The formation depth occurrence is expressed in terms of elevation (m) with the negative sign standing for values below the mean sea level.

Table 6.6: Literature Based Summary of Natural Materials' Bulk Resistivity

Natural material	Bulk resistivity φ_b(Ωm)		
	Marechal et al. (1970), De Moor and De Breuck (1964), Marechal et al. (1957)	Oyedele and Ekpoette (2011)	Sognon et al. (2018)
Dry sand	100–1000	100–724	-
Clay		2–21	-
Sandy Clay		32–39	-
TopSoil		16–92	-
Sand with fresh pore water	40–100	-	≥120
Loam with fresh pore water	25–40	-	
Arenaceous clay with fresh pore water	15–30	-	
Clay with fresh pore water	6–15	-	
Sediment with saline pore water	1–10	-	10–120 (saline and brackish)

The location of the seawater-freshwater interface was determined through a cross-validation process considering the lithology of the geophysical sites and geological formation bulk

resistivity (Tables 6.5-6.6) and the obtained true resistivity values (Figure 6.15). In addition, the cross-validation also considered the available physicochemical data from boreholes close to the geophysical profiles (TDS and chloride content). Finally, the interpretation of the findings is built around the profile obtained around Ahanoukopé, where almost all the geological materials in the study area are represented along with their depth of occurrence, as well as the profile along the seashore, which represents a uniform lithology.

In addition, it has been observed that a layer characterised by very low resistivity (≤1 Ωm) occurs at greater depth, corresponding to the upper limit of seawater resistivity (1 Ωm), better captured by a dipole-dipole array, and observed at a depth of 40 m b.s.l. and beyond. The ERT.2 (East–West) confirms the results of the ERT.1. These findings point to the presence of a mixing zone at Ahanoukopé, detected between 80 and 265 m of the lateral profile distance and at 20 m to more than 40 m b.s.l. or as shallow as 10 m b.s.l. These results are in accordance with geochemical results showing high salinity with TDS values greater than 4000 $mg.L^{-1}$ around Gbadago and Kodomé, which are quite close to these profiles (GCC80 and GCC95). Though close to the lagoon, those TDS values go beyond the TDS registered for the surrounding lagoons (< 2000 $mg.L^{-1}$), confirming marine intrusion (southern–eastern intrusion) around the Ahanoukopé area. In addition, shallow wells (5 m on average) considered around Ahanoukopé (GCC137, GCC138, GCC140, and GCC142) depict high EC/TDS ($\mu S.cm^{-1}$ / $mg.L^{-1}$) with observed values of 2930–10760/1647–8280.

The ERT 3 (North–South), carried out at 0.28 km from the seashore and along the beach trip, shows areas of low resistivity (0.2–10 Ωm) as a continuous layer between 2 and 20 m b.s.l. Nevertheless, this layer occurs as shallow as 5 m a.s.l. in some areas of the profile and as deep as 30 b.s.l. in the northern part of the profile. The layer is set as a sandwich between two layers (the shallow layer occurs between 5 m a.s.l. and 5 m b.s.l., while the deep layer starts occurring at 20 m b.s.l.) of moderate to high resistivity (> 10 Ωm) covering almost the entire profile. In a uniform geological setting (essentially clayey sand), the structure of layers suggests that the pore water of these various layers is different. Based on its resistivity distribution across the structure, it can be suggested that the layer with low resistivity represents clayey sand with saline pore water. Gardening wells sampled (on average 5 m deep) along the profile depict areas slightly affected (GCC147) by the seawater intrusion, showing an EC/TDS ($\mu S.cm^{-1}$/$mg.L^{-1}$) of 1405/925.

The ERT.4 (North–South), located in Cacaveli (8 km from the seashore), depicts a unique structure with high resistivity sections with a downward-decreasing pattern. It includes a discontinuous, thin, dry clayey sand layer at the top, 5 m deep, with general resistivity values

of 200 Ωm and reaching values of 300 Ωm in certain areas, which represents the shallow crown. Following this layer is a thick clayey sand layer depicting higher resistivity values compared to values obtained around Ahanoukopé, suggesting clayey sand with fresh pore water. At the bottom, a more uniform and continuous layer is observed starting from 0 m up to 20 m b.s.l. (10–50 Ωm), corresponding to the sand formation, thus representing sand formation with fresh pore water. These results are confirmed by a 37-m-deep (GCC20) sampled borehole located some meters from the profile, depicting a TDS of 718 $mg.L^{-1}$, corresponding to freshwater according to the WHO thresholds.

The ERT.5 (North–South), carried out within the University of Lomé, at around 6 km from the seashore, shows a heterogenous distribution of resistivities (1–300 Ωm) covering almost the entire profile, showing the geological structure, including basically clay, sand, and clayey sand. A three-layer structure can be observed through the profile, including the dry clayey sandy formation (≥ 200 Ωm) occurring consistently in low depths (from the surface and reaching 15 m a.s.l. in some areas) and randomly in middle and high depths (up to 25 m b.s.l.) in most cases as vertical formations (from the surface to the bottom). At the surface, this layer corresponds to a shallow crown, while those occurring at high depth may be artifacts. The second layer (15–100 Ωm), occurring generally from 15 m a.s.l. to 25 m b.s.l. in some areas, represents clay, sand, or clayey sand formations filled with freshwater. The last layer, occurring randomly, mostly at high depths (15 m a.s.l.–25 m b.s.l.) with rare occurrences at low depths (ranging between 20 and 25 m a.s.l.), shows low resistivities (≤10 Ωm), corresponding to clay or clayey sand (in the northern part) and sand formation (in the southern part of the profile) filled with saline pore water. These results are confirmed by the physicochemical characteristics of a 74-meter-deep piezometer capturing the CT aquifer (GCC49) located near the profile in its northern part with an EC/TDS value ($\mu S.cm^{-1}/mg.L^{-1}$) of 2160/1158, slightly above the threshold for drinking water (WHO, 2011). These results suggest the occurrence of punctual mixing zones across the profile, occurring at depths ranging between 15 m a.s.l. and 25 m b.s.l.

The ERT.6 (North–South), carried out 11 km away from the seashore (Agoè), depicts a heterogeneous distribution with an observed resistivity greater than 10 Ωm. The observed structures having resistivity ranging between 15 and 100 Ωm correspond to sand (occurring between 10 m a.s.l. and 20 m b.s.l. and as shallow as 40 m a.s.l.), while those having resistivity around 200 Ωm occurring between 40 m a.s.l. and 10 m b.s.l. represent clayey sand formations with fresh pore water. These results are in line with the physicochemical characteristics of a 43-m-deep borehole (GCC34) close to the profile and depict an EC/TDS value ($\mu S.cm^{-1}/mg.L^{-}$

^{1}) of 733/321, depicting freshwater. Besides, patches with very high resistivity (≥ 100 Ωm) have also been observed both at the surface and at high depth, suggesting a shallow crown and vertical or horizontal structures such as pipelines, respectively.

The ERT.7 (North–South), carried out at 10 km away from the seashore and close to the Togolaise des Eaux (TdE) pumping field, shows two zones of low resistivities (< 10 Ωm) around 107–145 m (at a depth of 5 m b.s.l.) and 205–360 m (at a depth ranging from 0 m to 15 m b.s.l.) of the lateral profile distance corresponding to sand formations. It is also observed that there is a very low resistivity layer (~1 Ωm) around 295–335 m at a depth of 1 m b.s.l., representing the upper limit of seawater. The physicochemical characteristics of a 37-m-deep borehole (GCC32), depicting respectively an EC/TDS value ($\mu S.cm^{-1}$/$mg.L^{-1}$) of 733/834, suggest an up-coning with mixing zones occurring around 107–145 of the lateral profile distance (at a depth of 5 m b.s.l.) and 205–360 m of the lateral profile distance (at a depth ranging between 0 m/15 m b.s.l. and 11/20 m b.s.l.). As a matter of fact, the hydraulic head of the CT aquifer in this zone is reported to be as low as 0 m, while at the same time hosting one of the largest pumping fields (managed by the Togolese water supply company), creating a possibility for an up coning.

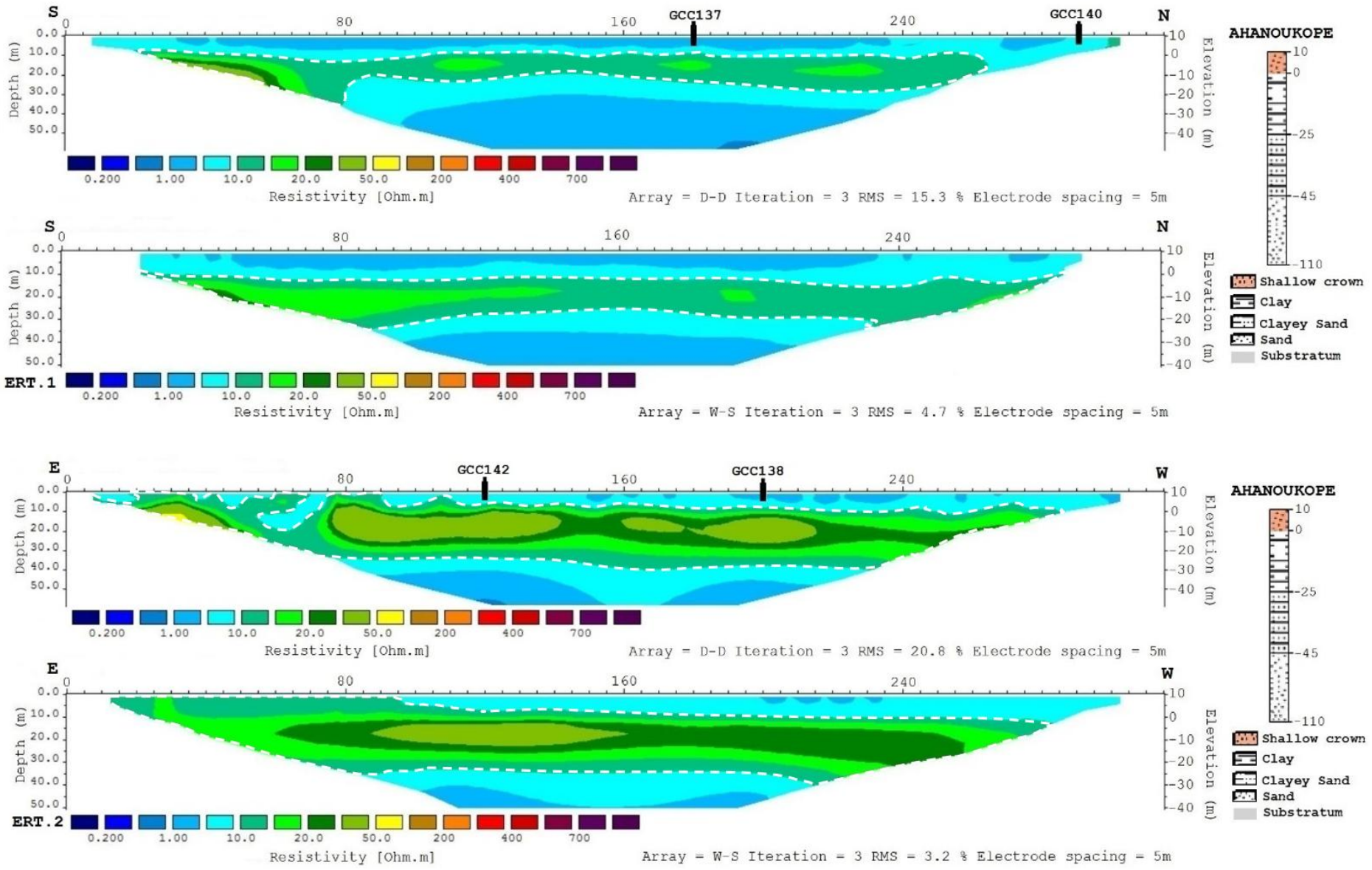
S
N
GCC137
GCC140
Depth (m)
Elevation (m)
Resistivity [Ohm.m]
0.200
1.00
10.0
20.0
50.0
200
400
700
Array = D-D Iteration = 3 RMS = 15.3 % Electrode spacing = 5m
Array = W-S Iteration = 3 RMS = 4.7 % Electrode spacing = 5m
ERT.1
E
W
GCC142
GCC138
Array = D-D Iteration = 3 RMS = 20.8 % Electrode spacing = 5m
Array = W-S Iteration = 3 RMS = 3.2 % Electrode spacing = 5m
ERT.2
AHANOUKOPE
Shallow crown
Clay
Clayey Sand
Sand
Substratum

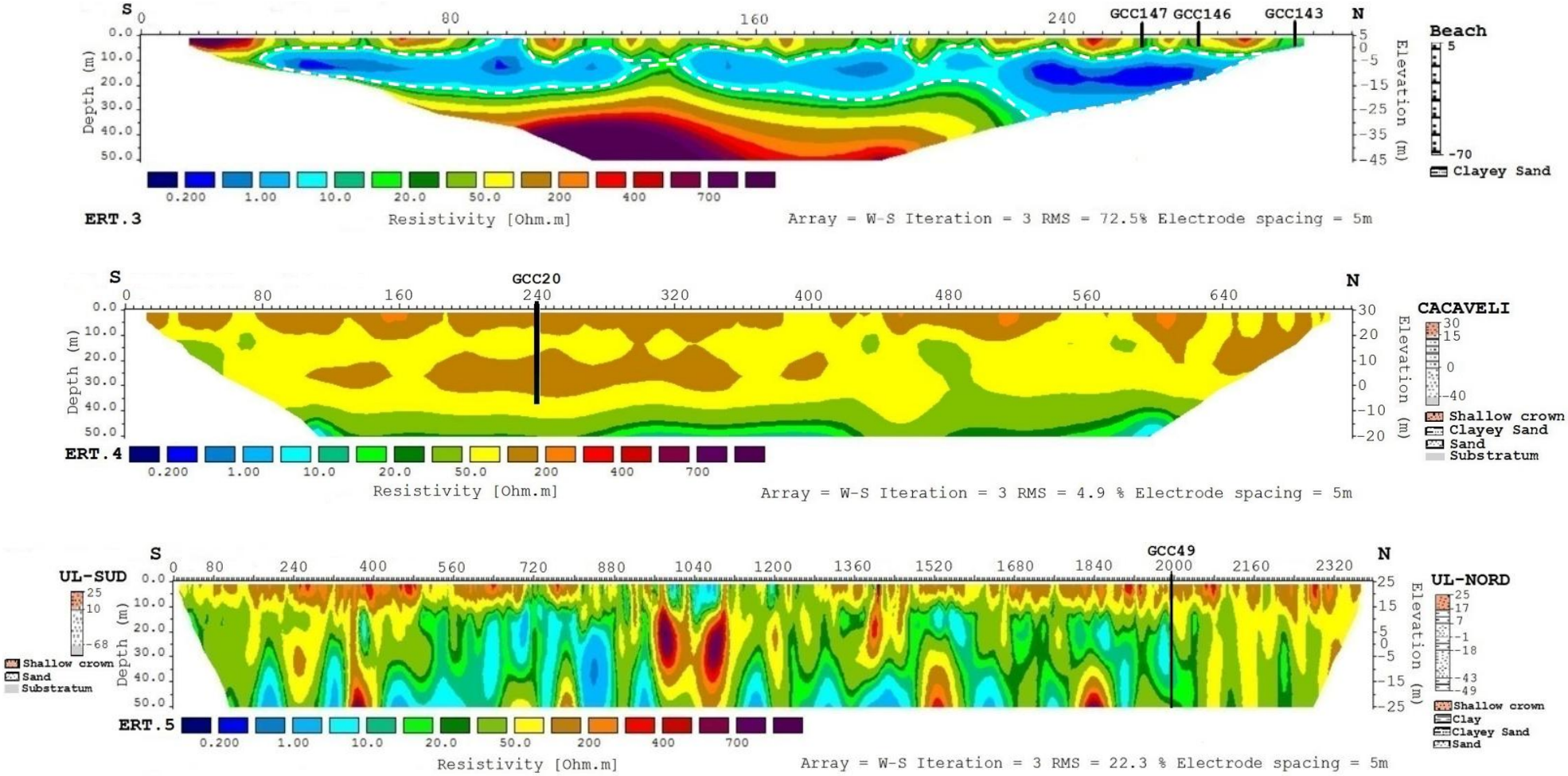
S
N
GCC147 GCC146 GCC143
Beach
Clayey Sand
Depth (m)
Elevation (m)
ERT.3
Resistivity [Ohm.m]
Array = W-S Iteration = 3 RMS = 72.5% Electrode spacing = 5m
GCC20
CACAVELI
Shallow crown
Clayey Sand
Sand
Substratum
ERT.4
Resistivity [Ohm.m]
Array = W-S Iteration = 3 RMS = 4.9 % Electrode spacing = 5m
GCC49
UL-SUD
UL-NORD
Shallow crown
Sand
Substratum
Clay
Clayey Sand
ERT.5
Resistivity [Ohm.m]
Array = W-S Iteration = 3 RMS = 22.3 % Electrode spacing = 5m

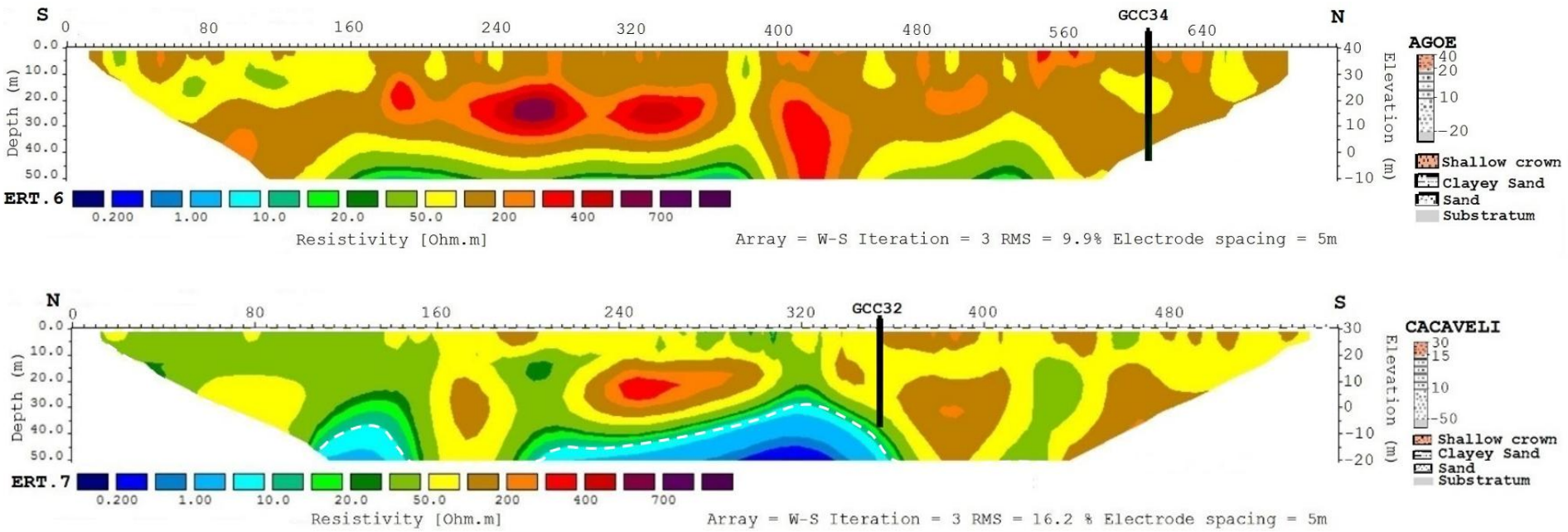

Figure 6.15: Sub-surface Resistivity Distribution in Selected Sites of the AP

The interface is captured in three areas based on the profiles carried, including areas such as Ahanoukopé (ERT.1 and ERT.2), the beach (ERT.3), and Cacaveli (ERT.7). The position and geometry (upper limit, lower limit, and the average thickness) are summarised in Table 6.7.

Table 6.7: Interface Position and Geometry in the AP

Profile	Distance from the Seashore (km)	Interface Elevation ~ depth (m)	Interface Geometry		Average Thickness (m)
			Upper limit (m)	Lower limit (m)	
ERT.1 + ERT.2	2.5	20 (b.s.l) ~30	20 (b.s.l)	40 (b.s.l)	20
ERT.3	0.28	2/5 (b.s.l) ~7/10	5/2 (b.s.l)	15/30 (b.s.l)	10–28
ERT.7	10.17	0/5 (b.s.l) ~30/35	0/5 (b.s.l)	11/20 (b.s.l)	11–15

Results suggest a mixing zone in the AP, confirming the findings of Sognon et al. (2018), who used geophysical methods as well to map out the salinity distribution in the sedimentary coastal basin of Benin and concluded the presence of an interface of a thickness ranging between 8 and 20 m. In addition, it is observed that the increase in distance from the seashore is associated with an increase in the depth of the interface and a decrease in the thickness of the mixing zone. These results corroborate the findings of Sognon et al. (2018) and Agossou et al. (2022), who used geophysical methods and a sharp model, respectively, to define the position of the interface in the CT aquifer of the Sedimentary Coastal Basin in Benin, and Oloruntola et al. (2019), who used geophysics to locate the seawater and freshwater interface in southwestern Nigeria. As a matter of fact, Oloruntola et al. (2019) and Agossou et al. (2022), as found in the AP, reported that the interface becomes deeper while moving inland.

Based on the lithology and the depth of occurrence of the geological formations found around Ahanoukopé and along the beach, it can be inferred for the AP aquifer that clayey sand formation with saline pore water has a resistivity ranging between 1 and 10 m, while clay formation with saline pore water occurring shows resistivity values ranging between 15 and 50 Ωm. In addition, the resistivities of sandy and clayey sandy formations with freshwater pores are inferred from profiles in Agoè (ERT6) and Cacaveli (ERT4), corresponding to ranges of 15–50 Ωm and 100–200 Ωm, respectively. Beyond these resistivity values are basement rocks or weathered rocks.

6.5 Partial Conclusion

The hydro-chemical and isotopic characterisation of the water samples from the existing aquifers in the AP provided a qualitative and quantitative assessment of the water in the multi-

layered aquifer and pinpointed the main processes driving its mineralisation. Furthermore, information on the hydraulic heads and true resistivity distribution helped to suggest the position and geometry of the seawater-freshwater interface in the study area. A multicriteria approach has been considered, combining statistical analysis methods (Principal Component Analysis and Ascendant Hierarchic Clustering), saturation indices, and conventional tools including diagrams and binary plots for hydro-chemical data analysis. For the isotopic dataset, common plots including chlorides versus $\delta^{18}O$, $\delta^{2}H$ versus $\delta^{18}O$, and EC versus $\delta^{18}O$ were considered. Finally, a combination of true resistivity data (which covered only the upper aquifers, including the CT aquifer and the MaS aquifer), lithological data, and physicochemical data of some of the sampled water points close to geophysical profiles has been considered for the characterisation of the seawater-freshwater interface.

The obtained results suggest:

- Potential seawater intrusion in the upper aquifers of AP, including the CT and MaS aquifers, characterised by a predominant presence of chlorinated sodic-potassic facies (Na-K-Cl) facies, which is equivalent to sea/saltwater facies.
- Contribution of the evaporitic mineral's dissolution, base exchange, and evaporation in the mineralisation of aquifers in the AP.
- Both lateral (reaching up to 2.5 km inland) and up-coning seawater intrusion, with a freshwater-saltwater interface found at an average depth of 21 m with a thickness ranging between 10 and 28 m.

CHAPTER SEVEN: DYNAMICS OF SEAWATER INTRUSION IN THE AP

This chapter aims at assessing the dynamics of SWI (in terms of the aquifer hydraulic heads, salinity, and intrusion extent) in the context of climate change (CC), land use, and land cover (LULC) change and continuous groundwater withdrawal, captured through various scenarios of recharge, as well as changes in sea level rise (associated with climate change) and continuous groundwater withdrawal. It is organised into two sections: (i) current and future recharge estimation under the changing climate (RCP 4.5 and RCP 8.5) and land use and land cover using the water balance method, and (ii) the response of the groundwater lens (upper aquifers) to the above-cited changes in the environment using the SEAWAT Model.

7.1 Recharge Estimation in the AP

Interannual Variation in Surface Runoff, Actual Evapotranspiration and Recharge

Current and future surface runoff (Q), actual evapotranspiration (AET), and recharge (R) for the AP have been estimated considering LULC data (Chapter four) and climate data (Chapter five) using the water balance method (Soil Conservation Service Curve Number method and the combined Coutagne-Turc method), with the results summarised in Figure 7.1, Table 7.1, and Annex 8c.

The obtained result of the surface runoff suggests a non-uniform pattern across the AP, just like the pattern shown by the LULC maps and the climatic parameters (temperature and rainfall). The obtained surface runoff ranges between 55 and 317 mm.year^{-1} (as of 2020), with the highest values observed in the southern part of the study area (sub-basin C) and under the "LULC and CC" scenario (as described in section 3.2.4.1: Table 3.14), while the lowest values are found in the northern part of the study area (sub-basin A) and under the “CC" scenario. Considering the year 2020 as the baseline, under the “LULC and CC (RCP 4.5)" scenario, runoff is expected to decrease by 13 mm.year^{-1}, 23 mm.year^{-1}, and 13 mm.year^{-1} for sub-basins A, B, and C, respectively, by 2030, while an increase of 26.9 mm.year^{-1} for sub-basin A and a decrease accounting for 19 mm.year^{-1} and 10 mm.year^{-1} are expected for sub-basins B and C, respectively, by 2050. Under RCP 8.5, the surface runoff is expected to increase by 48/113 mm.year^{-1}, 36/88 mm.year^{-1}, and 44/107 mm.year^{-1} for sub-basins A, B, and C, respectively, by 2030/2050. Under the "LULCC" scenario, the surface runoff is projected to increase by 14/52 mm.year^{-1}, 10 mm.year^{-1}, and 20 mm.year^{-1} for the sub-basins A, B, and C, respectively, for the years 2030/2050. Finally, under the "CC" scenario, the surface runoff is expected to decrease

under RCP 4.5 by 25/19 mm.year^{-1}, 32/28 mm.year^{-1}, and 33/29 mm.year^{-1} and increase under RCP 8.5 by 36/44 mm.year^{-1}, 27/75 mm.year^{-1}, and 26/81 mm.year^{-1} by 2030/2050 for sub-basins A, B, and C, respectively.

AET over the period of 2001–2050 is estimated to be on average 723 mm.year^{-1} (ranging between 631 and 814 mm.year^{-1}), 693 mm.year^{-1} (ranging between 625 and 760 mm.year^{-1}), and 708 mm.year^{-1} (ranging between 628 and 787 mm.year^{-1}), for the Coutagne method, Turc method, and combined Coutagne-Turc method. Considering the year 2020 as baseline (AET: 649 mm.year^{-1}), this parameter based on the combined Coutagne-Turc method is expected to increase by 18/33 and 29/138 mm.year^{-1} by 2030/2050 under RCP 4.5 and RCP 8.5, respectively.

Results show that recharge occurs in the northern part (sub-basin A) and, to a certain extent, in the central part (sub-basin B) of the AP, characterised by low or moderate runoff (Table 7.1). The annual recharge for the years 2001, 2011, and 2020 accounts for 72 mm.year^{-1}, 104 mm.year^{-1}, and 62 mm.year^{-1}, respectively. These results are in line with the findings of Struckmeier and Richts (2006), who reported an average recharge ranging between 15 and 150 mm.year^{-1} in the sedimentary coastal basin in the Gulf of Guinea. For the future recharge, both increasing and decreasing patterns are expected based on the scenario. For the "LULC and CC" scenario, recharge is expected to increase by 30/1 mm by 2030/2050 under the RCP 4.5 and decrease by 34/4 mm by 2030/2050 under the RCP 8.5. For the "LULCC" scenario, the recharge is expected to decrease by 14/52 mm by 2030/2050 in reference to the year 2020. Finally, the "CC" scenario depicts an expected increase in recharge of 51/55 mm by 2030/2050 under the RCP 4.5, a decrease of 21 mm by 2030, and an increase of 65 mm by 2050 under the RCP 8.5. It has been observed that the expected slight increasing (RCP 4.5) and decreasing (RCP 8.5) rainfall pattern against an increasing temperature pattern is expected to be associated with an increase in recharge under RCP 4.5 (both 2030 and 2050) and RCP 8.5 (2050) and a decrease in recharge under RCP 8.5 (2030). These results may be explained by the fact that the trend analysis was carried out over a period of 2021–2050, while the recharge estimation was carried out on a punctual basis (2020, 2030, and 2050 in this context). In this case, the selected years (2030 and 2050) depict higher rainfall values compared to the year 2020, the baseline. As a matter of fact, Abdelaziz et al. (2020) reported using a combined CN and method over Abidjan, an urban setting like the AP, and reported a decrease in rainfall over time associated with both a decrease in recharge and an increase in recharge (in reference to the year 1990) for the years 2000 and 2016, respectively.

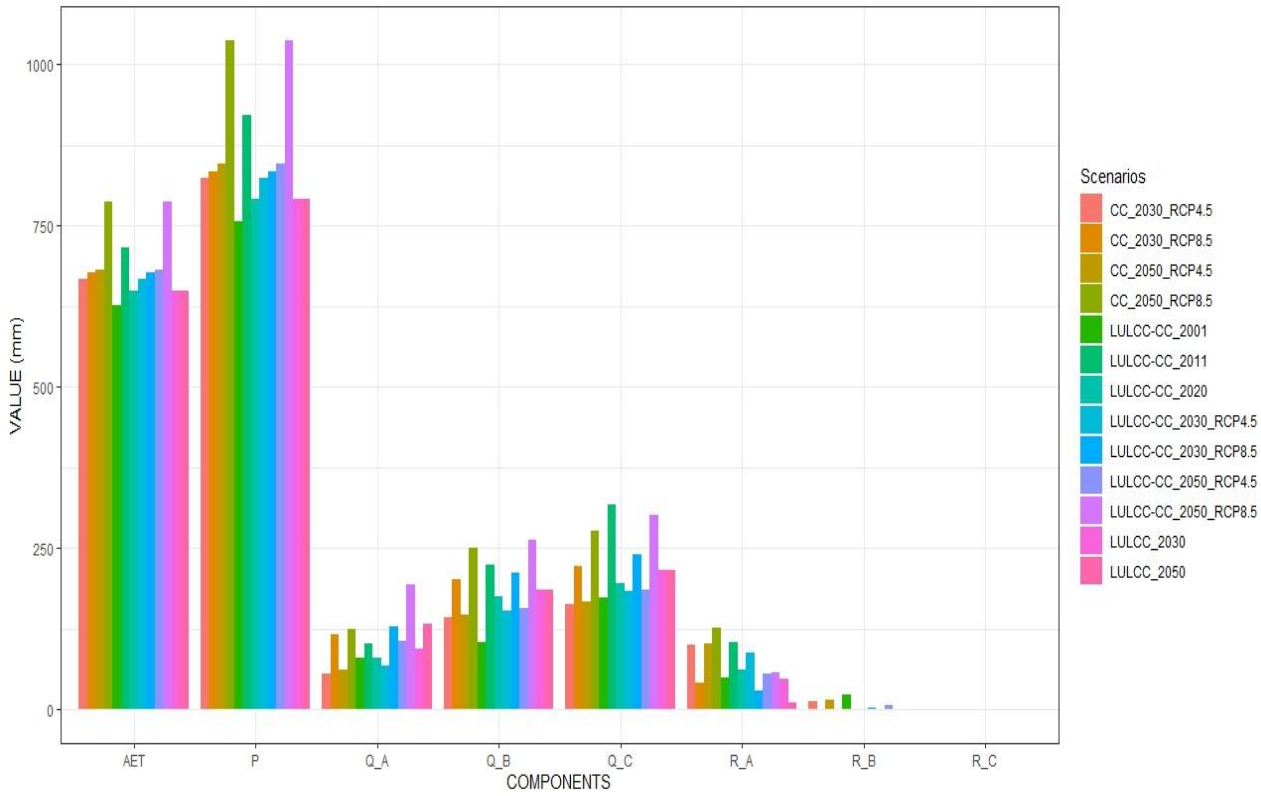

Figure 7.1: Chart Showing Precipitation, Actual Evapotranspiration, Runoff and Recharge under Various Scenarios in the AP

*P, AET, Q and R standing for precipitation, actual evapotranspiration, runoff and recharge.
* LULCC: Land use land cover change scenario; CC: climate change scenario and LULCC-CC: land use land cover change and climate change scenario.

Table 7.1: Statistics of Water Balance Components in the AP: Precipitation, Actual Evapotranspiration, Surface Runoff and Recharge under Various Scenarios

Parameters	Annual Precipitation	Average Temperature	Average AET (Coutagne-Turc)	Q_A	Q_B	Q_C	R_A	R_B	R_AP	R_AP (%)
SCENARIO 1: LULCC - CC										
2001	757	26.8	627.9	80.2	105.5	174.2	48.8	23.5	72.3	9.5
2011	922.6	26.7	716.6	102.2	223.6	317	103.8	-	103.8	11.3
2020	791.9	27	649.3	80.4	176.2	195.9	62.2	-	62.2	7.9
2030_RCP4.5	823.9	27.1	667.7	67.2	153.1	183.3	89	3.1	92.1	11.2
2030_RCP8.5	834.6	27.8	677.8	128.3	212.2	240.3	28.5	-	28.5	3.4
2050_RCP4.5	845.7	27.4	682	107.3	157.1	185.6	56.5	6.7	63.2	7.5
2050_RCP8.5	1038.3	28.6	787.2	193.1	263.7	302.4	58.1	-	58.1	5.6
SCENARIO 2: LULCC										
2030	791.9	27	649.3	94.2	185.9	215.6	48.4	-	48.4	6.1
2050	791.9	27	649.3	132.2	185.9	215.6	10.4	-	10.4	1.3

SCENARIO 3: CC										
2030_RCP4.5	823.9	27.1	667.7	55	143.8	162.9	101.1	12.4	113.5	13.8
2030_RCP8.5	834.6	27.8	677.8	116	203	222	40.8	-	40.8	4.9
2050_RCP4.5	845.7	27.4	682	61.7	148.1	166.7	102	15.6	117.6	13.9
2050_RCP8.5	1038.3	28.6	787.2	124.5	251	276.9	126.6	0.2	126.8	12.2

*LULCC: Land use land cover change; CC: climate change; LULCC-CC: combination of land use land cover change and climate change**;** Q: runoff; R: recharge and R (%): recharge rate.

7.2 Seawater Intrusion Modelling

This section presents the calibration and validation (steady and transient state) of the groundwater flow and solute transport model developed for the upper aquifers (CT aquifer and MaS aquifer) of the AP through the SEAWAT program/code, the simulated future groundwater response considering various scenarios (including single scenario-based recharge, sea level rise, continuous groundwater withdrawal, and a combined scenario) under transient state (hydraulic heads and salt concentration) and intrusion extent.

7.2.1 Model Calibration and Validation

The flow model and transport model were calibrated and validated using the measured hydraulic head and TDS data from the RS 2021 and DS 2022, respectively. The evaluation of the performance of the model developed is mainly based on the simulated versus observed hydraulic head and salt (TDS) concentration chart, captured in this context through the residual values, the water budget obtained during calibration, as well as some key metrics including the RMSE, R^2, PBIAS, and NSE (as described in section 3.2.2.1).

The calibration (Table 7.2 and Figure 7.2a) for both the steady and transient states of the flow model shows a very good fit between the simulated and observed data with a good NSE (NSE_{steady} = 0.86, $NSE_{transient}$ = 0.84), coefficient of correlation (r_{steady} = 0.93, $r_{transient}$ = 0.94), and coefficient of determination (R^2_{steady} = 0.86, $R^2_{transient}$ = 0.87). On the other hand, the calibration of the transport model (Table 7.2 and Figure 7.2a) shows satisfactory fit with a satisfactory NSE (NSE_{steady} = 0.66, $NSE_{transient}$ = 0.65), coefficient of correlation (r_{steady} = 0.82, $r_{transient}$ = 0.81), and coefficient of determination (R^2_{steady} = 0.66, $R^2_{transient}$ = 0.66).

Table 7.2: Statistics for the Calibration and Validation of the Flow Model

	Flow			**Transport**		
	Calibration		**Validation**	**Calibration**		**Validation**
	Steady	Transient	Transient	Steady	Transient	Transient

RMSE*	2.55	2.68	2.51	274.85	215.99	329.93
PBIAS (%)	2.2	2.4	-10.4	-4.6	3.3	11.5
NSE	0.86	0.84	0.71	0.66	0.65	0.54
R^2	0.86	0.87	0.77	0.66	0.66	0.57
r	0.93	0.94	0.88	0.82	0.81	0.76
KGE	0.92	0.88	0.82	0.73	0.68	0.65
SEE*	0.63	0.67	0.53	68.14	69.04	74.68
Residual mean*	0.26	0.28	-1.11	-35.54	25.14	91.98

*RMSE, SEE, and the residual mean are expressed in m for the hydraulic head and mg.L^{-1} for the salt concentration.

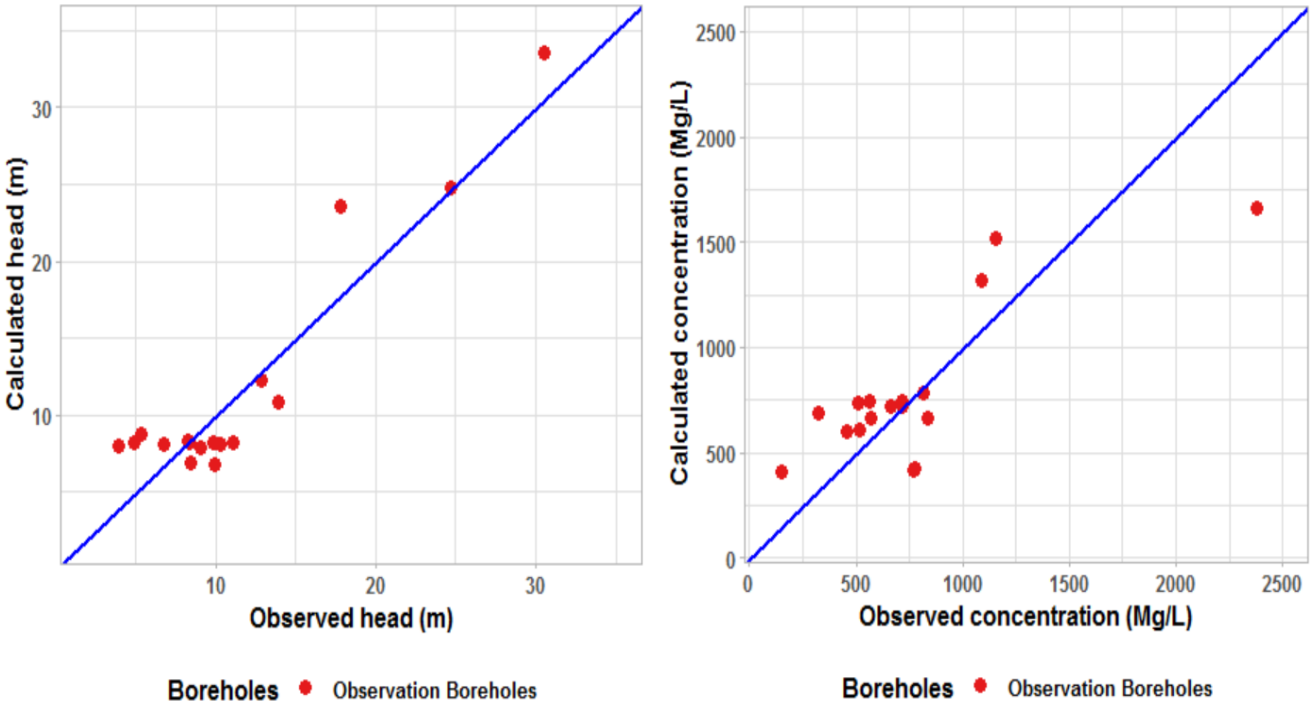

Figure 7.2a: Observed Vs. Calculated Hydraulic Head (Left) and Concentration (Right) during Model Calibration

During the model calibration (transient state), the calculated hydraulic head varies between 6.82 and 33.56 m (Annex 10). The resulting piezometric map captured the dome in the northern part, representing areas of recharge with high hydraulic heads as well as the water divide observed in the southern part (Figure 7.2b), reported by Bleza et al. (2020a).

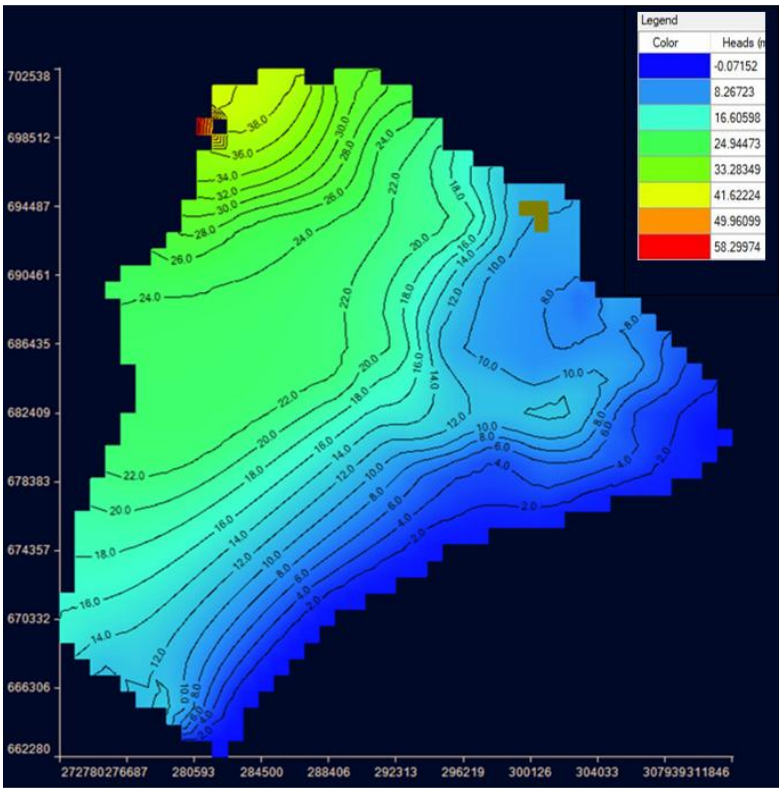

Figure 7.2b: Hydraulic Head Distribution under Transient State Simulation

Nevertheless, it has been observed that the simulated hydraulic head has been overestimated around the Cacaveli area and in the northern part of the study area (with residuals reaching values of 5 m) while being underestimated around the Klikamé and Agoè areas (with residuals reaching values of 3 m). For the salt concentrations, values range approximately between 412 and 1660 $mg.L^{-1}$ (Annex 10) during the same process. The observed difference between the simulated values and observed values, either with regard to the hydraulic head or the salt concentration, can be due to uncertainties in the model and, maybe, errors in the measurement, as most of the water points considered were not collected during the same month but over a season.

The validation of the ground flow model and transport model for both the steady and transient states are depicted in Figure 7.3 (in addition to Table 7.2). The validation of the ground flow gives a very good fit between the simulated and observed data with a good NSE ($NSE_{transient} = 0.71$), coefficient of correlation ($r_{transient} = 0.88$), and coefficient of determination ($R^2_{transient} = 0.77$). As for the transport model validation, a satisfactory fit is obtained with a satisfactory NSE ($NSE_{transient} = 0.54$), coefficient of correlation ($r_{transient} = 0.76$), and coefficient of determination ($R^2_{transient} = 0.57$) during the transient state run.

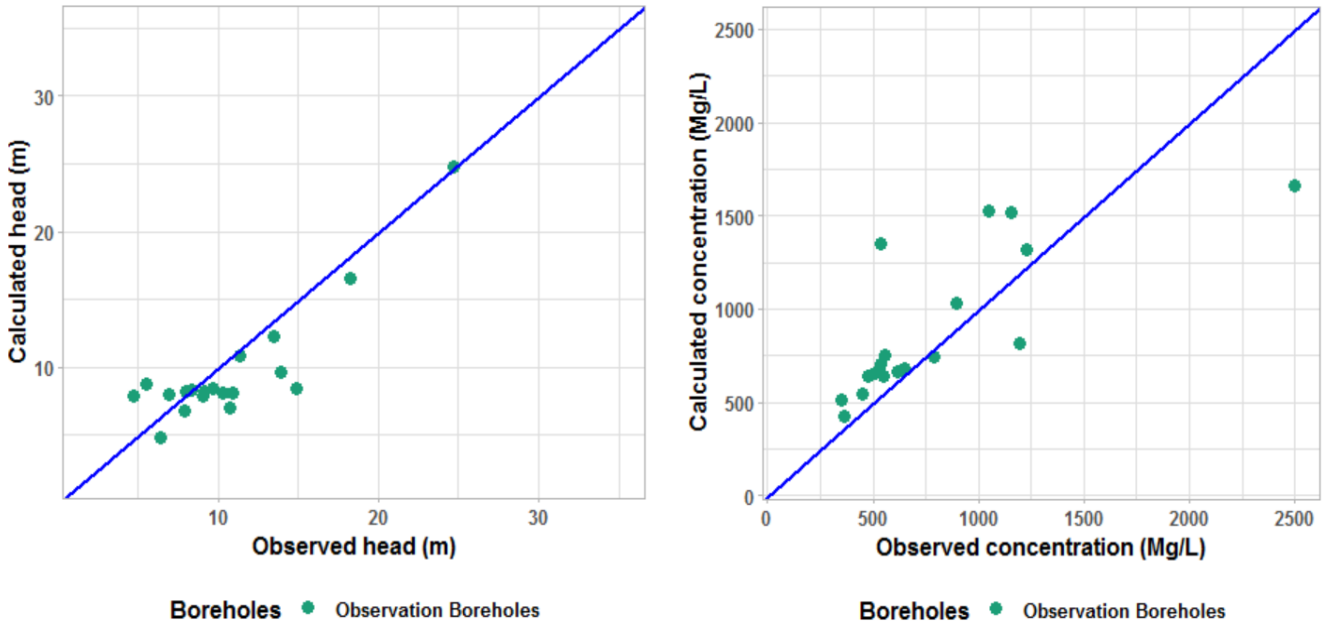

Figure 7.3: Observed Vs. Calculated Hydraulic Head (Left) and Concentration (Right) during Model Validation

The results from the scatter plot as well as the various metrics considered were cross-checked with the water balance captured through the water budget, as suggested by Touré et al. (2016) and summarised in Table 7.3.

The system is governed by inflows and outflows. In the case of the AP, at the steady state, water entering the system is found to be recharged not only from rainfall but also from boundaries (essentially rivers and oceans), accounting for 50% and 49.89%, respectively. On the other hand, discharge is done naturally (exchange with lower aquifers, rivers, and oceans) and artificially (groundwater withdrawal), accounting for approximately 93% and 6%, respectively. In the case of the AP, the balance is negative, showing slightly greater outflow than inflow. This can be explained by the highlighted decrease in recharge estimated at 104 $mm.year^{-1}$ in 2015 (as of 2011) against 62 $mm.year^{-1}$ in 2021 (as of 2020) or plausible flux exchange with other aquifers, apart from the constant heads and/or calculation/model error. The flux exchange between aquifers can be confirmed by various studies that reported that Pa and Ma aquifers are recharged by the CT aquifer in the northern part of the coastal sedimentary basin, where it lies directly on these formations (DHE, 1982; Gnazou, 2008; Gnazou et al., 2017; Akakpo, 2017). As a matter of fact, Gnazou et al. (2017) found using MARTHE while studying the coastal sedimentary basin of Togo that lower aquifers such as the Palaeocene and Maastrichtian are recharged by the CT aquifer under study in their northern part, exchanges that were not captured in this study.

Table 7.3: Water Balance for Upper Aquifers for the Year 2021: Steady (transient) State

COMPONENTS	INFLOW (m^3/day)	OUTFLOW (m^3/day)
STORAGE	0 (73170471)	0 (4344624.8)
CONSTANT HEAD	208004438.9 (208552487.4)	389912525.8 (379058066.7)
WELLS	12900 (12900)	27394063 (27878473.7)
RECHARGE	208801215.2 (129005360)	0
DCDT	109250.4 (242862)	33108 (110471.8)
TOTAL	416927804.6 (410984080.6)	417339696.9 (411391637)
INFLOW–OUTFLOW		-411892 (-407556)

*Discrepancy rate of -0.10 while values in the parathesis stand for the transient state run.

7.2.2 Seawater Intrusion: Upper Aquifers' Response to Environmental Changes

The impacts of CC, changes in LULC, continuous groundwater withdrawal and sea level rise (SLR), and the combination of all the scenarios on groundwater lens response quantity and quality were captured through current (2021) and future (2021–2050) system recharge, hydraulic head, and salinity concentration (TDS). Finally, the area affected by SWI (extent of the intrusion) was derived in reference to drinking water guidelines from the WHO.

7.2.2.1 Recharge Projection in the AP

Changes in the upper aquifers recharge in the AP are found to vary depending on the scenario considered. Results cover scenarios B1 (LULCC), B2 (CC), and B3 (LULC-CC). Both increases and decreases are expected by 2030 and 2050 (Annex 11). For the B1 scenario, the recharge is expected to greatly decrease (estimated at 22.23% and 83.50% by 2030 and 2050, respectively). Under the scenario B2, the recharge is expected to increase by 76.90% (2030) and 83.33% (2050) under the RCP 4.5, while the RCP 8.5 shows a decrease of 36.34% and an increase of 97.60% by 2030 and 2050, respectively. For the combined LULC and CC scenario (B3), the recharge is expected to increase (estimated at 47.95% and 1.51% by 2030 and 2050, respectively) and decrease (estimation of 55.61% and 9.50% by 2030 and 2050) under RCP 4.5 and RCP 8.5, respectively. This tendency of change confirms the results obtained using the combined Turc-Coutagne method. The expected increase in recharge by 2050 under the RCP 8.5 while rainfall is expected to undergo a decrease over the period of 2021–2050 under the same scenario can be explained by the fact that, contrary to the trend analysis where time series was considered, punctual years were considered for the estimation of the recharge. As a matter of fact, the annual rainfall reported over the AP in 2050 under the RCP 8.5 was 1038.3 mm compared to the baseline recording an annual rainfall of 791.9 mm.

7.2.2.2 Simulated Hydraulic Head and Salinity Concentration in the AP

The following results are presented within the framework of this study and give the evolution of the hydraulic head and salinity concentration (TDS) under different scenarios (described in section 3.2.4.2.7: Table 3.17) considered (Tables 7.4a-b and Figures 7.4a-c). Because of the limited spatial distribution of the initial observation points, additional points have been considered at the cell level (including points located in the extreme south and close to the ocean but also points close to the Cacaveli and Agoè Télessou water pumping fields: Obs 1–15).

For scenario A (continuous groundwater withdrawal), observation points depict an expected drop in the hydraulic heads ranging between 0.01/0.02 and 4.65/7.15 m by 2030/2050. These changes in areas close to the ocean (decrease in head estimated to range between 0.01/0.02 and 0.3/0.7 m by 2030/2050) are expected to be associated with an increase in salinity estimated to range between 2.5/71.3 and 8739.6/22799.6 $mg.L^{-1}$ by 2030/2050. Around Cacaveli and Agoè Télessou water pumping fields, apart from Obs14 (increase by 510.5/1708.9 $mg.L^{-1}$ by 2030/2050) and Obs15 (increase by 709.4/782.15 $mg.L^{-1}$ by 2030/2050), the decrease in the hydraulic head (estimated to range between 0.05/0.11 and 4.65/7.15 m) for the remaining water points shows no change in the salinity to refreshing for both 2030 and 2050.

For scenario B1 (LULC), over the study area, the hydraulic head is expected to decrease, ranging between 0.01/0.02 and 5.04/9.79 m by 2030/2050. In areas close to the ocean, the decrease in the hydraulic head (estimated to range between 0.01/0.02 and 0.32/0.7 m) is expected to be associated with an increase in the salinity, ranging between 7.33/142.73 and 8739.38/22776.98 $mg.L^{-1}$. Around Cacaveli and Agoè Télessou water pumping fields, except for Obs 14 (increase by 510.54/1198.22 $mg.L^{-1}$ by 2030/2050) and Obs 15 (increase by 734.48/752.04 $mg.L^{-1}$ by 2030/2050), the decrease in the hydraulic head (0.02/0.06–5.04/9.79 m) for the remaining water points shows no change in the salinity to refreshing for both years.

For scenario B2 (CC), some of the considered observation points are expected to depict a decreasing pattern while others show an increasing pattern in the hydraulic head. Under RCP 4.5, the decrease in the hydraulic head is expected to range between 0.01/0.01 and 0.28/0.73 m and reach values of 0.02/0.06 m by 2030/2050 for areas close to the ocean and areas close to Cacaveli and Agoè Télessou water pumping fields, respectively. For the RCP 8.5, the decrease will vary between 0.01/0.01 and 0.33/0.73 m by 2030/2050 and between 0.02 and 2.19 m by 2030 for areas close to the ocean and areas close to Cacaveli and Agoè Télessou water pumping fields, respectively. On the other hand, the expected increase in hydraulic head under the RCP 4.5 is estimated to vary between 0.01/0.04 and 0.15/0.23 m and between 0.03/0.06 and

0.43/1.18 m for areas close to the ocean and areas close to Cacaveli and Agoè Télessou water pumping fields, respectively. As for the RCP 8.5, the expected increase in the hydraulic head is estimated to vary between 0.05 and 0.23 m and between 0.06 and 0.97 m by 2050 for areas close to the ocean and areas close to Cacaveli and Agoè Télessou water pumping fields, respectively. This observed mixed pattern is expected to be associated with both salinisation and refreshing. As a matter of fact, the expected decrease in hydraulic head in areas close to the ocean will be associated with an increase in the salinity within the range of 243.5/701.28–8741/22842 $mg.L^{-1}$, and 236.5/719.34–8739.22/22835.39 $mg.L^{-1}$ by 2030/2050 for the RCP 4.5 and RCP 8.5, respectively. For areas close to Cacaveli and Agoè Télessou water pumping fields, except for Obs 14 (increase by 510.53/1709.06 $mg.L^{-1}$ and 510.51/1701.44 $mg.L^{-1}$ by 2030/2050 for the RCP 4.5 and RCP 8.5, respectively) and Obs 15 (increase estimated at 713.76/733.04 $mg.L^{-1}$ and 1050.02/782.22 by 2030/2050 for the RCP 4.5 and RCP 8.5, respectively), the remaining water points show no change in the salinity or refreshing. On the other hand, the increasing pattern of the hydraulic head is found to be associated with an increase in the salinity under RCP 4.5, ranging between 0/0 and 242.83/925.91 $mg.L^{-1}$ for areas close to the ocean. For areas close to Cacaveli and Agoè Télessou water pumping fields, except for Obs15 (depicting an increase of 763.88/653.65 $mg.L^{-1}$ for 2030/2050), the increase in the hydraulic head for the remaining water points shows no change in the salinity to refreshing for both 2030 and 2050. For the RCP 8.5, the increase in the hydraulic head observed by 2050 is expected to be associated with an increase in the salinity ranging between 0 and 933.82 $mg.L^{-1}$ for areas close to the ocean. As for areas close to Cacaveli and Agoè Télessou water pumping fields, except for Obs15 (increase by 861.94 $mg.L^{-1}$ by 2050), the increase in the hydraulic head for the remaining water points shows no change in the salinity to refreshing.

For scenario B3 (LULC-CC), the hydraulic head is expected to decrease in most of the cases. Under RCP 4.5, the decrease will range between 0.01/0.02 and 0.28/0.73 m and between 0.01/0.06 and 3.82/6.92 m by 2030/2050 around areas close to the ocean as well as areas close to Cacaveli and Agoè Télessou water pumping fields, respectively. On the other hand, under RCP 8.5, the decrease is expected to be within a range of 0.01/0.02–0.4/0.73 m and 0.02/0.06–2.64/3.56 m by 2030/2050 for areas around the ocean as well as areas close to Cacaveli and Agoè Télessou water pumping fields, respectively. Nevertheless, an increase in the hydraulic head is also expected under the RCP 4.5 in areas close to Cacaveli and Agoè Télessou water pumping fields, amounting to values ranging between 0.71 and 0.85 m (at the water points GCC49 and GCC15 located around Klikamé) only by 2030. The decreasing pattern in the

hydraulic head under the RCP 4.5 is expected to be associated with an increase in salinity ranging within 243.49/1363.51–8740.66/22810.65 mg.L^{-1} and 510.53/733.04–713.76/1709.06 mg.L^{-1} for areas close to the ocean as well as areas close to Cacaveli and Agoè Télessou pumping stations, respectively. Under RCP 8.5, a decrease in the hydraulic head is expected to be associated with an increase in the salinity ranging between 243.42/1363 and 8738.86/22798.76 mg.L^{-1}, and between 510.51/692.86 and 1050.02/1708.8 mg.L^{-1} by 2030/2050 for areas close to the ocean and areas close to Cacaveli and Agoè Télessou pumping stations, respectively. Furthermore, the increase in the hydraulic head to be observed under RCP 4.5 is expected to be associated with no change in salinity.

In scenario C (SLR), some of the considered observation points are expected to depict a decreasing pattern, while others show an increasing pattern in the hydraulic head. Under RCP 4.5, the expected decrease in the hydraulic head by 2030/2050 will amount, respectively, to values ranging between 0.03/0.05 and 0.22/0.58 m and between 0.03/0.09 and 4.65/7.15 m in areas close to the ocean but also in areas close to Cacaveli and Agoè Télessou water pumping fields. For the RCP 8.5, a decrease in the hydraulic head ranging between 0.02/0.04 and 0.22/0.57 m and between 0.03/0.09 and 4.65/7.15 m by 2030/2050 is expected for areas close to the ocean but also areas close to Cacaveli and Agoè Télessou water pumping fields, respectively. For this scenario, an increasing pattern in the hydraulic head is also expected, with values within the range of 0.07/0.04–0.22/0.2 m and reaching up to 0.21/0.17 m by 2030/2050 m under the RCP 4.5 for areas close to the ocean and areas close to Cacaveli and Agoè Télessou water pumping fields, respectively. Under the RCP 8.5, the expected increase in the hydraulic head will be within the range of 0.08/0.05–0.24/0.22 m to reach values of 0.23/0.19 m by 2030/2050 for areas close to the ocean and areas around the pumping stations, respectively. As a result, the decrease in hydraulic head in areas close to the ocean is expected to be associated with an increase in salinity within the range of 0.05/51.43–10165.61/25048.76 mg.L^{-1} and 80.36/237.74–10291.49/25228.78 mg.L^{-1} by 2030/2050, accounting for RCP 4.5 and RCP 8.5, respectively. Furthermore, except for Obs15 (depicting an increase of 707.18/782.15 mg.L^{-1} by 2030/2050 under the RCP 4.5/RCP 8.5), the decrease in the hydraulic head for the remaining water points close to Cacaveli and Agoè Télessou water pumping fields shows no change in the salinity or refreshing under both RCPs. On the other hand, under the RCP 4.5, the increase in salinity as a result of the increase in the hydraulic head is expected to range between 192.66/727.69 and 1011.62/3227.73 mg.L^{-1} and reach values of 509.4/1702.07 mg.L^{-1} by 2030/2050 in areas close to the ocean and areas close to Cacaveli and Agoè Télessou pumping

stations, respectively. For RCP 8.5, the increase in salinity as a result of the increase in the hydraulic head is expected to reach values ranging between 191.24/724.03 and 1011.67/3227.61 mg.L^{-1} and reaching values of 509.3/1701.44 mg.L^{-1} by 2030/2050 for areas around the ocean and areas around the pumping stations, respectively.

For scenario D (Scenario A + Scenario B3 + Scenario C), some of the considered observation points are expected to depict a decreasing pattern, while others show an increasing pattern in the hydraulic head. Under the RCP 4.5, the decrease in hydraulic head is expected to range between 0.03/0.07 and 0.12/0.58 m and between 0.02/0.09 and 3.82/6.93 m for areas close to the ocean and areas close to Cacaveli and Agoè Télessou water pumping fields, respectively. Under RCP 8.5, these values are expected to range, respectively, between 0.09/0.1 and 0.49/0.57 m and between 0.11/0.12 and 5.6/7.56 m for areas close to the ocean and water pumping fields. On the other hand, the expected increase in the hydraulic head in areas close to the ocean will account for values ranging between 0.04/0.03 and 0.22/0.2 m and between 0.02/0.03 and 0.24/0.22 m by 2030/2050 under RCP 4.5 and RCP 8.5, respectively. For areas close to the Cacaveli and Agoè Télessou water pumping fields, the increase in the hydraulic head is expected to range between 0.21/0 and 0.79/0.17 m while reaching values of 0.23/0.19 m by 2030/2050 under the RCP 4.5 and RCP 8.5, respectively. As a result, the decrease in the hydraulic head in areas close to the ocean is expected to be associated with an increase in salinity ranging between 0/44.38 and 10166.53/25047.75 mg.L^{-1} and between 14.55/86.9 and 10290.03/25211.85 mg.L^{-1} by 2030/2050, accounting for RCP 4.5 and RCP 8.5, respectively. Furthermore, apart from Obs 15 (increase by 705.18/750.54 mg.L^{-1} and 818.7/863.7 mg.L^{-1} by 2030/2050 for the RCP 4.5 and RCP 8.5, respectively), the decrease in the hydraulic head for the remaining water points close to Cacaveli and Agoè Télessou water pumping fields shows no change in the salinity to refreshing under both RCPs. On the other hand, changes in salinity resulting from the increase in the hydraulic heads in areas close to the ocean will amount to values ranging between 182.54/719.69 and 1011.66/3228.27 mg.L^{-1} and between 203.24/741.67 and 1011.62/3226.98 mg.L^{-1} by 2030/2050 for the RCP 4.5 and RCP 8.5, respectively. For areas close to Cacaveli and Agoè Télessou pumping fields, the salinity is expected to range between 0 and 509.41/1702.19 mg.L^{-1} and reach values of 509.29/1701.31 mg.L^{-1} for the RCP 4.5 and RCP 8.5, respectively.

In summary, the highest decrease in hydraulic head is expected under scenario B1 (reaching values of 5.04/9.79 m by 2030/2050 observed in the northern part), while the lowest decrease is expected under scenario B2 (with values reaching 0.33/0.73 m by 2030/2050 under

the RCP 8.5, observed in the southern part). On the other hand, the highest resulted increase in the salt concentration is expected under scenario C (estimated at 10291.49/25228.78 $mg.L^{-1}$ by 2030/2050 under RCP 8.5, observed in the southern part, close to the ocean). These results confirm that the salinisation of the upper aquifers in AP (Continental Terminal and Coastal Marine Sands) is sourced by the ocean located in the southern part of the study area. In addition, it has also been observed that, except for scenarios A (continuous groundwater withdrawal) and B (LULC), the hydraulic head is expected to increase in some parts of the study area while other parts will experience a decrease. Most of the observed decrease in the hydraulic heads is associated with an increase in salinity, but comparing the southern part of the study area to the other parts, it has been observed that the highest decrease in the hydraulic head is not always associated with the highest increase in salinity, highlighting the key role played by the location of a borehole (closeness to the ocean) on the magnitude of the phenomenon. Nevertheless, the presence of water points depicting a future increase in salinity in areas close to Cacaveli and Agoè Télessou water pumping fields confirms the suggestions made by geophysics results highlighting the presence of an up coning (see section 6.4) in these areas characterised by low hydraulic heads and constant pressure from the water pumping fields located around the Cacaveli area. It has also been observed that, except for scenarios A (continuous groundwater withdrawal) and B1 (LULCC), the hydraulic head is expected to increase in some parts of the study area while other parts will experience a decrease. These patterns are expected to be associated with salination in some parts and refreshing in other parts of the study area. This double pattern observed over the study area can be explained by a non-uniform flux exchange at different sections of the system with other hydrological or hydrogeological systems such as the ocean, rivers, and aquifers or by an error associated with the assumption that all the considered boreholes capture the entire thickness of the upper aquifers (which is not true). The latter reason is confirmed by the results of the HFE-D (see section 6.1.3.5), depicting both refreshing and seawater intrusion over AP.

Table 7.4a: Parameters of the Scenario Applied to the Reference Groundwater Model (2021), Resulting Changes in the Hydraulic Head and Salinity on the Observation Wells: 2030

		Scenario A	**Scenario B**					**Scenario C**		**Scenario D**	
			B1	B2-1	B2-2	B3-1	B3-2	C1	C2	D1	D2
Scenario description		Continuous GWW in 2030	Land use land use cover change	Change in climatic conditions (RCP 4.5)	Change in climatic conditions (RCP 8.5)	Combined Land use land cover change + Climate change under RCP 4.5 (Scenario B1+B2-1)	Combined Land use land cover change + Climate change under RCP 8.5 (Scenario B1+B2-2)	Sea level rise (RCP 4.5)	Sea level rise (RCP 8.5)	Combination of all the scenarios under the RCP 4.5 (Scenario A + B3-1 + C1)	Combination of all the scenarios under the RCP 8.5 (Scenario A+ B3-2 + C2)
Applied conditions	SLR	0	0	0	0	0	0	0.22	0.24	0.22	0.24
	Recharge	Baseline	-22.25	165.97	-34.26	48.03	-54.15	Baseline	Baseline	1.56	-6.65
	GWW	1.43	Baseline	Baseline	Baseline	Baseline	Baseline	Baseline	Baseline	1.43	1.43
Resulting hydraulic head change (m)	Obs 1	-0.3	-0.28	-0.28	-0.28	-0.28	-0.28	-0.11	-0.09	-0.11	-0.09
	Obs 2	-0.1	-0.09	-0.09	-0.09	-0.09	-0.09	-0.12	-0.12	-0.12	-0.12
	Obs 3	0	-0.02	-0.02	-0.02	-0.02	-0.02	0.2	0.22	0.2	0.22
	Obs 4	-0.03	-0.05	0.05	-0.06	0.02	-0.08	0.07	0.08	0.11	0.02
	Obs 5	-0.01	-0.01	0.01	-0.01	0	-0.02	0.08	0.09	0.09	0.08
	Obs 6	-0.09	-0.12	0.1	-0.14	0.03	-0.18	-0.05	-0.05	0.04	-0.18
	Obs 7	-0.01	-0.01	-0.01	-0.01	-0.01	-0.01	0.22	0.24	0.22	0.24
	Obs 8	-0.25	-0.32	0.15	-0.33	0	-0.4	-0.22	-0.22	-0.03	-0.49
	Obs 9	-0.08	-0.11	0.1	-0.13	0.03	-0.17	-0.03	-0.02	0.05	-0.15
	Obs 10	-0.01	-0.01	-0.01	-0.01	-0.01	-0.01	0.22	0.24	0.22	0.24
	Obs 11	-0.03	-0.03	-0.03	-0.03	-0.03	-0.03	0.2	0.22	0.2	0.22
	Obs 12	-0.02	-0.02	-0.02	-0.02	-0.02	-0.02	0.21	0.23	0.21	0.23

	Obs 13	-0.01	-0.01	-0.01	-0.01	-0.01	-0.01	0.21	0.24	0.21	0.24
	Obs 14	-0.02	-0.02	-0.02	-0.02	-0.02	-0.02	0.21	0.23	0.21	0.23
	Obs 15	-0.22	-0.28	0.13	-0.29	-0.01	-0.35	-0.2	-0.2	-0.03	-0.43
	G7	-0.05	-0.07	0.03	-0.07	0	-0.09	-0.05	-0.05	0	-0.11
	G16	-0.23	-0.3	0.14	-0.31	0	-0.39	-0.21	-0.21	-0.02	-0.47
	G32	-0.28	-0.37	0.16	-0.38	-0.01	-0.47	-0.26	-0.26	-0.03	-0.56
	G49	-0.09	-0.45	0.4	-1.71	0.85	-2.07	-0.03	-0.03	0.79	-1.1
	G22	-0.34	-0.38	0.08	-0.14	-0.25	-0.18	-0.34	-0.34	-0.25	-0.44
	G20	-0.21	-0.28	0.13	-0.29	0	-0.36	-0.19	-0.19	-0.02	-0.43
	G13	-0.25	-0.28	0.07	-0.12	-0.17	-0.15	-0.25	-0.25	-0.17	-0.34
	G15	-0.46	-0.89	0.43	-2.19	0.71	-2.64	-0.38	-0.38	0.63	-1.69
	G12	-4.65	-5.04	0.42	-1.77	-3.82	-2.15	-4.65	-4.65	-3.82	-5.6
	G47	-0.53	-0.71	0.28	-0.75	-0.09	-0.93	-0.51	-0.51	-0.1	-1
	G33	-0.3	-0.39	0.17	-0.4	-0.01	-0.49	-0.27	-0.27	-0.04	-0.6
	G31	-0.31	-0.4	0.18	-0.41	-0.01	-0.51	-0.28	-0.28	-0.04	-0.61
	G34	-0.3	-0.39	0.17	-0.39	-0.01	-0.48	-0.27	-0.27	-0.04	-0.59
	G30	-0.28	-0.37	0.16	-0.37	-0.01	-0.45	-0.25	-0.25	-0.03	-0.55
	G28	-0.28	-0.37	0.16	-0.38	-0.01	-0.47	-0.26	-0.26	-0.03	-0.57
	G6	-0.41	-0.53	0.21	-0.52	-0.03	-0.65	-0.37	-0.37	-0.07	-0.8
	G46	-0.26	-0.35	0.15	-0.35	0	-0.44	-0.24	-0.24	-0.03	-0.53
Resulting salinity change (mg. L^{-1})	Obs 1	8739.6	8739.38	8741	8739.22	8740.66	8738.86	10165.61	10291.49	10166.53	10290.03
	Obs 2	3019.7	3023.38	2996.17	3025	3005.15	3030.15	3802.7	3875.64	3790.94	3894.08
	Obs 3	628.6	628.61	628.66	628.61	628.64	628.6	627.95	627.89	627.97	627.87
	Obs 4	268.6	274.17	242.83	288.29	253.14	294.35	249.67	248.06	236.44	265.31
	Obs 5	208.6	213.22	190.46	221.77	197.95	226.12	192.66	191.24	182.54	203.24
	Obs 6	2.5	7.33	-19	11.89	-10.44	17.23	0.05	0	-11.06	14.55
	Obs 7	243.5	243.47	243.5	243.42	243.49	243.42	242.89	242.83	242.9	242.82

Obs 8	204	190.98	224.79	2.16	232.87	-22.02	212.32	212.32	229.56	139.45
Obs 9	89	95.76	54.62	103.58	68.13	111.63	80.91	80.36	64.19	103.62
Obs 10	415.3	415.25	415.29	415.26	415.28	415.26	414.41	414.33	414.42	414.32
Obs 11	1011.1	1011.11	1011.19	1011.06	1011.17	1011.04	1011.62	1011.67	1011.66	1011.62
Obs 12	823.5	823.44	823.56	823.31	823.52	823.28	821.65	821.48	821.7	821.43
Obs 13	602.5	602.51	602.53	602.51	602.53	602.51	601.26	601.15	601.27	601.14
Obs 14	510.5	510.52	510.54	510.52	510.53	510.51	509.4	509.3	509.41	509.29
Obs 15	709.4	734.48	763.88	985.91	713.76	1050.02	707.18	707.18	705.18	818.7
G7	-129.43	-110.22	-217.15	-60.28	-184.42	-44.22	-133.86	-133.87	-179.84	-74.57
G16	-284.67	-271.4	-282.77	-290.55	-288.26	-248.8	-284.75	-284.75	-291.59	-226.88
G32	-10.66	8.56	-98.37	123.01	-65.65	139.07	-15.09	-15.09	-61.07	44.2
G49	-0.06	-0.05	-0.13	-0.03	-0.1	-0.02	-0.06	-0.06	-0.1	-0.02
G22	0	0	0	0	0	0	0	0	0	0
G20	-8.33	-8.35	-8.27	-9.22	-8.29	-9.25	-8.33	-8.33	-8.29	-8.38
G13	-137.95	-116.52	-177.87	-63.76	-168.99	-16.95	-141.02	-141.02	-169.52	-55.79
G15	-0.06	-0.05	-0.11	-0.04	-0.09	-0.03	-0.06	-0.06	-0.09	-0.03
G12	0	0	0	0	0	0	0	0	0	0
G47	-0.06	-0.05	-0.12	-0.04	-0.09	-0.03	-0.06	-0.06	-0.09	-0.03
G33	-238.25	-234.44	-234.04	-250.71	-241.4	-239.19	-239.4	-239.4	-241.28	-223.77
G31	-326.03	-318.17	-319.82	-259.07	-331.81	-235.61	-327.97	-327.97	-332.33	-293.07
G34	-73.79	-86.29	-37.08	-332.99	-42.44	-348.5	-67.56	-67.56	-45.73	-127.25
G30	-188.13	-202.44	-128.03	-220.47	-143.24	-210.58	-181.25	-181.25	-147.86	-233.67
G28	-126.94	-128.76	-116.57	-109.44	-119.01	-98.42	-125.19	-125.19	-119.77	-133.61
G6	160.8	177.18	93.97	93.49	122.64	82.75	162.25	162.25	121.82	186.62
G46	21.69	34.94	-38.05	111.28	-13.08	126.48	19.82	19.82	-10.53	59.55

* SLR and GWW stand for Sea Level Rise and groundwater withdrawal, respectively.

*The groundwater withdrawal and recharge are expressed as a ratio and the changes in reference to the baseline, respectively.

Table 7.4b: Parameters of the Scenario Applied to the Reference Groundwater Model (2021), Resulting Changes in the Hydraulic Head and Salinity on the Observation wells: 2050

		Scenario A	Scenario B					Scenario C		Scenario D	
Scenario description		A Continuous GWW in 2050	B1 Land use land use cover change	B2-1 Change in climatic conditions (RCP 4.5)	B2-2 Change in climatic conditions (RCP 8.5)	B3-1 Combined Land use land cover change + Climate change under RCP 4.5 (Scenario B1'+B2-1'	B3-2 Combined Land use land cover change + Climate change under RCP 8.5 (Scenario B1'+B2-2')	C1 Sea level rise (RCP 4.5)	C2 Sea level rise (RCP 8.5)	D1 Combination of all the scenarios under the RCP 4.5 (Scenario A' + B3-1' + C1)	D2' Combination of all the scenarios under the RCP 8.5 (Scenario A' + B3-2' + C2)
Applied conditions	SLR	0	0	0	0	0	0	0.22	0.24	0.22	0.24
	Recharge	Baseline	-83.42	89.19	103.81	1.56	-6.65	Baseline	Baseline	1.56	-6.65
	GWW	1.86	Baseline	Baseline	Baseline	Baseline	Baseline	Baseline	Baseline	1.86	1.86
Resulting hydraulic Head change (m)	Obs 1	-0.7	-0.73	-0.73	-0.73	-0.73	-0.73	-0.58	-0.57	-0.58	-0.57
	Obs 2	-0.3	-0.35	-0.34	-0.34	-0.34	-0.34	-0.41	-0.42	-0.41	-0.42
	Obs 3	-0.1	-0.07	-0.07	-0.07	-0.07	-0.07	0.15	0.17	0.15	0.17
	Obs 4	-0.07	-0.14	0.04	0.05	-0.05	-0.07	0.04	0.05	0.03	0.03
	Obs 5	-0.03	-0.04	-0.01	-0.01	-0.03	-0.03	0.06	0.07	0.06	0.07
	Obs 6	-0.13	-0.31	0.15	0.16	-0.08	-0.13	-0.07	-0.06	-0.09	-0.13
	Obs 7	-0.03	-0.03	-0.03	-0.03	-0.03	-0.03	0.2	0.22	0.2	0.22
	Obs 8	-0.47	-0.95	0.23	0.23	-0.37	-0.45	-0.42	-0.42	-0.42	-0.56
	Obs 9	-0.12	-0.29	0.13	0.15	-0.08	-0.11	-0.05	-0.04	-0.07	-0.1
	Obs 10	-0.02	-0.02	-0.02	-0.02	-0.02	-0.02	0.2	0.22	0.2	0.22
	Obs 11	-0.09	-0.09	-0.09	-0.09	-0.09	-0.09	0.13	0.15	0.13	0.15
	Obs 12	-0.06	-0.06	-0.06	-0.06	-0.06	-0.06	0.17	0.19	0.17	0.19
	Obs 13	-0.03	-0.03	-0.03	-0.03	-0.03	-0.03	0.19	0.21	0.19	0.21

	Obs 14	-0.06	-0.06	-0.06	-0.06	-0.06	-0.06	0.17	0.19	0.17	0.19
	Obs 15	-0.41	-0.82	0.19	0.19	-0.32	-0.39	-0.36	-0.36	-0.37	-0.49
	G7	-0.11	-0.21	0.06	0.06	-0.08	-0.1	-0.09	-0.09	-0.09	-0.12
	G16	-0.45	-0.91	0.24	0.23	-0.35	-0.43	-0.4	-0.4	-0.4	-0.54
	G32	-0.55	-1.1	0.28	0.27	-0.43	-0.53	-0.48	-0.48	-0.49	-0.65
	G49	-0.67	-3.17	0.95	0.84	-0.17	-2.6	-0.45	-0.45	-0.38	-1.15
	G22	-0.48	-0.67	0.12	0.13	-0.46	-0.16	-0.48	-0.48	-0.46	-0.5
	G20	-0.42	-0.84	0.22	0.21	-0.33	-0.4	-0.37	-0.37	-0.37	-0.5
	G13	-0.36	-0.52	0.11	0.11	-0.35	-0.14	-0.36	-0.36	-0.35	-0.38
	G15	-1.28	-4.55	1.18	0.97	-0.56	-3.56	-0.96	-0.95	-0.86	-1.93
	G12	-7.15	-9.79	0.94	0.89	-6.92	-2.52	-7.15	-7.15	-6.93	-7.56
	G47	-0.66	-1.57	0.42	0.52	-0.58	-0.7	-0.61	-0.61	-0.61	-0.75
	G33	-0.59	-1.17	0.29	0.28	-0.46	-0.55	-0.52	-0.52	-0.53	-0.7
	G31	-0.6	-1.21	0.3	0.29	-0.47	-0.57	-0.53	-0.53	-0.54	-0.72
	G34	-0.58	-1.15	0.29	0.28	-0.45	-0.54	-0.51	-0.51	-0.51	-0.68
	G30	-0.54	-1.08	0.27	0.26	-0.42	-0.51	-0.48	-0.48	-0.48	-0.64
	G28	-0.55	-1.11	0.28	0.27	-0.43	-0.52	-0.49	-0.49	-0.5	-0.66
	G6	-0.79	-1.57	0.37	0.35	-0.63	-0.74	-0.71	-0.71	-0.71	-0.94
	G46	-0.51	-1.03	0.26	0.25	-0.4	-0.49	-0.45	-0.45	-0.46	-0.61
Resulting salinity change ($mg.L^{-1}$)	Obs 1	22799.6	22776.9	22842	22835.39	22810.65	22798.76	25048.76	25228.78	25047.75	25211.85
	Obs 2	11221.5	11353.1	11005.55	10996.73	11178.4	11209.86	13485.76	13683.47	13508.3	13744.77
	Obs 3	2114.4	2113.88	2115.35	2114.84	2114.72	2114.2	2108.39	2107.85	2108.69	2107.5
	Obs 4	1012.6	793.7	925.91	933.82	996.59	1017.48	963.03	958.97	960.48	980.52
	Obs 5	769.4	602.49	701.28	719.34	756.02	782.83	727.69	724.03	719.69	741.67
	Obs 6	71.3	142.73	-51.01	-28.07	42.18	86.18	51.43		44.38	86.97
	Obs 7	820.2	576.52	820.8	819.95	820.46	819.66	816.94	816.64	817.13	816.4
	Obs 8	230.3	292.41	117.55	157.57	238.93	151.32	237.75	237.74	233.37	198.75

Obs 9	409.2	403	251.83	287.59	370.79	425.12	373.25	371.29	364.66	418.61
Obs 10	1363.3	947.73	1363.88	1363.34	1363.51	1363.01	1357.84	1357.35	1358.07	1357.1
Obs 11	3229.1	2216.93	3230.97	3229.72	3229.65	3228.47	3227.73	3227.61	3228.27	3226.98
Obs 12	2679.4	1854.65	2681.75	2679.94	2680.21	2678.39	2668.64	2667.67	2669.39	2666.78
Obs 13	1988.7	1385.77	1989.64	1988.87	1989.03	1988.34	1980.92	1980.22	1981.25	1979.86
Obs 14	1708.9	1198.22	1709.33	1709.06	1709.06	1708.8	1702.07	1701.44	1702.19	1701.31
Obs 15	742.2	752.04	653.65	861.94	733.04	692.86	782.15	782.22	750.54	863.7
G7	-348.68	-340.7	-356.38	-364.46	-349.14	-359.78	-348.87	-348.87	-348.89	-346.12
G16	-187.45	-110.2	-373.66	-436.75	-236.33	-211.35	-205.93	-205.98	-221.59	-162.22
G32	-133.41	-41.63	-225.05	-133.76	-155.01	-46.1	-130.88	-130.89	-145.08	-132.61
G49	-0.21	-0.06	-0.39	-0.33	-0.24	-0.15	-0.21	-0.21	-0.24	-0.17
G22	0	0	0	0	0	0	0	0	0	0
G20	-28.37	-30.47	-25.54	-26.89	-27.84	-29.95	-28.36	-28.36	-27.85	-29.09
G13	-102.76	-178.21	-260.21	-276.77	-128.79	-145.39	-108.42	-108.45	-118.52	-136.48
G15	-0.21	-0.07	-0.37	-0.33	-0.24	-0.17	-0.21	-0.21	-0.24	-0.17
G12	0	0	-0.01	-0.01	-0.01	0	0	0	-0.01	0
G47	-0.22	-0.08	-0.39	-0.34	-0.25	-0.17	-0.22	-0.22	-0.25	-0.17
G33	-202.64	-268.06	-250.51	-197.53	-200.37	-258.73	-195.22	-195.2	-198.29	-252.09
G31	-202.64	-221.13	-241.05	-162.02	-206.61	-208.17	-194.5	-194.49	-200.98	-251.16
G34	-182.54	-274.85	-256.5	-313.66	-223.19	-301.12	-193.24	-193.26	-222.07	-187.69
G30	-224.18	-298.02	-265.81	-169.77	-254.05	-201.86	-227.16	-227.16	-248.78	-260.29
G28	-154.81	-197.64	-177.68	-87.39	-150.6	-149.19	-147.82	-147.81	-150.03	-198.55
G6	-124.2	-19.89	-154.93	-66.64	-133.78	20.89	-126.76	-126.76	-136.34	-71.29
G46	-77.71	-10.84	-153.13	-83.96	-76.34	-29.9	-72.96	-72.96	-72.43	-88.88

* SLR and GWW stand for Sea Level Rise and groundwater withdrawal, respectively.

*The groundwater withdrawal and recharge are expressed as a ratio and the changes in reference to the baseline, respectively.

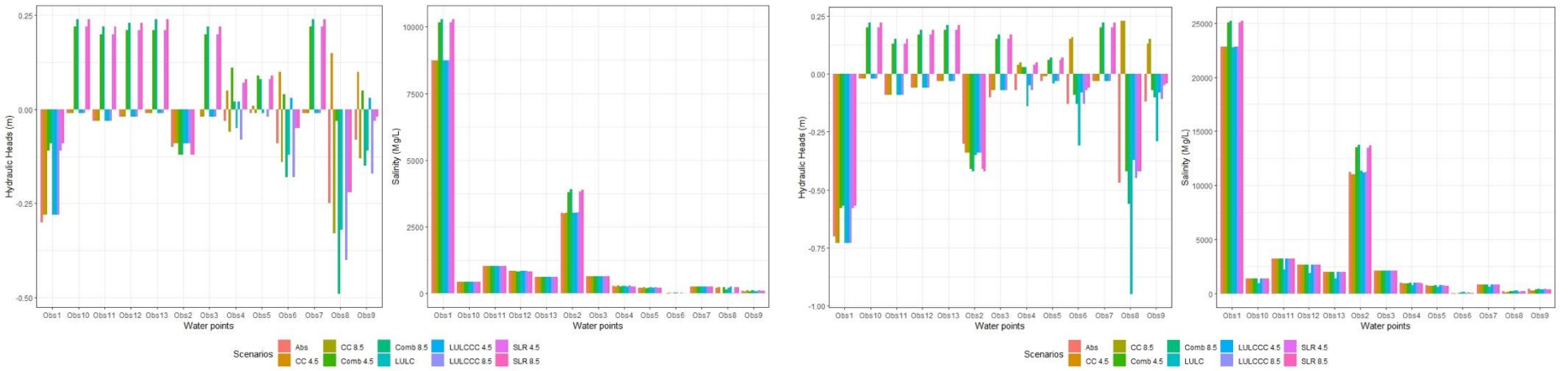

Figure 7.4a: Dynamics of the Hydraulic Head and Salinity (TDS) for Water Points Located in the Southern Part of the AP for 2030 (Left) and 2050 (Right)

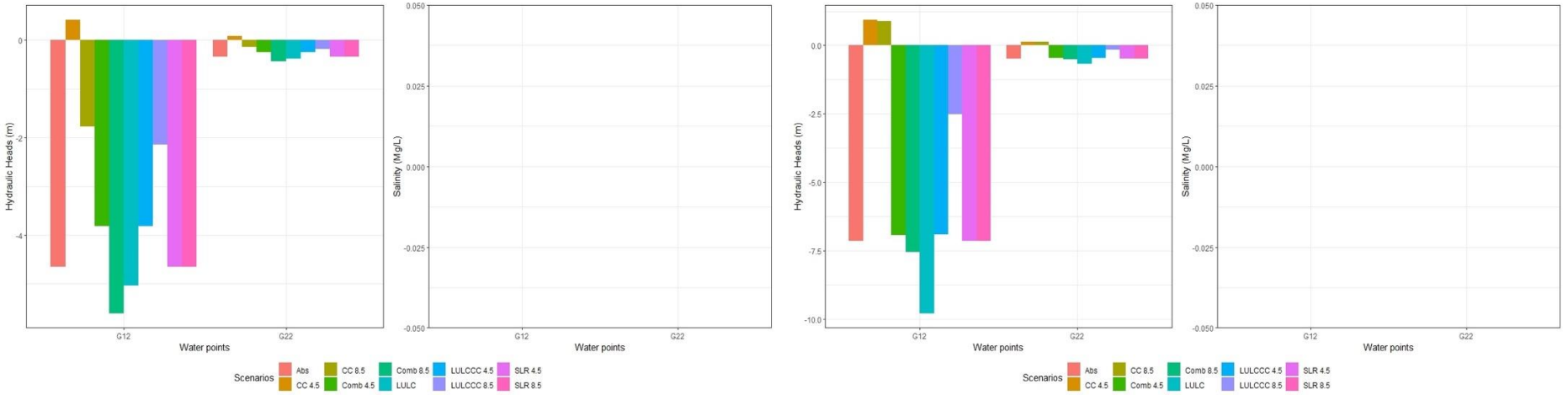

Figure 7.4b: Dynamics of the Hydraulic Head and Salinity (TDS) for Water Points Located in the Northern part of the AP for 2030 (Left) and 2050 (Right)

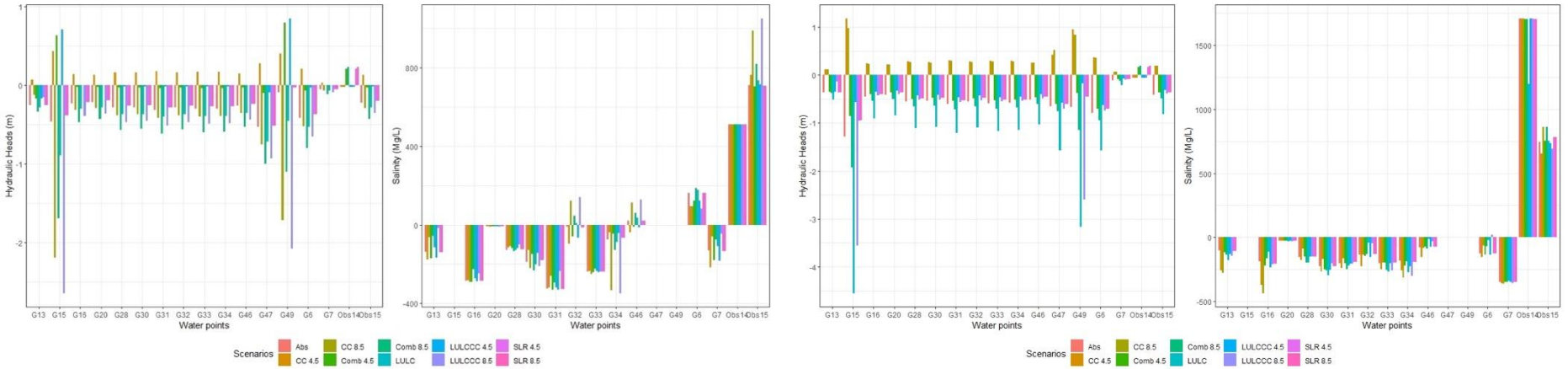

Figure 7.4c: Dynamics of the Hydraulic Head and Salinity (TDS) for Water Points Located around Cacaveli for 2030 (Left) and 2050 (Right)

Based on scenario D (Figures 7.5a-b and Figures 7.6a-f), considered as the most probable (changes in climate parameters, changes in LULC, increasing groundwater withdrawal, and sea level rise), seawater intrusion occurs northward (with the ocean located in the southern part), with the transition zone extending up to around 5 km inland. These findings validate the geophysical finding (see section 6.4), which suggested that there is no lateral intrusion around the Cacaveli area, indicating rather that the observed and expected increase in salinity around Cacaveli areas is as a result of an up coning. In addition, the simulated extent of the intrusion (toe of the interface or the transition zone), considering the limit of freshwater of 1000 $mg.L^{-1}$ shows an increase in the intruded area estimated at 140.92 km^2, 144.03 km^2, and 145.25 km^2 for the years 2021, 2030, and 2050, respectively. Though the observed change over time in the intruded area seems to be slight, there is a need to highlight that the salt concentration of the transition zone, or the toe of the interface, highly varies, with values ranging between 1000 and 8635 $mg.L^{-1}$, between 1000 and 18800 $mg.L^{-1}$, and between 1000 and 33600 $mg.L^{-1}$ for the years 2021, 2030, and 2050, respectively.

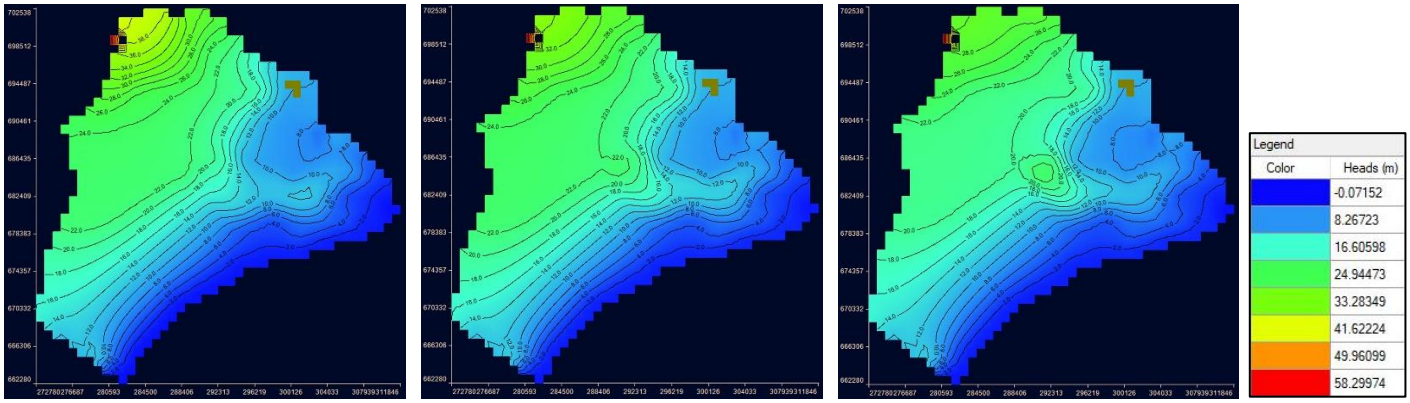

Figure 7.5a: Simulated Hydraulic Head for the Years 2021, 2030, and 2050 (Left to Right)

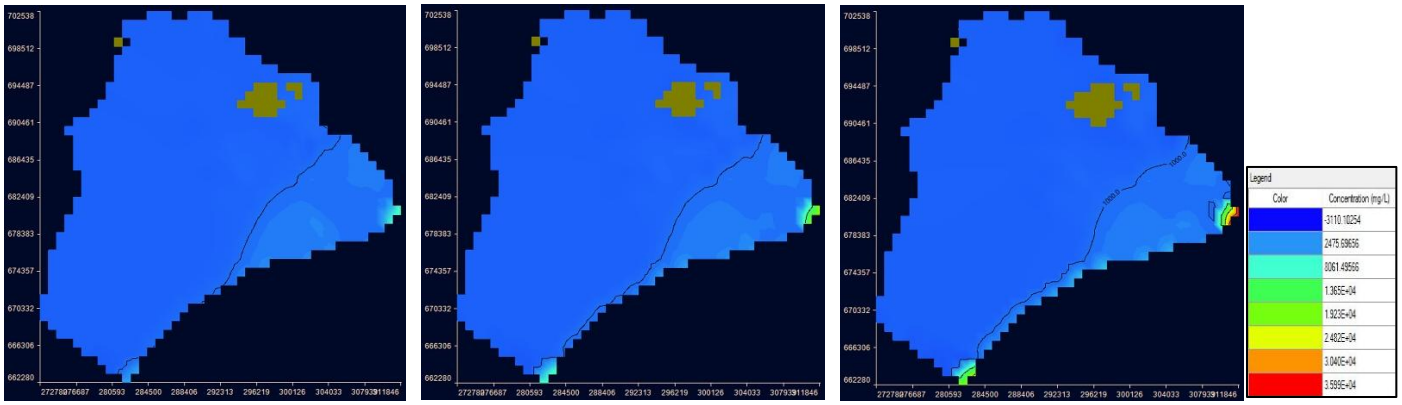

Figure 7.5b: Simulated Salinity (TDS) for the Years 2021, 2030, and 2050 (Left to Right)

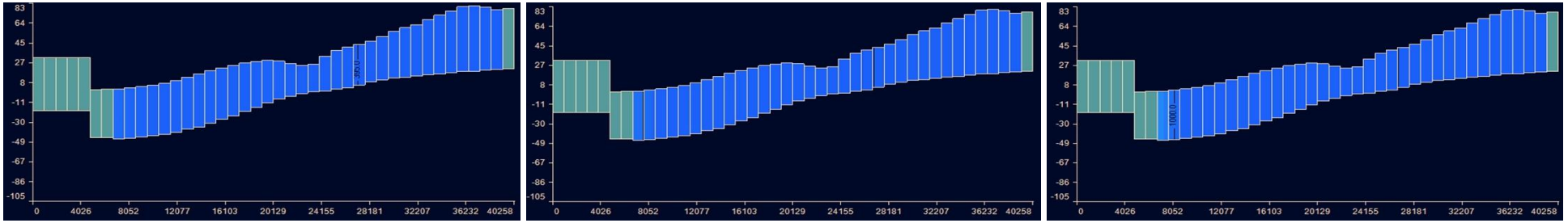

Figure 7.6a: S–N Cross-section of the Model Domain (Col 17) Showing the Calculated Salt Concentration for the year 2021, 2030, 2050 (Left to Right)

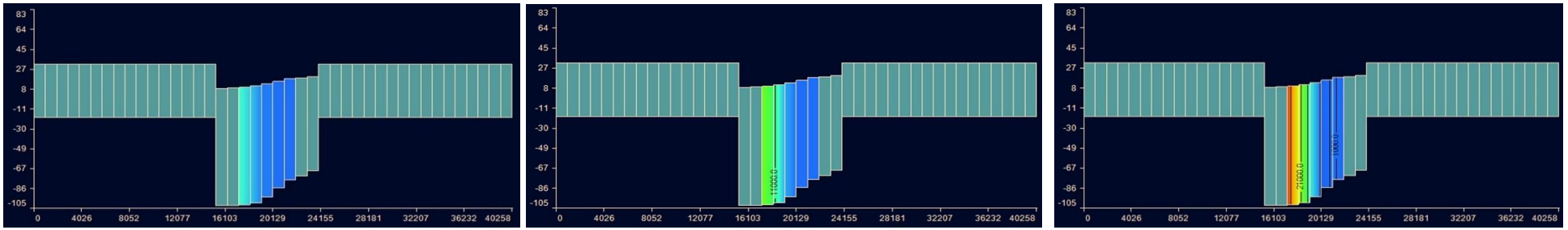

Figure 7.6b: S–N Cross-section of the Model Domain (Col 43) Showing the Calculated Salt Concentration for the year 2021, 2030, 2050 (Left to Right)

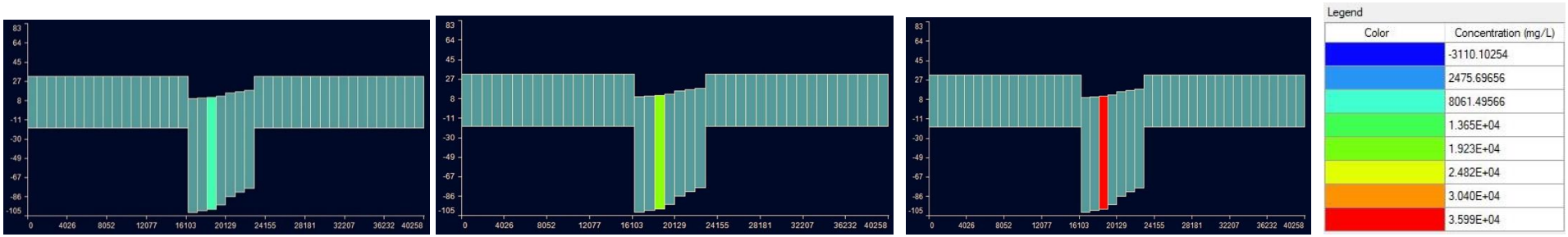

Figure 7.6c: S–N Cross-section of the Model Domain (Col 44) Showing the Calculated Salt Concentration for the year 2021, 2030, 2050 (Left to Right)

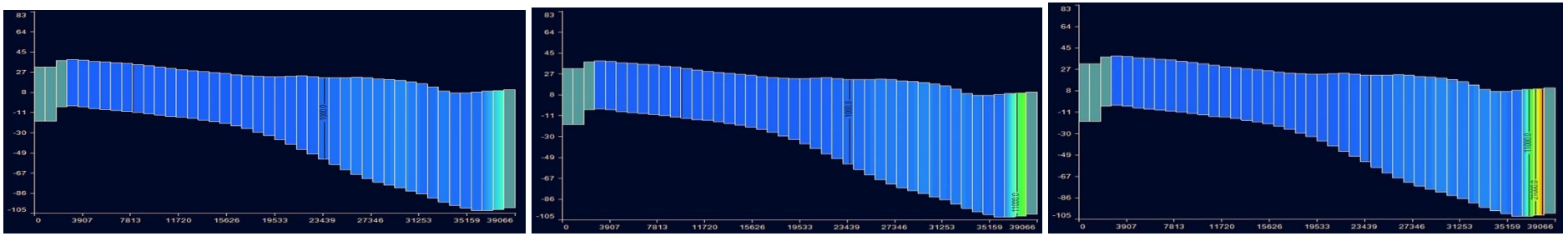

Figure 7.6d: W–E Cross-section of the Model Domain (Row 24) Showing the Calculated Salt Concentration for the year 2021, 2030, 2050 (Left to Right)

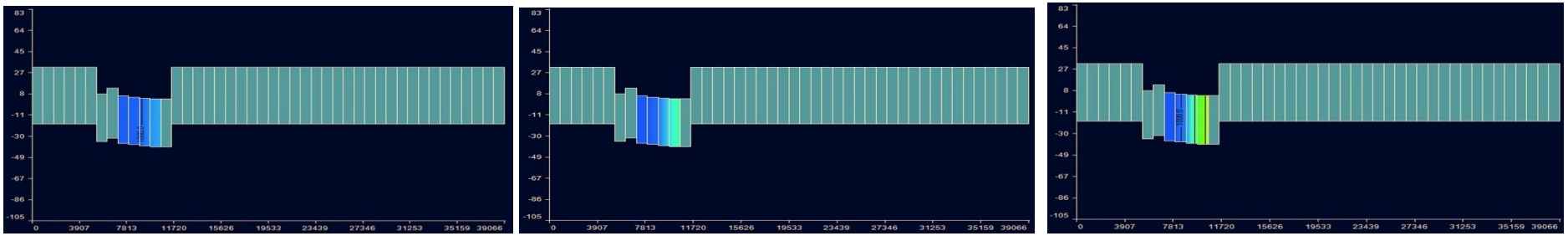

Figure 7.6e: W–E Cross-section of the Model Domain (Row 41) Showing the Calculated Salt Concentration for the year 2021, 2030, 2050 (Left to Right)

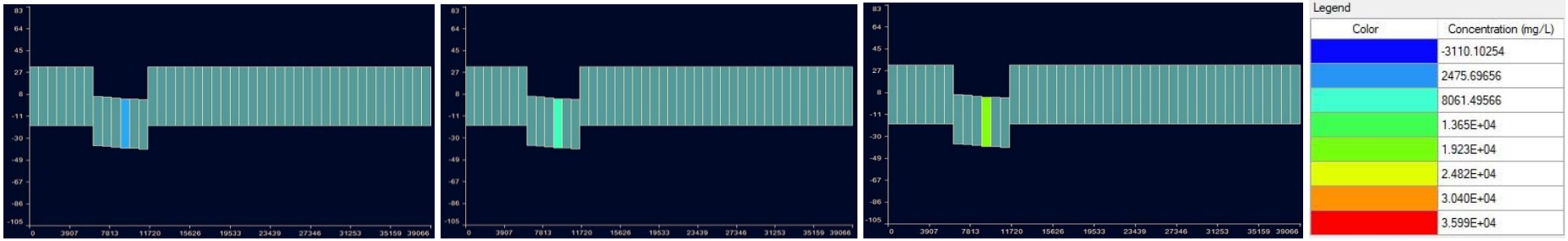

Figure 7.6f: W–E Cross-section of the Model Domain (Row 42) Showing the Calculated Salt Concentration for the year 2021, 2030, 2050 (Left to Right)

7.3 Partial Conclusion

The SEAWAT code was considered in capturing the dynamics of seawater intrusion (evolution of salinity over time) under various scenarios, including climate change (precipitation and temperature), land use and land cover change (LULCC), combined climate change and LULCC, sea level rise, and continuous groundwater withdrawal. Prior to simulating the groundwater dynamics in terms of its hydraulic head and salt concentration, the recharge of the upper aquifers was estimated using the water balance method, considering the Soil Conservation Service Curve Number (SCS-CN) method and the combined Coutagne-Turc method. The simulation of the groundwater lens response results:

- Reveal an expected double pattern in hydraulic heads (increase and decrease) and the associated salt concentrations (salinisation and refreshing) under almost all the scenarios except for scenarios A (continuous groundwater withdrawal) and B1 (LULCC).
- Confirm both a lateral intrusion and an up coning in the upper aquifers sourced by the ocean, with a transition zone under the most probable scenario (D) extending up to 5 km inland.
- Reported an expected increase (in reference to the year 2021) of the intruded area by 2.2% and 3.1% by 2030 and 2050, respectively.

A continuous increase in the salinity concentration over time in the multilayered aquifer in the AP is likely to be associated with the closure of some boreholes, especially those close to the ocean and around Cacaveli and Agoè Télessou water pumping fields. In addition, this phenomenon can be a source of pollution for the deep aquifers that it recharges, which will undermine water security in the study area.

CHAPTER EIGHT: GENERAL CONCLUSIONS AND PERSPECTIVES

This research project's investigations in the Agoènyivé Plateau (AP) have addressed three major threats to groundwater in coastal settings, including climate change (CC), land use and land cover change (LULCC), and the continuous groundwater withdrawal (resulting from population growth) and their impacts on groundwater resources, thus contributing to efforts to ensure sustainable management of these resources in the Sedimentary Coastal Basin of Togo.

The current study went beyond the existing research works in the study area, which mostly focused on the definition of the structure of the existing aquifers, the quantification of the water resources for each aquifer, and the definition of groundwater exploitation conditions, with only a few of them having considered a combination of hydrochemistry, isotopy, and modelling to understand seawater intrusion (essentially limited to deep aquifers such as Palaeocene and Maastrichtian). In fact, this study combined geophysics, hydrochemistry, isotopy, and hydrogeological modelling to bring out an understanding of the dynamics of seawater intrusion in the multilayered aquifer of the AP under CC, LULC, and continuous groundwater withdrawal. The objectives set to assess the dynamics of seawater intrusion in the AP were achieved and include:

(i) Historical and Future LULC in the AP

LULC was assessed considering Landsat 5 and 7 images (1986, 2001, 2011, and 2020), reference data, and local perceptions of LULC dynamics using ENVI and the Land Change Modeller. The results revealed that AP has been subject (1986–2020) to an increasing trend in built-up areas (38.71% land gain) at the expense of mixed vegetation/savannah, cropland, and wetlands. This observed pattern (increase of built-up areas) is expected to continue in the future (2030 and 2050) under the Business as Usual (BAU) scenario, with an expected additional increase of 7.79% and 19.79% by 2030 and 2050, respectively. Nevertheless, the building policy scenario, if considered, is expected to alleviate the expected decrease in the other classes.

(ii) Climatic Trends and Future projections in AP

It was captured considering observations time series from satellite-based products and in situ stations (1991–2020) as well as Regional Climate Models (CanESM2-RCA4, NorESM1-RCA4, CCLM4-8-17, and RACMO22T) outputs (2021–2050). The results using the Mann-Kendall and the Modified Mann-Kendall tests along with the Sen' slope test depict a non-significant ($p > 0.05$) increasing trend in annual rainfall (estimated at 0.81 mm annually) against a significant ($p < 0.05$) increasing trend in the average temperature (estimated at 0.02 °C

annually) over the period 1991–2020. In the future (2021–2050), the climate is expected to be drier, characterised respectively by a non-significant ($p > 0.05$) slight increasing trend (accounting for 0.05 mm annually) and a decreasing trend in the annual rainfall (accounting for 0.69 mm annually) under RCP 4.5 and RCP 8.5 (in reference to the period of 1991–2020). Additionally, the average temperature is expected to significantly ($p < 0.05$) increase by 0.01 °C (RCP 4.5) and 0.02 °C (RCP 8.5) annually.

(iii) Characteristics of Existing Aquifers (in term of Hydrochemistry, Isotopy, Hydraulic Heads, and True Resistivity Distribution) in the AP.

A combination of geochemical, isotopic, and geophysical methods was considered in the characterisation of the existing aquifers in the AP. The results confirmed that the upper aquifers, including the Continental Terminal and the Coastal Marine Sands, are those subject to constant seawater intrusion with observed chlorinated sodic-potassic (Na-K-Cl) facies and even hyper-chlorinated sodic facies. Furthermore, both lateral intrusion (for areas close to the ocean like the beach and Ahanoukopé reaching up to around 2.5 km) and an up coning (around the Cacaveli pumping field) of seawater are suggested, with a mixing zone found at an average depth of 21 m with a thickness ranging between 10 and 28 m.

(iv) Future Groundwater Lens Response (Hydraulic Head, Salinity, and Intrusion Extent) to CC, LULCC and Increasing Groundwater Withdrawal in the AP.

The successfully calibrated and validated SEAWAT model, along with the considered scenarios including A (based on groundwater withdrawal rate), B1, B2, and B3 (based on the recharge estimated considering current and future LULC and climate parameters), C (sea level rise), and D (combination of all the scenarios) depict in most cases a decrease in the hydraulic heads ranging between 0.01/0.02 and 5.6/9.79 m associated with an increase in the salinity ranging between 0.05/44.38 and 10291.49/25228.78 $mg.L^{-1}$ by 2030/2050 (with the highest values observed under the scenario C) . Though the aquifer is expected to experience salinisation in some parts and refreshing in others, the observed and expected increase in salinity in areas close to the ocean, as well as areas close to Cacaveli and Agoè Télessou water pumping fields, confirm the lateral intrusion (reaching 5 km inland) and an up coning, respectively. The intruded area accounts for 140.92 km^2 in 2021, with an expected increase in the areas by 2.2% and 3.1% (under scenario D) by 2030 and 2050, respectively, in reference to the year 2021.

Based on the obtained results and challenges encountered throughout the research work as well as the limitations of this study, this study recommends:

FOR THE GOVERNMENT (MINISTRY OF WATER AND VILLAGE HYDRAULICS)

(i) To consider additional water sources and/or redefine the exploitation conditions of the CT aquifer in the AP.

The expected continuous increase in salinity over the AP under climate change, LULC change, continuous groundwater withdrawal, and sea level rise calls for actions. Additional water sources may include surface water, harvested rainwater, and the consideration of deep aquifers.

(ii) More collaboration between countries sharing the Sedimentary Coastal Basin in the Gulf of Guinea.

There is a need to highlight that the consideration of the results should be done with a certain level of discretion, as the general spatial and temporal geochemical, hydrological, and hydrogeological data (from the Ghanaian side) used were very limited due to limited collaboration between riparian countries, something that needs to be improved.

(iii) **To build a strong and representative piezometric network over the basin.**

This research work represents an alarm to the authorities responsible for the management of the existing aquifers in the basin, as most of the boreholes accessible are private but, in most cases, do not cover the entire thickness of the aquifers because of financial limitations, thus not that reliance for sound research work.

(iv) **To build a database on drillings/boreholes and reinforce the laws in place to regulate the indiscriminate drilling.**

A lot of discrepancies and gaps in the available technical data on the boreholes tapping a particular aquifer, including the number of boreholes as well as their characteristics (depth, initial hydraulic head, and physicochemical parameters), especially for the private ones, were faced. In addition, long-term pumping test data are very limited, thus constraining accurate accountability for the heterogeneity of key hydraulic dispersivity parameters across the study area, key to flow and solute transport modelling.

FOR FUTURE RESEARCH

(i) Improve SEAWAT outputs.

Though the SEAWAT model built for the AP shows robustness ranging from acceptable to good, a lot of assumptions were made because of the limited data, thus giving room for improvement in order to have a groundwater monitoring system for the AP.

(ii) Consider other approaches to LULC assessment.

To minimise the confusion between natural vegetation and agricultural lands, a mono-temporal dataset (dry season) has been considered in this context. Nevertheless, the use of a multi-temporal dataset has been reported to better capture land classes with different spectral signatures across seasons, such as cropland, which is found in the study area, using vegetation indices or deep learning techniques, among others. In addition, though several long-term policies and targets were considered, factors such as constraints and economic incentives were not captured in this study. Another aspect that was not considered in this study is the temporal dynamics of roads and urban zones, which represents a general model shortcoming and could give a better estimate if considered. Furthermore, direct drivers such as climate change and climate variability were not considered in the study. All these shortcomings leave room for future research for a more holistic estimation.

(iii) Further investigation of the location and geometry of seawater-freshwater

In the context of this research work, due to the allocated time and resources, only the true resistivity distribution obtained during the rainy season has been considered to determine the location and geometry of the seawater-freshwater interface; thus, considering both seasons may give more information, especially the seasonal shift of the interface. In addition, because the study area belongs to an urban setting, the required space was limited for performing continuous profiles, thus requiring other geophysical methods that require less experimental space or apparatus that will help cover the study area in a continuous way.

(iv) Investigate the recharge over the AP, considering other methods and approaches

Though the obtained recharge estimate is very fair, the method employed in this study was based on field constraints (limited data, financial resources, and allocated time). So, with more data, other empirical methods, such as chloride mass balance, the Penman method, and the Thornthwaite method, or numerical models, can be considered to improve the results.

REFERENCES

Abd-Elaty, I., & Zelenakova, M. (2022). Saltwater intrusion management in shallow and deep coastal aquifers for high aridity regions. *Journal of Hydrology: Regional Studies*, 40,101026. https://doi.org/10.1016/j.ejrh.2022.101026

Abdalla, O., Ali, M., Al-Higgi, K., Al-Zidi, H., El-Hussain, I., & Al-Hinai, S. (2010). Rate of seawater intrusion estimated by geophysical methods in an arid area: Al Khabourah, Oman. *Hydrogeology Journal*, *18*(6), 1437–1445. https://doi.org/10.1007/s10040-010-0606-0

Abdelaziz, K. K., Yalo, N., Séguis, L., Ouattara, I., Moussa, O., Auguste, K., Kamagaté, B., & Diakaria, K. (2020). Influence of land use land cover change on groundwater recharge in the continental terminal area of Abidjan, Ivory Coast. *Journal of Water Resource and Protection*, 12 (05), 431 – 453. https://doi.org/10.4236/jwarp.2020.125026

Adeyeri, O. E., Lawin, A. E., Laux, P., Ishola, K. A., & Ige, S. O. (2019). Analysis of climate extreme indices over the Komadugu-Yobe basin, Lake Chad region: Past and future occurrences. *Weather and Climate Extremes*, *23*, 100194. https://doi.org/10.1016/j.wace.2019.100194

Agossou, A., Yang, J., & Lee, J. (2022). Evaluation of potential seawater intrusion in the coastal aquifers system of Benin and effect of countermeasures considering future sea level rise. *Water*, 14(24), 4001. https://doi.org/10.3390/w14244001

Ahokpossi, Y. (2018). Analysis of the rainfall variability and change in the Republic of Benin (West Africa). *Hydrological Sciences Journal*, *63* (15–16), 2097–2123. https://doi.org/10.1080/02626667.2018.1554286

Akakpo, Y. (2017). *Caractérisation hydro géochimique de l'aquifère du paléocène à l'ouest du fleuve Zio au Togo* [Unpublished master's thesis]. Université d'Abomey Calavi, Bénin

Akbarpour, S., & Niksokhan, M. H. (2018). Investigating effects of climate change, urbanization, and sea level changes on groundwater resources in a coastal aquifer: an integrated assessment. *Environmental Monitoring and Assessment* 190. 10.1007/s10661-018-6953-3

Akinsanola, A. A., & Ogunjobi, K. O. (2015a). Recent homogeneity analysis and long-term spatio-temporal rainfall trends in Nigeria. *Theoretical and Applied Climatology*, *128* (1–2), 275–289. https://doi.org/10.1007/s00704-015-1701-x

Akinsanola, A. A., Ogunjobi, K. O., Gbode, I. E., & Ajayi, V. O. (2015b). Assessing the Capabilities of Three Regional Climate Models over CORDEX Africa in Simulating West African Summer Monsoon Precipitation. *Advances in Meteorology*, *2015*, 1–13. https://doi.org/10.1155/2015/935431

Akodéwou, A., Oszwald, J., Saïdi, S., Gazull, L., Akpavi, S., Akpagana, K., & Gond, V. (2020). Land Use and Land Cover Dynamics Analysis of the Togodo Protected Area and its surroundings in southeastern Togo, West Africa. *Sustainability*, *12*(13), 5439. https://doi.org/10.3390/su12135439

Akouvi, A. (2005). *Étude géochimique et hydrogéologique des eaux souterraines d'un basin sédimentaires côtier en zone tropicale. Implications sur la gestion, la protection et la préservation des ressources en eau du Togo* [Doctoral thesis, Université Pierre et Marie Curie, France]. Theses.fr. https://theses.fr/2001PA066495

Akouvi, A., Dray, M., Violette, S., De Marsily, G., & Zuppi, G. M. (2008). The sedimentary coastal basin of Togo: example of a multilayered aquifer still influenced by a palaeo-seawater intrusion. *Hydrogeology Journal*, *16*(3), 419–436. https://doi.org/10.1007/s10040-007-0246-1

Akpataku, K. V., Prakash, S., Gnazou, M. D., Tampo, L., Bawa, L. M., Djanéyé-Boundjou, G., & Faye, S. (2019). Hydrochemical and isotopic characterization of groundwater in the southeastern part of the Plateaux Region, Togo. *Hydrological Sciences Journal*, *64*(8), 983–1000. https://doi.org/10.1080/02626667.2019.1615067

Akpegnon, L. A. (2021). *Analyse de la variabilité hydro-climatique dans le bassin du Zio entre 1960 et 2019* [Unpublished master's thesis]. Université de Lomé, Togo

Ali, S.M., & Mohammed, M.J. (2013). Gap-filling restoration methods for ETM sensor images. *Iraqi J. Sci.* 54 (1), 206–214

Alshari, E. A., & Gawali, B. W. (2021). Development of classification system for LULC using remote sensing and GIS. *Global Transitions Proceedings*, *2*(1), 8–17. https://doi.org/10.1016/j.gltp.2021.01.002

Amegadje, M.K. (2007). *Profil Environnemental du Togo.* Rapport final. Retrieved May 5, 2020, from https://www.scribd.com/document/498663977/cep-togo-2007-fr

Amoussou, E., Camberlin, P., & Mahé, G. (2012) Impact de la variabilité climatique et du barrage Nangbéto sur l'hydrologie du système Mono-Couffo (Afrique de l'Ouest). *Hydrological Sciences Journal* 57 (2), 1 –13

Amoussou, E., Vodounon, H. S. T., Houessou, S., Tramblay, Y., Camberlin, P., Houndénou, C., Boko, M., Mahe, G., & Paturel, J. (2015). *Application d'un modèle conceptuel à l'analyse de la dynamique hydrométéorologique des crues dans un bassin-versant en milieu tropical humide : cas du fleuve Mono.* (Actes duXXVIIIe Colloque de l'Association International de Climatologie, 1-4 juillet 2015, Liège, Belgique, pp. 17–23). Retrieved from https://hal.archives-ouvertes.fr/hal-01300493

Andaryani, S., Sloan, S., Nourani, V., & Keshtkar, H. (2021). The utility of a hybrid GEOMOD-Markov Chain model of land-use change in the context of highly water-demanding agriculture in a semi-arid region. *Ecological Informatics*, *64*, 101332. https://doi.org/10.1016/j.ecoinf.2021.101332

ANTEA. (2013). Modélisation des aquifères du bassin sédimentaire côtier. *Rapport du Ministere de l 'Eau, de l'Assainissement et de l'Hydraulique villageoise MEAHV*, 25p

ANTEA. (2017). *West Africa Coastal Areas Management Program (WACA)-plan d'actions pour le developpement et l'adaptation aux changements climatiques du littoral Togolais.* Rapport final. The World Bank, Ministère de l'Environnement et des ressources forestières: Washington, Togo. Retrieved August 5, 2020, from https://documents1.worldbank.org/curated/fr/613381527758998181/pdf/Programme-

de-Gestion-du-Littoral-Ouest-Africain-Plan-dAction-pour-le-Developpement-et-lAdaptation-aux-Changements-Climatiques-du-Littoral-Togolais.pdf

Anyamba, A., Small, J., Britch, S. C., Tucker, C. J., Pak, E., Reynolds, C., Crutchfield, J., & Linthicum, K. J. (2014). Recent weather extremes and impacts on agricultural production and Vector-Borne disease outbreak patterns. *PLOS ONE*, *9*(3), e92538. https://doi.org/10.1371/journal.pone.0092538

Archie, G. E. (1942). The electrical resistivity log as an aid in determining some reservoir characteristics. *Transactions of the AIME*, *146*(01), 54–62. https://doi.org/10.2118/942054-g

Arsanjani, J. J. (2011). *Dynamic land use/cover change modelling: Geosimulation and multiagent-based modelling* (1st ed.). Retrieved February 5, 2021, from https://www.amazon.com/Dynamic-land-cover-change-modelling-ebook/dp/B007EMRA8C

Ashaley, J., Anornu, G. K., Awotwi, A., Gyamfi, C., & Anim-Gyampo, M. (2020). Performance evaluation of Africa CORDEX regional climate models: case of Kpong irrigation scheme, Ghana. *Spatial Information Research*, *28*(6), 735–753. https://doi.org/10.1007/s41324-020-00331-z

Association Française de Normalisation (AFNOR) (1997). *Qualité de l'eau : Recueil des Normes Françaises Environnement (Tomes 1- 4).* Paris, France : AFNOR

Auguie, B., & Antonov, A. (2017). gridExtra: Miscellaneous Functions for "Grid" Graphics. R Package Version 2.3. https://CRAN.R-project.org/package=gridExtra.

Avumadi, A. (2019). *Dynamique des apports fluviaux dissous et particuliaires au lac Togo : bilans, origines et devenir, mécanismes et facteurs de contrôle* [Doctoral thesis, Institut National Polytechnique de Toulouse et l'Université de Lomé, France et Togo]. HAL. https://theses.hal.science/tel-04169673/document

Ayolabi, E. A., Folorunso, A. F., Odukoya, A. M., & Adeniran, A. F. (2013). Mapping saline water intrusion into the coastal aquifer with geophysical and geochemical techniques: the University of Lagos campus case (Nigeria). *SpringerPlus*, *2*(1). https://doi.org/10.1186/2193-1801-2-433

Batayneh, A. T., Elawadi, E., & Al-Arifi, N. (2010). Use of geoelectrical technique for detecting subsurface fresh and saline water: a case study of the Eastern Gulf of Aqaba Coastal Aquifer, Jordan. *Journal of Coastal Research*, *26*, 1079–1084. https://doi.org/10.2112/jcoastres-d-09-00006.1

Bawa A. (2017). *Mutations Des Peripheries Urbaines Au Sud Du Togo. Des espaces ruraux à l'épreuve du peuplement et de la marchandisation des terres* [Doctoral thesis, Université de Montpellier, France]. Cirad-Agritrop. https://agritrop.cirad.fr/591671/

Bear, J., & Zhou, Q. (2007). Sea water intrusion into coastal aquifers. In J. W. Delleur (Ed.) The handbook of groundwater engineering. second ed. (pp 12-11-12-29). Boca Raton, Florida: CRC Press,Taylor and Francis Group. Doi :10.1201/9781420006001.ch12

Bear, J., Cheng, A.H.D., Sorek, S., Ouazar, D., & Herrera, I. (1999). Seawater Intrusion in Coastal Aquifers: Concepts, Methods and Practices. Dordrecht, The Netherlands: Kluwer Academic Publishers. Doi :10.1007/978-94-017-2969-7_1

Bleza, A. (2017). *Caractérisation piézométrique et physicochimique de l'aquifère du continental terminal du plateau d'Agoè* [Unpublished master's thesis]. Université de Lomé, Togo

Bleza, A., Gnazou, M.D.-T, & Gnazou, M.E. (2020b). Contribution à l'étude hydrogéologique de l'Aquifère du Continental Terminal à l'ouest du Zio (Togo*). Journal de la Recherche Scientifique de l'Université de Lomé* 22 (3). https://www.ajol.info/index.php/jrsul/article/view/204760

Bleza, A., Gnazou, M.D.-T, Gnazou, M.E., Boguido, G., Yomo, M., Akpatakou, K. V., Djaneye-Boundjou, G., & Bawa, M. (2020a). Physicochemicalcharacterization of the continental terminal aquifer in the Agoè plateau (Togo). *Asian Journal of Scientific and Engineering* Research https://docplayer.net/202530219-Asian-journal-of-scientific-and-engineering-research-physico-chemical-characterization-of-the-continental-terminal-aquifer-in-the-agoe-plateau-togo.html

Boampong, J. N. (2020). *An Assessment of Land use/ landcover and Shoreline Changes in the Coastal zone of Greater Accra region, Ghana* [Master's thesis, UiT The Arctic University of Norway, Norway]. UiT Munin. https://hdl.handle.net/10037/19345

Bobba, A. G. (2002). Numerical modelling of salt-water intrusion due to human activities and sea-level change in the Godavari Delta, India. *Hydrological Sciences Journal*, *47*(sup1), S67–S80. https://doi.org/10.1080/02626660209493023

Boerner, A., & Weaver, C. (2012). Nebraska recharge estimation from chloride mass balance. GIS in Water Resources. Nebraska, USA. Retrieved May 21, 2020, from https://www.yumpu.com/en/document/view/7617685/nebraska-recharge-estimation-from-chloride-mass-balance

Bouderbala, A., & Rémini, B. (2014). Geophysical approach for assessment of seawater intrusion in the coastal aquifer of Wadi Nador (Tipaza, Algeria). *Acta Geophysica*, *62*(6), 1352–1372. https://doi.org/10.2478/s11600-014-0220-y

Bourhane, A. (2014). *Méthodes d'investigation de l'intrusion marine dans les aquifères volcaniques (La Réunion et La Grande Comore)*[Doctoral thesis, Université de La Réunion, France]. HAL. https://core.ac.uk/download/pdf/46813374.pdf

Boyd, E., Nykvist, B., Borgstro¨m, S., & Stacewicz, I.A. (2015). Anticipatory governance for social ecological resilience. Ambio 44 (S1), 149–161. https://doi.org/ 10.1007/s132800140604X

Brent, R. P. (1971). An algorithm with guaranteed convergence for finding a zero of a function. *The Computer Journal*, *14*(4), 422–425. https://doi.org/10.1093/comjnl/14.4.422

Buishand, T. A. (1982). Some methods for testing the homogeneity of rainfall records. *Journal of Hydrology*, *58*(1–2), 11–27. https://doi.org/10.1016/0022-1694(82)90066-x

Buishand, T. A. (1984). Tests for detecting a shift in the mean of hydrological time series. *Journal of Hydrology*, *73*(1–2), 51–69. https://doi.org/10.1016/0022-1694(84)90032-5

Bureau de Recherches Geologiques et Minieres (BRGM). (1986). Carte géologique de Togo et Notice explicative de la carte géologique au 1/200.000. Feuille de Lomé. 1ere édition. Mémoire n° 5, BNRM. Togo, BRGM, Orléans, France.

Carr, T.W., Mkuhlani, S., Segnon, A. C., Ali, Z., Zougmoré, R. B., Dangour, A. D., Green, R., & Scheelbeek, P. (2022). Climate change impacts and adaptation strategies for crops in West Africa: a systematic review. *Environmental Research Letters* 17(5), 1-14. https://doi.org/10.1088/1748-9326/ac61c8

Casillas-Trasvina, A., Zhou, Y., Stigter, T., Mussáa, F. E. F., & Juízo, D. (2019). Application of numerical models to assess multi-source saltwater intrusion under natural and pumping conditions in the Great Maputo aquifer, Mozambique. *Hydrogeology Journal*, *27*(8), 2973–2992. https://doi.org/10.1007/s10040-019-02053-5

Chabaane, A., Redhaounia, B., Gabtni, H., & Amiri, A. (2018). Contribution of geophysics to geometric characterization of freshwater–saltwater interface in the Maâmoura region (NE Tunisia). *Euro-Mediterranean Journal for Environmental Integration*, *3*(1). https://doi.org/10.1007/s41207-018-0068-7

Cherlet, M., Hutchinson, C., Reynolds, J., Hill, J., Sommer, S., & Von Maltitz, G. (2018). *World Atlas of Desertification: Rethinking Land Degradation and Sustainable Land Management*

Chow, V., Maidment, D., & Mays, L. (1988). Applied Hydrology. In : Eliassen, R., King, H.P., LinsleyK. R. (Eds.), *Series in Water Resources and Environmental Engineering* (pp.110-565). Boston, USA: McGraw-Hill

Christensen, M. M., & Arsanjani, J. J. (2020). Stimulating implementation of sustainable development goals and conservation action: Predicting Future Land Use/Cover Change in Virunga National Park, Congo. *Sustainability*, *12*(4), 1570. https://doi.org/10.3390/su12041570

Chun, J. A., Lim, C., Kim, D., & Kim, J. S. (2018). Assessing impacts of climate change and Sea-Level rise on seawater intrusion in a coastal aquifer. *Water*, *10*(4), 357. https://doi.org/10.3390/w10040357

Comte, J-C. (2008). *Apport de la tomographie électrique à la modélisation des écoulements densitaires dans les aquifères côtiers - Application à trois contextes climatiques contrastés (Canada, Nouvelle-Calédonie, Sénégal)* [Doctoral thesis, Université d'Avignon, France]. HAL theses. fhttps://theses.hal.science/tel-00381767/document

Comte, J., Join, J., Banton, O., & Nicolini, E. (2014). Modelling the response of fresh groundwater to climate and vegetation changes in coral islands. *Hydrogeology Journal*, *22*(8), 1905–1920. https://doi.org/10.1007/s10040-014-1160-y

Comte, J.C., & Banton, O. (2007). Comparaison de dispositifs d'acquisition ERT pour l'imagerie géo-électrique des intrusions salines dans les aquifères côtiers. 6ième colloque GEOFCAN – 25-26/09/2007 – Bondy, France. 5p

Congalton, R. G. (1991). A review of assessing the accuracy of classifications of remotely sensed data. *Remote Sensing of Environment*, *37*(1), 35–46. https://doi.org/10.1016/0034-4257(91)90048-b

Coutagne, A. (1954) Quelques considérations sur le pouvoir évaporant de l'atmosphère, le déficit d'écoulement effectif et le déficit d'écoulement maximum. *La Houille Blanche* 360–374

Craig, H. (1961a). Isotopic variations in meteoric waters. *Science, 133*(3465), 1702–1703. https://doi.org/10.1126/science.133.3465.1702

Craig, H. (1961b). Standard for Reporting Concentrations of deuterium and oxygen-18 in natural waters. *Science, 133*(3467), 1833–1834. https://doi.org/10.1126/science.133.3467.1833

Crosbie, R., Scanlon, B. R., Mpelasoka, F., Reedy, R. C., Gates, J. B., & Zhang, L. (2013). Potential climate change effects on groundwater recharge in the High Plains Aquifer, USA. *Water Resources Research, 49*(7), 3936–3951. https://doi.org/10.1002/wrcr.20292

Custódio, E. (2009). Coastal aquifers of Europe: an overview. *Hydrogeology Journal, 18*(1), 269–280. https://doi.org/10.1007/s10040-009-0496-1

Custodio, E., & Bruggeman, G.A. (1987). *Groundwater Problems in Coastal Areas*. Paris, France: UNESCO.

Da Costa ,Y. D., P. (2005). *Biostratigraphie et Paléogéographie du bassin sédimentaire du Togo* [Unpublished doctoral thesis]. Université de Lomé, Togo

Dahlin, T. (2001). The development of DC resistivity imaging techniques. *Computers & Geosciences, 27*(9), 1019–1029. https://doi.org/10.1016/s0098-3004(00)00160-6

Daron, J.D. (2014). *Regional climate messages: West Africa* (Scientific report from the CARIIA Adaptation at Scale in Semi-Arid Regions Project). Ottawa, Canada: CARIAA and ASSAR. https://idl-bnc-idrc.dspacedirect.org/server/api/core/bitstreams/df9b1695-e5a5-461c-8a41-9cd5c78255f8/content

De Breuck, W., & De Moor, G. (1969). The water-table aquifer in the Eastern coastal area of Belgium. *International Association of Scientific Hydrology. Bulletin, 14*(3), 137–155. https://doi.org/10.1080/02626666909493739

De Carvalho, J. W. L. T., Iensen, I. R. R., & Santos, I. D. (2021). Resilience of Hydrologic Similarity Areas to extreme climate change scenarios in an urban watershed. *Urban Water Journal, 18*(10), 817–828. https://doi.org/10.1080/1573062x.2021.1941136

De Moor, G., & De Breuck, W. (1964). Geo-elektrisch onderzoek bij de geologische overzichtskartering van West-Vlaanderen. *Natuurwetenschappelijk Tijdschrift,* 46, 215-240

Deslauriers, S., & Mahdi, T.-F. (2018). Flood modelling improvement using automatic calibration of two dimensional river software SRH-2D. *Natural Hazards, 91*(2), 697-715. https://doi.org/10.1007/s11069-017-3150-6

Dhali, K., Chakraborty, M., & Sahana, M. (2019). Assessing spatio-temporal growth of urban sub-centre using Shannon's entropy model and principle component analysis: A case from North 24 Parganas, lower Ganga River Basin, India. *The Egyptian Journal of Remote Sensing and Space Science, 22*(1), 25–35. https://doi.org/10.1016/j.ejrs.2018.02.002

Diasso, U. J., & Abiodun, B. J. (2015). Drought modes in West Africa and how well CORDEX RCMs simulate them. *Theoretical and Applied Climatology, 128*(1–2), 223–240. https://doi.org/10.1007/s00704-015-1705-6

Diersch, H. G. (1988). Finite element modelling of recirculating density-driven saltwater intrusion processes in groundwater. *Advances in Water Resources*, *11*(1), 25–43. https://doi.org/10.1016/0309-1708(88)90019-x

Direction de l'Hydraulique et de l'Energie (DHE) (1982). Surveillance piézométrique et chimique des nappes du bassin sédimentaire côtier du Togo. Synthèse des connaissances hydrogéologiques. Rapport 82 AGE 036, DHE-Togo, BRGM, Orléans, France

Direction de l'Hydraulique et de l'Energie (DHE) (1983). Alimentation en eau de Lomé. Ressources en eau souterraine. Synthèse des données hydrogéologiques. Rapport 83 AGE 040, DHE-Togo, BRGM, Orléans, France

Direction de l'Hydraulique et de l'Energie (DHE) (1984). Alimentation en eau de Lomé. Modèle mathématique préliminaire des nappes du continental terminal et du Paléocène. Rapport BRGM84 AGE 008. BCEOM/BRGM, Orléans, France

Direction Générale de la Statistique et de la Comptabilité Nationale (DGSCN) (2011). Recensement général de la population et de l'habitat/Résultats définitifs. https://inseed.tg/statistiques-demographiques/

Diwediga, B., Wala, K., Foléga, F., Dourma, M., Woegan, Y. A., Akpagana, K., & Le, Q. B. (2015). Biophysical and anthropogenous determinants of landscape patterns and degradation of plant communities in Mo hilly basin (Togo). *Ecological Engineering*, *85*, 132–143. https://doi.org/10.1016/j.ecoleng.2015.09.059

Djaman, K., Sharma, V., Rudnick, D. R., Koudahe, K., Irmak, S., Amouzou, K. A., & Sogbedji, J. M. (2017). Spatial and temporal variation in precipitation in Togo. *International Journal of Hydrology*, *1*(4). https://doi.org/10.15406/ijh.2017.01.00019

Djibril, S. H., & Agrell, B. (2011). Impacts des Changements Climatiques sur le Rendement de L'exploitation des Ressources en Eau : Cas de la Société Togolaise des Eaux

Doğan, A. U., & Fares, A. (2008). Effects of land-use changes and groundwater pumping on saltwater intrusion in coastal watersheds. In *WIT transactions on state-of-the-art in science and engineering* (pp. 219–249). https://doi.org/10.2495/978-1-84564-091-0/08

Eastman, J.R. (2012). *IDRISI Selva Tutorial (Manual Version 17)*. Worcester, USA: IDRISI Production, Clark Labs-Clark University 45 http://uhulag.mendelu.cz/files/pagesdata/eng/gis/idrisi_selva_tutorial.pdf

Eastman, J.R. (2016). IDRISI Terrset Manual. IDRISI Production: Worcester, MA, USA

Edet, A., & Okereke, C. (2001). A regional study of saltwater intrusion in southeastern Nigeria based on the analysis of geoelectrical and hydrochemical data. *Environmental Geology*, *40*(10), 1278–1289. https://doi.org/10.1007/s002540100313

El Hamidi, M. J. E., Larabi, A., & Faouzi, M. (2021). Numerical modeling of saltwater intrusion in the RMEl-Oulad Ogbane Coastal Aquifer (Larache, Morocco) in the climate Change and Sea-Level Rise Context (2040). *Water*, *13*(16), 2167. https://doi.org/10.3390/w13162167

El Mokhtar, M., Chibout, M., El Mansouri, B., & Chao, J. (2018). Modeling of the Groundwater Flow and Saltwater Intrusion in the Coastal Aquifer of Fum Al Wad, Province of Laayoun, Morocco. *International Journal of Geosciences* 09(01):71-92. DOI:10.4236/ijg.2018.91005

Ern H (1979). The Vegetation of Togo. Gliederrung, Gefährdung, Erhaltung. Willdenowia, 9:295-312

Escadafal, R. (2007). Les bases de la surveillance de la désertification par satellites. *Sècheresse (Montrouge)*, *18*(4), 263–270

Etcheverry, D. (2002). *Valorisation des méthodes isotopiques pour les questions pratiques liées aux eaux souterraines. Isotopes de l'oxygène et de l'hydrogène* (Rapports de l'OFEG, Série Géologie 2). Office Fédéral des Eaux et de La Géologie. https://www.bafu.admin.ch/dam/bafu/fr/dokumente/hydrologie/uw-umwelt-wissen/valorisation_desmethodesisotopiquespourlesquestionspratiquesliee.pdf.download.pdf/valorisation_desmethodesisotopiquespourlesquestionspratiquesliee.pdf

Field, C.B., Barros, V.R., Mach, K.J., Mastrandrea, M.D., van Aalst, M., Adger, W.N., Arent, D.J., Barnett, J., Betts, R., Bilir, T.E., Birkmann, J., Carmin, J., Chadee, D.D., Challinor, A.J., Chatterjee, M., Cramer, W., Davidson, D.J., Estrada, Y.O., Gattuso, J.-P, Hijioka, Y., Hoegh-Guldberg, O., Huang, H.Q., Insarov, G.E., Jones, R.N., Kovats, R.S., Romero-Lankao, P., Larsen, J.N., Losada, I.J., Marengo, J.A., McLean, R.F., Mearns, L.O., Mechler, R., Morton, J.F., Niang, I., Oki, T., Olwoch, J.M., Opondo, M., Poloczanska, E.S., Pörtner, H.-O., Redsteer, M.H., Reisinger, A., Revi, A., Schmidt, D.N., Shaw, M.R., Solecki, W., Stone, D.A., Stone, J.M.R., Strzepek, K.M., Suarez, A.G., Tschakert, P., Valentini, R., Vicuña, S., Villamizar, A., Vincent, K.E., Warren, R., White, L.L., Wilbanks, T.J., Wong, P.P., & Yohe, G.W. (2014). Technical summary. In: Field, C.B., Barros, V.R., Dokken, D.J., Mach, K.J., Mastrandrea, M.D., Bilir, T.E., Chatterjee, M., Ebi, K.L., Estrada, Y.O., Genova, R.C., Girma, B., Kissel, E.S., Levy, A.N., MacCracken, S., Mastrandrea P.R., & White L.L. (Eds.), *Climate Change 2014: Impacts, Adaptation, and Vulnerability. Part A: Global and Sectoral Aspects (*pp. 35-94.), *Contribution of Working Group II to the Fifth Assessment Report of the Intergovernmental Panel on Climate Change.*United Kingdom and New York, USA : Cambridge University Press

Fisher, R. S., & Mullican, W. F. (1997). Hydrochemical evolution of Sodium-Sulfate and Sodium-Chloride groundwater beneath the Northern Chihuahuan Desert, Trans-Pecos, Texas, USA. *Hydrogeology Journal*, *5*(2), 4–16. https://doi.org/10.1007/s100400050102

Fofana, M., Adounkpè, J., Larbi, I., Hounkpè, J., Koubodana, H. D., Toure, A., Bokar, H., Dotse, S-Q., & Limantol, A. M. (2022). Urban flash flood and extreme rainfall events trend analysis in Bamako, Mali. *Environmental Challenges*, *6*, 100449. https://doi.org/10.1016/j.envc.2022.100449

Foléga, F., Andrianamenoso, R. M., Wala, K., Agbelessessi, W. Y., Kanda, M., Pereki, H., Polo-Akpisso, A., Batawila, K., & Akpagana, K. (2017). Écologie et dynamique spatio-temporelle des mangroves au Togo. *VertigO*, 17 (3). https://doi.org/10.4000/vertigo.18791

Fontaine, B. (1991). Variations pluviométriques et connexions climatiques : l'exemple des aires de mousson indienne et ouest-africaine. *Science Et Changements Planétaires / Sécheresse*, *2*(4), 259–264. Retrieved from http://www.jle.com/fr/revues/sec/e-docs/variations_pluviometriques_et_connexions_climatiques_lexemple_des_aires_de_mousson_indienne_et_ouest_africaine_271063/article.phtml

Fontes, J. C. (1976). *Isotopes du milieu et cycles des eaux naturelles : quelques aspects* [Unpublished doctoral thesis]. Université Pierre et Marie Curie, France

Forkuor, G. (2014). *Agricultural Land Use Mapping in West Africa Using Multi-Sensor Satellite Imagery* [Doctoral thesis, Julius-Maximilians-Universität, Germany]. OPUS Würzburg. https://opus.bibliothek.uni-wuerzburg.de/opus4-wuerzburg/frontdoor/deliver/index/docId/10868/file/thesis_gerald_forkuor_2014.pdf

Frind, E. O. (1982). Simulation of long-term transient density-dependent transport in groundwater. *Advances in Water Resources*, *5*(2), 73–88. https://doi.org/10.1016/0309-1708(82)90049-5

Fritz, P., & Fontes, J. (1980). *Handbook of Environmental Isotope Geochemistry. Volume 1, The Terrestrial Environment, A.* Amsterdam, Netherlands: Elsevier Scientific Publishing Company

Gadedjisso-Tossou, A., Adjegan, K.I., & Kablan, A.K.M. (2021). Rainfall and Temperature Trend Analysis by Mann–Kendall Test and Significance for Rainfed Cereal Yields in Northern Togo. *Sci.*, 3 (17), 1-20. https://doi.org/10.3390/sci3010017

Gallo, G. (1974). *Rapport final sur les études isotopiques appliquées à l'hydrogéologie du bassin sédimentaire côtier du Togo* (IAEA Internal Report TOG 71/511). Vienna, Austria : IAEA

Ganyaglo, S. Y., Osae, S., Akiti, T. T., Armah, T., Gourcy, L., Vitvar, T., Ito, M., & Otoo, I. A. (2017). Application of geochemical and stable isotopic tracers to investigate groundwater salinity in the Ochi-Narkwa Basin, Ghana. *Hydrological Sciences Journal*, 62(8), 1301–1316. https://doi.org/10.1080/02626667.2017.1322207

Gao, Z., Wang, Z., Wang, S., Wu, X., An, Y., Wang, W., & Liu, J. (2019). Factors that influence the chemical composition and evolution of shallow groundwater in an arid region: a case study from the middle reaches of the Heihe River, China. *Environmental Earth Sciences*, *78*(14). https://doi.org/10.1007/s12665-019-8391-0

Garcia, G.M., Hidalgo M.D.V., & Blesa M.A. (2001). Geochemistry of groundwater in the alluvial plain of Tucuman province, Argentina. *Hydrogeology Journal* 9(6) : 597-610

Gassama-Jallow, A. (2021). *Assessment of the impact of climate change on groundwater resources of the Greater Banjul areas (GBA) in the Gambia* [Doctoral thesis, University of Abomey Calavi, Benin]. WASCAL. https://wascal-uac.org/thesis/Thesis_Gassama-Djallow_2021.pdf

Gibson, L., Münch, Z., Palmer, A., & Mantel, S. (2018). Future land cover change scenarios in South African Grasslands-Implications of altered biophysical drivers on land management. *Heliyon* 4, e00693. https://doi.org/10.1016/j.heliyon.2018.e00693.

Giménez-Forcada, E. (2010). Dynamic of Sea Water Interface using Hydrochemical Facies Evolution Diagram. *Groundwater*, *48*(2), 212–216. https://doi.org/10.1111/j.1745-6584.2009.00649.x

Giménez-Forcada, E., & Sánchez San Román, F.J. (2014). An Excel Macro to plot the HFE-Diagram to identify seawater intrusion phases. *Groundwater*. DOI: 10.1111/gwat.12280

Giorgi, F. (2019). Thirty Years of Regional Climate Modeling: Where Are We and Where Are We Going next? *Journal of Geophysical Research: Atmospheres*, *124*(11), 5696–5723. https://doi.org/10.1029/2018jd030094

Giorgi, F., & Mearns, L. O. (1999). Introduction to special section: Regional Climate Modeling Revisited. *Journal of Geophysical Research*, 104 (D6), 6335–6352. https://doi.org/10.1029/98jd02072

Girard, M.C., & Girard, C.M. (1999). *Traitement des données de télédétection*. Dunod. https://books.google.tg/books?id=R_ymAAAACAAJ

Gnazou, M. D.-T. (2008). *Etude hydrodynamique, hydrochimique, isotopique et modélisation de l'aquifère du bassin sédimentaire côtier du Togo* [Unpublished doctoral thesis]. Université de Lomé, Togo

Gnazou, M. D.-T., Sabi, B. E., Da Costa, P. Y. D., & Tairou, M. S. (2015a). Etude structurale et hydrodynamique de l'aquifère du Continental Terminal du plateau d'Agoè. *Journal de la Recherche Scientifique de l'Université de Lomé,* 17 (3). https://www.ajol.info/index.php/jrsul/article/view/134805

Gnazou, M. D.-T., Sabi, B. E., Lavalade, J., Schwartz, J., Akakpo, W., & Tozo, A. (2017). Multilayered aquifer modeling in the coastal sedimentary basin of Togo. *Journal of African Earth Sciences*, *125*, 42–58. https://doi.org/10.1016/j.jafrearsci.2016.10.008

Gnazou, M. D.-T., Sabi, E.B., Tairou, S.M., Akakpo, W., Agouda, K., Upton, K., Ó Dochartaigh, B.É., & Bellwood-Howard, I. (2018). Africa Groundwater Atlas: Hydrogeology of Togo. British Geological Survey. Retrieved May 21, 2020, from http://earthwise.bgs.ac.uk/index.php/Hydrogeology_of_Togo

Gnazou, M.D.T., Sabi, B. E., Togbe, K.A., Da Costa, Y.D., & Agouda K. (2015b). Actualisation Structurale de L'aquifère du Paléocène dans le Bassin Côtier du Togo. *European Scientific Journal*, 11(27). https://eujournal.org/index.php/esj/article/view/6262

Gopinath, S., Srinivasamoorthy, K., Saravanan, K., Suma, C. S., Prakash, R., Senthilnathan, D., . Chandrasekaran, N., Srinivas, Y., & Sarma, V. S. (2016). Modeling saline water intrusion in Nagapattinam coastal aquifers, Tamilnadu, India. *Modeling Earth Systems and Environment*, *2*(1). https://doi.org/10.1007/s40808-015-0058-6

Gudmundsson, L., Bremnes, J. B., Haugen, J., & Skaugen, T. (2012). Technical Note: Downscaling RCM Precipitation to the Station Scale Using Quantile Mapping – A Comparison of Methods. *Hydrology and Earth System Sciences Discussions*, 9, 6185-6201. 10.5194/hessd-9-6185-2012

Gunavathi, S., & Selvasidhu, R. (2021). Assessment of various bias correction methods on precipitation of regional climate model and future projection. *Research Square (Research Square)*. https://doi.org/10.21203/rs.3.rs-339080/v1

Guo, W., & Langevin, C.D. (2002). *User's guide to SEAWAT: A computer program for the simulation of three-dimensional variable-density ground-water flow*. *USGS Techniques of Water Resources Investigations* (Book 6, Chapter A7). Tallahassee, Florida, USA: USGS. Retrieved from https://fl.water.usgs.gov/PDF_files/twri_6_A7_guo_langevin.pdf

Guvanasen, V., Wade, S.C., & Barcelo, M.D. (2000). Simulation of regional groundwater flow and saltwater intrusion in Hernando County, Florida. *Groundwater* 38, 772–783

Han, R. (2014). Land Use and Land Cover Mapping Using Fuzzy Logic. In: Cao, BY., Ma, SQ., Cao, Hh. (Eds,), *Ecosystem Assessment and Fuzzy Systems Management. Advances in Intelligent Systems and Computing*, vol 254. Switzerland: Springer, Cham. https://doi.org/10.1007/978-3-319-03449-2_14

Hassen, E.E., & Assen, M. (2018). Land use/cover dynamics and its drivers in Gelda catchment, Lake Tana watershed, Ethiopia. *Environ Syst Res,* **6** (4). https://doi.org/10.1186/s40068-017-0081-x

Heidelberg Cement (2021). Rapport Annuel 2021, 48 p. Retrieved May 15, 2022, from https://www.heidelbergcement.tg/sites/default/files/2022-05/Rapport20de20responsabilitC3A920sociale20de20l27entreprise202021.pdf

Herzberg, A. (1901). Die wasserversorgung einiger Nordseebäder. *Journal für Gasbeleuchtung und Wasserversorgung*, 44, 815-819

Heydarian, P., Rangzan, K., Maleki, S., & Taghizadeh, A. (2013). Monitoring land use change using comparison method after Landsat satellite images (case study: lands of Tehran). *Remote Sensing and Geographic Information System*, 4 (4), 1–10

Hirsch, R. M., Slack, J. R., & Smith, R. A. (1982). Techniques of trend analysis for monthly water quality data. *Water Resources Research*, *18*(1), 107–121. https://doi.org/10.1029/wr018i001p00107

Houedakor, K.Z. (1997). *La dynamique de la dégradation de l'environnement dans le Sud-Est du Togo : essai de cartographie* [Master's thesis, Université du Benin, Togo]. https://www.memoireonline.com/03/20/11645/m_Developpement-des-espaces-geographiques-Exemple-du-terroir-d-Assome-dans-la-basse-vallee-du59.html

Hounsinou, S. P. (2020). Assessment of potential seawater intrusion in a coastal aquifer system at Abomey - Calavi, Benin. *Heliyon*, *6*(2), e03173. https://doi.org/10.1016/j.heliyon.2020.e03173

Houteta, D. K., Adounkpè, J., Atchonouglo, K., Djaman, K., Larbi, I., Lombo, Y., & Kpemoua, K. (2021). Modelling of streamflow before and after dam construction in the Mono River Basin in Togo-Benin, West Africa. *International Journal of River Basin Management*, *21*(2), 265–281. https://doi.org/10.1080/15715124.2021.1969943

Houteta, D. K., Adounkpè, J., Tall, M., Amoussou, E., Atchonouglo, K., & Mumtaz, M. (2020). Trend Analysis of Hydro-climatic Historical Data and Future Scenarios of Climate Extreme Indices over Mono River Basin in West Africa. *Journal of Rural and Development*, *8*(1), 37–52. https://doi.org/10.12691/ajrd-8-1-5

Houteta, D. K., Diekkrüger, B., Näschen, K., Adounkpè, J., & Atchonouglo, K. (2019). Impact of the Accuracy of Land Cover Data sets on the Accuracy of Land Cover Change Scenarios in the Mono River Basin, Togo, West Africa. *International Journal of Advanced Remote Sensing and GIS*, *8*(1), 3073–3095. https://doi.org/10.23953/cloud.ijarsg.422

Howard, K.W. F. (1987). Beneficial Aspects of Sea-Water Intrusion. *Ground Water*, 25 (4), 398-406. Doi:10.1111/j.1745-6584. 1987.tb02144. x

Howard, K.W. F., & Lloyd, J.W. (1983). Major ion chemical characteristics of coastal saline groundwater. *Ground water*, 21, 429-437

Hubbert, M.K. (1940). The theory of ground-water motion. *Journal of Geology*, 48 (8), 785-944

Hussain, M. S., & Javadi, A. A. (2016). Assessing impacts of sea level rise on seawater intrusion in a coastal aquifer with sloped shoreline boundary. *Journal of Hydro-environment Research*, *11*, 29–41. https://doi.org/10.1016/j.jher.2016.01.003

Idrissou, M., Diekkrüger, B., Tischbein, B., Op de Hipt, F., Näschen, K., Poméon, T., Yira, Y., & Ibrahim, B. (2022). Modeling the impact of climate and land use/land cover change on water availability in an inland valley catchment in Burkina Faso. *Hydrology* 9 (1), 12. https://doi.org/10.3390/hydrology9010012

Institut Géographique National/Direction de la Cartographie Nationale et du Cadastre-Ministère de l'Equipement, des mines, des postes et Télécommunications (IGN/DCNC). (1980). *Carte au 1 :200 000. I.N.G.* Paris, France : IGN

Inter-governmental Panel on Climate Change (IPCC) (2007). Climate Change 2007 : Impacts, Adaptation and Vulnerability. In: Parry, M.L., Canziani, O.F., Palutikof, J.P., van der Linden, P.J., & Hanson, C.E. (Eds), *Climate Change 2007 (*pp.1-976), *Contribution of Working Group II to the Fourth Assessment Report of the Intergovernmental Panel on Climate Change.* Cambridge, UK: Cambridge University Press

Inter-governmental Panel on Climate Change (IPCC) (2018). Annex I: Glossary. In: Masson-Delmotte, V., Zhai, P., Pörtner, H.-O., Roberts, D., Skea, J., Shukla, P.R., Pirani, A., Moufouma-Okia, W., Péan, C., Pidcock, R., Connors, S., Matthews, J.B.R., Chen, Y., Zhou, X., Gomis, M.I., Lonnoy, E., Maycock, T., Tignor, M., & Waterfield, T. (Eds.), *Global Warming of 1.5°C. An IPCC Special Report on the impacts of global warming of 1.5°C above pre-industrial levels and related global greenhouse gas emission pathways, in the context of strengthening the global response to the threat of climate change, sustainable development, and efforts to eradicate poverty (pp. 541-562).* Cambridge, UK and New York, USA: Cambridge University Press. Doi:10.1017/9781009157940.008

International Atomic Energy Agency (IAEA) (1981). *Stable Isotope Hydrology, Deuterium and Oxygen-18 in the Water Cycle* (Technical Reports Series No. 210). Vienna, Austria : IAEA

Jakovovic, D., Werner, A. D., De Louw, P. G., Post, V. E., & Morgan, L. K. (2016). Saltwater upconing zone of influence. *Advances in Water Resources*, *94*, 75–86. https://doi.org/10.1016/j.advwatres.2016.05.003

Johnson, A. I. (1967). Specific yield—Compilation of specific yields for various materials (Vol. 1662-D). United Sates Government Printing Office, Washington, DC: U.S. Geological Survey Water Supply Paper

Johnson, A.K.C. (1987). *Le bassin côtier à phosphates du Togo (Maastrichtien-Eocène moyen)* [Doctoral thesis, Université de Bourgogne et Université du Bénin, France and Togo]. theses.fr. https://theses.fr/1987DIJOS010

Johnson, T. (2007). Battling Seawater Intrusion in the Central and West Coast Basins. *WRD Tech. Bull* 13, 1–2

Jonhson, A.K., M. K., Rat, P., & Lang, J. (2000). Le bassin sédimentaire a phosphates du Togo (Maastrichtien-Eocène) : stratigraphie, environnements et évolution. *Journal of African Earth Sciences*, *30*(1), 183–200. https://doi.org/10.1016/s0899-5362(00)00015-4

Kaliraj, S., Chandrasekar, N., Ramachandran, K. K., Srinivas, Y., & Saravanan, S. (2017). Coastal landuse and land cover change and transformations of Kanyakumari coast, India using remote sensing and GIS. *The Egyptian Journal of Remote Sensing and Space Science*, *20*(2), 169–185. https://doi.org/10.1016/j.ejrs.2017.04.003

Karambiri, H., Galiano, S. G. G., Giraldo, J. D., Yacouba, H., Ibrahim, B., Barbier, B., & Polcher, J. (2011). Assessing the impact of climate variability and climate change on runoff in West Africa: the case of Senegal and Nakambe River basins. *Atmospheric Science Letters*, *12*(1), 109–115. https://doi.org/10.1002/asl.317

Ketabchi, H., Mahmoodzadeh, D., Ataie-Ashtiani, B., & Simmons, C. T. (2016). Sea-level rise impacts on seawater intrusion in coastal aquifers: Review and integration. *Journal of Hydrology*, *535*, 235–255. https://doi.org/10.1016/j.jhydrol.2016.01.083

Kim, G., Cha, D.-H., Lee, G., Park, C., Jin, C.-S., Lee, D.-K., Suh, M.-S., Ahn, J.-B., Min, S.-K., & Kim, J. (2020). Projection of future precipitation change over South Korea by regional climate models and bias correction methods. *Theoretical and Applied Climatology*, 141, 1415–1429. https://doi.org/10.1007/ s00704-020-03282-5

Knippertz, P., & Fink, A. H. (2008). Dry-Season Precipitation in Tropical West Africa and Its Relation to Forcing from the Extratropics. *Mon. Wea. Rev.*, 136, 3579–3596, https://doi.org/10.1175/2008MWR2295.1

Koglo, Y. S., Agyare, W. A., Diwediga, B., Sogbedji, J. M., Adden, A. K., & Gaiser, T. (2018). Remote Sensing-Based and participatory analysis of forests, agricultural land dynamics, and potential land conservation measures in Kloto District (Togo, West Africa). *Soil Systems*, *2*(3), 49. https://doi.org/10.3390/soilsystems2030049

Kolb, M., Mas, J.F., & Galicia, L. (2013). Evaluating drivers of land-use change and transition potential models in a complex landscape in Southern Mexico. *Int. J. Geogr. Inf. Sci.*, 27 (9), 1804e1827 https://doi.org/10.1080/13658816.2013.770517

Kooi, H., Groen, J., & Leijnse, A. (2000). Modes of seawater intrusion during transgressions. *Water Resources Research*, *36*(12), 3581–3589. https://doi.org/10.1029/2000wr900243

Kotchoni, D. O. V., Vouillamoz, J., Lawson, F. M. A., Adjomayi, P. A., Boukari, M., & Taylor, R. G. (2018). Relationships between rainfall and groundwater recharge in seasonally humid Benin: a comparative analysis of long-term hydrographs in sedimentary and crystalline aquifers. *Hydrogeology Journal*, *27*(2), 447–457. https://doi.org/10.1007/s10040-018-1806-2

Kouamé, K.J., Jourda, J.P., Saley, M.B., Deh, S.K., Anani, A.T., Leblanc, Y., Cloutier, V., & Biémi, J. (2013). Modeling of Groundwater Flow and Drawdown Evolution Simulation of Abidjan Aquifer (Côte d'Ivoire). *Journal of Asian Scientific Research*, 3, 344-364

Koudahe, K., Kayode, A. J., Samson, A. O., Adebola, A. A., & Djaman, K. (2017). Trend analysis in Standardized Precipitation Index and Standardized Anomaly Index in the

context of climate change in Southern Togo. *Atmospheric and Climate Science*, *07*(04), 401–423. https://doi.org/10.4236/acs.2017.74030

Koumoi, Z., Alassane, A., Djangbedja, M., Boukpessi, T., & Kouya, A.-E. (2013). Dynamique spatio-temporelle de L'occupation du sol dans Lecentre-Togo. *Ahoho - Revue de Géographie du LARDYMES*, 7 (10), 163–172 hal-01564256

Kouzana, L., Abdallah Ben Mammou, A.B., & Gaaloul, N. (2007). Seawater intrusion and salinization in a coastal water table (Korba, Cap-Bon, Tunisia). *Geo. Eco. Trop.* 31, 57–70

Kowarik, A., & Templ, M. (2016). Imputation with the R Package VIM. *Journal of Statistical Software*, *74*(7). https://doi.org/10.18637/jss.v074.i07

Kpedenou, K.D., Djagnikpo, K., Boukpessi, T., Tanzidani, T., & Tchamie, K. (2016). Quantification des changements de l'occupation du sol dans la préfecture de Yoto (Sud Est Togo) à l'aide de l'imagerie satellitaire Landsat. Rev. Sc. Env. 13, 137–156 hal-01409418

Kpedenou, K.D., Drabo, O., Ouoba, A.P., Dapola, C. E. D., & Tanzidani, T.K.T. (2017). Analyse de l'occupation du sol pour le suivi de l'évolution du paysage du territoire Ouatchi au Sud-Est Togo entre 1958 et 2015. *Cahiers du Cerleshs*, XXXI (55), 203-228

Kuan, W. K., Jin, G., Xin, P., Robinson, C. E., Gibbes, B., & Li, L. (2012). Tidal influence on seawater intrusion in unconfined coastal aquifers. *Water Resources Research*, *48*(2). https://doi.org/10.1029/2011wr010678

Kwawuvi, D., Mama, D., Agodzo, S. K., Hartmann, A., Larbi, I., Bessah, E., Limantol, A. M., Dotse S.-Q., & Yangouliba, G. I. (2022). Spatio temporal variability and change in rainfall in the Oti River Basin, West Africa. *Journal of Water and Climate Change*, 13 (3),1151–1169. https://doi.org/10.2166/wcc.2022.368

Laattoe, T., Werner, A.D., & Simmons, C.T. (2013). Seawater Intrusion Under Current Sea-Level Rise: Processes Accompanying Coastline Transgression. In C. Wetzelhuetter (Ed.), *Groundwater in the Coastal Zones of Asia-Pacific* (pp. 295-313*)*. Dordrecht, The Netherlands: Coastal Research Library (7), Springer. https://doi.org/10.1007/978-94-007-5648-9_14

Lamouroux, M. (1969). N*otice explicative de la carte pédologique du Togo*. Paris, France : ORSTOM.

Langevin, C.D., Thorne, D.T., Jr., Dausman, A.M., Sukop, M.C., & Guo, W. (2007). *SEAWAT Version 4: A Computer Program for Simulation of Multi-Species Solute and Heat Transport: U.S. Geological Survey Techniques and Methods (Book 6*, Chapter A22). Reston, Virginia, USA: U.S. Geological Survey

Langley, S. K., Cheshire, H. M., & Humes, K. S. (2001). A comparison of single date and multitemporal satellite image classifications in a semi-arid grassland. *Journal of Arid Environments*, 49, 401-411. doi:10.1006/jare.2000.0771

Larbi, I., Forkuor, G., Hountondji, F. C. C., Agyare, W. A., & Mama, D. (2019). Predictive Land Use Change under Business-As-Usual and Afforestation Scenarios in the Vea Catchment, West Africa. *International Journal of Advanced Remote Sensing and GIS*, *8*(1), 3011–3029. https://doi.org/10.23953/cloud.ijarsg.416

Larbi, I., Hountondji, F. C. C., Dotse, S., Mama, D., Nyamekye, C., Adeyeri, O. E., Djan'na Koubodana, H., Odoom, P.R.E., & Asare, Y.M. (2021). Local climate change projections and impact on the surface hydrology in the Vea catchment, West Africa. *Hydrology Research, 52*(6), 1200–1215. https://doi.org/10.2166/nh.2021.096

Larbi, I., Hountondji, F.C.C., Annor, T., Agyare, W.A., Gathenya, J.M., & Amuzu, J. (2018). Spatio-temporal trend analysis of rainfall and temperature extremes in the Vea catchment, Ghana. *Climate*, 6 (4),87. https://doi.org/10.3390/cli6040087

Larbi, I., Nyamekye, C., Dotse, S-Q., Danso, D. K., Annor, T., Bessah, E., Limantol, A. M., Attah-Darkwa, T., Kwawuvi, D., & Yomo, M. (2022). Rainfall and temperature projections and the implications on streamflow and evapotranspiration in the near future at the Tano River Basin of Ghana. *Scientific African journal* 15 e01071. https://doi.org/10.1016/j.sciaf.2021.e0107

Lawin, A. E., Lamboni, B., Manirakiza C., & Kamou, H. (2019). Future Extremes Temperature: Trends and Changes Assessment over the Mono River Basin, Togo (West Africa). *Journal of Water Resource and Protection*, *11*(01), 82–98. https://doi.org/10.4236/jwarp.2019.111006

Le Barbé, L., & Lebel, T. (1997). Rainfall climatology of the HAPEX-Sahel region during the years 1950 – 1990. *J. Hydrol.*, 188-189, 43-73

Le Barbé, L., Ale, G., Millet, G., Texier, H., Borel, Y., & Gualde, R. (1993). *Les ressources en eaux superficielles de la République du Bénin*. Paris, France : ORSTOM

Le Roux, R., Henrico, S., Bezuidenhout, J., & Henrico, I. (2023). Inverse Distance Weighting as an alternative interpolation method to create radiometric maps of natural radionuclide concentrations using QGIS. *Proceedings of the ICA*, *5*, 1–7. https://doi.org/10.5194/ica-proc-5-10-2023

Lee, A.F.S., & Heghinian, S.M. (1977). A shift of the mean level in a sequence of independent normal random variables: a Bayesian approach. *Technometrics* 19 (4): 503-506

Lee, C. H., & Cheng, R. T. (1974). "On seawater encroachment in coastal aquifers. *Water Resour. Res.*, 10(5), 1039–1043

Lerner, D. N. (1990). Groundwater recharge in urban areas. *Atmospheric Environment. Part B. Urban Atmosphere*, 24(1), 29–33. https://doi.org/10.1016/0957-1272(90)90006-g

Li, C., Wang, J., Wang, L., Hu, L., & Gong, P. (2014). Comparison of classification algorithms and training sample sizes in urban land classification with Landsat thematic mapper imagery. *Rem. Sens.* 6, 964–983. https://doi.org/10.3390/rs6020964

Liechti, T. C., Matos, J. P., Boillat, J., & Schleiss, A. (2012). Comparison and evaluation of satellite derived precipitation products for hydrological modeling of the Zambezi River Basin. *Hydrology and Earth System Sciences*, *16*(2), 489–500. https://doi.org/10.5194/hess-16-489-2012

Liu, Y., Jiao, J. J., Liang, W., & Kuang, X. (2017). Hydrogeochemical characteristics in coastal groundwater mixing zone. *Applied Geochemistry*, 85, 49-60

Loke, M. H. (1999). *Electrical Imaging Surveys for Environmental and Engineering Studies. A Practical Guide to 2-D and 3-D Surveys. Notes.* Retrieved March 10, 2021 from https://pages.mtu.edu/~ctyoung/LOKENOTE.PDF

Loke, M. H. (2006). *RES2DINV ver.3.55, Rapid 2-D resistivity and IP inversion using the least-squares method. Software manual 139*. Penang, Malaysia: Geotomo Software

Loke, M., & Barker, R. D. (1996). Rapid least-squares inversion of apparent resistivity pseudosections by a quasi-Newton method. *Geophysical Prospecting*, *44*(1), 131–152. https://doi.org/10.1111/j.1365-2478.1996.tb00142.x

Loke, M.H. (2000). Electrical Imaging Surveys for Environmental and Engineering Studies. A Practical Guide to 2-D and 3-D Surveys. Notes. 67p. https://personales.upv.es/jpadin/lokenote.pdf

M'Po, Y. N., Lawin, A. E., Oyerinde, G. T., Yao, B. K., & Afouda, A. A. (2016). Comparison of daily precipitation bias correction methods based on four regional climate model outputs in Ouémé Basin, Benin. *Hydrology*, *4*(6), 58. https://doi.org/10.11648/j.hyd.20160406.11

Mahmoud, S. H., & Alazba, A. A. (2016). Land cover change dynamics mapping and predictions using EO data and a GIS-cellular automata model: the case of Al-Baha region, Kingdom of Saudi Arabia. *Arabian Journal of Geosciences*, *9*(5). https://doi.org/10.1007/s12517-016-2439-1

Mama, A., Sinsin, B., De Canniere, C., & Bogaert, J. (2013). Anthropisation et dynamisation des paysages en zone soudanienne au nord du Bénin. *Tropicultura* 31 (1): 78-88

Maraun, D., Wetterhall, F., Ireson, A. M., Chandler, R. E., Kendon, E. J., Widmann, M., ., Brienen, S., Rust, H. W., Sauter, T., Themeßl, M., Venema, V. K. C., Chun, K. P., Goodess, C. M., Jones, R. G., Onof, C., Vrac, M., & Thiele-Eich, I. (2010). Precipitation downscaling under climate change: Recent developments to bridge the gap between dynamical models and the end user. *Reviews of Geophysics*, *48*(3). https://doi.org/10.1029/2009rg000314

Maréchal, R., De Breuck, W., & De Moor, G. (1957). Geo-elektrische prospectie in het Kustgebied en in de Vlaamse Vallei. *Half-jaarlijks Tijdschrift Becewa*, 14, 1-7

Maréchal, R., De Breuck, W., De Moor, G., & Henriet, J.P. (1970). Geo-elektrische prospektie bij het hydrologisch onderzoek. *Informatieblad Navewa*, 192, 2-13

Megahed, Y., Cabral, P., Silva, J., & Caetano, M. (2015). Land cover mapping analysis and urban growth modelling using remote sensing techniques in Greater Cairo Region—Egypt. *ISPRS International Journal of Geo-information*, *4*(3), 1750–1769. https://doi.org/10.3390/ijgi4031750

Mendez, M., Maathuis, B., Hein-Griggs, D., & Alvarado-Gamboa, L. (2020). Performance Evaluation of Bias Correction Methods for Climate Change Monthly Precipitation Projections over Costa Rica. *Water*, *12*(2), 482. https://doi.org/10.3390/w12020482

Mezghani, A., Dobler, A., Haugen, J.E., Benestad, R.E., Parding, K.M., Piniewski, M., Kardel, I., & Kundzewicz, Z.W. (2017). CHASE PL climate projection dataset over Poland—bias adjustment of EURO-CORDEX simulations. *Earth Syst Sci Data* 9 :905–925. https ://doi.org/10.5194/essd-9-905-2017

Millet, B. (1986). *Hydrologie et hydrochimie d'un milieu lagunaire tropical : le lac Togo* [Doctoral thesis, Université de Paris Sud, France]. Open Access Library (OALib). https://horizon.documentation.ird.fr/exl-doc/pleins_textes/divers17-01/010015178.pdf

Ministère de l'Agriculture, de l'Élevage et de l'Hydraulique (MAEH/PNIASAN). (2018). *Programme National d'Investissement Agricole, de Sécurité Alimentaire et Nutritionnelle. Plan d'Investissement 2017-2026. Version post_validation*. Retrieved July 5, 2020, from https://agriculture.gouv.tg/wp-content/uploads/2020/06/PNIASAN-_apres-atelier-de-validation-_-11_01_2018.pdf

Ministère de l'Environnement et des Ressources (MERF). (2018a). *Stratégie nationale de réduction des émissions dues à la déforestation et à la dégradation des forêts (REDD+) 2020-2029. Version 1 finale.* Retrieved July 5, 2020, from https://faolex.fao.org/docs/pdf/Tog183988.pdf

Ministère de l'Environnement et des Ressources Forestières/Inventaire forestier national (MERF/IFN). (2016). *Rapport Inventaire Forestier National du Togo 2015-2016.* Retrieved July 5, 2020, from https://docplayer.fr/225363887-Rapport-inventaire-forestier-national-du-togo.html

Ministère de l'Urbanisme et de l'Habitat (MUH). (2013). *Politique Nationale de l'Habitat et du Développement Urbain (PNHDU).* Retrieved July 5, 2020, from https://docplayer.fr/180194993-Table-des-matieres-page-i-ministere-de-l-urbanisme-et-de-l-habitat-_-politique-nationale-de-l-habitat-et-du-developpement-urbain-pnhdu.html

Ministère de l'Environnement et des Ressources Forestière (MERF/CNI). (2001). *Communication National Initiale*. Togo : Presse de l'Université de Lomé. Retrieved July 5, 2020, from https://unfccc.int/resource/docs/natc/tognc1.pdf

Ministère de l'Environnement et des Ressources Forestière (MERF/PANA). (2009). *Plan D'action National D'adaptation aux Changements Climatiques-PANA*. Retrieved July 5, 2020, from https://faolex.fao.org/docs/pdf/Tog184779.pdf

Ministère de l'Environnement et des Ressources Forestière (MERF/TNC). (2015). *Troisième Communication Nationale Sur Les Changements Climatiques*. Retrieved July 5, 2020, from https://unfccc.int/sites/default/files/resource/tgonc3.pdf

Ministère de l'Environnement et des Ressources Forestières (MERF-REDD+/ ONF International / LGE International). (2018b). *Étude sur l'utilisation des terres et les options stratégiques futures pour l'aménagement du territoire au Togo*. *Rapport Final*. Retrieved April 13, 2020, from https://www.reddtogo.tg/index.php/ressources/rapports-ressources/rapports-des-etudes-analytiques/send/11-rapports-des-etudes-analytiques/98-rapport-final-etude-sur-utilisation-des-terres-et-les-options-strategiques

Ministère de l'Environnement et des Ressources Forestières/ West Africa Coastal Areas Management Program (MERF/WACA-TOGO). (2017). Projet d'investissement de la resilience des zones cotieres en Afrique de l'Ouest. Rapport final. Retrieved May 15, 2020, from http://www.environnement.gouv.tg/sites/default/files/documents/rapport_-du-cadre_de_gestion_environnementale_et_sociale_cges_-_du_projet_waca_togo_version_finale.pdf

Minville, M., Brissette, F., Krau, S., & Leconte, R. (2009). Adaptation to climate change in the management of a Canadian Water-Resources system exploited for hydropower. *Water*

Resources Management, *23*(14), 2965–2986. https://doi.org/10.1007/s11269-009-9418-1

Mishra, V. N., Kumar, P., & Mohan, K. (2014). Prediction of land use changes based on land change modeler (LCM) using remote sensing: A case study of Muzaffarpur (Bihar), India. *Zbornik Radova: Geografski Institut Jovan Cvijić*, *64*(1), 111–127. https://doi.org/10.2298/ijgi1401111m

Mithun, S.K., Sahana, M., Chattopadhyay, S., Chatterjee, S., Islam, J., & Costache, R. (2022) Comparative framework for spatially explicit urban growth modeling for monitoring urban land-use efficiency and sustainable urban development (SDG 11.3.1): a study on Kolkata metropolitan area, India. *Geocarto International*, 37(27), 17933-17970, DOI: 10.1080/10106049.2022.2136259

Monciardini, C., Andreieff P., Blondeau A., Carbonnel C., Castaing C., Châteauneuf J. J., Farjanel G., Lenindre Y., Marteau P., Podevin G., Salin, C., Slansky M., & Tchota K. (1986). Synthèse géologique du bassin côtier Crétacé Supérieur et Tertiaire du Togo et Recherche de tourbe, lignite, charbon et autres substances industrielles. Rapport 85TGO O56 GEO, BRGM, Orléans

Monteiro, L. A., Sentelhas, P. C., & Pedra, G. U. (2017). Assessment of NASA/POWER satellite-based weather system for Brazilian conditions and its impact on sugarcane yield simulation. *International Journal of Climatology*, *38*(3), 1571–1581. https://doi.org/10.1002/joc.5282

Motz, L.H. (2004). Representing the Saltwater-Freshwater Interface in Regional Groundwater Flow Models. In: Araguas, L., Custodio E., & Manzano, M. (Eds.), *Proceedings* of the *Saltwater Intrusion Meeting, Hydrogeology and Groundwater Series 15*, 33–39. http://www.swim-site.nl/pdf/swim18/swim18_003.pdf

Moussa, A. B., Zouari, K., Vallès, V., & Jlassi, F. (2012). Hydrogeochemical analysis of groundwater pollution in an irrigated land in Cap Bon peninsula, North-Eastern Tunisia. *Arid Land Research and Management*, *26*(1), 1–14. https://doi.org/10.1080/15324982.2011.631688

Müller, K., Steinmeier, C., & Küchler, M. (2010). Urban growth along motorways in Switzerland. *Landscape and Urban Planning*, *98*(1), 3–12. https://doi.org/10.1016/j.landurbplan.2010.07.004

Munthali, M.G., Mustak, S., Adeola, A., Botai, J., Singh, S.K., & Davis, N.(2020). Modelling land use and land cover dynamics of Dedza district of Malawi using hybrid Cellular Automata and Markov model. *Remote Sensing Applications: Society and Environment*, 17, 100276. https://doi.org/10.1016/j.rsase.2019.100276

Mutasa, C. (2011). *Impacts of climate change on groundwater resources: a case study of the Sardon catchment, Spain*. Retrieved September 12, 2020, from https://essay.utwente.nl/85006/

Muthu, A. C. L., & Santhi, M. H. (2015). Estimation of Surface Runoff Potential using SCS-CN Method Integrated with GIS. *Indian Journal of Science and Technology*, *8*(28). https://doi.org/10.17485/ijst/2015/v8i28/83324

N'dim, B. B. (2002). Inventaire des forages exploités par la Régie Nationale des Eaux du Togo

Nahian, M. A., Ahmed, A., Laz´ar, A. N., Hutton, C. W., Salehin, M., & Streatfield, P. K. (2018). Drinking water salinity associated health crisis in coastal Bangladesh. *Elementa: Science of the anthropocene*, 6:1–14

Nahib, I., Turmudi, T., Windiastuti, R., Suryanta, J., Dewi, R.S., & Lestari, S.(2018). Comparing of Land Change Modeler and Geomod Modeling for the Assessment of Deforestation (Case Study: Forest Area at Poso Regency, Central Sulawesi Province). *Int. J. Adv. Eng. Manag. Sci.*, 4, 597–607. DOI:10.22161/ijaems.4.8.4

Najib, S., Fadili, A., Mehdi, K., Riss, J., & Makan, A. (2017). Contribution of hydrochemical and geoelectrical approaches to investigate salinization process and seawater intrusion in the coastal aquifers of Chaouia, Morocco. *Journal of Contaminant Hydrology*, *198*, 24–36. https://doi.org/10.1016/j.jconhyd.2017.01.003

Nash, J., & Sutcliffe, J. V. (1970). River flow forecasting through conceptual models part I — A discussion of principles. *Journal of Hydrology*, *10*(3), 282–290. https://doi.org/10.1016/0022-1694(70)90255-6

Nasiri, M., Kardan, H. M., & Hamidi, M. (2021). Development of Multi-Criteria Decision Making Methods for Reduction of Seawater Intrusion in Coastal Aquifers Using SEAWAT Code. *Journal of Contaminant Hydrology*, 242, 103848. https://doi.org/10.1016/j.jconhyd.2021.103848

Ndehedehe, C. E., Usman, M., Okwuashi, O., & Ferreira, V. G. (2021). Modelling impacts of climate change on coastal West African rainfall. *Modeling Earth Systems and Environment*, *8*(3), 3325–3340. https://doi.org/10.1007/s40808-021-01302-5

Niang, I., Dansokho, M., Faye, S., Gueye, K., & Ndiaye, P. (2010). Impacts of climate change on the Senegalese coastal zones: Examples of the Cap Vert peninsula and Saloum estuary. *Global and Planetary Change*, *72*(4), 294–301. https://doi.org/10.1016/j.gloplacha.2010.01.005

Niang, I., Ruppel, O.C., Abdrabo, M.A., Essel, A., Lennard, C., Padgham, J. , & Urquhart, P. (2014). Africa. In: Barros, V.R., Field, C.B., Dokken, D.J., Mastrandrea, M.D., Mach, K.J., Bilir, T.E., Chatterjee, M., Ebi, K.L., Estrada, Y.O., Genova, R.C., Girma, B., Kissel, E.S., Levy, A.N., MacCracken, S., Mastrandrea, P.R., & White, L.L. (Eds.), *Climate Change 2014: Impacts, Adaptation, and Vulnerability. Part B: Regional Aspects* (pp. 1199-1265). *Contribution of Working Group II to the Fifth Assessment Report of the Intergovernmental Panel on Climate Change*. Cambridge, United Kingdom: Cambridge University Press. https://doi.org/10.2134/agronj2010.0303

Nicholson, S. E. (2013). The West African Sahel: A review of recent studies on the rainfall regime and its interannual variability. *ISRN Meteorology (Print)*, 1–32. https://doi.org/10.1155/2013/453521

Nowroozi, A. A., Horrocks, S. B., & Henderson, P. (1999). Saltwater intrusion into the freshwater aquifer in the eastern shore of Virginia: a reconnaissance electrical resistivity survey. *Journal of Applied Geophysics*, 42, 1–22

Ogbu, K. N., Hounguè, N. R., Gbode, I. E., & Tischbein, B. (2020). Performance Evaluation of Satellite-Based Rainfall Products over Nigeria. *Climate*, *8*(10), 103. https://doi.org/10.3390/cli8100103

Ohwoghere-Asuma, O., & Essi, O. E. (2017). Investigation of Seawater Intrusion into Coastal Groundwater Aquifers of Escravos, Western Niger Delta, Nigeria. *Journal of Applied Sciences and Environmental Management*, *21*(2), 362. https://doi.org/10.4314/jasem.v21i2.18

Okafor, G. C., Annor, T., Odai, S. N., & Agyekum, J. (2019). Volta basin precipitation and temperature climatology: evaluation of CORDEX-Africa regional climate model simulations. *Theoretical and Applied Climatology*, *137*(3–4), 2803–2827. https://doi.org/10.1007/s00704-018-2746-4

Olmedo, M.T.C., Pontius, R.G., Paegelow, M., & Mas, J-F. (2015). Comparison of simulation models in terms of quantity and allocation of land change. *Environmental Modelling and Software,* 69, 214-221. ff10.1016/j.envsoft.2015.03.003ff. ffhal-01453031f

Oloruntola, M. O., Folorunso, A. F., Bayewu, O. O., Mosuro, G. O., & Adewale, S. (2019). Baseline evaluation of freshwater–saltwater interface in coastal aquifers of Badagry, south-western Nigeria. *Applied Water Science*, *9*(4). https://doi.org/10.1007/s13201-019-0957-1

Oude Essink, G.H. (2001). Salt Water Intrusion in a Three-dimensional Groundwater System in The Netherlands: A Numerical Study. *Transport in Porous Media*, 43, 137–158 https://doi.org/10.1023/A:1010625913251

Owojori, A., & Xie, H. (2005). Landsat image-based LULC changes of San Antonio, Texas using Advanced atmospheric correction and Object-oriented image analysis Approaches. *Proceedings of the 5th International Symposium on Remote Sensing of Urban Areas*, Tempe, AZ, USA. https://www.isprs.org/proceedings/xxxvi/8-w27/owojori.pdf

Oyedele, K. F., & Ekpoette, K. (2011). Resistivity attributes of foundation beds in a sedimentary terrain: Implications on geo-engineering soil conditions. *American Journal of Scientific and Industrial Research*, *2*(5), 734–739. https://doi.org/10.5251/ajsir.2011.2.5.734.739

Padgham, J., Jabbour, J., & Dietrich, K. (2015). Managing change and building resilience: A multi-stressor analysis of urban and peri-urban agriculture in Africa and Asia. *Urban Climate, 12*, 183–204. https://doi.org/10.1016/j.uclim.2015.04.003

Park, H., Jang, K., Ju, J. W., & Yeo, I. W. (2012). Hydrogeological characterization of seawater intrusion in tidally-forced coastal fractured bedrock aquifer. *Journal of Hydrology*, *446–447*, 77–89. https://doi.org/10.1016/j.jhydrol.2012.04.033

Patchali, T. E., Ajide, O. O., Matthew, O. J., Salau, T. A. O., & Oyewola, O. M. (2020). Examination of potential impacts of future climate change on solar radiation in Togo, West Africa. *SN Applied Sciences*, *2*(12). https://doi.org/10.1007/s42452-020-03738-3

Payne, B. R., & Halevy, E. (1983). Guidebook on nuclear techniques in hydrology (Technical Reports series 91). Vienna, Austria: IAEA. Retrieved from https://inis.iaea.org/collection/NCLCollectionStore/_Public/14/805/14805939.pdf

Pazdirek, O., & Bláha, V. (1996). Examples of resistivity imaging using ME-100 resistivity field acquisition system. Paper presented at the EAGE 58th Conference and Technical

Exhibition Extended Abstracts, Amsterdam, The Netherlands. Retrieved from https://doi.org/10.3997/2214-4609.201408817

Pettitt, A. N. (1979). A Non-Parametric approach to the Change-Point problem. *Journal of the Royal Statistical Society Series C: Applied Statistics, 28*(2), 126-135.https://doi.org/10.2307/2346729

Pidwirny, M. (2006). *Actual and Potential Evapotranspiration Fundamentals of Physical Geography, (2nd Edition)*. Retrieved February 8, 2021, from http://www.physicalgeography.net/fundamentals/8j.html

Pinder, G. F., & Cooper, H. H. (1970). "A numerical technique for calculating the transient position of the saltwater front". *Water Resources Research*, 6(3), 875- 882

Polo-Akpisso, A., Wala, K., Ouattara, S., Foléga, F., Akpagana, K., & Tano, Y. (2020). Assessment of Habitat Change Processes within the Oti-Keran-Mandouri Network of Protected Areas in Togo (West Africa) from 1987 to 2013 Using Decision Tree Analysis. *Sci*, *2*(1), 1. https://doi.org/10.3390/sci2010001

Pontius Jr, R. G. (2000). Quantification error versus location error in comparison of categorical maps. *Photogrammetric Engineering and Remote Sensing*, 66(8). https://trid.trb.org/view/658972

Pontius Jr., R. G., & Chen, H. (2006). *GEOMOD Modeling. Chapter of help system in J Ronald Eastman. Idrisi 15: The Andes Edition.* Worcester MA: Clark Labs. https://www2.clarku.edu/faculty/rpontius/pontius_chen_2006_idrisi.pdf

Prince Edward Island Department of Environment, Labour and Justice (PEIDELJ). (2011). Saltwater Intrusion and Climate Change. A primer for local and provincial decision-makers. In: Linzey, D. (Ed.), *Saltwater Intrusion and Climate Change* (pp.1-26). Charlottetown, Canada: Atlantic Climate Adaptation Solutions Association. Retrieved from www.atlanticadaptation.ca

Programme des Nations Unie pour le Développement (PNUD). (1975). *Prospection des eaux souterraines dans la zone côtière (TOGO) : Conclusions et recommandations* (DP/UN/TOG-70-511/1). New York, USA: Nations Unies

Projet de Réduction des Risques Environnementaux et Sanitaires liés à l'Activité des Vendeurs d'Eau de Forage dans le Grand-Lomé (PRRESAF). (2015). Rapport de synthese hydrogeologique du grand Lome et ses environs.32p.

Qu, L., Xiao, H., Zheng, N., Zhang, Z., & Xu, Y. (2017). Comparison of four methods for spatial interpolation of estimated atmospheric nitrogen deposition in South China. *Environ. Sci. Pollut. Res.*, 24, 2578-2588. https://doi.org/10.1007/s11356-016-7995-0

Rallison, R. E. (1980). Origin and evolution of the SCS runoff equation. *Proceedings of the Symposium on Watershed Management (*pp. 912-924). New York, USA: ASCE

Rao, G. T., Rao, V. V. S. G., Padalu, G., Dhakate, R., & Sarma, V. S. (2013). Application of electrical resistivity tomography methods for delineation of groundwater contamination and potential zones. *Arabian Journal of Geosciences*, *7*(4), 1373–1384. https://doi.org/10.1007/s12517-013-0835-3

Rathjens, H., Bieger, K., Srinivasan, R., & Arnold, J.G. (2016). *CMhyd User Manual Documentation for preparing simulated climate change data for hydrologic impact studies*. Texas, USA: SWAT

Regmi, R.R., Saha, S.K., & Subedi, D.S. (2017). Geospatial Analysis of Land Use Land Cover Change Modeling in Phewa Lake Watershed of Nepal by Using GEOMOD Model. *Himal. Phys.*, 6, 65–72

Revelle, R. (1941). Criteria for recognition of the sea water in ground-waters. *Transactions*, *22*(3), 593–597. https://doi.org/10.1029/tr022i003p00593

Reynolds, J. M. (2011). *An introduction to applied and environmental geophysics* (2nd Ed). New York, USA: Wiley-Blackwell

Robertson, G. P., & Swinton, S. M. (2005). Reconciling agricultural productivity and environmental integrity: a grand challenge for agriculture. *Frontiers in Ecology and the Environment*, *3*(1), 38–46. https://doi.org/10.1890/1540-9295(2005)003

Robinson, C. E., Li, L., & Barry, D. A. (2007). Effect of tidal forcing on a subterranean estuary. *Advances in Water Resources*, *30*(4), 851–865. https://doi.org/10.1016/j.advwatres.2006.07.006

Rose, C. W., & Sharma, M.L. (1984). Summary and recommendations of the Workshop on "Evapotranspiration from plant communities." *Agricultural Water Management*, *8*(1–3), 325–342. https://doi.org/10.1016/0378-3774(84)90061-1

Rosenfield, G. H., & Fitzpatrick-Lins, K. (1986). A coefficient of agreement as a measure of thematic classification accuracy. *Photogrammetric Engineering and Remote Sensing*, *52*(2), 223–227. Retrieved from https://pubs.er.usgs.gov/publication/70014667

Roy, H. G., Fox, D., & Emsellem, K. (2014). Predicting Land Cover Change in a Mediterranean Catchment at Different Time Scales. *Transactions on Computational Science*, 8582, 315 - 330. ffhal-02572363f

Ruelland, D., Ardoin-Bardin, S., Billen, G., & Servat, É. (2008). Sensitivity of a lumped and semi-distributed hydrological model to several methods of rainfall interpolation on a large basin in West Africa. *Journal of Hydrology*, *361*(1–2), 96–117. https://doi.org/10.1016/j.jhydrol.2008.07.049

Safi, A., Rachid, G., El-Fadel, M., Doummar, J., Najm, M. A., & Alameddine, I. (2018). Synergy of climate change and local pressures on saltwater intrusion in coastal urban areas: effective adaptation for policy planning. *Water International*, *43*(2), 145–164. https://doi.org/10.1080/02508060.2018.1434957

Salazar, L. F., & Poveda, G. (2006). Validation of Diverse Evapotranspiration Estimation Methods using the Long-term Water Balance in the Amazon River Basin. *Proceedings of 8 ICSHMO in Foz do Iguaçu, Brazil*, 815-820. http://mtc-m16b.sid.inpe.br/col/cptec.inpe.br/adm_conf/2005/10.31.16.29/doc/815-820.pdf

Sanford, W. E., & Pope, J. P. (2010). Current challenges using models to forecast seawater intrusion: Lessons from the Eastern Shore of Virginia. *Hydrogeology Journal*, 18, 73–93

Sanogo, K., Dayamba, D. S., Villamor, G. B., & Bayala, J. (2020). Impacts of climate change on ecosystem services of agroforestry Systems in the West African Sahel: a review. In *Springer eBooks* (pp. 213–224). https://doi.org/10.1007/978-981-15-4136-0_7

Santhi, C, Arnold, J. G., Williams, J. R., Dugas, W. A., Srinivasan, R., & Hauck, L. M. (2001). Validation of the SWAT model on a large river basin with point and nonpoint sources. *Journal of the American Water Resources Association*, 37(5),1169-1188

Scanlon, B. R., Healy, R. W., & Cook, P. G. (2002). Choosing appropriate techniques for quantifying groundwater recharge. *Hydrogeology Journal*, *10*(1), 18–39. https://doi.org/10.1007/s10040-001-0176-2

Selmi, A. (2013). *Groundwater management and modeling of a coastal aquifer case study (Gaza strip)* [Doctoral thesis, University of Milan Bicocca, Italy]. Bicocca Open Archive. https://boa.unimib.it/handle/10281/40833

Sen, P. K. (1968). Estimates of the regression coefficient based on Kendall's TAU. *Journal of the American Statistical Association*, *63*(324), 1379–1389. https://doi.org/10.1080/01621459.1968.10480934

Servat, E., Paturel, J.-E., Kouame, B., Travaglio, M., Ouedraogo, M., Boyer, J.-F., Lubes, N. H., Fritsch, J.-M., Masson, J.M., & Marieu, B. (1998). Identification, caractérisation et conséquences d'une variabilité hydrologique en Afrique de l'Ouest et centrale. In: Servat, E., Hughes, D., Fritsch, J.-M., & Hulme, M. (Eds), *Water resources variability in Africa during the 20th century* (pp. 323-337). Wallingford, UK: AISH

Seto, K. C., Güneralp, B., & Hutyra, L. R. (2012). Global forecasts of urban expansion to 2030 and direct impacts on biodiversity and carbon pools. *Proceedings of the National Academy of Sciences of the United States of America*, *109*(40), 16083–16088. https://doi.org/10.1073/pnas.1211658109

Sherif, M., Mohamed, M. M., Kacimov, A. R., & Shetty, A. (2011). Assessment of groundwater quality in the northeastern coastal area of UAE as precursor for desalination. *Desalination*, *273*(2–3), 436–446. https://doi.org/10.1016/j.desal.2011.01.069

Simler, R. (2005). Logiciel d'hydrochimie (DIAGRAMMES). Retrieved from www.lha.univavignon.fr/logiciel.htm

Slansky, M. (1962). Contribution à l'étude géologique du Bassin sédimentaire cotier du Dahomey et du Togo (Mémoire 1). Orléans, France: Bureau de Recherches Géologiques et Minières (no 11). https://openlibrary.org/works/OL963592W/Contribution_a %CC %80_l %27e %CC %81tude_ge %CC %81ologique_du_bassin_se %CC %81dimentaire_co %CC %82tier_du_Dahomey_et_du_Togo

Sognon, L., Yalo, N., Lawson, F., & Alle, C. (2018). Geophysical characterization of salted bevel of the Continental Terminal aquifer at the southwestern edge of Lake Nokoué in Benin. *LARHYSS Journal*, (34), 69–95. Retrieved from http://larhyss.net/ojs/index.php/larhyss/article/download/588/602

Sophiya, M. S., & Syed, T. H. (2013). Assessment of vulnerability to seawater intrusion and potential remediation measures for coastal aquifers: a case study from eastern India. *Environmental Earth Sciences*, *70*(3), 1197–1209. https://doi.org/10.1007/s12665-012-2206-x

Sterckx, A. (2021). Groundwater in fast growing cities in Western Africa. Retrieved February 5, 2023, from https://www.un-igrac.org/sites/default/files/resources/files/Groundwater%20in %20fast %20growing %20cities %20in %20Western %20Africa %20-%20IGRAC %202021_0.pdf

Steyl, G., & Dennis, I. (2010). Review of coastal-area aquifers in Africa. *Hydrogeology Journal*, *18*(1), 217–225. https://doi.org/10.1007/s10040-009-0545-9

Struckmeier, W., & Richts, A. (2006). WHYMAP and the World Map of Transboundary Aquifer Systems at the scale of 1: 50 000 000 (Special Edition for the 4th World Water Forum, Mexico City, March 2006). *Episodes*, *29*(4), 274–278. https://doi.org/10.18814/epiiugs/2006/v29i4/005

Sultan, B., Defrance, D., & Iizumi, T. (2019). Evidence of crop production losses in West Africa due to historical global warming in two crop models. *Scientific Reports*, 9(1). https://doi.org/10.1038/s41598-019-49167-0

Supriyadi, K., & Putro, A. S. P. (2017). Geophysical and Hydrochemical Approach for Seawater Intrusion in North Semarang, Central Java, Indonesia. *International Journal of Geomate* 12(31):134-140. Doi: 10.21660/2017.31.50405

Sylla, M. B., Diallo, I., & Pal, J. S. (2013). West African Monsoon in State-of-the-Science Regional Climate Models. In A. Tarhule (Ed.), *Climate Variability - Regional and Thematic Patterns* (pp. 4-36). https://doi.org/10.5772/55140

Sylla, M. B., Nikiema, P. M., Gibba, P., Kebe, I., & Klutse, N. a. B. (2016). Climate Change over West Africa: Recent Trends and Future Projections. In *Springer eBooks* (pp. 25–40). https://doi.org/10.1007/978-3-319-31499-0_3

Sylvain, J.P., Aregba, A., Assih-Edeou, P., Castaing, C., Chevremont, J., Collart, J., Monciardini, C., Marteau, P., Ouasane, I., & Tchota. (1986). *Notice explicative de la carte géologique à 1/200000. Feuille de Lomé* (Mémoire n° 5 DGMG/BNRM 1e édition. 64p + 2 annexes). Lomé, Togo : DGMG/BNRM

Tappan, G.G., Cushing, W.M., Cotillon, S.E., Mathis, M.L., Hutchinson, J.A., Herrmann, S.M., & Dalsted, K.J. (2016). West Africa Land Use Land Cover Time Series. U.S. Geological Survey. Retrieved March 21, 2021, from https://doi.org/10.5066/F73N21JF

Tastet, J.P. (1979). *Environnements sédimentaires et structuraux quaternaires du littoral du golfe de Guinée, Cote d'Ivoire, Togo, Bénin* [Doctoral thesis, Université de Bordeaux 1, France]. Bibliothèques de l'OCA. https://biblio-n.oca.eu/biblio/pmb3.0/opac_css/index.php?lvl=serie_see&id=1703

Tetra Tech, A. R. D. (2014). An Introduction to the ARCC Climate Change and Water Resources in West Africa Series. Retrieved March 4, 2023, from https://www.climatelinks.org/sites/default/files/asset/document/TBW_%2000_%20WA%20Water %20Studies %20Overview_CLEARED.pdf

Teutschbein, C., & Seibert, J. (2010). Regional Climate Models for Hydrological Impact Studies at the Catchment Scale: A review of recent modeling Strategies. *Geography Compass*, *4*(7), 834–860. https://doi.org/10.1111/j.1749-8198.2010.00357.x

Teutschbein, C., & Seibert, J. (2012). Bias correction of regional climate model simulations for hydrological climate-change impact studies: Review and evaluation of different

methods. *Journal of Hydrology, 456–457,* 12–29. https://doi.org/10.1016/j.jhydrol.2012.05.052

Themeßl, M., Gobiet, A., & Heinrich, G. (2011). Empirical-statistical downscaling and error correction of regional climate models and its impact on the climate change signal. *Climatic Change*, *112*(2), 449–468. https://doi.org/10.1007/s10584-011-0224-4

Thiam, S., Salas, E. A. L., Hounguè, N. R., Almoradie, A., Verleysdonk, S., Adounkpè, J., & Komi, K. (2022). Modelling land use and land cover in the transboundary mono river catchment of Togo and Benin using Markov chain and stakeholder's perspectives. *Sustainability*, *14*(7), 4160. https://doi.org/10.3390/su14074160

Touré, A., Diekkrüger, B., & Mariko, A. (2016). Impact of climate change on groundwater resources in the Klela Basin, southern Mali. *Hydrology*, *3*(2), 17. https://doi.org/10.3390/hydrology3020017

Trisos, C.H., Adelekan, I.O., Totin, E., Ayanlade, A., Efitre, J., Gemeda, A., Kalaba, K., Lennard, C., Masao, C., Mgaya, Y., Ngaruiya, G., Olago, D., Simpson, N.P., & Zakieldeen, S. (2022). Africa. In: Pörtner, H.O., Roberts, D.C., Tignor, M., Poloczanska, E.S., Mintenbeck, K., Alegría, A., Craig, M., Langsdorf, S., Löschke, S., Möller, V., Okem, A., & Rama B. (Eds.), *Climate Change 2022: Impacts, Adaptation and Vulnerability (pp. 1285–1455). Contribution of Working Group II to the Sixth Assessment Report of the Intergovernmental Panel on Climate Change*. Cambridge, UK and New York, USA: Cambridge University Press. Doi:10.1017/9781009325844.011

Turc, L. (1954). Le bilan d'eau des sols : relations entre les précipitations, l'évaporation et l'écoulement. *Actes de la Troisième journée de l'hydraulique in Alger*, 3_1, 36-43. https://www.persee.fr/doc/jhydr_0000-0001_1955_act_3_1_3278

Turc, L. (1961). Évaluation des besoins en eau d'irrigation ; évapotranspiration potentielle. *Ann. Agr.* 12, 13-49

United States Agency for International Development (USAID). (2018). Climate Risks in West Africa: Regional Risk profile. In USAID, The Adaptation Thought Leadership and Assessments (Task Order No. AID-OAA-I-14- 00013, pp.1-27). USA: USAID. Retrieved May 15, 2021, from https://www.climatelinks.org/sites/default/files/asset/document/West_Africa_CRP_Final.pdf

United States Department of Agriculture (USDA) (1972). *Soil Conservation Service, National Engineering Handbook. Hydrology Section 4*. Washington, DC: USDA

Van Der Heiden, F., & Lithén, J. (2011). *Groundwater Modelling of the Vårgårda Aquifer* [Master's thesis, Chalmers University of Technology, Göteborg, Sweden]. Chalmers Publication Library. https://publications.lib.chalmers.se/records/fulltext/149363.pd

Van Meir, N., Jaeggi, D., Herfort, M., Low, S., Lods, G., Pezard, Ph & Gouze, Ph. (2004). "Development of a test site for the investigation of saltwater intrusion process in a karstified limestone aquifer (Campos Mallorca, Spain)". In L. Araguas, E. Custodio & M. Manzano (Eds.), *proceedings of the 18th Salt Water Intrusion Meeting* Cartagena, Spain, 289-303. http://www.swim-site.nl/pdf/swim18/swim18_027.pdf

Van Soesbergen, A. (2016). *A review of land-use change models*. Cambridge, UK: UNEP-WCMC. https://wcmc.io/29b1

Veldkamp, A., & Lambin, É. F. (2001). Predicting land-use change. *Agriculture, Ecosystems & Environment*, *85*(1–3), 1–6. https://doi.org/10.1016/s0167-8809(01)00199-2

Vincent, L. A., Peterson, T. C., Barros, V. R., Marino, M. B., Rusticucci, M., Carrasco, G., Ramirez, E., Alves, L. M., Ambrizzi, T., Berlato, M. A., Grimm, A. M., Marengo, J. A., Molion, L., Moncunill, D. F., Rebello, E., Anunciação, Y. M. T., Quintana, J., Santos, J. L., Baez, J., Coronel, G., Garcia, J., Trebejo, I., Bidegain, M., Haylock, M. R., & Karoly, D. (2005). Observed Trends in Indices of Daily Temperature Extremes in South America 1960–2000. *Journal of Climate*, 18(23), 5011-5023. https://doi.org/10.1175/JCLI3589.1

Voss, C.I., & Provost, A.M. (2010). *SUTRA-A Model forSaturated–Unsaturated Variable-Density Ground-WaterFlow with Solute or Energy Transport* (Report no. 02-4231). Reston, VA,USA: US Geological Survey (USGS), Water Resources Investment

Walraevens, K., Mjemah, I. C., Mtoni, Y. E., & Van Camp, M. (2015). Sources of salinity and urban pollution in the Quaternary sand aquifers of Dar es Salaam, Tanzania. *Journal of African Earth Sciences*, *102*, 149–165. https://doi.org/10.1016/j.jafrearsci.2014.11.003

Wang, Z., Su, Q., Wang, S., Gao, Z., & Liu, J. (2021). Coupling hydrochemistry and stable isotopes (Δ2H and Δ18O) to identify the major factors affecting hydrochemical evolution of groundwater in the Western Yellow Sea Coast, China. *Authorea (Authorea)*. https://doi.org/10.22541/au.163255073.39312751/v1

Ward, D.S., & Benegar, J. (1998). Data Input Guide for SWIFT-98, version 2.57, HSI Geotrans, Inc., Sterling, Va

Ward, S. (1989). Resistivity and induced polarization methods. In: Ward, S. (Eds.), *Investigations in geophysics 5, geotechnical and environmental geophysics 1(*pp. 147–189). Tulsa, USA: SEG

Werner, A. D., & Gallagher, M. (2006). Characterisation of sea-water intrusion in the Pioneer Valley, Australia using hydrochemistry and three-dimensional numerical modelling. *Hydrogeology Journal*, *14*(8), 1452–1469. https://doi.org/10.1007/s10040-006-0059-7

Werner, A. D., Bakker, M., Post, V., Vandenbohede, A., Lu, C., Ataie-Ashtiani, B., Simmons, C. T., & Barry, D. A. (2013). Seawater intrusion processes, investigation and management: Recent advances and future challenges. *Advances in Water Resources*, *51*, 3–26. https://doi.org/10.1016/j.advwatres.2012.03.004

Wickham, H., Averick, M., Bryan, J., Chang, W., McGowan, L. D., François, R., Grolemund , G., Hayes, A., Henry, L., Hester, J., Kuhn , M., Pedersen, T. L., Miller, E., Bache, S. M.,Müller, K., Ooms, J., Robinson, D.,Seide, D. P., Spinu, V., Takahashi, K.,Vaughan, D., Wilke, C., Woo, K., & Yutani, H. (2019). Welcome to the Tidyverse. *Journal of Open Source Software*, *4*(43), 1686. https://doi.org/10.21105/joss.01686

Wilmet, J. (1995). Evolution récente des méthodes d'analyse des images satellitaires par télédétection numérique. *Bulletin De La Classe Des Sciences. Académie Royale De Belgique*, *6*(7), 319–337. https://doi.org/10.3406/barb.1995.27659

World bank (2020). *Effects of climate change on coastal erosion and flooding. Technical Report in Benin, Côte d'Ivoire, Mauritania, Senegal, and Togo.* Retrieved March 17, 2021, from https://www.wacaprogram.org/sites/waca/files/knowdoc/West_%20Africa%20Climate %20Change %20Assessment_April %202020 %20FINAL.pdf

World Health Organisation (WHO) (2011). *Guidelines for drinking-water quality (4th ed).* Geneva, Switzerland: WHO Press. https://iris.who.int/bitstream/handle/10665/44584/9789241548151_eng.pdf

Xie, Y. (2014). "knitr: A Comprehensive Tool for Reproducible Research in R." In V. Stodden, F. Leisch, R.D. Peng (Eds.), Implementing Reproducible Computational Research (pp. 3–31). Florida, USA: Chapman and Hall/CRC. ISBN 978-1466561595

Yao, F. Z., Reynard, E., Fallot, J.M., Ouattara, I., Kouakou, E., & Savane, I. (2018). A new statistical approach to assess climate variability in the white Bandama watershed, Northern Côte d'Ivoire. *Atmospheric and Climate Sciences*, 8, 410–430

Yeboah, K. A., Akpoti, K., Kabo-Bah, A. T., Ofosu, E. A., Siabi, E. K., Mortey, E. M., & Okyereh, S. A. (2022). Assessing climate change projections in the Volta Basin using the CORDEX-Africa climate simulations and statistical bias-correction. *Environmental Challenges*, *6*, 100439. https://doi.org/10.1016/j.envc.2021.100439

Yira, Y., Diekkrüger, B., Steup, G., & Bossa, A. Y. (2016). Modeling land use change impacts on water resources in a tropical West African catchment (Dano, Burkina Faso). *Journal of Hydrology*, *537*, 187–199. https://doi.org/10.1016/j.jhydrol.2016.03.052

Yomo, M., Yalo, N., Gnazou, M.D., Silliman, S.E., Larbi, I., & Mourad, K. A. (2023). Forecasting land use and land cover dynamics using combined remote sensing, machine learning algorithm and local perception in the Agoènyivé Plateau, Togo. *Remote Sensing Applications: Society and Environment*, *30*, 100928. https://doi.org/10.1016/j.rsase.2023.100928

Yomo, M. (2018) Investigating Institutional Readiness in Enabling Adaptation to Future Changes in the Climate: A Case Study of Institutions Working with Frafras Farming Communities within the Semi-Arid Ecosystem of Northern Ghana. *Journal of Energy and Natural Resource Management*, 1(2):100-107. https://jenrm.uenr.edu.gh/index.php/uenrjournal/article/view/138/93

Zheng, C., & Wang, P. P. (1999). *"MT3DMS, a modular three-dimensional multispecies transport model for advection, dispersion and chemical reactions of contamination and user's guide"* (Report SERDP-99-1). US: AERDCC

Zoungrana, B.J.-B., Conrad, C., Amekudzi, L.K., Thiel, M., Da, E.D., Forkuor, G., & Löw, F. (2015). Multi-temporal Landsat images and ancillary data for land use/cover change LULCC detection in the Southwest of Burkina Faso, West Africa. *Rem. Sens.* 7 (9), 12076–12102. https://doi.org/10.3390/rs70912076

ANNEXES

Annex 1: RCMs Monthly and Seasonal Performance for Rainfall (Temperature): PBIAS (BIAS)

MON	RAINFALL (TEMPERATURE)						PBIAS (BIAS)				
	Observation	CanESM2	NorESM1	MPI-ESM-LR	RACMO22T	ENS MEAN	CanESM2-RCA4	NorESM1-RCA4	CCLM4-8-17	RACMO22T	ENS MEAN
Jan	10.79 (27.39)	8.67 (27.85)	10.38 (27.87)	10.81 (27.87)	10.78 (27.87)	10.16 (27.87)	-19.7(0.46)	-3.80 (0.48)	0.19 (0.48)	-0.09 (0.48)	-5.84 (0.48)
Feb	20.58 (28.35)	20.7 (28.8)	19.04 (28.85)	20.58 (28.85)	20.58 (28.85)	20.22 (28.84)	0.58 (0.45)	-7.48 (0.5)	0 (0.5)	0 (0.51)	-1.75 (0.49)
Mar	67.94 (28.3)	64.72 (28.77)	62.69 (28.73)	67.94 (28.73)	67.94 (28.73)	65.82 (28.74)	-4.74 (0.47)	-7.73 (0.43)	0 (0.43)	0 (0.43)	-3.12 (0.44)
April	124 (27.85)	122.6(28.26)	126.8 (28.22)	124 (28.22)	124 (28.22)	124.4 (28.23)	-1.15 (0.41)	2.28 (0.37)	0 (0.37)	0 (0.37)	0.28 (0.38)
May	146.9 (27.23)	146.8 (27.57)	142.3 (27.52)	146.9 (27.52)	146.9 (27.52)	145.73 (27.5)	-0.05 (0.34)	-3.13 (0.29)	0 (0.29)	0 (0.29)	-0.80 (0.30)
June	150 (25.97)	147.6 (26.32)	147.7 (26.23)	150 (26.23)	150 (26.23)	148.8 (26.25)	-1.59 (0.35)	-1.53 (0.26)	0 (0.26)	0 (0.26)	-0.78 (0.28)
July	65.22 (24.73)	63.46 (25.14)	69.71 (25.06)	65.22 (25.06)	65.22 (25.06)	65.9 (25.08)	-2.70 (0.410	6.88 (0.33)	0 (0.33)	0 (0.33)	1.04 (0.35)
Aug	25.94 (24.47)	36.34 (24.82)	32.56 (24.86)	25.94 (24.86)	25.93 (24.86)	30.19 (24.85)	40.09 (0.36)	25.52 (0.39)	0 (0.39)	-0.04 (0.39)	16.38 (0.38)
Sept	73.93 (25.21)	74.34 (25.52)	73.57 (25.59)	73.93 (25.59)	73.92 (25.59)	73.94 (25.58)	0.55 (0.31)	-0.49 (0.38)	0 (0.38)	-0.01 (0.38)	0.01(0.37)
Oct	107.55 (26)	106.3(26.28)	107.2 (26.31)	107.6(26.31)	107.6 (26.31)	107.2 (26.31)	-1.17 (0.28)	0.29 (0.31)	0 (0.31)	0 (0.31)	-0.36 (0.31)
Nov	41.13 (27.1)	40.08 (27.4)	42.52 (27.44)	41.13 (27.44)	41.12 (27.44)	41.21 (27.43)	-2.55 (0.31)	3.38 (0.35)	0 (0.35)	-0.02 (0.35)	0.19 (0.34)
Dec	9.38 (27.48)	11.74 (27.85)	8.78 (27.91)	9.38 (27.91)	9.38 (27.91)	9.82 (27.9)	25.16 (0.37)	-6.40 (0.43)	0 (0.43)	0 (0.43)	4.69 (0.42)
MAMJJ	554.1(26.82)	545.2 (27.21)	549.2 (27.15)	554.1 (27.15)	554.1 (27.15)	550.6 (27.17)	-1.60 (0.40)	-0.87 (0.34)	0 (0.34)	0 (0.34)	-0.62 (0.35)
SON	222.6 (26.10)	220.7 (26.40)	223.3 (26.45)	222.61(26.45)	222.6(26.45)	222.31(26.44)	-0.85 (0.30)	0.32 (0.34)	0 (0.34)	-0.01 (0.34)	-0.13 (0.34)
DJF	40.75 (27.74)	41.1 (28.17)	38.2 (28.21)	40.77 (28.21)	40.74 (28.21)	40.2 (28.20)	0.88 (0.43)	-6.26 (0.47)	0.05 (0.47)	-0.02 (0.47)	-1.35 (0.46)
A	25.94 (24.47)	36.3 (24.82)	32.56 (24.86)	25.94 (24.86)	25.93 (24.86)	30.19 (24.85)	40.09 (0.35)	25.52 (0.39)	0 (0.39)	-0.04 (0.39)	16.4 (0.38)

Annex 2a: Pearson Correlation Coefficient (r) Matrix Statistics between Major Anions and Cations for RS (DS)

	Variables	TDS	T°C	pH	c25°C	Ca++	Mg++	Na+	K+	HCO3-	Cl-	SO4--	NO3-
CT	TDS	**1**											
	T (°C)	0.23 (0.07)	**1**										
	pH	0.33 (0.24)	0.06 (0.17)	**1**									
	c25°C	**0.95 (0.96)**	0.21 (0.09)	0.26 (0.12)	**1**								
	Ca++	**0.84 (0.86)**	0.13 (0.08)	0.47 (0.35)	**0.79 (0.85)**	**1**							
	Mg++	0.69 (0.90)	0.10 (0.04)	0.20 (0.31)	**0.75 (0.90)**	0.51 (0.96)	**1**						
	Na+	**0.94 (0.95)**	0.24 (0.04)	0.18 (0.10)	**0.93 (0.92)**	0.63 (0.68)	0.74 (0.76)	**1**					
	K+	0.68 (0.39)	0.16 (0.12)	0.34 (0.40)	0.54 (0.31)	0.74 (0.24)	0.04 (0.23)	0.47 (0.37)	**1**				
	HCO3-	0.65 (0.33)	0.1 (0.13)	0.51 (0.70)	0.49 (0.27)	0.78 (0.45)	0.05 (0.38)	0.42 (0.16)	0.89 (0.68)	**1**			
	Cl-	**0.91 (0.96)**	0.16 (0.06)	0.14 (0.19)	**0.95 (0.94)**	0.69 (0.87)	**0.82 (0.92)**	**0.95 (0.91)**	0.39 (0.21)	0.36 (0.21)	**1**		
	SO4--	0.74 (0.73)	0.26 (0.06)	0.33 (0.10)	0.68 (0.68)	0.51 (0.47)	0.65 (0.50)	0.76 (0.77)	0.38 (0.50)	0 (0.19)	0.67 (0.60)	**1**	
	NO3-	0.22 (0.17)	0.24 (0)	-0.09 (-0.19)	0.21 (0.13)	0.06 (0.01)	0.26 (0.04)	0.21 (0.16)	0.08 (0.06)	-0.12 (-0.14)	0.11 (-0.02)	0.24 (0.14)	**1**
Pa	TDS	**1**											
	T (°C)	0.27 (0.42)	**1**										
	pH	-0.47(0.09)	-0.50 (0.05)	**1**									
	c25°C	**0.83 (0.96)**	-0.1 (0.43)	-0.26 (0)	**1**								
	Ca++	0.47 (0.76)	-0.1 (0.15)	-0.12 (-0.09)	0.39 (0.76)	**1**							
	Mg++	0.31 (0.93)	-0.16 (0.48)	0.010 (0)	0.48 (0.94)	0.54 (0.78)	**1**						
	Na+	**0.98 (0.92)**	0.31 (0.41)	-0.50 (0.12)	0.79 (0.87)	0.32 (0.48)	0.13 (0.77)	**1**					
	K+	**0.84 (0.14)**	0.33 (0.13)	-0.30 (0.56)	0.77 (0.03)	0.07 (-0.28)	0.17 (-0.12)	**0.86 (0.36)**	**1**				
	HCO3-	0.04 (0.44)	-0.18 (0.18)	0.37 (0.71)	0.19 (0.33)	0.11 (0.47)	0.67 (0.37)	-0.09 (0.30)	0.15 (0.34)	**1**			
	Cl-	**0.97 (0.96)**	0.30 (0.42)	-0.51 (-0.09)	**0.78 (0.94)**	0.39 (0.63)	0.12 (0.88)	**0.99 (0.95)**	**0.81 (0.1)**	-0.17 (0.18)	**1**		
	SO4--	0.31 (0.92)	0.07 (0.40)	-0.36 (-0.06)	0.15 (0.94)	0.66 (0.89)	0.15 (0.96)	0.26 (0.73)	-0.01 (-0.2)	-0.57 (0.35)	0.36 (0.86)	**1**	
	NO3-	-0.10 (-0.06)	0.23 (-0.06)	-0.52 (-0.78)	-0.25 (0.06)	0.04 (-0.16)	-0.33 (0.03)	-0.05 (0.04)	-0.34 (-0.4)	-0.81 (-0.88)	0.03 (0.20)	0.65 (0.03)	**1**
	TDS	**1**											
	T (°C)	-0.4 (-0.24)	**1**										
	pH	0.94 (0.90)	-0.09 (-0.34)	**1**									
	c25°C	**0.96 (0.87)**	-0.67 (-0.03)	0.80 (0.60)	**1**								

	Ca++	**1 (0.79)**	-0.50 (-0.49)	0.91 (0.84)	0.98 (0.50)	**1**							
Ma	Mg++	**0.98 (0.60)**	-0.21 (0.15)	0.99 (0.39)	0.87 (0.78)	0.95 (0)	**1**						
	Na+	0.71 (0.63)	**-0.94** (0.25)	0.42 (0.32)	0.88 (0.89)	0.76 (0.07)	0.53 (0.94)	**1**					
	K+	**0.99 (0.66)**	-0.30 (-0.26)	0.98 (0.77)	0.91 (0.33)	0.98 (0.47)	1 (0.42)	0.60 (0.26)	**1**				
	HCO3-	**0.97 (0.54)**	-0.20 (-0.38)	0.99 (0.79)	0.88 (0.07)	**0.95 (0.77)**	**1** (-0.16)	0.53 (-0.24)	**1 (0.75)**	**1**			
	Cl-	**0.90 (0.54)**	-0.78 (0.14)	0.70 (0.19)	0.99 (0.87)	0.94 (0.07)	**0.78 (0.82)**	**0.94 (0.92)**	0.83 (-0.04)	0.78 (-0.42)	**1**		
	SO4--	0.55 (-0.10)	**-0.99** (-0.74)	0.23 (-0.20)	0.76 (-0.10)	0.62 (0.19)	0.35 (-0.36)	**0.98** (-0.28)	0.43 (-0.19)	0.34 (-0.06)	0.86 (-0.10)	**1**	
	NO3-	-0.54 (0.21)	0.99 (0.45)	-0.22 (-0.12)	-0.76 (0.64)	-0.61 (-0.27)	-0.34 (0.71)	**-0.98 (0.83)**	-0.4 (-0.31)	-0.34 (-0.67)	**-0.85 (0.91)**	-1 (-0.29)	**1**
	TDS	**1**											
	T (°C)	0.69 (0.09)	**1**										
	pH	-0.7 (-0.20)	-0.41 (0.13)	**1**									
	c25°C	**0.67 (0.99)**	0.33 (0.06)	-0.78 (-0.28)	**1**								
	Ca++	0.85 (0.41)	0.72 (-0.10)	-0.33 (-0.04)	0.26 (0.49)	**1**							
	Mg++	**0.77 (0.90)**	0.45 (0.13)	-0.75 (-0.03)	**0.94 (0.87)**	0.46 (0.14)	**1**						
	Na+	**0.87 (0.97)**	0.61 (0.08)	-0.52 (-0.31)	0.32 (0.97)	0.83 (0.51)	0.38 (0.78)	**1**					
Ma	K+	0.62 (0.71)	0.55 (0.15)	-0.59 (0)	0.11 (0.65)	0.56 (-0.25)	0.15(0.87)	0.72 (0.56)	**1**				
S	HCO3-	0.22 (0.52)	0.36 (0.16)	-0.31 (0.46)	-0.29 (0.41)	0.27 (-0.24)	-0.23(0.73)	0.42 (0.34)	**0.84 (0.82)**	**1**			
	Cl-	**0.77 (0.92)**	0.32 (0.08)	-0.79 (-0.33)	0.96 (0.97)	0.38 (0.57)	**0.94 (0.80)**	0.47 (0.94)	0.15 (0.50)	-0.25 (0.26)	**1**		
	SO4--	**0.91 (0.85)**	0.77 (0.03)	-0.50 (-0.43)	0.42 (0.85)	0.97 (0.49)	0.61 (0.62)	**0.79 (0.90)**	0.61 (0.39)	0.28 (0.15)	0.50 (0.80)	**1**	
	NO3-	-0.08 (0.41)	-0.11 (-0.13)	0.38 (-0.51)	-0.23 (0.42)	-0.03 (0.50)	-0.36 (0.09)	0.21 (0.48)	-0.1 (-0.02)	-0.13 (-0.36)	-0.16 (0.40)	-0.18 (0.7)	**1**

*Values in the parentheses stand for DS

* T (°C), c25°C and TDS stand for the temperature, Electrical conductivity and Total Dissolved Solids, respectively.

Annex 2b: Coefficient of Determination (R^2) Matrix Statistics between Major Anions and Cations for RS and DS

Variables	TDS	T°C	pH	c25°C	Ca++	Mg++	Na+	K+	HCO3-	Cl-	SO4--	NO3-
TDS	**1**											
T (°C)	0.1 (0.01)	**1**										
pH	0.11 (0.06)	0.003 (0.03)	**1**									
c25°C	**0.90 (0.93)**	0.04 (0.01)	0.07 (0.02)	**1**								

CT	Ca++	0.71 (0.74)	0.02 (0.01)	0.22 (0.12)	0.62 (0.72)	**1**							
	Mg++	0.47 (0.81)	0.01 (0)	0.04 (0.10)	0.57 (0.80)	0.26 (0.92)	**1**						
	Na+	**0.89 (0.90)**	0.06 (0)	0.03 (0.01)	**0.87 (0.84)**	0.40 (0.47)	0.54 (0.57)	**1**					
	K+	0.46 (0.15)	0.03 (0.01)	0.11 (0.16)	0.29 (0.10)	0.55 (0.06)	0.002 (0.05)	0.22 (0.14)	**1**				
	HCO3-	0.42 (0.11)	0.01 (0.02)	0.26 (0.49)	0.24 (0.07)	0.61 (0.20)	0.003 (0.14)	0.18 (0.02)	0.79 (0.46)	**1**			
	Cl-	**0.83** (0.92)	0.03 (0)	0.02 (0.04)	**0.90** (0.89)	0.48 (0.75)	0.67 (0.85)	**0.91 (0.83)**	0.15 (0.04)	0.13 (0.05)	**1**		
	SO4--	0.55 (0.53)	0.07 (0)	0.11 (0.01)	0.45 (0.47)	0.26 (0.22)	0.43 (0.25)	0.57 (0.59)	0.14 (0.25)	0.09 (0.04)	0.45 (0.36)	**1**	
	NO3-	0.05 (0.03)	0.06 (0)	0.01 (0.03)	0.04 (0.02)	0.004 (0)	0.07 (0)	0.04 (0.03)	0.01 (0)	0.02 (0.02)	0.01 (0)	0.1 (0.02)	**1**
	TDS	**1**											
	T (°C)	0.07 (0.18)	**1**										
Pa	pH	0.22 (0.01)	0.25 (0)	**1**									
	c25°C	0.69 (0.93)	0.01 (0.18)	0.07 (0)	**1**								
	Ca++	0.22 (0.58)	0.01 (0.02)	0.01 (0.01)	0.15 (0.57)	**1**							
	Mg++	0.1 (0.86)	0.02 (0.23)	0 (0)	0.15 (0.88)	0.29 (0.60)	**1**						
	Na+	**0.96** (0.85)	0.1 (0.17)	0.25 (0.01)	0.63 (0.75)	0.10 (0.23)	0.02 (0.59)	**1**					
	K+	0.70 (0.02)	0.11 (0.02)	0.09 (0.31)	0.59 (0)	0.004 (0.08)	0.03 (0.01)	0.75 (0.13)	**1**				
	HCO3-	0.002 (0.20)	0.03 (0.03)	0.14 (0.50)	0.037 (0.11)	0.01 (0.22)	0.44 (0.14)	0.01 (0.09)	0.02 (0.11)	**1**			
	Cl-	**0.95 (0.91)**	0.09 (0.17)	0.27 (0.01)	0.606 (0.88)	0.15 (0.39)	0.01 (0.77)	**0.99 (0.91)**	0.66 (0.02)	0.03 (0.03)	**1**		
	SO4--	0.09 (0.85)	0.01 (0.16)	0.13 (0)	0.023 (0.88)	0.43 (0.79)	0.02 (0.93)	0.07 (0.54)	0 (0.04)	0.32 (0.12)	0.13 (0.74)	**1**	
	NO3-	0.01 (0)	0.05 (0)	0.27 (0.61)	0.065 (0)	0(0.03)	0.109 (0)	0.003 (0)	0.12 (0.15)	0.65 (0.78)	0 (0.04)	0.42 (0)	**1**
	TDS	**1**											
	T (°C)	0.18 (0.06)	**1**										
Ma	pH	**0.88 (0.81)**	0.01 (0.12)	**1**									
	c25°C	**0.92 (0.76)**	0.44 (0)	0.64 (0.36)	**1**								
	Ca++	0.99 (0.62)	0.25 (0.24)	0.82 (0.71)	0.96 (0.25)	**1**							
	Mg++	0.95 (0.36)	0.05 (0.02)	0.98 (0.15)	0.76 (0.61)	0.91 (0)	**1**						
	Na+	0.50 (0.40)	0.89 (0.06)	0.18 (0.10)	**0.77 (0.78)**	0.58 (0)	0.28 (0.88)	**1**					
	K+	0.98 (0.44)	0.09 (0.07)	0.95 (0.59)	0.83 (0.11)	0.95 (0.22)	0.99 (0.18)	0.36 (0.07)	**1**				
	HCO3-	0.95(0.29)	0.04 (0.14)	0.99 (0.62)	0.75 (0)	0.90 (0.59)	1 (0.02)	0.28 (0.06)	0.99 (0.57)	**1**			

XXX

	Cl-	0.81 (0.29)	0.60 (0.02)	0.48 (0.04)	**0.98 (0.76)**	0.87 (0.01)	0.61 (0.67)	**0.89 (0.85)**	0.70 (0)	0.60 (0.18)	**1**		
	SO4--	0.30 (0.01)	0.98 (0.54)	0.05 (0.04)	0.58 (0.01)	0.38 (0.03)	0.12 (0.13)	0.96 (0.08)	0.18 (0.04)	0.12 (0)	0.73 (0.01)	**1**	
	NO3-	0.29 (0.04)	0.98 (0.21)	0.05 (0.02)	0.58 (0.41)	0.38 (0.07)	0.12 (0.51)	0.96 (0.68)	0.18 (0.09)	0.11 (0.46)	0.73 (0.83)	1 (0.08)	**1**
	TDS	**1**											
	T (°C)	0.48 (0.01)	**1**										
	pH	0.530 (0.04)	0.17 (0.02)	**1**									
MaS	c25°C	0.45(0.97)	0.11 (0)	0.61 (0.08)	**1**								
	Ca++	0.72 (0.17)	0.52 (0.01)	0.11 (0)	0.07 (0.24)	**1**							
	Mg++	0.59 (0.81)	0.20 (0.02)	0.57 (0)	**0.89 (0.76)**	0.21 (0.02)	**1**						
	Na+	**0.76 (0.94)**	0.37 (0.01)	0.27 (0.09)	0.10 (0.95)	0.69 (0.26)	0.14 (0.62)	**1**					
	K+	0.38 (0.51)	0.30 (0.02)	0.35 (0)	0.01 (0.42)	0.32 (0.06)	0.02 (0.75)	0.52 (0.31)	**1**				
	HCO3-	0.05 (0.27)	0.13 (0.03)	0.09 (0.21)	0.08 (0.17)	0.07 (0.06)	0.05 (0.53)	0.18 (0.12)	0.71 (0.66)	**1**			
	Cl-	0.59 (0.85)	0.10 (0.01)	0.62 (0.11)	**0.92 (0.94)**	0.14 (0.33)	0.89 (0.63)	0.22 (0.89)	0.02 (0.25)	0.06 (0.07)	**1**		
	SO4--	**0.83 (0.73)**	0.60 (0)	0.25 (0.18)	0.18 (0.72)	0.94 (0.24)	0.38 (0.38)	0.63 (0.82)	0.37 (0.15)	0.08 (0.02)	0.25 (0.64)	**1**	
	NO3-	0.01 (0.17)	0.01 (0.02)	0.14 (0.26)	0.05 (0.17)	0.001 (0.3)	0.13 (0.01)	0.04 (0.23)	0.01 (0)	0.02 (0.13)	0.03 (0.16)	0.03 (0.4)	**1**

*Values in the parentheses stand for DS

* T (°C), c25°C and TDS stand for the temperature, Electrical conductivity and Total Dissolved Solids, respectively.

Annex 3a: Stiff Diagrams for the Ocean (a) Lagoon (b), Continental Terminal(c), Coastal Marine Sand (d), Palaeocene (e), and Maastrichtian Aquifers (f): RS 2021

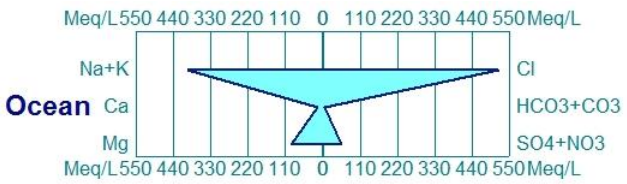

a

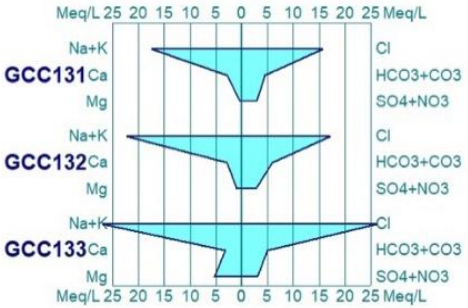

b

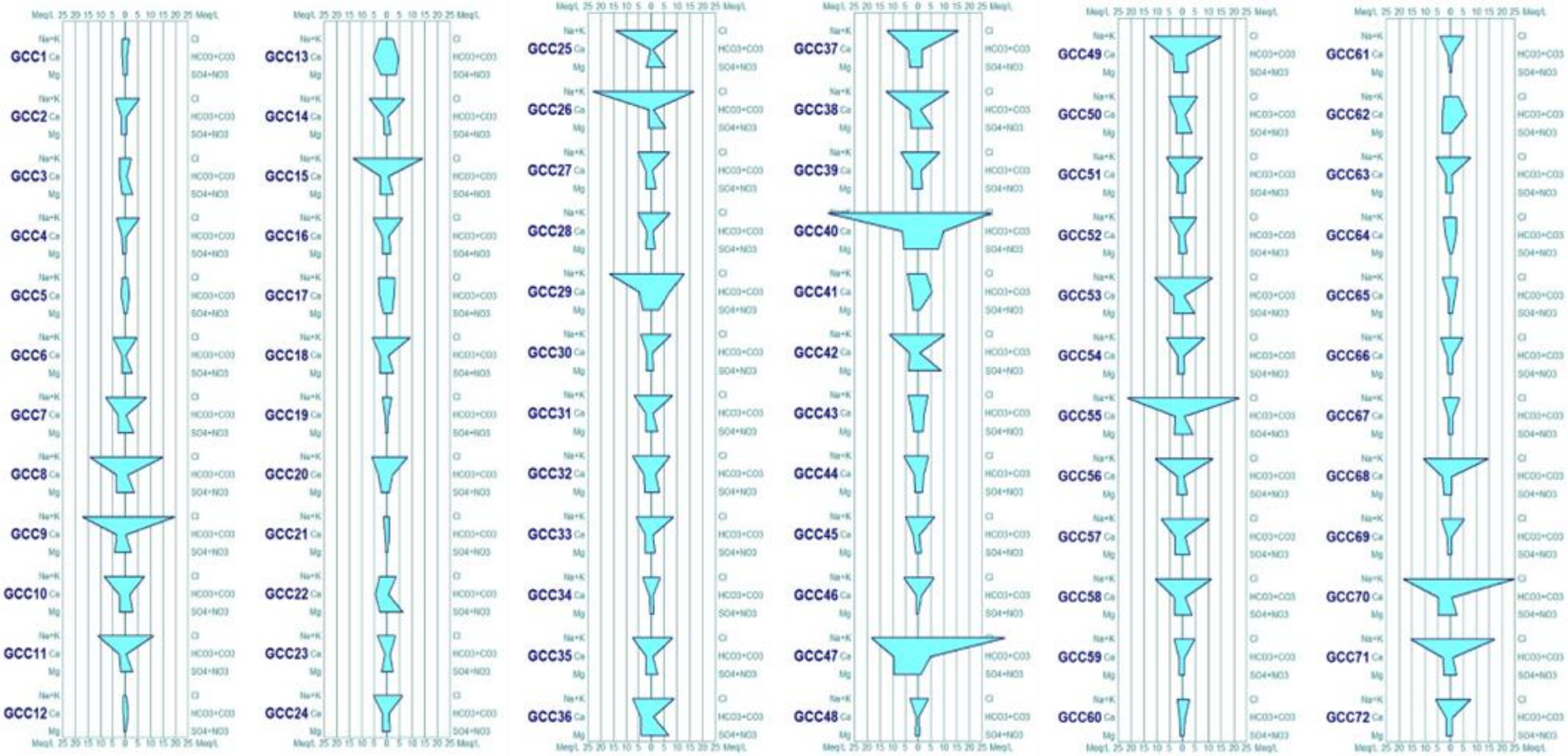
Meq/L 25 20 15 10 5 0 5 10 15 20 25 Meq/L
Na+K
Ca
Mg
Cl
HCO3+CO3
SO4+NO3
GCC1
GCC2
GCC3
GCC4
GCC5
GCC6
GCC7
GCC8
GCC9
GCC10
GCC11
GCC12
GCC13
GCC14
GCC15
GCC16
GCC17
GCC18
GCC19
GCC20
GCC21
GCC22
GCC23
GCC24
GCC25
GCC26
GCC27
GCC28
GCC29
GCC30
GCC31
GCC32
GCC33
GCC34
GCC35
GCC36
GCC37
GCC38
GCC39
GCC40
GCC41
GCC42
GCC43
GCC44
GCC45
GCC46
GCC47
GCC48
GCC49
GCC50
GCC51
GCC52
GCC53
GCC54
GCC55
GCC56
GCC57
GCC58
GCC59
GCC60
GCC61
GCC62
GCC63
GCC64
GCC65
GCC66
GCC67
GCC68
GCC69
GCC70
GCC71
GCC72

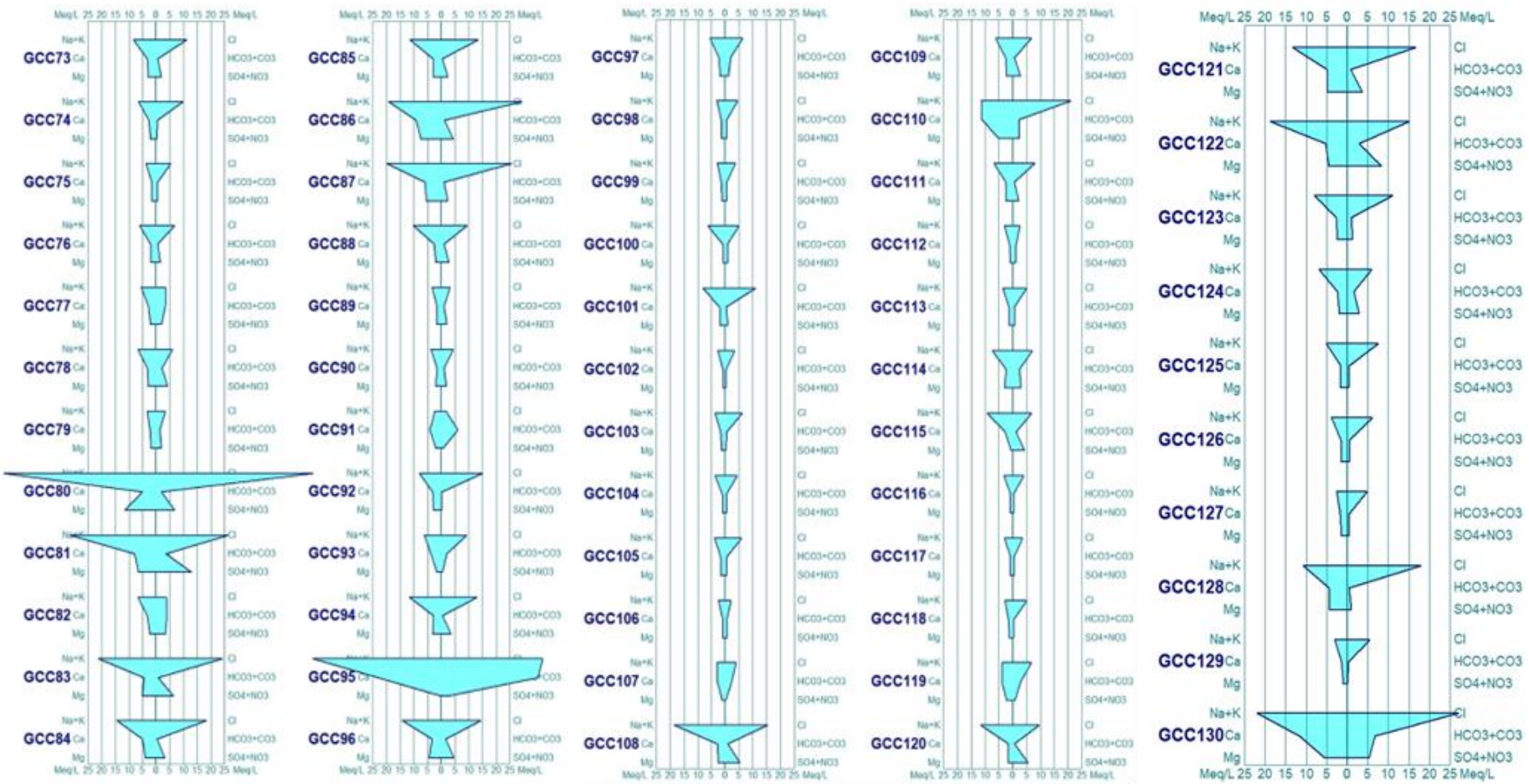
Meq/L 25 20 15 10 5 0 5 10 15 20 25 Meq/L
Na+K
Ca
Mg
Cl
HCO3+CO3
SO4+NO3
GCC73
GCC74
GCC75
GCC76
GCC77
GCC78
GCC79
GCC80
GCC81
GCC82
GCC83
GCC84
GCC85
GCC86
GCC87
GCC88
GCC89
GCC90
GCC91
GCC92
GCC93
GCC94
GCC95
GCC96
GCC97
GCC98
GCC99
GCC100
GCC101
GCC102
GCC103
GCC104
GCC105
GCC106
GCC107
GCC108
GCC109
GCC110
GCC111
GCC112
GCC113
GCC114
GCC115
GCC116
GCC117
GCC118
GCC119
GCC120
GCC121
GCC122
GCC123
GCC124
GCC125
GCC126
GCC127
GCC128
GCC129
GCC130

c

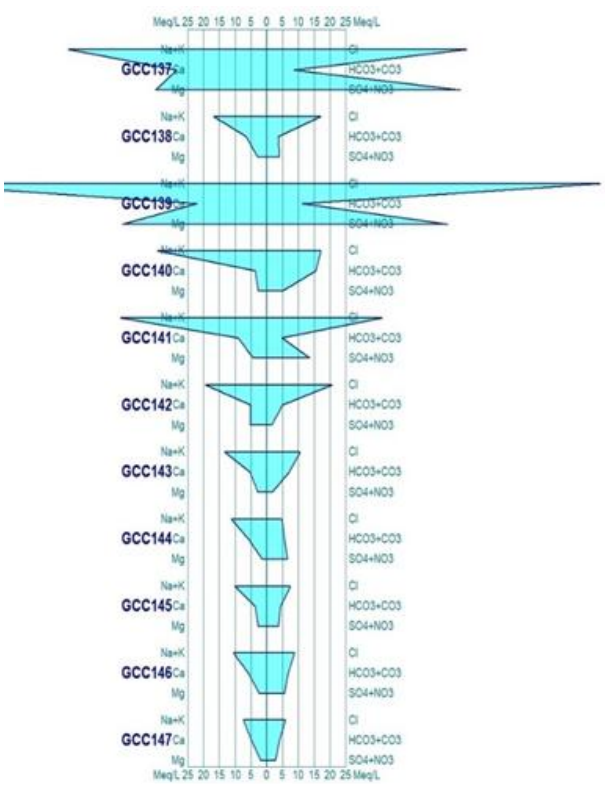
Meq/L 25 20 15 10 5 0 5 10 15 20 25 Meq/L
GCC137
GCC138
GCC139
GCC140
GCC141
GCC142
GCC143
GCC144
GCC145
GCC146
GCC147
Na+K
Ca
Mg
Cl
HCO3+CO3
SO4+NO3

d

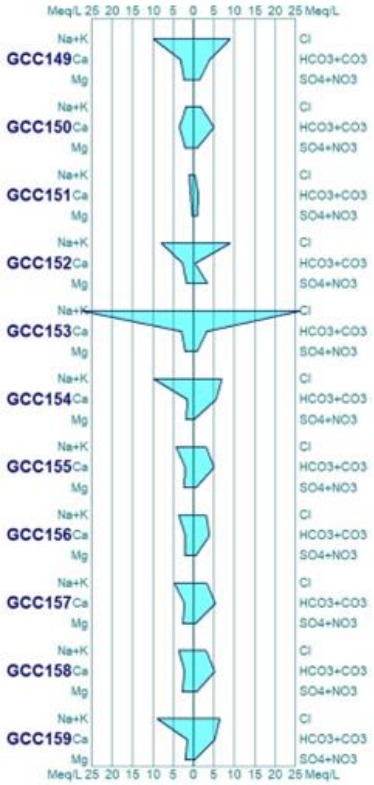
Meq/L 25 20 15 10 5 0 5 10 15 20 25 Meq/L
GCC149
GCC150
GCC151
GCC152
GCC153
GCC154
GCC155
GCC156
GCC157
GCC158
GCC159
Na+K
Ca
Mg
Cl
HCO3+CO3
SO4+NO3

e

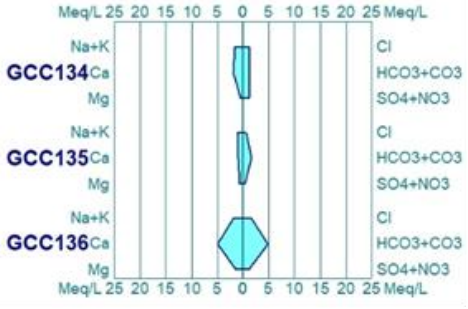
Meq/L 25 20 15 10 5 0 5 10 15 20 25 Meq/L
GCC134
GCC135
GCC136
Na+K
Ca
Mg
Cl
HCO3+CO3
SO4+NO3

f

Annex 3b: Physicochemical Parameters and Seawater Intrusion Potential Results: RS 2021

ID	Aquifer	pH	Temp	Cond	Mg	Ca	HCO3	NH4	NO3	NO2	Cl	SO4	Ox KMnO4	PO4	Na	K	**RI**	**CEV**	**Na/Cl**	**RI+CEV+ (Na/Cl)**	**AHC**	**Stiff-D**	**HFE-D**	**SWI**
GCC1	CT	5.83	32.8	338	10.56	23.2	36.6	0.01	45.78	0	60.07	3.19	0.2	0.08	28	3.2	1.6	0.5	0.47	+	1	2	2	2
GCC2	CT	5.04	30.6	840	16.8	32	24.4	0.02	7.91	0	200.2	15.24	0.3	0	89	2.1	8.2	0.5	0.44	++	1	1	1	1
GCC3	CT	5.58	32.8	576	14.4	44	36.6	0	189.4	0	90.1	4.64	0.5	0.13	35.5	41	2.5	0.2	0.39	+	2	2	2	2
GCC4	CT	5.67	31.2	699	12.96	28	24.4	0.02	4.74	0	200.2	6.25	0.6	0.13	82	0.5	8.2	0.6	0.41	++	1	1	1	1
GCC5	CT	6.44	33	330	6.24	32	97.6	0	12.52	0	35.04	23.67	0.5	0.1	26	3.1	0.4	0.2	0.74	-	3	3	3	3
GCC6	CT	5.24	28.3	889	15.84	29.6	12.2	0.34	163.2	0	170.2	8.48	5.1	0.37	114	2.9	14	0.3	0.67	++	1	1	1	1
GCC7	CT	5.25	29.8	1520	36	57.6	30.5	0	188.7	0	300.3	19.94	0.6	0.03	180	2.3	9.8	0.4	0.6	++	1	1	1	1
GCC8	CT	5.59	33.5	2310	43.2	72	67.1	0	220.4	0	540.6	14.04	0.3	0	324	5.1	8.1	0.4	0.6	++	1	1	1	1
GCC9	CT	4.89	33	2780	52.8	72.8	18.3	0.01	28.57	0.02	700.8	101.1	1	0	388	5.2	38.3	0.4	0.55	++	1	1	1	1
GCC10	CT	5.51	30.9	1388	28.8	52	109.8	0.03	109	0	270.3	71.53	0.2	0.03	180	24	2.5	0.2	0.67	+	1	1	1	1
GCC11	CT	4.88	32.9	1800	24	52	30.5	0	74.09	0	400.4	85.99	0.4	0	248	5.1	13.1	0.4	0.62	++	1	1	1	1
GCC12	CT	6	32.7	197.6	3.84	16	79.3	0.02	5.39	0	13.02	11.14	0.2	0.16	18.6	2	0.2	-0.6	1.43	- (*)	3	3	3	4
GCC13	CT	7.1	32.3	1106	31.2	108	286.7	0	0.69	0	87.59	181.3	0.1	0	69	5.8	0.3	0.1	0.79	-	3	3	3	3
GCC14	CT	4.98	33.1	1080	13.92	29.6	24.4	0	68.47	0	250.3	27.77	0.6	0.04	160	3.5	10.3	0.3	0.64	++	1	1	1	1
GCC15	CT	5.21	33.4	2080	36	56	36.6	0	72.82	0	510.6	63.1	0.5	0.04	308	4.4	13.9	0.4	0.6	++	1	1	1	1
GCC16	CT	5.73	30.4	1020	21.6	40	48.8	0	75.16	0	220.4	24.88	0.2	0	128.5	3.2	4.5	0.4	0.58	+	1	1	1	1
GCC17	CT	6.93	32.6	960	16.8	64	183	0	0.4	0	120.1	99.25	0.1	0	77	5.2	0.7	0.3	0.64	+	1	2	2	2
GCC18	CT	5.34	31.5	1463	36	60	36.6	0	146.9	0	330.4	20.3	0.4	0	132	5.9	9	0.6	0.4	++	1	1	2	1
GCC19	CT	5.52	31.6	322	4.8	16	36.6	0	0	0	65.07	14.64	0.2	0	40.5	1.6	1.8	0.4	0.62	+	1	1	1	1
GCC20	CT	5.04	31.1	1368	28.8	72	134.2	0.04	23.75	0	295.3	22.83	0.1	0.03	135	5.6	2.2	0.5	0.46	+	1	1	1	1
GCC21	CT	5.84	32.3	209	4.8	16	61	0.05	9.73	0	40.04	1.51	0.2	0.05	30.4	2.5	0.7	0.2	0.76	+	3	2	2	2
GCC22	CT	5.79	32.9	1217	36	96	42.7	0.01	383.5	0	130.1	9.59	0.4	0.11	68	6.8	3	0.4	0.52	+	2	2	2	2
GCC23	CT	5.03	31	757	28.8	16	73.2	0.01	124.7	0	125.1	16.2	0.3	0	87	3.2	1.7	0.3	0.7	+	1	2	2	2
GCC24	CT	5.86	31.1	978	21.6	36	54.9	0.03	42.01	0	225.3	26.57	0.1	0.04	120	7.6	4.1	0.4	0.53	+	1	1	1	1
GCC25	CT	5.44	31.5	1845	26.4	8	42.7	0	299.7	0	365.4	44.42	0.4	0	320	6.2	8.6	0.1	0.88	++	1	1	1	1
GCC26	CT	5.51	31.4	2580	12	20	48.8	0.01	163	0.02	590.6	147.8	0.5	0	510	26.4	12.1	0.1	0.86	++	1	1	1	1

GCC27	CT	5.21	32.5	1060	26.4	44	30.5	0.039	90.38	0	250.3	21.51	0.3	0.057	122	3.2	8.2	0.5	0.49	++	1	1	1	1
GCC28	CT	5.47	32.1	1043	28.8	36	42.7	0.015	55.17	0	255.3	27.56	0.1	0.044	122	3	6	0.5	0.48	++	1	1	1	1
GCC29	CT	6.98	32.1	2480	43.2	100	433.1	0	31.8	0	460.5	122.3	1.9	0.42	350	47.5	1.1	0.1	0.76	+	1	2	1	1
GCC30	CT	5.35	31.7	900	26.4	36	30.5	0	25.78	0	270.3	19.05	0.4	0.061	97	2.8	8.9	0.6	0.36	+	1	2	1	1
GCC31	CT	5	32.4	1285	28.8	44	36.6	0	132.5	0	295.3	19.54	0.2	0.055	158	3	8.1	0.5	0.54	++	1	1	1	1
GCC32	CT	5.63	31.8	1375	33.6	64	103.7	0	133.7	0	260.3	60.53	0.1	0.065	162	16.4	2.5	0.3	0.62	++	1	1	1	1
GCC33	CT	5.25	32.8	1222	31.2	52	42.7	0	60.43	0	310.3	22.5	0.4	0.071	138	2.6	7.3	0.5	0.44	++	1	1	1	1
GCC34	CT	5.45	32.2	733	3.84	16	36.6	0	30.45	0	126.1	25.22	0.3	0.036	81	1.3	3.4	0.3	0.64	+	1	1	1	1
GCC35	CT	5.19	32	1292	28.8	40	36.6	0	97.9	0	295.3	42.01	0	0	170	3.3	8.1	0.4	0.58	++	1	1	1	1
GCC36	CT	5.66	31.3	1828	50.4	88	54.9	0	394.7	0	320.4	16.33	0	0	168	4	5.8	0.5	0.52	+	1	2	2	2
GCC37	CT	5.27	32	2120	40.8	84	103.7	0	24.71	0	560.6	63.61	0	0.036	280	7	5.4	0.5	0.5	+	1	1	1	1
GCC38	CT	5.88	31.9	1298	36.48	68	48.8	0	191.7	0	420.5	135.8	0	0.038	288	9.6	8.6	0.3	0.68	++	1	1	1	1
GCC39	CT	6.16	29.8	1717	29.28	52	73.2	0	40.43	0	300.3	48.67	1.3	0.218	156	5.4	4.1	0.5	0.52	+	1	1	1	1
GCC40	CT	5.28	32	2030	69.6	124	610	0	46.43	0	1011	343.3	0.2	0.028	770	74	1.7	0.2	0.76	+	2	2	1	2
GCC41	CT	6.36	31.3	901	26.4	56	329.4	0.013	3.82	0	120.1	27.07	0.2	0.046	90	16	0.4	0.1	0.75	-	3	3	3	3
GCC42	CT	5.57	29.3	1543	48	72	36.6	0	315.3	0	375.4	212.4	0.2	0.079	252	7.4	10.3	0.3	0.67	++	1	1	1	1
GCC43	CT	6.13	31.4	838	22.08	52	146.4	0	91.72	0	140.2	15.83	0	0.051	95	0.7	1	0.3	0.68	+	1	2	2	2
GCC44	CT	5.37	31.4	1937	14.4	32	134.2	0	74.31	0	145.2	24.51	0.7	0.218	128	4.8	1.1	0.1	0.88	+	1	1	1	1
GCC45	CT	5.21	31.9	1401	12.96	40	24.4	0	41.28	0	230.3	26.08	0.3	0.081	116	1.1	9.4	0.5	0.5	++	1	1	1	1
GCC46	CT	6.05	30.5	835	9.6	13.6	79.3	0.18	2.67	0.02	218.2	1.66	0.9	0.09	128	5	2.8	0.4	0.59	+	1	1	1	1
GCC47	CT	6.97	27.4	4420	115.2	196	298.9	1.79	7.96	1.173	1201	44.19	1.4	0.455	510	6.2	4	0.6	0.42	+	1	2	2	2
GCC48	CT	5.07	27.5	610	14.4	16	18.3	0.071	13.53	0.001	145.2	21.87	0.1	0.024	76	1	7.9	0.5	0.52	++	1	1	1	1
GCC49	CT	5.73	29.5	2160	40.8	80	97.6	0.134	25.2	0.014	540.6	78.44	0.2	0.159	284	11.7	5.5	0.5	0.53	+	1	1	1	1
GCC50	CT	5.83	31.4	1162	31.2	55.2	61	0.085	118.5	0.036	210.2	85.78	1	0	119	12	3.4	0.4	0.57	+	1	1	1	1
GCC51	CT	5.86	31.3	1148	26.88	37.6	48.8	0.077	48.02	0	280.3	16.92	0.5	0	146	4.1	5.7	0.5	0.52	+	1	1	1	1
GCC52	CT	5.55	31.7	857	19.68	31.2	48.8	0.013	73.82	0	200.2	20.56	1	0.074	118	2.7	4.1	0.4	0.59	+	1	1	1	1
GCC53	CT	5.3	30.2	1903	42.24	76.8	42.7	0.021	208	0	410.5	67.85	0.2	0	248	5.5	9.6	0.4	0.6	++	1	1	1	1
GCC54	CT	5.3	30.4	1071	24.48	37.6	24.4	0.009	40.62	0	310.3	8.75	0	0	146	1.6	12.7	0.5	0.47	++	1	1	1	1
GCC55	CT	5.49	32.2	2910	39.36	57.6	36.6	0.038	90.2	0	780.9	131.2	0.4	0	490	7.4	21.3	0.4	0.63	++	1	1	1	1

GCC56	CT	5.3	31.1	1588	27.36	42.4	30.5	0.08	88.8	0.008	420.5	18.74	0.2	0	244	2.7	13.8	0.4	0.58	++	1	1	1	1
GCC57	CT	5.63	31.5	1596	36.48	59.2	61	0.033	95.58	0.003	370.4	66.95	0.6	0	194	6.7	6.1	0.5	0.52	+	1	1	1	1
GCC58	CT	5.67	32.1	1660	36.96	68	61	0.058	98.8	0.005	400.4	103.7	0.6	0	240	9.4	6.6	0.4	0.6	+	1	1	1	1
GCC59	CT	5.51	30.1	687	15.36	29.6	48.8	0	26.43	0	172.2	6.75	0	0	74	2.4	3.5	0.6	0.43	+	1	1	1	1
GCC60	CT	5.92	30	420	11.04	26.4	61	0	9.51	0	93.1	5.84	0	0	45	2	1.5	0.5	0.48	+	1	2	2	2
GCC61	CT	5.63	30.6	723	6	20	42.7	0.065	4.999	0.005	185.2	9.29	0.6	0	96	1.2	4.3	0.5	0.52	+	1	1	1	1
GCC62	CT	6.78	30.6	928	42.72	68.8	378.2	0.017	0.045	0	111.1	24.56	0	0	62	4.2	0.3	0.4	0.56	-	3	3	3	3
GCC63	CT	5.38	29.6	1085	23.28	38.4	30.5	0.026	42.12	0	280.3	11.29	0.4	0	134	1.6	9.2	0.5	0.48	++	1	1	1	1
GCC64	CT	6.28	29.3	548	4.32	41.6	122	0.016	13.42	0	82.09	20.02	0.8	0	64	1.2	0.7	0.2	0.78	+	1	2	2	1
GCC65	CT	5.97	29.5	527	10.08	21.6	103.7	0.492	19.82	3.48	94.1	10.93	1.8	2.46	75	4.4	0.9	0.2	0.8	+	1	1	1	1
GCC66	CT	5.75	32	707	13.92	27.2	48.8	0.019	22.84	0	173.2	16.92	0.5	0	91	1.9	3.5	0.5	0.53	+	1	1	1	1
GCC67	CT	5.54	31.7	552	11.04	22.4	48.8	0.021	27.81	0	127.1	16.2	0	0	72	1.8	2.6	0.4	0.57	+	1	1	1	1
GCC68	CT	5.31	30	1756	32.64	66.4	30.5	0	8.73	0	520.6	6.02	0.6	0	244	1.6	17.1	0.5	0.47	++	1	1	1	1
GCC69	CT	5.26	30	706	12	30.4	30.5	0	16.38	0	193.2	4.2	0	0	88	0.7	6.3	0.5	0.46	+	1	1	1	1
GCC70	CT	5.1	32.7	3000	60.72	98.4	30.5	0.031	105.6	0.02	881	38.32	0.2	0	425	2.6	28.9	0.5	0.48	++	1	1	1	1
GCC71	CT	5.64	32	2250	33.6	61.6	48.8	0.047	74.59	0	610.7	47.41	0.4	0	360	1.6	12.5	0.4	0.59	++	1	1	1	1
GCC72	CT	5.52	31.3	1007	20.16	39.2	42.7	0.038	9.84	0	280.3	12.92	0.3	0	134	4.3	6.6	0.5	0.48	+	1	1	1	1
GCC73	CT	5.63	30.2	1575	36.48	64.8	42.7	0.002	72.56	0	395.4	44.68	0	0	190	3.8	9.3	0.5	0.48	++	1	1	1	1
GCC74	CT	5.61	30.1	1240	24.96	56	42.7	0.024	15.41	0	355.4	4.2	0	0	148	1.4	8.3	0.6	0.42	++	1	1	1	1
GCC75	CT	5.15	30	760	17.28	32	36.6	0	25.44	0.001	195.2	8.38	0	0	86	0.8	5.3	0.6	0.44	+	1	1	1	1
GCC76	CT	5.11	30	1060	23.28	41.2	36.6	0.0004	90.7	0	245.3	8.38	0.5	0	136	1.1	6.7	0.4	0.55	++	1	1	1	1
GCC77	CT	6.14	30.2	1016	24.72	58.8	213.5	0.0009	70.93	0.005	135.1	49.68	2.5	0.165	110	22.4	0.6	0	0.81	+	1	2	2	2
GCC78	CT	5.96	30.2	1309	35.76	65.2	134.2	0.009	103.5	0.05	215.2	125.6	0	0	144	18.4	1.6	0.2	0.67	+	1	2	2	2
GCC79	CT	6.16	31.7	718	23.04	45.6	85.4	0.06	69.6	0.012	125.1	46.37	0	0	72	7.7	1.5	0.4	0.58	+	1	2	2	2
GCC80	CT	6.63	32.1	6890	139.2	104	128.1	0.047	0	0.024	2037	330.2	0.8	0.002	1280	1.3	15.9	0.4	0.63	++	1	1	1	1
GCC81	CT	6.3	31.6	4420	78.72	160	225.7	0.038	326.1	0.389	936	389.3	2.6	0	630	156	4.1	0.2	0.67	+	1	1	1	1
GCC82	CT	6.98	32.3	1189	28.8	68	250.1	0.07	93.29	0	140.2	100.1	0.6	0	146	11.1	0.6	-0.1	1.04	- (*)	1	3	3	4
GCC83	CT	5.45	32.4	3400	64.32	92.8	48.8	0.111	258.7	0.01	861	121.2	0.6	0	485	7.1	17.6	0.4	0.56	++	1	1	1	1
GCC84	CT	5.51	31.4	2540	47.52	104	30.5	0.069	123.7	0	660.7	56.95	0.4	0	328	4.1	21.7	0.5	0.5	++	1	1	1	1

GCC85	CT	5.27	32.7	1850	35.04	64	24.4	0.011	133.2	0	480.5	22.74	0.9	0	264	2.7	19.7	0.4	0.55	++	1	1	1	1
GCC86	CT	5.77	32.2	3770	91.2	187.2	79.3	0.048	2.05	0	1051	217.5	0.9	0.033	440	7	13.3	0.6	0.42	++	1	1	1	1
GCC87	CT	5.35	30.5	3250	66.72	120	67.1	0.012	4.54	0	916	122.1	0.4	0	455	4.6	13.7	0.5	0.5	++	1	1	1	1
GCC88	CT	5.71	32.3	1521	24.96	52.8	61	0.012	123.9	0	340.4	40.14	1.6	0	236	2.9	5.6	0.3	0.69	+	1	1	1	1
GCC89	CT	5.62	30.6	712	20.16	34.4	67.1	0.033	115	0	115.1	14.92	0	0	80	3.4	1.7	0.3	0.69	+	1	2	2	2
GCC90	CT	5.66	30.5	854	24.48	35.2	67.1	0.008	103.2	0	160.2	8.93	0	0	89	4.2	2.4	0.4	0.56	+	1	1	1	1
GCC91	CT	6.77	30.3	804	24.48	88	366	0.058	0.343	0	70.08	26.95	0.6	0	54	5.5	0.2	0.2	0.77	- (*)	3	3	2	4
GCC92	CT	4.78	29.9	1746	34.56	64.8	18.3	0.007	2.304	0	535.6	5.29	0.4	0	188	1.3	29.3	0.6	0.35	+	1	1	1	1
GCC93	CT	6.09	29.6	1251	20.64	79.2	122	0.015	9.129	0	335.4	7.65	0.3	0	140	6.2	2.7	0.6	0.42	+	1	1	1	1
GCC94	CT	5.49	30.1	1875	39.36	58.4	24.4	0.174	181.6	0.007	465.5	39.5	0.8	0	268	3.2	19.1	0.4	0.58	+	1	1	1	1
GCC95	CT	7.07	32.3	6820	0	464	2159.4	0.508	1.46	0.043	1321	109.2	48	0	860	375	0.6	0.1	0.65	-	3	3	3	3
GCC96	CT	5.73	32.3	2300	56.4	72	97.6	0.525	181.8	0.081	520.6	90.96	1.3	0.111	324	13	5.3	0.4	0.62	+	1	1	1	1
GCC97	CT	5.88	30.2	1007	23.04	46.4	122	0.027	42.38	0	230.3	28.93	0	0	122	2.1	1.9	0.5	0.53	+	1	1	1	1
GCC98	CT	5.27	30.2	652	14.88	29.6	36.6	0	20.91	0	170.2	5.65	0	0	70	1.5	4.6	0.6	0.41	+	1	1	1	1
GCC99	CT	5.63	29.8	592	13.92	27.2	42.7	0	19.82	0	142.2	9.29	0	0	66	1.1	3.3	0.5	0.46	+	1	1	1	1
GCC100	CT	5.21	30.5	850	8.16	17.6	48.8	0.045	2.56	0	188.2	51.05	0.9	0	142	3.3	3.9	0.2	0.75	+	1	1	1	1
GCC101	CT	5.45	30.2	1427	23.04	41.6	24.4	0.047	39.92	0	390.4	21.84	0.2	0	184	1.9	16	0.5	0.47	++	1	1	1	1
GCC102	CT	5.38	30.1	462	6.96	16	24.4	0	12.59	0	122.1	2.75	0.8	0	64	0.8	5	0.5	0.52	+	1	1	1	1
GCC103	CT	5.18	30.1	775	14.88	34	42.7	0	7.81	0	218.2	2.93	0	0	83	3.6	5.1	0.6	0.38	+	1	1	1	1
GCC104	CT	5.37	31.3	652	11.04	19.2	30.5	0.025	25.15	0	160.2	9.1	0.3	0	87	1.7	5.3	0.4	0.54	+	1	1	1	1
GCC105	CT	5.56	30.4	808	18	31.6	42.7	0	21.75	0	213.2	10.56	0.5	0	91	1.8	5	0.6	0.43	+	1	1	1	1
GCC106	CT	5.7	30.1	419	10.56	16	42.7	0	36.6	0	81.09	6.56	0	0	58	1.7	1.9	0.3	0.72	+	1	1	1	1
GCC107	CT	5.97	29.8	722	13.92	56.8	158.6	0	10.76	0	147.2	4.75	0.4	0	68	1.4	0.9	0.5	0.46	+	1	2	2	2
GCC108	CT	5.56	32.2	2470	30.72	57.6	61	0.068	259.1	0	555.6	71.5	0.8	0	425	5.1	9.1	0.2	0.76	++	1	1	1	1
GCC109	CT	5.05	30.4	1231	27.6	54	36.6	0.197	170.9	0.019	245.3	11.29	0.3	0	142	2.8	6.7	0.4	0.58	++	1	1	1	1
GCC110	CT	6.62	30.4	2800	62.4	224	146.4	0.026	24.03	0.039	755.8	95.27	0.8	0.034	260	5.3	5.2	0.6	0.34	+	1	2	2	2
GCC111	CT	5.56	32.2	1214	29.28	52.8	42.7	0.037	119.8	0	290.3	19.47	0	0	156	3.5	6.8	0.5	0.54	++	1	1	1	1
GCC112	CT	5.79	30.4	546	9.6	24	73.2	0.055	52.99	0	94.1	8.38	0.3	0	70	2.5	1.3	0.2	0.74	+	1	1	1	1
GCC113	CT	5.31	30.7	733	15.84	28.8	36.6	0.386	25.51	0.008	181.2	18.02	0.3	0	84	3.4	5	0.5	0.46	+	1	1	1	1

GCC114	CT	6.41	31.9	1343	37.68	48.8	152.5	0.072	121.5	0.006	250.3	57.86	0.4	0	140	54	1.6	0.2	0.56	+	1	1	1	1
GCC115	CT	5.96	32.2	1398	8.64	56.8	79.3	0.045	179.9	0.016	245.3	71.95	0.5	0	192	37.5	3.1	0.1	0.78	+	1	1	1	1
GCC116	CT	5.04	30.3	568	10.56	16	18.3	0.03	13.08	0	149.2	12.93	0.4	0	74	1.1	8.2	0.5	0.5	++	1	1	1	1
GCC117	CT	5.17	30.3	532	11.04	17.6	24.4	0.075	17.82	0	130.1	15.65	0.2	0	68	3.4	5.3	0.5	0.52	+	1	1	1	1
GCC118	CT	5.31	30.1	664	15.36	34.8	30.5	0	12.42	0	183.2	4.02	0.4	0	65	0.8	6	0.6	0.35	+	1	2	2	2
GCC119	CT	6.53	30.3	1108	27.12	83.6	183	0.003	13.47	0	240.3	31.49	0.1	0	87	9	1.3	0.6	0.36	+	1	2	2	2
GCC120	CT	5.34	32	1777	19.68	32.8	36.6	0.09	163.9	0.15	345.4	147.5	0.8	0	256	22.8	9.4	0.2	0.74	++	1	1	1	1
GCC121	CT	5.52	32.1	2370	58.8	100	54.9	0.142	156.3	0.096	595.7	67.86	0.7	0	292	24.4	10.8	0.5	0.49	++	1	1	1	1
GCC122	CT	6.41	31.3	2700	53.76	107.2	183	0.115	336.2	0.094	540.6	142.1	1.1	0	425	16	3	0.2	0.79	+	1	1	1	1
GCC123	CT	5.85	31.3	1493	30.24	55.2	61	0.077	51.18	0	395.4	25.65	0.5	0	184	7.3	6.5	0.5	0.47	+	1	1	1	1
GCC124	CT	5.89	31.2	1169	24.48	48.8	103.7	0.023	114.7	0.197	210.2	54.68	0.6	0	146	24	2	0.2	0.69	+	1	1	1	1
GCC125	CT	5.11	28.7	975	19.68	34.4	30.5	0.027	10.28	0	270.3	4.93	0.4	0	118	1.5	8.9	0.6	0.44	++	1	1	1	1
GCC126	CT	5.35	30.1	821	18.72	33.6	36.6	0.017	18.1	0	220.2	5.47	0.5	0	91	1.6	6	0.6	0.41	+	1	1	1	1
GCC127	CT	5.52	30	672	17.28	37.6	30.5	0.002	16.05	0	171.2	10.2	0	0	62	1.6	5.6	0.6	0.36	+	1	2	2	2
GCC128	CT	4.88	30.7	2150	52.8	89.6	30.5	0.152	37.73	0	635.7	18.56	0.4	0	248	3.7	20.8	0.6	0.39	++	1	1	1	1
GCC129	CT	5.63	30.5	659	11.52	30.4	18.3	0.025	0.877	0	193.2	2.93	0.5	0	74	0.6	10.6	0.6	0.38	++	1	2	1	1
GCC130	CT	6.9	32	3920	67.2	238.4	420.9	0.186	3.83	0.026	961.1	257.7	2.1	0.269	475	52	2.3	0.5	0.49	+	1	1	1	1
GCC131	LAG	8.51	31.2	2530	4.8	60	274.5	5.19	30.55	0	560.6	116.4	5.4	1.2	368	61	-	-	-	-	-	-	-	-
GCC132	LAG	7.98	31.3	2780	12	60	366	5.86	10.98	0	610.7	128.8	5.7	0.03	485	46.5	-	-	-	-	-	-	-	-
GCC133	LAG	9.2	31.9	3610	64.8	68	305	0	0.098	0	926	155.6	5.2	0.569	590	49	-	-	-	-	-	-	-	-
GCC134	Ma	6	31	504	6.24	40	79.3	0.004	1.25	0	45.05	57.63	0.7	0.23	35	2.5	0.6	0.2	0.78	+	1	2	2	2
GCC135	Ma	6.14	32.6	273	7.2	20	97.6	0.01	13.66	0	25.03	10.78	0.1	0.09	27.2	2.2	0.3	-0.2	1.09	- (*)	3	3	3	4
GCC136	Ma	6.68	31.4	807	19.2	100	298.9	0	2.7	0.557	60.06	52.47	1.7	0.024	36	15	0.2	0.15	0.6	-	3	3	3	3
GCC137	MaS	4.98	32.5	10760	429.6	576	530.7	0.38	0.49	3.38	2252	2954	3.8	0.49	1320	216	4.2	0.3	0.59	+	1	1	1	1
GCC138	MaS	6.75	30	2930	36	132	237.9	0.03	87.96	0	610.7	128.5	0.9	0.92	360	54	2.6	0.3	0.59	+	1	1	1	1
GCC139	MaS	4.98	30.6	15280	444	0	0.03	6.94	2.37	3754	2752	4.9	0.86	2520	158	0.66	5.4	0.29	0.06	+	1	1	1	1
GCC140	MaS	5	31	3830	33.6	76	951.6	0.19	19	3.26	610.7	231.2	2.8	0.03	647.5	252	0.6	-0.5	1.06	- (*)	1	2	2	2
GCC141	MaS	6.7	30.8	5460	52.8	184	298.9	0.26	458.4	4.54	1301	312.5	2.2	0.04	1010	99	4.4	0.1	0.78	+	1	1	1	1
GCC142	MaS	6.69	30.5	3050	64.8	104	305	0.011	0.137	0	740.8	81.25	2.2	0.132	430	28.4	2.4	0.4	0.58	+	1	1	1	1

GCC143	MaS	7.13	31.3	2110	36	108	439.2	0	51.38	0	380.4	49.42	5	3.218	284	37	0.9	0.2	0.75	+	1	1	1	1
GCC144	MaS	7.28	31.2	1661	19.2	116	347.7	0	262.6	0.01	170.2	124.7	0.6	1.132	240	36	0.5	-0.6	1.41	- (*)	1	3	3	4
GCC145	MaS	6.99	31.3	4740	33.6	76	262.3	0	80.51	0.41	270.3	119.8	1.6	0.563	192	74	1	0	0.71	+	1	2	2	2
GCC146	MaS	7.36	30.3	2160	31.2	116	414.8	12.13	138.9	1.077	310.3	176.1	6.8	0.895	208	65	0.7	0.1	0.67	+	1	2	2	2
GCC147	MaS	7.6	30.4	1405	24	96	250.1	0.505	51.9	0.85	215.2	97.81	1.7	0.595	150	40	0.9	0.1	0.7	+	1	2	2	2
GCC148	OC	8.04	31	52800	1210	384	170.8	0	0	0.01	18420	2695	5.5	0.048	9100	320	-	-	-	-	-	-	-	-
GCC149	Pa	6.83	31.4	1601	31.2	68	244	0.03	12.86	0	320.4	67.02	0.6	0.08	215	27.2	1.3	0.2	0.67	+	1	1	1	1
GCC150	Pa	7.44	30.3	732	25.44	73.6	305	0.02	7.56	0	64.07	29.3	0.4	0.04	44	2.7	0.2	0.27	0.69	-	3	3	3	3
GCC151	Pa	7.47	31.4	221	4.8	16	67.1	0.01	30.53	0	10.01	13.67	0.4	0.04	19.6	12	0.1	-2.16	1.96	- (*)	3	3	3	4
GCC152	Pa	5.47	31.6	931	23.04	56	18.3	0	117.2	0	320.4	82.75	0.1	0	184	7.8	17.5	0.4	0.57	+	1	1	1	1
GCC153	Pa	6.07	31.8	3290	26.4	63.2	201.3	2.02	0	0.14	926	43.58	2.1	0.07	610	41	4.6	0.3	0.66	+	1	1	1	1
GCC154	Pa	7.59	30.9	1253	24	32	335.5	7.35	0	0.001	250.3	0	0.5	0.026	212	24	0.7	0.1	0.85	+	1	1	1	1
GCC155	Pa	7.41	30.5	841	31.2	44	305	0.047	4.35	0.049	110.1	23.77	0.5	0.024	90	14.8	0.4	0.05	0.82	-	3	3	3	3
GCC156	Pa	7.11	27.4	792	26.4	44	244	4.27	0.49	0.028	110.1	24.48	0.3	1.632	82	9.8	0.5	0.17	0.74	-	3	3	3	3
GCC157	Pa	7.3	27.6	2550	33.6	48	329.4	0.5	0.76	0.935	120.1	19.54	0.1	0.063	100	17	0.4	0	0.83	-	1	3	3	3
GCC158	Pa	7.47	32.2	829	36	48	317.2	2.05	0.43	0.001	110.1	29.07	0.3	0.024	80	14	0.3	0.15	0.73	-	3	3	3	3
GCC159	Pa	5.23	33.6	1180	26.4	32	311.1	2.269	11.64	0.001	230.2	0	0.1	0.024	192	23	0.7	0.1	0.83	+	1	1	1	1

With (-*), (-), (+) and (++) standing for anthropogenic polluted, unaffected, slightly affected, and severely affected water samples, respectively. On the other hand, numbers such as “1,” “2,” and “3” stand for severely affected, slightly affected, and unaffected water samples, respectively. The temperature, electrical conductivity, concentration of ions, and oxydability to the KMnO4 are expressed in °C, µS.cm^{-1}, and mg.L^{-1} and mgO$_2$.L^{-1}, respectively.

Annex 4: Values of $\delta^{18}O$ and $\delta^{2}H$ and Cl^- for the CT, MaS, Pa and Ma aquifers

Sample ID	Source	$\delta^{18}O$ (‰)	$\delta^{2}H$ (‰)	Cl^- (mg.L^{-1})	Sample ID	Source	$\delta^{18}O$ (‰)	$\delta^{2}H$ (‰)	Cl^- (mg.L^{-1})
SS7	CT	-3.06	-14.91	350.385	SS25	Lag	-0.09	-0.22	961.056
SS8	CT	-3.11	-15.13	340.374	SS99	Ma	-2.98	-15.45	70.077
SS17	CT	-2.85	-14.07	370.407	SS10	MaS	-3.06	-14.5	770.847
SS18	CT	-2.75	-13.98	230.253	SS12	MaS	-3.02	-14.53	880.968

SS21	CT	-3.14	-15.1	350.39	SS13	MaS	-2.67	-12.74	320.352
SS22	CT	-3.09	-14.84	520.572	SS14	MaS	-2.99	-13.99	280.308
SS24	CT	-2.09	-11.59	310.341	SS15	MaS	-2.98	-14.61	210.231
SS31	CT	-3.22	-15.69	600.66	SS16	MaS	-3.65	-18.77	180.198
SS32	CT	-3.06	-14.74	470.517	SS26	MaS	-2.81	-13.23	300.33
SS33	CT	-3.12	-14.95	326.359	SS28	MaS	-3.42	-17.96	200.22
SS36	CT	-3.31	-15.97	250.275	SS29	MaS	-3.12	-16.07	310.341
SS37	CT	-3.27	-16.21	1401.54	SS30	MaS	-3.59	-17.86	160.176
SS43	CT	-2.98	-14.32	18.4	SS67	MaS	-2.89	-14	480.528
SS46	CT	-3.09	-13.76	70.077	SS70	MaS	-3.01	-15.6	890.979
SS48	CT	-2.92	-14.53	250.275	SS71	MaS	-3.66	-19	130.143
SS51	CT	-3.04	-13.66	170.187	SS72	MaS	-3.28	-16.35	230.253
SS53	CT	-2.74	-13.11	158.174	SS73	MaS	-3.3	-16.38	270.297
SS59	CT	-2.45	-11.93	190.209	SS74	MaS	-3.87	-19.98	100.11
SS62	CT	-3.01	-13.84	200.22	SS75	MaS	-3.48	-17.48	150.165
SS65	CT	-3.06	-14.27	158.174	SS80	MaS	-3.02	-14.43	200.22
SS69	CT	-3.23	-15.41	700.77	SS82	MaS	-3.2	-15.18	760.836
SS93	CT	-3.05	-14.25	210.231	SS39	Pa	-3.16	-16.57	140.154
SS102	CT	-3.12	-14.76	230.253	SS86	Pa	-2.89	-14.92	110.121
SS107	CT	-3.32	-16.61	1321.45	SS97	Pa	-3.14	-17.42	190.209
SS9	Lag	-0.02	-1.27	800.88					

Annex 5a: Evolution of Hydraulic Head and Precipitation for the CT Aquifer (2016—2019)

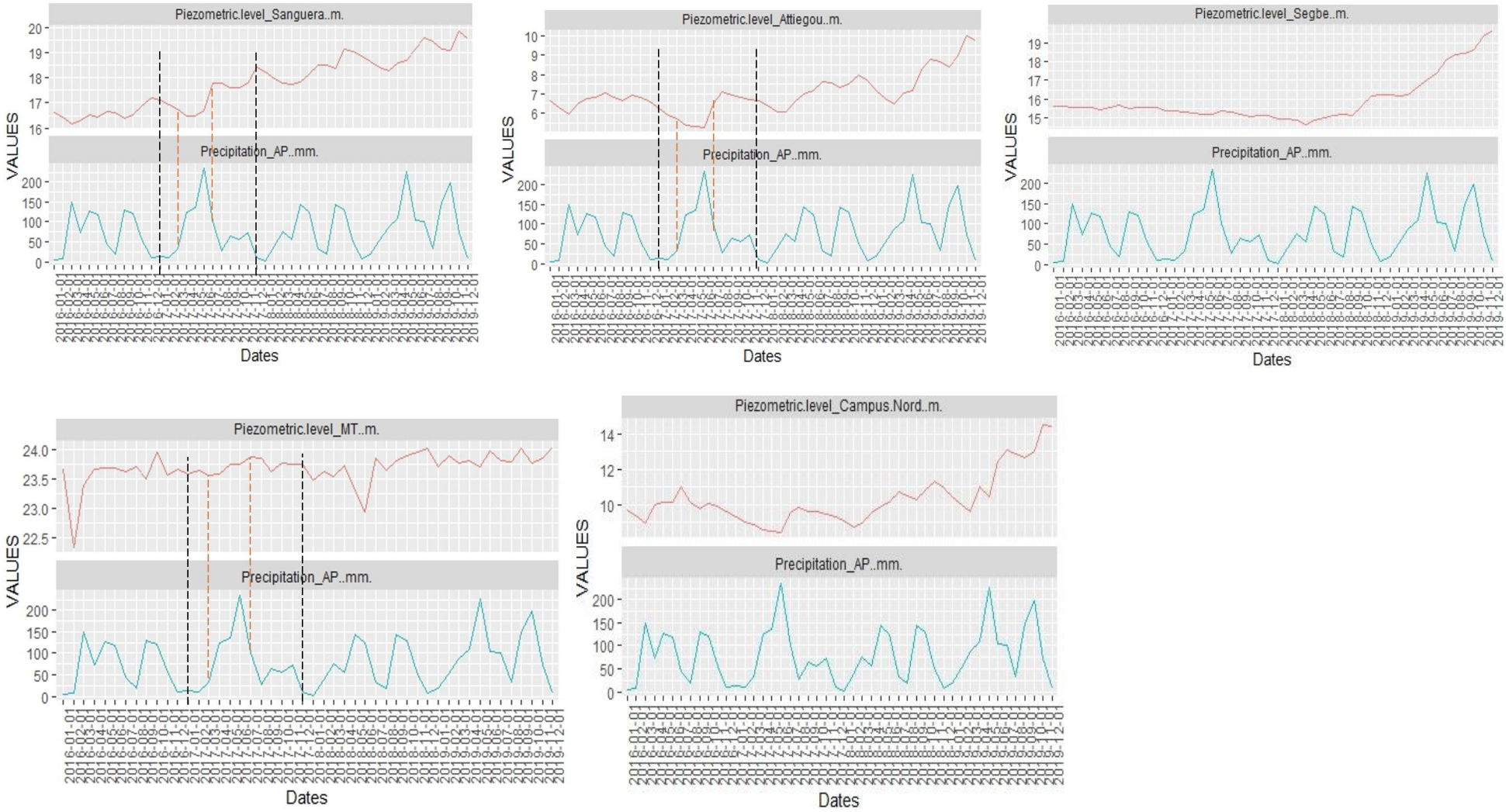

*For all the figures, the black dotted line and the red dotted line represent the annual cycle and the main season respectively

Annex 5b: Evolution of Hydraulic Head and Precipitation for the Pa Aquifer (2016—2019)

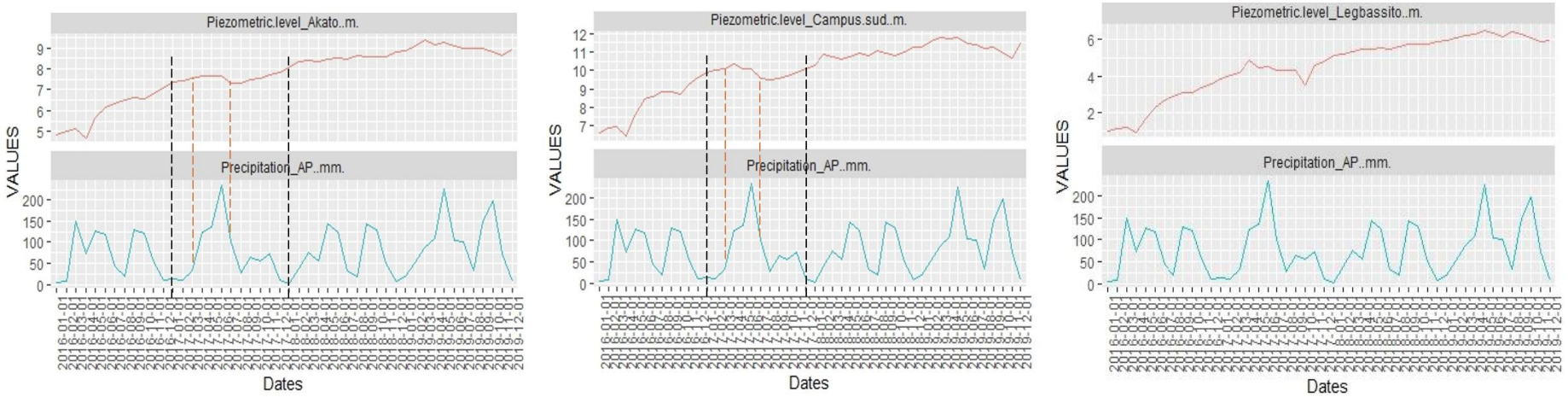

*For all the figures, the black dotted line and the red dotted line represent the annual cycle and the main season respectively

Annex 5c: Evolution of Hydraulic Head and Precipitation for the Ma aquifer (2016—2019)

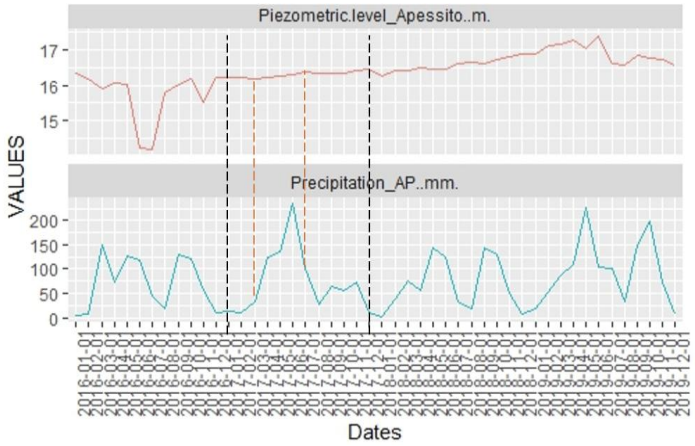

*For all the figures, the black dotted line and the red dotted line represent the annual cycle and the main season respectively

Annex 5d: Summary of the Hydraulic Head over the AP for the RS (DS)

	CT-MaS aquifer	Ma aquifer	Pa aquifer
Min	-0.74 (-2.19)	17.87 (17.43)	-13.61 (-16.91)
Max	29.50 (23.18)	30.01 (30.864)	-7.94 (-9.24)
Average	8.90 (9.42)	23.94(24.15)	-10.88 (-12.38)

Annex 5e: Hydraulic Head Computation in the AP for the RS and DS

RS 2021							DS 2022						
Aquifer	Sample	X	Y	Altitude	NS (m)	NP (m)	Aquifer	Sample	X	Y	Altitude	NS (m)	NP (m)
CT	Péage Sanguera	1.098	6.236	27.03	8.31	18.72	CT	Etat Major General-Terrain	1.210	6.208	34.681	25.21	9.471
CT	Kovié Ananisimé	1.066	6.304	77.311	47.81	29.501	CT	Tokoin Elavagnon (Near Lycée Tokoin)	1.226	6.149	19.801	6.7	13.101
CT	USP/CMS Segbé	1.112	6.194	34.06	14.89	19.17	CT	Adewi (Near EAMAU)	1.219	6.160	25.331	10.75	14.581
CT	Mission Tové Kpodonou	1.119	6.316	65.181	43.91	21.271	CT	Campus Nord	1.209	6.186	27.19	15.79	11.4
CT	EPP Mission Tové	1.119	6.316	65.181	45.55	19.631	CT	Agbalepedo	1.203	6.197	20.543	12.2	8.343
CT	Klikamé	1.208	6.18	23.465	6.97	16.495	CT	Cacaveli	1.199	6.204	29.445	26.03	3.415
CT	Reserve Escadron	1.191	6.207	32.655	24.41	8.245	CT	Kégué (Opposite stadium)	1.239	6.196	27.69	16.06	11.63
CT	Reserve 1	1.191	6.214	34.515	28.12	6.395	CT	Lycée Technique Attiegou	1.259	6.197	21.97	14.07	7.9
CT	Klikamé site 4	1.209	6.177	19.282	7.73	11.552	CT	Attiegou Station	1.266	6.187	20.207	13.96	6.247
CT	Reserve 2	1.19	6.212	34.66	28.18	6.48	CT	CMS Mission Tove	1.118	6.322	62.03	38.85	23.18
CT	Reserve Infirmerie	1.193	6.214	35.067	28.35	6.717	CT	Agoè Demakpoé	1.193	6.237	43.857	29.59	14.267

CT	Etat Major General-Méolite Next	1.223	6.207	30.162	21.01	9.152	CT	Reserve Commandement	1.193	6.211	37.002	29.39	7.612
CT	Etat Major General-Nouveau Mess	1.211	6.214	32.808	25.63	7.178	CT	Reserve Place d'armes	1.193	6.209	33.373	28.4	4.973
CT	Reserve Place d'armes	1.192	6.209	33.373	27.28	6.093	CT	Reserve SRI	1.196	6.212	37.332	29.62	7.712
CT	Agoè Télessou (TdE/F304)	1.179	6.217	38.443	31.76	6.683	CT	Reserve Logement	1.196	6.214	36.694	31.02	5.674
CT	Reserve Commandement	1.192	6.21	37.002	28.69	8.312	CT	Reserve Infirmerie	1.193	6.215	35.067	28.68	6.387
CT	Cacaveli (Ecole Neo-Humaniste)	1.197	6.203	29.537	24.44	5.097	CT	Wuiti	1.232	6.166	21.897	10.27	11.627
CT	Campus Nord	1.209	6.186	27.19	13.23	13.96	CT	Segbé Apedokoé	1.135	6.203	32.874	12.81	20.064
CT	Reserve SRI	1.195	6.211	37.332	29.47	7.862	CT	Péage Sanguera	1.098	6.237	27.03	8.4	18.63
CT	Klikamé site 2	1.209	6.169	23.602	8.1	15.502	CT	USP/CMS Segbé	1.112	6.194	34.06	14.92	19.14
CT	Reserve Logement	1.196	6.213	36.694	30.99	5.704	CT	Be Kpota	1.261	6.158	17.26	7.65	9.61
CT	Lycée Technique Attiegou	1.258	6.197	21.97	13.52	8.45	MaS	Novissi 1	1.210	6.169	23.504	1.59	21.914
CT	Cacaveli	1.198	6.204	29.445	25.95	3.495	MaS	Hanoukopé	1.217	6.138	4.159	0.5	3.659
CT	Cacaveli (A cote de la brasserie)	1.206	6.208	30.645	27.39	3.255	MaS	Nyékonakpoé 1	1.208	6.133	5.743	0.94	4.803
CT	CMS Mission Tové	1.117	6.322	62.03	38.85	23.18	MaS	Nyékonakpoé 2	1.208	6.132	5.259	1.76	3.499
CT	Agoè Koffi Panou	1.224	6.221	32.62	21.91	10.71	MaS	Nyékonakpoé (Market)	1.201	6.129	7.459	2.3	5.159
CT	Cacaveli (TdE)	1.201	6.206	38.561	32.17	6.391	MaS	Kodjoviakopé	1.209	6.119	7.219	2.38	4.839
CT	Mission Tové	1.12	6.322	57.275	41.15	16.125	MaS	Be-Amoutivé	1.207	6.168	20.137	1.85	18.287
CT	Etat Major General-Terrain	1.21	6.208	34.681	25.18	9.501	MaS	Beach (WACA Project)	1.220	6.119	0	2.19	-2.19

CT	Mission Tove Kpodonou	1.12	6.322	57.275	47.99	9.285	MaS	Gbadago	1.215	6.151	12.191	1.31	10.881
Ma	EPC Apéssito	1.138	6.288	56.67	38.8	17.87	MaS	Age Akomé	1.232	6.133	8.287	2.3	5.987
Ma	Kovié Sévagbleta	1.082	6.306	80.154	50.14	30.014	MaS	Béniglato	1.234	6.131	6.755	2.65	4.105
MaS	Hanoukopé 1	1.215	6.14	2.281	1.34	0.941	MaS	Souza Netigomé	1.243	6.134	6.99	1.61	5.38
MaS	Hanoukopé 2	1.217	6.138	4.159	0.46	3.699	MaS	Be Kamalado	1.247	6.134	4.432	2.2	2.232
MaS	Hanoukopé 3	1.215	6.14	2.262	1.33	0.932	MaS	Be Château (Near fraternité school)	1.247	6.139	7.927	1.69	6.237
MaS	Hanoukopé 4	1.214	6.141	4.475	1.22	3.255	Ma	Kovié Sévagbleta	1.083	6.307	80.154	49.29	30.864
MaS	Gbadago 3	1.217	6.142	7.083	2.21	4.873	Ma	EPC Apéssito	1.139	6.289	56.67	39.24	17.43
MaS	Hanoukopé 5	1.216	6.138	2.549	0.15	2.399	Pa	Campus Sud	1.212	6.171	23.75	40.66	-16.91
MaS	Kotokoukondji 1	1.255	6.132	1.592	1.23	0.362	Pa	EPP Akato-Segbé	1.103	6.186	32.01	42.99	-10.98
MaS	Kotokoukondji 2	1.277	6.141	7.626	1.05	6.576	Pa	CEG Légbassito	1.155	6.263	60	69.24	-9.24
MaS	Gbadago	1.218	6.142	6.526	3.42	3.106							
MaS	Along the beach 1	1.256	6.132	0.14	0.58	-0.44							
MaS	Along the beach 2	1.255	6.132	0.008	0.75	-0.742							
Pa	CEG Légbassito	1.154	6.263	60	67.94	-7.94							
Pa	Boka (TdE)	1.2	6.134	4.836	15.83	-10.994							
Pa	EPP Akato-Segbé	1.102	6.186	32.01	42.98	-10.97							
Pa	Campus Sud	1.212	6.171	23.75	37.36	-13.61							

Annex 6: Lithological Materials Succession for the CT Aquifer

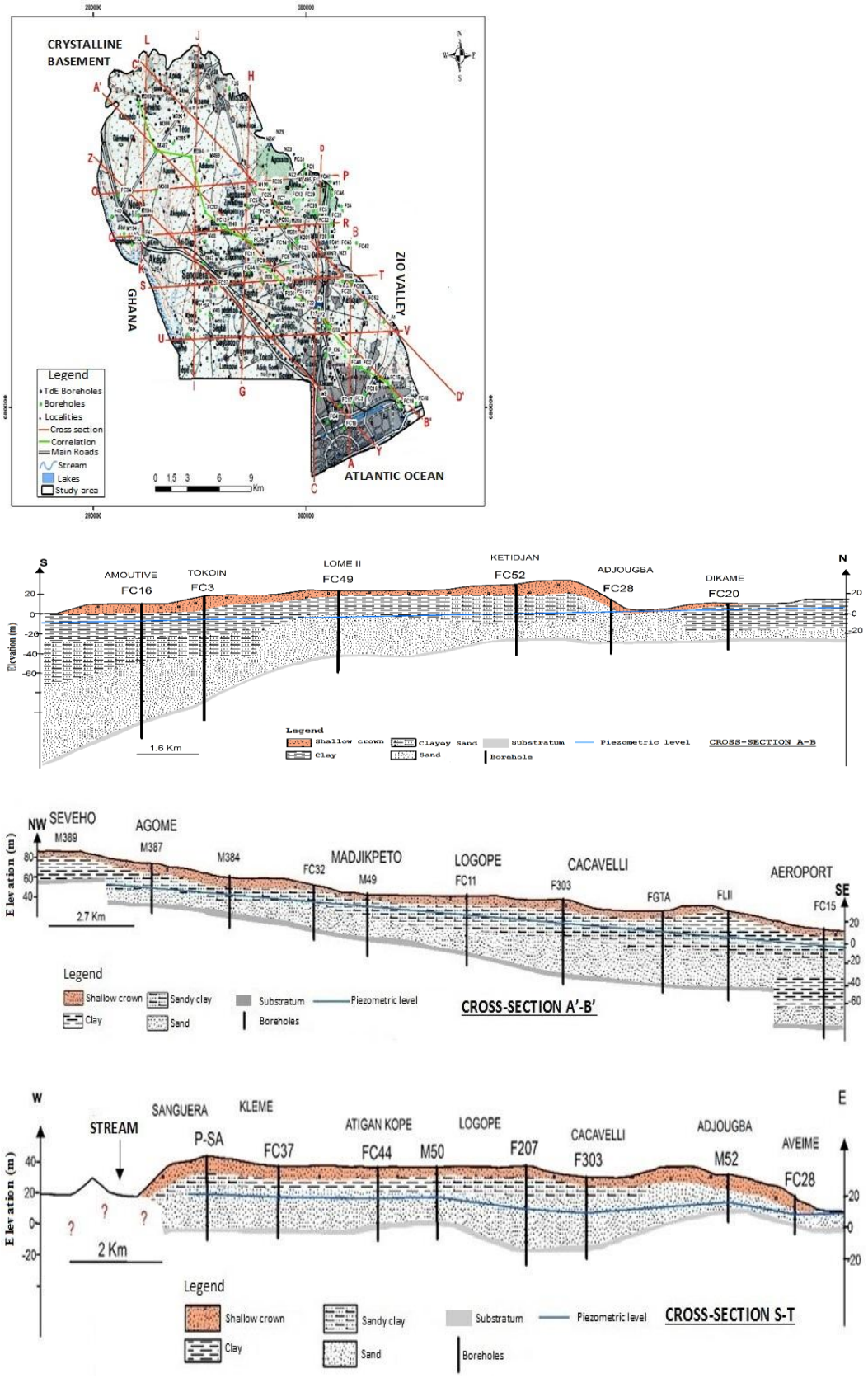

Source : Bleza et al., 2020b (Modified)

Annex 7: Stratigraphic Log of Borehole in Ramatou Beach

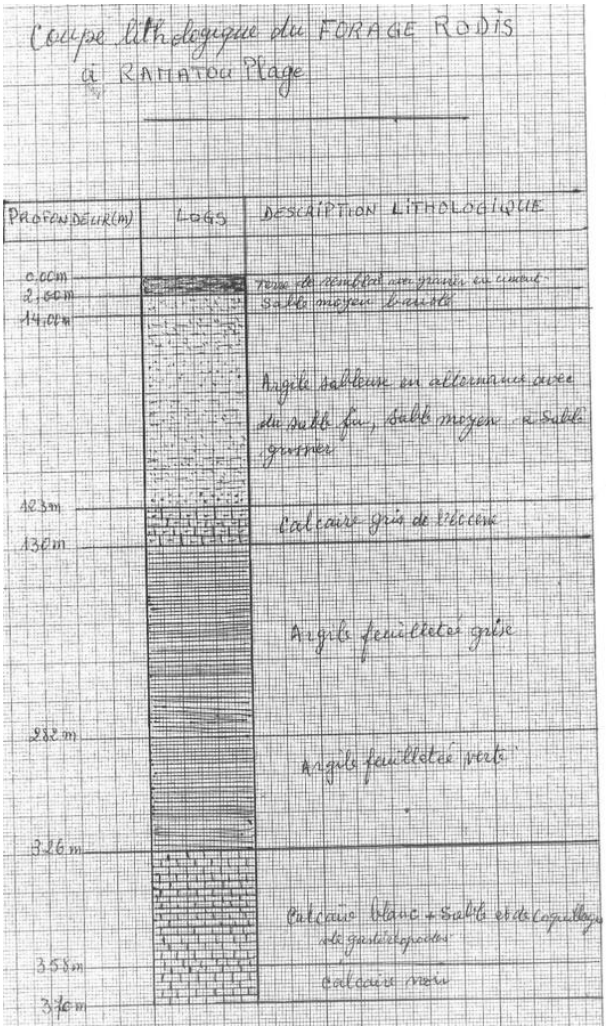

Annex 8a: LULC Classes Distribution by Sub-basin for 2001, 2011, 2020 and 2050 (km^2)

Sub-basin	LULC	Years				
		2001	2011	2020	2030	2050
A	Built-up Areas	12.71	7.12	33.72	58.58	107.17
	Croplands/Bare Surfaces	102.59	149.96	129.33	110.16	64.73
	Mixed Vegetation/Savannah	30.32	16.82	10.57	4.62	1.57
	Water Bodies	0.0072	0.0009	0.0009	0	0
	Wetlands	28.43	0.16	0.43	0.19	0.09
	Total area	174.06	174.06	174.06	173.55	173.57
B	Built-up Areas	46.31	93.03	123.26	127.13	129.94
	Croplands/Bare Surfaces	77.99	37.53	7.36	3.50	1.07
	Mixed Vegetation/Savannah	1.67	0.02	0.45	0.33	0.05
	Water Bodies	0.07	0	0.012	0.008	0.008
	Wetlands	5.23	0.70	0.20	0.10	0.03
	Total area	131.28	131.28	131.28	131.08	131.10
C	Built-up Areas	85.61	97.69	104.91	109.73	110.03
	Croplands/Bare Surfaces	25.13	4.60	4.80	0.68	2.01
	Mixed Vegetation/Savannah	0	0	1.71	1.26	0

	Water Bodies	2.91	2.90	2.33	2.12	2.119
	Wetlands	0.94	9.40	0.35	0.42	0.040
	Total area	114.59	114.59	114.59	114.20	114.199

Annex 8b: CN Values Sub-Basin Over the Considered Years

Sub-basin	Parameters	Years				
		2001	2011	2020	2030	2050
A	Total area	174.06	174.06	174.06	173.55	173.57
	Ultimate CN	68.60	65.67	68.63	71.02	75.05
	Approximative CN	69	66	69	71	75
B	Total area	131.28	131.28	131.28	131.08	131.10
	Ultimate CN	73.28	76.91	79.46	79.79	80.10
	Approximative CN	73	77	79	80	80
C	Total area	114.59	114.59	114.59	114.20	114.20
	Ultimate CN	79.76	83.21	81.25	81.79	82.09
	Approximative CN	80	83	81	82	82

Annex 8c: Estimate of Runoff using Curve Number Method

Months	Rainfall (mm)	S_A	Ia_A	S_B	Ia_B	S_C	Ia_C	Q_A	Q_B	Q_C
LULC_CC_2001										
Ann Total	756.95	3475.09	695.02	2956.67	591.33	2037.12	407.42	80.22	105.48	174.2
Run Coef								0.11	0.14	0.23
LULC_CC_2011										
Ann Total	922.56	3919.93	783.99	2317.32	463.46	1638.36	327.67	102.15	223.59	317
Run Coef								0.1	0.22	0.25
LULC_CC_2020										
Ann Total	791.85	3471.84	694.37	2124.63	424.93	1947.36	389.47	80.39	176.24	195.9
Run Coef								0.1	0.22	0.25
LULC_CC (RCP4.5) _2030										
Ann Total	823.86	3182.21	636.44	2021.76	404.35	1773.46	354.69	67.19	153.12	183.3
Run Coef								0.08	0.19	0.22
LULC_CC(RCP8.5) _2030										
Ann Total	834.65	3081.74	616.35	1955.82	391.16	1715.66	343.13	128.34	212.16	240.3
Run Coef								0.15	0.25	0.29
LULC_CC (RCP4.5) _2050										
Ann Total	845.74	2624.34	524.87	2040.84	408.17	1790.18	358.04	107.26	157.09	185.6
Run Coef								0.13	0.19	0.22

LULC_CC(RCP8.5) _2050										
Ann Total	1038.31	2526.95	505.39	1962.56	392.51	1721.57	344.31	193.08	263.7	302.4
Run Coef								0.19	0.25	0.29
CC_RCP4.5_2030										
Ann Total	823.86	3450.14	690.03	2110.88	422.18	1934.57	386.91	55.03	143.82	162.9
Run Coef								0.07	0.17	0.2
CC_RCP8.5_2030										
Ann Total	834.65	3342.59	668.52	2043.13	408.63	1870.46	374.09	115.98	203.03	222
Run Coef								0.14	0.24	0.27
CC_RCP4.5_2050										
Ann Total	845.74	3480.93	696.19	2130.16	426.03	1953.1	390.62	61.74	148.14	166.7
Run Coef								0.07	0.18	0.2
CC_RCP8.5_2050										
Ann Total	1038.31	3353.6	670.72	2050.07	410.01	1877.02	375.4	124.53	250.99	277
Run Coef								0.12	0.24	0.27
LULC2030										
Ann Total	791.9	3202.6	640.5	2034.9	407	1785	357	94.22	185.86	215.6
Run Coef								0.12	0.23	0.27
LULC 2050										
Ann Total	791.85	2617.34	523.47	2034.91	406.98	1784.98	357	132.25	185.86	215.6
Run Coef								0.17	0.23	0.27

*Run Coef stands for Runoff Coefficient and Ann Total stands for Annual total

Annex 9a: Recharge Estimation over AP (based on Coutagne method for the AET Estimate)

Time steps	P_{annual}	T_{mean}	l/8	l/2	1-p/l	$P_{annual} * \frac{1 - P_{annual}}{l}$	Effective Rain	Q_A	Q_B	Q_C	R_A	R_B	R_C	R_A (%)	R_B (%)	R_C (%)
Scenario 1: LULC and CC																
2001	757.0	26.8	568.4	2273.8	0.8	631.0	126.0	80.2	105.5	174.2	45.8	20.5	-48.2	6.0	2.7	-6.4
2011	922.6	26.7	567.1	2268.4	0.8	735.0	187.6	102.2	223.6	317.0	85.4	-36.0	-129.4	9.3	-3.9	-14.0
2020	791.9	27.0	572.2	2288.6	0.8	654.9	137.0	80.4	176.2	195.9	56.6	-39.3	-58.9	7.1	-5.0	-7.4
2030_RCP4.5	823.9	27.1	573.7	2294.8	0.8	676.0	147.9	67.2	153.1	183.3	80.7	-5.2	-35.4	9.8	-0.6	-4.3
2030_RCP8.5	834.6	27.8	585.8	2343.1	0.8	686.0	148.7	128.3	212.2	240.3	20.3	-63.5	-91.6	2.4	-7.6	-11.0
2050_RCP4.5	845.7	27.4	580.3	2321.1	0.8	691.7	154.1	107.3	157.1	185.6	46.8	-3.0	-31.6	5.5	-0.4	-3.7
2050_RCP8.5	1038.3	28.6	601.0	2404.2	0.8	814.1	224.2	193.1	263.7	302.4	31.1	-39.5	-78.2	3.0	-3.8	-7.5
Scenario 2: LULCC																
2030	791.9	27.0	572.2	2288.6	0.8	654.9	137.0	94.2	185.9	215.6	42.8	-48.9	-78.6	5.4	-6.2	-9.9
2050	791.9	27.0	572.2	2288.6	0.8	654.9	137.0	132.2	185.9	215.6	4.7	-48.9	-78.6	0.6	-6.2	-9.9
Scenario 3: CC																
2030_RCP4.5	823.9	27.1	573.7	2294.8	0.8	676.0	147.9	55.0	143.8	162.9	92.9	4.1	-15.0	11.3	0.5	-1.8
2030_RCP8.5	834.6	27.8	585.8	2343.1	0.8	686.0	148.7	116.0	203.0	222.0	32.7	-54.4	-73.4	3.9	-6.5	-8.8
2050_RCP4.5	845.7	27.4	580.3	2321.1	0.8	691.7	154.1	61.7	148.1	166.7	92.3	5.9	-12.6	10.9	0.7	-1.5
2050_RCP8.5	1038.3	28.6	601.0	2404.2	0.8	814.1	224.2	124.5	251.0	276.9	99.7	-26.8	-52.7	9.6	-2.6	-5.1

Annex 9b: Recharge Estimation over AP (based on Turc Method for the AET Estimate)

Time steps	P_{annual}	T_{mean}	l_T	$\frac{P}{l_T}$	$\frac{P_{annual}}{\sqrt{0.9 + \frac{P_{annual}^2}{l_T^2}}}$	Q_A	Q_B	Q_C	R_A	R_B	R_C	R_A (%)	R_B (%)	R_C (%)
Scenario 1: LULCC and CC														
2001	757.0	26.8	1005.03	0.75	624.91	80.2	105.5	174.2	51.8	26.6	-42.2	6.8	3.5	-5.6
2011	922.6	26.7	1002.92	0.92	698.15	102.2	223.6	317.0	122.2	0.8	-92.6	13.3	0.1	-10.0

LI

2020	791.9	27.0	1010.90	0.78	643.64	80.4	176.2	195.9	67.8	-28.0	-47.7	8.6	-3.5	-6.0
2030_RCP4.5	823.9	27.1	1013.36	0.81	659.41	67.2	153.1	183.3	97.3	11.3	-18.8	11.8	1.4	-2.3
2030_RCP8.5	834.6	27.8	1032.51	0.81	669.66	128.3	212.2	240.3	36.6	-47.2	-75.3	4.4	-5.7	-9.0
2050_RCP4.5	845.7	27.4	1023.78	0.83	672.32	107.3	157.1	185.6	66.2	16.3	-12.2	7.8	1.9	-1.4
2050_RCP8.5	1038.3	28.6	1056.77	0.98	760.23	193.1	263.7	302.4	85.0	14.4	-24.3	8.2	1.4	-2.3
Scenario 2: LULCC														
2030	791.9	27.0	1010.90	0.78	643.64	94.2	185.9	215.6	54.0	-37.7	-67.4	6.8	-4.8	-8.5
2050	791.9	27.0	1010.90	0.78	643.64	132.2	185.9	215.6	16.0	-37.7	-67.4	2.0	-4.8	-8.5
Scenario 3: CC														
2030_RCP4.5	823.9	27.1	1013.36	0.81	659.41	55.0	143.8	162.9	109.4	20.6	1.5	13.3	2.5	0.2
2030_RCP8.5	834.6	27.8	1032.51	0.81	669.66	116.0	203.0	222.0	49.0	-38.0	-57.1	5.9	-4.6	-6.8
2050_RCP4.5	845.7	27.4	1023.78	0.83	672.32	61.7	148.1	166.7	111.7	25.3	6.7	13.2	3.0	0.8
2050_RCP8.5	1038.3	28.6	1056.77	0.98	760.23	124.5	251.0	276.9	153.5	27.1	1.1	14.8	2.6	0.1

Annex 10: Comparison of Observed and Calculated Heads and Concentration for the Year 2021

Well characteristics			Head (m)			Concentration ($mg.L^{-1}$)		
Well ID	X[m]	Y[m]	Observed	Calculated	Residual	Observed	Calculated	Residual
GCC2	303412.1	686479.2	8.81	8.05	-0.76	388	895.46	507.46
GCC6	298535.7	687589.0	5.31	8.80	3.49	517	397.4	-119.6
GCC7	303552.5	688072.8	9.99	6.82	-3.17	815	351.03	-463.97
GCC12	286048.9	697242.5	30.53	33.56	3.03	149	412.31	263.31
GCC13	291997.6	698564.5	17.84	23.57	5.73	770	375.43	-394.57
GCC15	301831.3	683130.6	12.83	12.33	-0.50	1088	1320.95	232.95
GCC16	301538.2	686577.2	3.92	7.95	4.03	563	748.3	185.3
GCC20	301947.3	686567.6	9.06	7.90	-1.16	718	870.34	152.34
GCC22	291771.6	699223.8	24.73	24.82	0.08	773	425.32	-347.68
GCC23	302150.0	687245.4	6.01	7.76	1.76	474	856.98	382.98

GCC28	300387.1	686938.5	11.08	8.17	-2.91	571	522.21	-48.79
GCC30	300450.7	687192.5	10.32	8.15	-2.17	508	511.36	3.36
GCC31	299927.1	686470.1	8.26	8.31	0.06	718	516.04	-201.96
GCC32	300591.8	686086.3	4.87	8.17	3.30	834	611.62	-222.38
GCC33	300060.0	686862.7	9.87	8.27	-1.61	660	502.11	-157.89
GCC34	300116.4	687294.1	8.36	8.25	-0.11	321	480.87	159.87
GCC46	300951.8	686389.3	6.75	8.07	1.31	458	635.73	177.73
GCC47	307343.6	685319.7	8.45	6.91	-1.54	2380	1659.56	-720.44
GCC49	301838.7	684143.5	13.96	10.87	-3.09	1158	1515	357

Annex 11: Changes in the Recharge over the AP based on MODFLOW Run Results (m^3/year)

Baseline (2021)	CC 4.5		CC 8.5		LULC		LULC-CC4.5		LULC-CC8.5	
	2030	2050	2030	2050	2030	2050	2030	2050	2030	2050
129150309.80	228205411 (76.90%)	236510005 (83.33%)	82120971 (-36.34%)	254908803 (97.60%)	100325982 (-22.23%)	21290501 (-83.50%)	190864062 (47.95%)	130954645 (1.51%)	57267514 (-55.61%)	116746904 (-9.50%)

*Values in parentheses represent changes in recharge estimated in percentage

*CC, LULC LULC-CC stand for Climate Change, Land Use Land Cover and a combination of Land use land cover and Climate change, respectively.

Annex 12: List of Publications

Yomo, M., Yalo, N., Gnazou, M.D., Silliman, S.E., Larbi, I., Mourad, K. A. (2023). Forecasting land use and land cover dynamics using combined remote sensing, machine learning algorithm and local perception in the Agoènyivé Plateau, Togo. *Remote Sensing Applications: Society and Environment, 30*, 100928. https://doi.org/10.1016/j.rsase.2023.100928

CANDIDATE BIOGRAPHY

Togolese by nationality, Miss Mawulolo Yomo is a PhD candidate in the Graduate Research Program in Climate Change and Water Resources Program (University of Abomey-Calavi, Benin) under the West African Science Service Center on Climate Change and Adapted Land Use (WASCAL), funded by the German Government. Her journey began at the University of Lomé, where she earned her bachelor's degree in environmental sciences in 2011. Standing for research-driven decision-making in a changing environment, she secured German government scholarships under WASCAL and the Pan African University Institute of Water and Energy Sciences (PAUWES), crowned with master's degrees in climate change and human security in 2015 (University of Lomé, Togo) and water science in 2018 (University of Tlemcen, Algeria), respectively. Her research achievements and future endeavors to contribute to water security have won her the L'Oréal-UNESCO For Women in Science award in 2022. She authored the article "Forecasting land use and land cover dynamics using combined remote sensing, machine learning algorithms, and local perception in the Agoènyivé Plateau, Togo."

ABSTRACT

In coastal settings where groundwater is an important resource for industries and serves as the source of drinking water for a growing population, such as the Agoènyivé plateau (AP) – which holds up to 25 percent of the national population and is characterised by strong population growth and urbanisation rates – anticipating the response of groundwater lens (its quality and quantity) to changes in climate, land use and land cover (LULC), as well as continuous groundwater withdrawal, becomes essential. This step is required to ensure the sustainability of the resource but also protect the ecosystem that holds it.

The hydrochemistry and isotopic signatures of water samples considered in the AP revealed that seawater is one of the key pathways for the mineralization of existing aquifers, especially for the upper aquifers (Continental Terminal and the Coastal Marine Sands), with the occurrence of chlorinated sodic-potassic and hyper-chlorinated sodic facies. These findings were confirmed by the Electrical Resistivity Tomography profiles, suggesting both a lateral intrusion (2.5 km inland) and an up coning, with the seawater-freshwater interface, found at an average depth of 21 m with a thickness between 10 and 28 m.

The successfully calibrated and validated SEAWAT model for the upper aquifers of the AP, which showed R^2, KGE, and NSE ranging between 0.6 and 0.9, 0.7 and 0.9, and 0.5 and 0.9, respectively, captured the dynamics of seawater intrusion under various scenarios. These scenarios included increasing groundwater withdrawal rate (A); recharge estimates based on current and future LULC and climate parameters (B1, B2, B3); sea level rise (C); and a combination of all scenarios (D). The results revealed an expected increase in salinity (TDS) in areas close to the ocean and near the Cacaveli and Agoè Télessou water pumping fields (Obs 14 and Obs 15). By 2030/2050, salinity values are projected to range between 2.5/71.3 and 8739.6/22799.6 $mg.L^{-1}$ for scenario A, 7.33/142.73 and 8739.38/22776.98 $mg.L^{-1}$ for scenario B1, 236.5/1363.51 and 8741/22842 $mg.L^{-1}$ for scenario B2, 243.42/1363 and 8740.66/22810.65 $mg.L^{-1}$ for scenario B3, 0.05/51.43 and 10291.49/25228.78 $mg.L^{-1}$ for scenario C, and 0/44.38 and 10290.03/25211.85 $mg.L^{-1}$ for scenario D. These findings confirm the lateral intrusion and up coning of seawater in the upper aquifers of the AP, as highlighted by other methods. The intruded area is expected to increase by 2.2% and 3.1% by 2030 and 2050, respectively under scenario D, compared to 2021.

***Key Words*:** Agoènyivé Plateau, Climate change, Electrical Resistivity Tomography, Land use and land cover change, Modelling, SEAWAT

PhD

Mawulolo YOMO

DYNAMICS OF SEAWATER INTRUSION IN THE COASTAL SEDIMENTARY BASIN OF TOGO UNDER CLIMATE CHANGE AND LAND USE AND LAND COVER CHANGE. A CASE STUDY OF THE MULTI-LAYERED AQUIFER OF THE AGOENYIVE PLATEAU

GRP/CCWR/INE/WASCAL – UAC, November 2024